University of Alberta

Serviceability of Graphitized Carbon Steel

by

Evan Vokes

©

A thesis submitted to the Faculty of Graduate Studies and Research in partial fulfillment of the

requirements for the degree of *Master of Science*

in

Materials Engineering

Department of *Chemical and Materials Engineering*

Edmonton, Alberta

Spring 2005

0-494-08166-X

Library and Archives Canada

Published Heritage Branch

395 Wellington Street
Ottawa ON K1A 0N4
Canada

Bibliothèque et Archives Canada

Direction du Patrimoine de l'édition

395, rue Wellington
Ottawa ON K1A 0N4
Canada

Your file *Votre référence*
ISBN:
Our file *Notre reference*
ISBN:

NOTICE:
The author has granted a non-exclusive license allowing Library and Archives Canada to reproduce, publish, archive, preserve, conserve, communicate to the public by telecommunication or on the Internet, loan, distribute and sell theses worldwide, for commercial or non-commercial purposes, in microform, paper, electronic and/or any other formats.

The author retains copyright ownership and moral rights in this thesis. Neither the thesis nor substantial extracts from it may be printed or otherwise reproduced without the author's permission.

AVIS:
L'auteur a accordé une licence non exclusive permettant à la Bibliothèque et Archives Canada de reproduire, publier, archiver, sauvegarder, conserver, transmettre au public par télécommunication ou par l'Internet, prêter, distribuer et vendre des thèses partout dans le monde, à des fins commerciales ou autres, sur support microforme, papier, électronique et/ou autres formats.

L'auteur conserve la propriété du droit d'auteur et des droits moraux qui protège cette thèse. Ni la thèse ni des extraits substantiels de celle-ci ne doivent être imprimés ou autrement reproduits sans son autorisation.

In compliance with the Canadian Privacy Act some supporting forms may have been removed from this thesis.

While these forms may be included in the document page count, their removal does not represent any loss of content from the thesis.

Conformément à la loi canadienne sur la protection de la vie privée, quelques formulaires secondaires ont été enlevés de cette thèse.

Bien que ces formulaires aient inclus dans la pagination, il n'y aura aucun contenu manquant.

Canada

DEDICATION

To my eternal supporters

Thank you for making it possible

Elizabeth and Earle Vokes

Lorinda Scott

ABSTRACT

Serviceability of Graphitized Carbon Steel

Evan Vokes

Department of Chemical and Materials Engineering

University of Alberta, Edmonton, Alberta, Canada T6G 2G6

Long service periods of stress near 0.4 Tm of A106 Gr. B plain carbon steel power piping has resulted in significant degradation in microstructure in the heavily mechanically deformed fittings and elbows, but minimal microstructure degradation in the seamless piping. Effects of microstructure changes for plain carbon steels have not been documented in these applications. The characterization of microstructure damage was most often manifested as random graphite but a limited amount of planar graphite was present. The study looked at: creep deformation mechanisms, fracture mechanisms, mechanical properties and evolution of microstructure. Results include: failure criteria, serviceability rankings and remaining life prediction, as well as practical models and techniques for in situ life prediction.

ACKNOWLEDGEMENTS

The author would like to express his heartfelt gratitude to Dr Chen for giving this project to myself and furthermore for understanding during the tribulations endured with this project

The author would also like to thank many outside persons for assistance in this endeavour

The dedicated computer specialist who spent many nights on the phone

Robert Marcil

My peers who helped when the call went out

Preston Holloway

Walid Bouaeshi

Mutual Assistance from Canspec Material Engineering with special thanks to

Rob Stewart

Kurtis Kaminsky

Spark analysis services from

Alta Steel

Department Staff who went out of their way to help

Walter Bodez and Les Dean

Tina Barker

Financial Assistance by Natural Science and Engineering Research Council

Financial and Machine Shop services from Nova Chemicals who exercised due diligence to investigate this problem

TABLE OF CONTENTS

1. PREFACE 1

1.1. PROBLEM DEFINITION 1

1.2. RESEARCH OBJECTIVES 2

1.3. THESIS OUTLINE 3

2. MATERIAL PERFORMANCE REQUIREMENTS FOR HIGH TEMPERATURE, HIGH PRESSURE CARBON STEEL PIPING 5

2.1. DESIGN REQUIREMENTS 5

2.2. MANUFACTURE OF SEAMLESS PIPING MATERIALS 5

2.3. JOINING PROCESS 7

2.4. HIGH TEMPERATURE MATERIAL DESIGN REQUIREMENTS 8

3. SECONDARY GRAPHITIZATION IN CARBON STEELS OPERATED AT HIGH TEMPERATURE AND HIGH PRESSURE 9

3.1. HISTORY OF SECONDARY GRAPHITIZATION 9

3.1.1. Discovery and History of Secondary Graphitization Failures 9

3.1.2. Historically Accepted Graphite Formation Mechanisms 11

3.2. FACTORS CONTROLLING GRAPHITIZATION 13

3.2.1. Chemistry 13

3.2.2. Thermodynamic Driving Force 15

3.2.3. Evidence of the Thermodynamic Driving Force 18

3.2.4. Unstable Precursory Microstructures 18

3.2.5. Effects of Plastic Deformation on Metastable Microstructure 20

3.2.6. Nucleation of Graphite in Weldments 22

3.3. GROWTH OF SECONDARY GRAPHITE 23

3.4. EFFECT OF GRAPHITIZATION ON SERVICEABILITY 24

4. FITNESS FOR SERVICE (FFS) REQUIREMENTS FOR HIGH TEMPERATURE DAMAGED COMPONENTS 28

4.1. RATIONALIZATION OF METHODS OF ANALYSIS 28

4.1.1. Effects of Carbide Forming Elements and Microstructure 29

4.1.2. Strain Capacity and Ductility of Materials 30

4.1.3. Effects of Aging Materials 31

4.2. CREEP BASED LIFE PREDICTION 32

4.2.1. Creep Testing and Creep Deformation 32

4.2.2. Creep Life Prediction Fundamentals 35

4.3. MICROSTRUCTURE CONCERNS 54

4.3.1. What Constitutes Microstructure Damage 54

4.3.2. Damage Measurement by Microstructure Methods 56

4.3.3. Effect of Creep on Joined Piping Materials 59

4.4. FRACTURE MECHANICS BASED METHODS 62

4.4.1. Potential for Fracture 63

4.4.2. Low Temperature Fracture 65

4.5. IN-SITU METHODS FOR LIFE PREDICTION 66

4.5.1. Non-Destructive Examination 66

4.5.2. Small Punch Testing 67

4.5.3. Damage Measurement by Hardness Based Methods 69

4.5.4. Neutron Diffraction 71

4.6. METHODOLOGY OF FITNESS FOR SERVICE 73
4.6.1. Historic Accepted FFS methods 73
4.6.2. API RP 579 74
4.7. NECESSITY OF UNDERSTANDING ALL CONDITIONS AFFECTING THE FITNESS FOR SERVICE PROBLEM 76
5. PIPING SELECTION AND PRELIMINARY RESULTS 78
5.1. DIRECTION OF INVESTIGATION 78
5.2. PIPING SCHEMATIC AND PRELIMINARY MATERIAL SELECTION 78
5.3. PRELIMINARY MICROSTRUCTURE AND HARDNESS FOR CURRENT INVESTIGATION 80
6. EXPERIMENTAL METHODS 83
6.1. CHEMISTRY 83
6.2. MICROSTRUCTURE AND PHASE DETERMINATION 83
6.2.1. Sample Preparation 83
6.2.2. Microstructure and Image Analysis 84
6.2.3. Macrostructure 85
6.2.4. Graphitization Analysis 85
6.2.5. Sulfur Printing 86
6.3. HARDNESS TESTING 86
6.4. TENSILE TESTING 88
6.5. HOT TENSILE TESTING 88
6.6. CREEP TESTING 91
6.6.1. Collection of Data 92

6.6.2. Creep Material Selection and Evolution 93
6.7. FRACTURE MECHANICS 94
7. RESULTS 97
7.1. QUANTITATIVE CHEMISTRY RESULTS 97
7.2. CHARACTERIZATION OF MICROSTRUCTUE AND PHASE DEGRADATION 98
7.2.1. Characterization of Microstructure 98
7.2.2. Graphitization Results 111
7.2.3. Qualitative Chemistry and Phase Analysis 117
7.2.4. Sulfur Print Results 118
7.2.5. Neutron Scattering Results 121
7.3. CHARACTERIZATION BY HARDNESS TESTING 121
7.4. CHARACTERIZATION BY TENSILE TESTING 125
7.5. CHARACTERIZATION OF ELEVATED TEMPERATURE PROPERTIES BY HOT TENSILE TESTING 131
7.6. CHARACTERIZATION OF FRACTURE POTENTIAL 135
7.7. CHARACTERIZATION OF CREEP PROPERTIES 137
7.7.1. Creep Characteristics 137
7.7.2. Creep Data Summary 140
7.7.3. Stress Sensitivity of Norton's Law 143
7.7.4. Relationship of Creep Elongation to Creep Life 147
7.7.5. Microstructure Effects of Graphite on Creep 148
7.7.6. Creep Mechanisms of Graphitized Steel 150

7.7.7. Creep Effects of Graphite on Weld Microstructure 151
7.8. PRELIMINARY CREEP RANKINGS OF MATERIALS 153
8. CREEP RESULT ANALYSIS 157
8.1. PARAMETRIC METHODS RESULTS 157
8.1.1. Larson Miller Parameter 157
8.1.2. Sherby-Dorn Parameter Results 165
8.1.3. Manson-Haferd Parameter Results 173
8.1.4. Aggregate Parametric Method Results 175
8.2. STRAIN RATE BASED METHODS 176
8.2.1. Monkman-Grant Method 176
8.2.2. Continuum Damage Mechanics 178
8.2.3. Omega Method 180
9. DISCUSSION 182
9.1. REPLICATION AND MICROSTRUCTURE 182
9.1.1. Evaluation of Replication 182
9.1.2. Evaluation of Microstructure 183
9.2. ROOM TEMPERATURE MECHANICAL PROPERTIES 184
9.2.1. Hardness as a Fitness For Service Method. 185
9.2.2. Comparison of Elevated and Room Temperature Mechanical Properties 190
9.3. EFFECT OF GRAPHITE ON MECHANICÀL PROPERTIES 192
9.3.1. Effect of Analysed Carbon Content on Tensile properties 192
9.3.2. Effect of Graphite on Tensile Properties 193

9.3.3. Effect of Graphite on Hardness Properties 195
9.4. DETERMINING GRAPHITE MORPHOLOGY FROM MECHANICAL PROPERTIES 197
9.4.1. Separating out Planar Graphite 197
9.4.2. Separating out Quantities of Random Graphite 198
9.4.3. Detecting Extent of Graphitization 198
9.5. EFFECT OF GRAPHTITE ON FRACTURE PROPERTIES 199
9.6. EFFECT OF GRAPHITE ON CREEP 200
9.6.1. Creep Interaction 200
9.6.2. Parametric Method Results 201
10. FUTURE WORK 207
11. CONCLUSIONS 209
11.1. CHARACTERISTICS OF MICROSTRUCTURES 209
11.1.1. Planar Graphite 209
11.1.2. Random Graphite 210
11.2. FITNESS FOR SERVICE RECOMMENDATIONS 210
11.2.1. Short Term Mechanical Properties Assessment 210
11.2.2. Residual Life Assessment 211
11.2.3. Operation and Inspection Recommendations 212
12. REFERENCES 214
13. APPENDICES 229

LIST OF TABLES

Table 2.2-1ASME SA106, SA234 and SA105 chemical specifications for pressure piping 7

Table 2.4-1 Summarized ASME design criteria [14] 8

Table 3.2-1 Diffusion data for steels showing dramatic increase in carbon diffusion rates over narrow range [30] 16

Table 4.2-1 Survey of published creep life prediction accuracies [60] 41

Table 4.3-1 McLean's methods of separating microstructural damage [74] 55

Table 4.3-2 Summary of creep designations and method proposed by Neubauer/Webel [76] 57

Table 4.5-1 NDT correlations flow sheet that may be adapted to fit particular materials [80] 67

Table 5.3-1 Compilation of Tables used to select piping materials. Based on graphitization, E1 materials elbows and fittings were researched. 82

Table 7.1-1 Nova E1 power piping section chemistries given in weight percent as per Alta Steel spark analysis. 97

Table 7.2-1 Summary of microstructure observations for E1 piping analysed in this investigation 99

Table 7.2-2 Variation of graphite volume percentage and morphology for selected E1 piping materials 112

Table 7.3-1 Hardness results showing range and average of the four methods used. 122

Table 7.4-1 Summary of room temperature tensile testing results for selected materials 126

Table 7.4-2 Ratio of mechanical strengths for materials tested 127

Table 7.5-1 Summary of Mechanical properties as determined by hot tensile testing at 427 °C 132

Table 7.7-1 Raw data from creep testing based on ASTM DS11S1 design data 142

Table 7.7-2 Matrix of creep results showing variation of temperature (°C) at prescribed stresses (psi/MPa) to set up rupture time estimations 143

Table 7.7-3 Rupture based parameters based on method from API 530 and design values. 144

Table 7.7-4 Strain rate based summary of creep stress exponent n for graphitized materials 146

Table 7.8-1 Summary of creep ranking based on raw data 156

Table 8.1-1 Variation in Sherby-Dorn parameter by material type 168

Table 8.2-1 Constant m values as derived from slope of Monkman-Grant Analysis 177

Table 8.2-2 Tabulated damage exponent ν as determined graphically using Leckie's method 179

Table 9.6-1 Subjective rankings of materials based on stress rupture performance 205

LIST OF FIGURES

Figure 3.2-1 Iron-Carbon phase diagram showing preferential stability of carbon over cementite [29] 16

Figure 3.4-1 Failure due to planar graphitization of 100 000 hr service exposed C-Mo steel [35] 27

Figure 4.1-1 Steam piping ruptured due to planar graphitization [34] 29

Figure 4.2-1 Ashby maps of pure iron and Cr Mo steels showing effects of chemistry on creep rates [53] 35

Figure 4.2-2 Effect of stress accelerated testing for ferritic materials [61] 42

Figure 4.2-3 Leckie's interpretations of microstructure conditions that determine creep damage for a low alloy steel exhibiting brittle behaviour at 500°C [68] 48

Figure 4.2-4 Criteria for Omega test validity [71] which is obtain from creep curve. Slope is $1/\Omega p$ 51

Figure 4.2-5 Important features of constant load creep curves according to Prager [70] ... 52

Figure 4.3-1 Relationship of weld damage to both microstructure and phase diagram. Types of damage in welds are shown and associated with expected microstructure (above) and critical temperatures for weld microstructure development (right) [62][80] 60

Figure 4.5-1 Relationship between hardness and creep damage for 1Cr ½ Mo rotor forgings according to Endo [94] 70

Figure 4.5-2 Neutron diffraction maps for strain analysis for one load and unload cycle [95] 72

Figure 4.5-3 Elemental sensitivity of neutron scattering contrasted with X-ray scattering [96] 72

Figure 4.6-1 Crack growth assessment from API 579 based on a FAD [98] 76

Figure 4.7-1 Estimated lifetime for different components under creep load [76] 77

Figure 5.2-1 Piping schematic from E1 WHB showing Non-Destructive Examination sites adjacent to boiler. Most of the research material comes from this section of piping and appropriate materials are labelled with their respective research designations. 79

Figure 5.3-1 Typical A106 piping microstructure consisting of proeutectic ferrite and degenerated pearlite 80

Figure 6.5-1 MTS/Instron servo-hydraulic tensile tester with hot tensile furnace and ATS extensometer is shown in the picture a. Detail of the specimen, thermocouples and extensometer are revealed in picture b..... 90

Figure 6.6-1 Custom extensometer showing split couplings used to mount dumbbell shaped samples..... 92

Figure 6.7-1 Fixture for bending SENB specimens for fracture toughness testing 96

Figure 7.1-1 Graphical representation of results of spark analysis chemistry for Nova power piping sections showing conformance to design standard. Graph b shows expanded chemistry for residual elements. 98

Figure 7.2-1 Low magnification SEM image of random graphitized Elbow 7 showing graphite nodules among proeutectic ferrite and degraded pearlite colonies..... 100

Figure 7.2-2 Planar graphitized Reducer 3 showing graphite nodules and spheroidized iron carbides in degraded pearlite colonies..... 102

Figure 7.2-3 Representative low magnification microstructure from Elbow 3 showing planar graphitization. 104

Figure 7.2-4 Elbow 7 low magnification picture which is part of a series of images used to develop macrographs 105

Figure 7.2-5 Macrostructure pictures of Elbow 4 show random graphitization in hoop direction. A slight tendency for banding may be observed. The individual overlapped micrographs are 2mm high and 3mm wide resulting in a full section nominal thickness of 12 mm 107

Figure 7.2-6 Macrostructure pictures of Elbow 4 show random graphitization in longitudinal direction. Banding of graphite nodules is apparent in this orientation. The individual overlapped micrographs are 2mm high and 3mm wide resulting in a full section nominal thickness of 12 mm..... 108

Figure 7.2-7 Macrostructure pictures of Reducer3 shows planar graphitization in hoop direction similar to Figure 4.3-.1 109

Figure 7.2-8 Macrostructure pictures of Reducer3 shows planar graphitization in longitudinal directions.. The individual overlapped micrographs are 2mm high and 3mm wide resulting in a full section nominal thickness of 12 mm 110

Figure 7.2-9 Relationship of graphite location to average graphite composite for selected material types, location as well as average composite density for hoop direction. 112

Figure 7.2-10 Relationship of graphite density relative to wall location as well as average composite density for longitudinal direction 113

Figure 7.2-11 Lack of relationship between graphite volume fraction depending on wall location for selected piping materials 115

Figure 7.2-12 SEM image of Elbow 7 inclusion showing EDX points (a) and EDX analysis (b) 117

Figure 7.2-13 Sulfur print of Elbow 3 45°, which contained graphite planes that were observable to the naked eye. The hoop direction appears on top and longitudinal direction on the bottom (a). SEM image of planar graphite in Reducer 3 showing presence of MnS (b) 118

Figure 7.2-14 Sulfur print of Elbow 1 longitudinal direction showing Pipe 1 to the left of the multipass weld and graphitized Elbow 1 to the left. Segregation of Sulfur to the center of the weld was also observed 119

Figure 7.2-15 Full wall thickness longitudinal section of Elbow 1 with outside diameter at top. The change of graphite size and density is noticeable but graphite distribution cannot be absolutely associated with sulfur distribution in the Figure 7.2-11 Elbow 1 sulfur print 120

Figure 7.3-1 Plot of relative hardnesses to show variation of hardness across selected materials and new baseline material. There is no hardness distinction between planar graphitized Reducer 3 and the random graphitized fittings and elbows although softening is evident. 123

Figure 7.3-2 Deviation of hardness methods from average hardness for selected materials and methods. Brinell hardness and Vickers hardness give the largest variation for most selected materials. Graphite morphology has no distinct effect on hardness value variation 124

Figure 7.3-3 Normalized deviation from average hardness values for selected materials and methods showing how relative error in the method increases for indentation depth methods 125

Figure 7.4-1 Exploitable mechanical properties relationships based on averaged tensile testing results. Groupings separate into 3 distinct categories 127

Figure 7.4-2 Exploitable mechanical properties relationships based on averaged tensile testing results. shows relationship between ultimate strength and elongation..... 128

Figure 7.4-3 Analysis in terms of yield strength and elongation offers similar property groupings but no exploitable trend. 129

Figure 7.4-4 Extrema of tensile testing showing high strength, limited ductility of Flange 6, and lower strength high ductility of Elbow 1 Serrated yielding is typical for all testing 130

Figure 7.5-1 Strength relationship for hot tensile testing plotted with literature values for A 106 type carbon steels. Intersection of lines is minimum design strength specified by API 530 so desired properties are in the upper right quadrant. 133

Figure 7.5-2 Hot tensile results are similar to room temperature results showing significant difference in material types. 135

Figure 7.6-1 Surface resulting from compliance testing of Elbow 1 showing fracture surface due to ductile tearing 136

Figure 7.6-2 SEM image of ductile tearing surface of Elbow 1 after compliance testing and morphology of unusual shaped graphite nodules. 137

Figure 7.7-1 Matlab generated creep curve typical of graphitized A 234 type steel showing ductile creep characteristics. New Elbow 7 tested at 525 °C and 12000 psi (82.7 MPa)..... 138

Figure 7.7-2 Matlab generated creep rate curve showing change in acceleration of true strain over time during testing. New Elbow 7 tested at 525 °C and 12000 psi (82.7 MPa) 139

Figure 7.7-3 Typical isothermal relation graph tabulated in Table 7.6-3 to determine stress exponent 'n' 145

Figure 7.7-4 Response of stress exponent of service exposed materials against expected API 530 exponential trend. Elbow 7 and New Elbow 7 should be duplicates 147

Figure 7.7-5 Strain to failure relationship for selected materials. The extreme performers are Elbow 1 and Reducer 3, where the data includes all temperatures and stresses within the selected range. 148

Figure 7.7-6 Elbow 1 tested at 550 °C and 8000psi (55.2 MPa) fracture cone (a) showing lines of graphitization that may be associated with final fracture. Cross section of the same sample (b) showing plane of graphite adjacent to fracture tip..... 150

Figure 7.7-7 Post-creep optical micrographs for Elbow 7(a) and Reducer 3(b) taken at 600 °C and 68.9MPa (10000psi) near the fracture surface 151

Figure 7.7-8 Post creep micrograph of Elbow 1 Weld tested at 525°C and 12000 psi(82.7 MPa) with direction of stress shown. Lines have been added to show the A3 temperature zone, A1 temperature zone and fusion line. The presence of graphitization starts after the A1 temperature line indicating the graphite is not a weld related effect. 152

Figure 7.8-1 Isostress analysis of materials at 10000 psi (68.9 MPa) showing 3 distinct groupings..... 154

Figure 7.8-2 Isostress analysis of materials at 8000 psi (55.2 MPa) showing similar ranking trend but lacks the 3 distinct groupings 154

Figure 7.8-3 Isothermal analysis of materials at 575 °C showing similar ranking trend but lacks the 3 distinct groupings. Elbow 7 shows significant deviation behaviour..... 155
Figure 7.8-4 Isothermal analysis of materials at 550 °C showing similar ranking trend but lacks the 3 distinct groupings. Elbow 7 shows significant deviation behaviour..... 155
Figure 8.1-1 Compilation of Stress rupture data for the universally accepted Larson-Miller parameter (LMP). Stresses ranged from 34.5MPa (5000psi) to 137.9MPa (20000psi) while temperatures ranged from 475 °C to 670 °C. 158
Figure 8.1-2 Aggregate Larson-Miller constants C for all materials. There is no trend between the materials or within groups of materials. 159
Figure 8.1-3 A full stress range of testing using Flange 6 material to develop a comprehensive Larson-Miller master for the service degraded materials. 161
Figure 8.1-4 Comparison of the New Elbow 7 and Elbow 7creep rupture properties. The rupture times and temperatures are similar for both 8000 psi (55.2 MPa) and 10000 psi (69.0 MPa) but deviate for 12000 psi (82.7 MPa) 162
Figure 8.1-5 Larson-Miller estimation for Reducer 3 showing a service exposed material that has better than average life remaining. The lower stresses show a divergent trend showing a change of creep mechanism..... 163
Figure 8.1-6 Larson –Miller parameter value scatter for Elbow 1 materials..... 164
Figure 8.1-7 Plot of Sherby-Dorn activation energy as determined from activation energy slopes as described in Figure 8.1-8. Line shows expected regression trend..... 165
Figure 8.1-8 Plot of Sherby Dorn activation energy as determined from rupture time. Value of slope is Q/R where Q is in Joules where R is the universal gas constant. The statistical correlation is very good but the values of Q/R do not follow a logical trend. 166

Figure 8.1-9 Activation energy as determined from secondary creep strain plotted as isostress creep curves. 167

Figure 8.1-10 Sherby-Dorn parameters based on secondary creep strain rate showing similar patterns but significantly more scatter range over the values of PSD. Desired trend is marked on graph 168

Figure 8.1-11 Best fit Sherby-Dorn correlation based on steady state strain rate, averaged for all materials developed using activation energy aggregate for entire data set. Valid trend line can not be developed for this material. 170

Figure 8.1-12 Rupture based Sherby-Dorn method showing usable trend for Elbow 1 material. 171

Figure 8.1-13 Strain rate based Sherby-Dorn showing improved correlation of parametric values. 172

Figure 8.1-14 Elbow 4 comparing ε_{ss} to t_r based methods. The t_r based method is more conservative until the higher stress. 173

Figure 8.1-15 Plot of Manson-Haferd parameter to determine common isostress line intersection. Point of line intersection would determine master rupture life diagram. ... 174

Figure 8.1-16 Mason-Haferd method for Flange 6 showing good statistical R^2 agreement with the data but lack of correlation of isostress lines 175

Figure 8.2-1 Composite strain rate based Monkman-Grant relationship showing loose isostress relationship to k=log tr x log εss 176

Figure 8.2-2 Isothermal plot to determine continuum damage mechanics values of ν. . 178

Figure 8.2-3 Reverse creep plot for Elbow 1 showing deviation from linear trend, negating useful Omega analysis 181

Figure 8.2-4 Strain acceleration for Elbow 1 525 °C 55.2MPa (8000psi) showing minimum creep rate achieved at half of rupture life 181

Figure 9.1-1 Sketch of Replication sites of E2 WHB showing locations only taken on piping and adjacent to weld on piping side [2] 183

Figure 9.2-1 Relationship between selected hardness methods and ultimate tensile strength. Theoretical Brinell hardness is plotted to give a reference trend. Planar graphitized Reducer 3 is found at 460 MPa while Flange 6 is shown at 495 MPa. 186

Figure 9.2-2 Raw data showing scatter for all three HRB hardness tests taken on each tensile test sample. Due to scatter in the results, only Flange 6 at 495 MPa would be distinguishable from other materials 187

Figure 9.2-3 Relationship between selected hardness methods and yield strength. Theoretical Vickers hardness is plotted to give a reference trend. Planar graphitized Reducer 3 is found at 240 MPa while Flange 6 is shown at 275 MPa 188

Figure 9.2-4 Brinell hardness relationships with respect to ductility showing poor correlations but reasonable groupings. The planar graphite shows relatively hard microstructure and is associated with the low ductility grouping 190

Figure 9.2-5 Change in tensile properties with temperature for Flange 6 and Elbow 1. This comparison shows the significant loss of strength with increased temperature. The apparent changes in ductility are not convertible due to different gauge lengths used at the different temperatures. 191

Figure 9.3-1 Effect of carbon content on mechanical strengths showing good correlation for ultimate tensile and yield strength with the exception of ultimate strength of planar graphitized Reducer 3 192

Figure 9.3-2 Relationship between volume percent graphite and average ultimate tensile strength. The planar graphite shown at 460 MPa cannot be separated from the other materials as the volume of graphite overlaps..... 194

Figure 9.3-3 Relationship between room temperature elongation and graphite volume The Planar graphite at 35 % cannot be separated from the other materials as the volume of graphite overlaps. 195

Figure 9.3-4 Relationship between hardness testing and degree of graphitization The series starts from the left with randomly graphitized Elbows 7, 12, 4, 1 and 11 and then finishes with planar graphitized Reducer 3 and finishes with random graphitized Flange 6 196

1. PREFACE

The knowledge that irons and steels may separate out free graphite from solution over time at elevated temperature has been known for 70 years. While graphitization is a highly desired characteristic of the well studied cast irons systems, it has been associated with catastrophic failure in high temperature steels. Graphite in service exposed high temperature steels was identified more than 50 years ago and is termed secondary graphitization. Secondary graphitization of high carbon steels during box annealing operations has been researched for many years but base metal graphitization of high temperature piping materials is a poorly understood problem.

1.1. PROBLEM DEFINITION

Unexpected secondary graphitization was found during a surface replication of waste heat boiler power piping that had been operated near the conservative safe design temperature. This precipitated a piping replacement program. Subsequent sectioning of one of the affected sections showed that the graphitization was observed to occur in both the base metal and near the heat affected zone. The results of the replications and microstructure investigations were presented in three Canspec Materials Engineering projects [1][2][3].

Concern was expressed at the time of the engineering analysis as the form of graphitization was not the classic form of graphitization found near welds [4] and did not fit well with accepted graphitization literature [4][5][6]. Furthermore, the accepted literature focused on steels with secondary carbide forming elements such as Chrome and

Molybdenum which have a different carbide life cycle than the basic carbide found in carbon steel, iron carbide.

1.2. RESEARCH OBJECTIVES

This study was designed to allow the client to exercise due diligence and make informed decisions with respect to safety and economy of operation of power piping. The damage is generally exemplified as microstructure degradation and the associated mechanical property degradation. Microstructure damage is embodied by the existence of coarsened or spheroidized metal carbides, graphitization and deformation of grains themselves. The mechanical damage is often accompanied by loss of mechanical strength and ductility, loss of hardness and opening of creep voids.

A proposal was put forward to characterize the degraded piping materials with three major goals of the research:

a) How dangerous is the microstructure degradation.

b) If there is no eminent danger, how much life is left in the affected materials?

c) What material properties will allow quantitative field detection of the microstructure damage?

The initial proposal suggested a broad scope of work consisting of several methods that could potentially be developed to assist in field detection of that microstructure damage.

a) Time-Temperature-Hardness Diagram

b) Hardness-Microstructure Diagram

c) Hardness-Mechanical properties Diagram

d) Residual life diagram for material with creep voids and graphite particles

Functionally, the client required a game plan to allow non destructive examination to ascertain when to take a suspect material out of service. The information presented is of a broad scope to allow comparison of facts and methods.

1.3. THESIS OUTLINE

Chapter 2 is dedicated to explaining how the material of interest is manufactured and incorporated into a design. This allows familiarity with subsequent terminology.

Chapter 3 shows the history of secondary graphitization and sums the current knowledge of what is known about graphitization in service exposed steels.

Chapter 4 consists of a comprehensive overview of fitness for service philosophy and includes methodology to characterize performance of material and potential methods to exploit the character of the material for non-destructive examination purposes.

Chapter 5 is used to explore the initial findings and how this determined the subsequent direction of the research. This work determined type and quantity of testing performed.

Chapter 6 is a summary of methods used to characterize the material, some of which are non-standard due to the unique problems posed by the material itself and by the form of the material. The methods used are predominately modeled on accepted standards.

Chapter 7 summarizes results, some of which require further analysis to comprehend.

Chapter 8 is an indepth analysis of creep results and the implications of the analysis methods used.

Chapter 9 attempts to draw damage correlation between physical properties and testing methods and the effect of graphite on these properties.

Chapter 10 summarizes work that is in progress and needs to be completed and work that should be done to exploit the character of graphitized carbon steel pipe.

Chapter 11 concludes the findings from the points of view of the material, the graphitization phenomenon and recommendations for fitness for service.

Chapter 12 References

Chapter 13 Appendixes of information that was hard to include in the thesis body or is good for future reference

2. MATERIAL PERFORMANCE REQUIREMENTS FOR HIGH TEMPERATURE, HIGH PRESSURE CARBON STEEL PIPING

2.1. DESIGN REQUIREMENTS

Seamless carbon steel power piping was developed in the early years of boilers to deal with the low quality of seam welding that was predominant in longitudinal welding. The design conditions of power and process piping are covered under ASME B31.1 and B31.3. The piping and elbows are joined using standard industry accepted methods under ASME IX [8]. These piping materials are designated ASTM grades that become material accepted by ASME with the designation SA. Since Division II ASME SA standards are the same as their respective ASTM standards for these carbon steel power piping grades we can refer to the materials by ASTM grade designations [9]. Once a material is in service, subsequent material and design evaluations are then compared to design requirement the year the system was designed.

2.2. MANUFACTURE OF SEAMLESS PIPING MATERIALS

SA 106 grade B seamless tubing is manufactured at hot forging temperatures by piercing a blank of steel and drawing to size over a mandrel. This process can lead to wall thickness variations with nominal permissible tolerance of $^{+1}/_{16}$ / $^{-1}/_{32}$ inch (+1.6/-0.8 mm).This tubing has specified maximum operating pressures of 10.8ksi at 800°F (74MPa at 427°C) for long-term operation and short-term operations of 5.0ksi at 900°F (34MPa at 482°C) and 1.5ksi at 1000°F (10MPa at 537°C) as per ASME section II [9]. SA106 grade B pipe is semikilled steel with minimum yield strength of 240 MPa, minimum ultimate

tensile strength of 415MPa and elongation of 30% [10]. The material composition is specified in Table 2.1-1. Due to problems associated with long term microstructure stability, the ASME accepted long-term service temperature limit is 800°F (427°C) to avoid the onset of microstructure degradation.

The SA234 WPB elbows are manufactured from A106 piping and therefore have similar chemical composition limits (Table 2.1-1). The SA234 WPB fittings and elbows are specified as having an ultimate tensile strength range from 415-585 MPa, yield strength of 240MPa and elongation of 22% [11]. The piping is cut to length and heated in about four minutes, between 700-760 °C depending on carbon content, and the subsequent reforming is conducted at temperatures near 700 °C [12], which should maintain grain sizes similar to the parent material. The cold forging process introduces residual stress into the forged material. Although there is much published information on residual strain in elbows, the only detail that is relevant to this investigation is that the accumulated strain and residual stress are significantly greater for elbows than for piping.

Accumulated strain is also a characteristic of SA105 forgings tabulated in Table 2.1-1 having significantly different chemical and microstructure characteristics than the wrought SA106, 234 type materials. SA105 designates carbon steel forged fittings requiring processing above the A3 temperature, and the strength requirements are different at 70 ksi (485MPa) ultimate tensile strength and 36 ksi (250MPa) yield strength [13].

Element	SA 106 Grade B Composition %	SA 234 WPB Grade B Composition %	SA 105 Composition %
Carbon max	0.30	0.30	0.35
Manganese	0.29-1.06	0.29-1.06	0.60-1.05
Phosphorous max	0.035	0.050	0.035
Sulphur max	0.035	0.058	0.040
Silicon min	0.10 min	0.10 min	0.10-0.0.35
Chrome max	0.40	0.40	0.30
Copper max	0.40		0.40
Molybdenum max	0.15	0.15	0.12
Nickel max	0.40	0.40	0.40
Vanadium max	0.08	0.08	0.08
Niobium max		0.02	0.02
Niobium max		0.02	0.02

Table 2.2-1ASME SA106, SA234 and SA105 chemical specifications for pressure piping

2.3. JOINING PROCESS

The joining process for this particular schedule and size of power piping is generally Shielded Metal Arc Welding (SMAW) conducted under ASME IX [8]. The SMAW process is achieved with a root pass of E6010 cellulosic type electrode and the fillet filled with multiple passes of low hydrogen E7018 electrodes. Each weld bead acts like a small work hardening sequence and adds strength to multipass welds but adds stress concentration to heat affected zones. The micrographs of SMAW welds show uniform heat affected zones (HAZ) that may be associated with A1 and A3 phase transformation temperatures, but micrographs cannot show residual stress. The high chill rates along the welds also increase the potential for generation of martensite along the fusion line. Both residual stress and presence of martensite may be mitigated by post weld stress relieving, which is typically performed by electric resistance heating to slightly above the A1 temperature.

2.4. HIGH TEMPERATURE MATERIAL DESIGN REQUIREMENTS

Table 2.4-1 shows there are four basic criteria for ASME design for temperatures under the creep range and three basic criteria for ASME design in the creep range [9] according to Parker [14]. The criteria suggest that the minimum value of either column should be used dependent on the temperature. Unfortunately the actual physical criteria for material in the cusp between temperature regimes are poorly defined as a material may fit both criteria.

Below creep regime	In creep regime
25% of room temperature tensile strength	100% of stress to cause 1% strain in 10^5 hrs
25% of hot tensile strength	67% of ave stress to cause failure in 10^5 hrs
62.5% of room temperature yield strength	80% of min stress to cause failure in 10^5 hrs
62.5% of hot yield strength	

Table 2.4-1 Summarized ASME design criteria [14]

3. SECONDARY GRAPHITIZATION IN CARBON STEELS OPERATED AT HIGH TEMPERATURE AND HIGH PRESSURE

Steel in its basic form is a metastable mixture of iron and carbon designated as ferrite and cementite. Cementite may be subject to further decomposition to ferrite and carbon which in cast iron is known as graphitization. Secondary graphitization is the undesired decomposition of cementite in a solid solution of steel under the influence of time at temperature into the more thermodynamically stable forms of graphite and ferrite [49].

3.1. HISTORY OF SECONDARY GRAPHITIZATION

3.1.1. Discovery and History of Secondary Graphitization Failures

The study of secondary graphitization as an engineering problem began in 1943 after HAZ graphitization caused a steam explosion in a power plant at Springdale Pennsylvania. After this incident, a joint ASTM-ASME committee extensively tested welded C-Mo piping to determine cause and effects of HAZ graphitization. Eberle [16] found that C-Mo steels that were highly deoxidized with aluminium and extensively cold worked, were susceptible to HAZ graphitization after only 3000 hrs. Not only was this phenomenon found to be dependent on time at temperature in service, but it was observed that heating steel into the austenite phase during working also caused graphite nodules to nucleate readily [16] As a result of this investigation it was recommended that working be performed below the A3 temperature to avoid graphitization failures [16].

The first industrial mention of non-weld related graphitization also came from the Springdale power station that suffered the first weld related failure. Re-evaluation of the original material revealed the presence of localized graphite nodules in base metal within 12 inches (0.30 m) of the original failure, which had not been noted in the original failure analysis [17]. Emerson and Morrow [17] term this new secondary graphitization phenomenon as *Slip-Plane* graphitization and note that it was found in association with plastically deformed pipe and characterized by the planar appearance of graphite which occurs at oblique angles to the axial direction of the piping. It was indicated that the affected plastically deformed piping was reformed to change size and direction although no indication was given for manufacturing technique. Emerson and Morrow [17] further postulated that the cold work in the absence of welding was enough for graphite nucleation but did not explain the lack of consistency of graphite nodules in the affected piping.

Concern for unfired pressure vessels operating at high temperatures in petroleum refining led to an extensive survey and review of graphitization by the API in 1955[7]. The study was motivated by the failure of three catalytic crackers due to design fault. The fault was officially blamed on the dissimilar metal stresses of the clad vessels but extensive graphitization was noted. The study itself [7] was conducted with hundreds of service exposed samples from several different thermal plants and subsequently tested serviced aged samples using criteria set forth by Thielsch [5]. Wilson [18] found that A106 piping was susceptible to both HAZ and base-metal graphitization. Wilson used random graphitization to describe base metal graphitization conditions and segregated

graphitization to describe chain graphitization (eyebrows) or planar graphitization near HAZ. The A106 was found to graphitize in the HAZ 30% of the time while the balance of the graphitzation were nodules in the base metal. Unfortunately the statistical tables based on artificial aging did not include A106 materials, but rather ASTM A201grade A samples which are plain carbon plate of similar composition but contain more silicon and lower carbon content and correspondingly should be less prone to graphitization. The testing showed A201 had a significant propensity to graphitize at 800-850°F (427-454°C) and carried the trend through all temperature ranges to 1000-1100° F (537-593°C).

3.1.2. Historically Accepted Graphite Formation Mechanisms

As part of the 1943 joint ASME-ASTM committee on the comprehensive review of effects of welding on heat affected zone graphitization, Emerson [19] looks at carbide instability as the root of the graphitization. Emerson concentrates on effects of aluminium deoxidation on the stability of the carbides, but does not explain why the carbides would not tend to spheroidize rather than nucleate graphite. Emerson does indicate that the nucleation point is around Widmanstatten grains in the coarse grain HAZ, leading to chain (planar) graphitization. In the same series, Weisberg [4] noted the suspected presence of Widmanstatten microstructure in the coarse grain HAZ being responsible for the nucleation and growth of planar graphitization.

Emerson [19] further elaborates on the cause of random graphitization as being an artefact of decomposition of fine grain pearlite. The decomposition is related to the nucleation of the grains at the former austenite grain boundaries. A marginal α-γ transformation will

occur at a point on the grain boundary during welding operations. A fine grain that is near the transformation temperature will allow an entire grain to transform but a large grain cannot transform in its entirety. Emerson [19] claims that the large grain will now graphitize along the grain boundaries and the fine grain will graphitize entirely which leads to the two different types of graphitization in heat affected zones.

Eberle [16] shows that aluminium deoxidized steels are very susceptible to graphitization after post weld heat treatment. He suggests that there is a chemical driving force for sub-microscopic precipitation that responsible for secondary graphitization. The temperature of the heat treatment and the cooling rate would then dictate the potential of graphite forming. Smith et al. [20] found that the graphite could be composed of many small crystals or one large crystal using polarized light suggesting that more than one nucleation mechanism may be at work.

Although historically the focus of graphitization investigations only concentrated on weld related graphitization, Kerr and Eberle [21] noted the presence of base metal graphitization of a formed hemispherical cap away from the heat affected zone. This graphitization was found while investigating C-Mo sample welds but in this case secondary graphitization had occurred at the point of transition from residual tensile stress to residual compressive stress in a forged cap. Unfortunately Kerr and Eberle never investigated the phenomenon further or looked for a potential cause [21].

3.2. FACTORS CONTROLLING GRAPHITIZATION

3.2.1. Chemistry

Much of what is known about secondary graphitization is derived from investigations on graphitization and nodularizing cast irons. Some work has been performed to explore the possibility of a link between graphite formation in cast irons and secondary graphitization in steels. Russian work by Zhukov[22] covering the effects of elements on stability of graphite in cast iron and steels points to an anomaly in Hund's rules of orbital filling has a distinct effect on which elements will promote graphitization. Zukov[22] claims almost all elements that participate in the graphitization can be fitted to an Equation based on pi bond strength, and may be either donors or acceptors of electrons which change the bond characteristics, lowering the activity coefficient of carbon in solution. The change in the orderly filling of the *d* orbital has a definite effect on the pi bond strength. Manganese suffers from a loss of strength of pi bonds that is not attributed to *d* group transition metals and therefore forms weak carbon bonds as compared to all other transition metals. The synergistic effects of alloying are attributed to the ability of all transition elements except manganese to compress the lattice; reinforcing atomic bond strength. Zhukov [22] also talks about the metalloid metal combinations that form in both liquid and solid solutions of Fe-C-Si and Fe-C-Al, which refine grain size. Initially these complexes are stable but as the stoichiometric ratio changes the complexes may break down promoting graphite formation due to the preferential formation of Fe-Si and Fe-Al complexes, as metal-metal bonds are stronger than metalloid bonds. This preferred electronic bonding phenomenon is termed micro-liquation and operates in the temperature range of recrystallization.

The question of secondary recrystallization is now a question of the intensification of metal bonds and chemical potential. Il'inkii [23] shows that heating to the intercritical temperature causes the segregation of Si into austenite and Mn into ferrite phases due to the increased chemical potential at the point of phase change causing an effective polarization of the matrix which may be reversed upon complete austenization. If the polarized solution is cooled, the formation of cementite will coexist with the formation of graphite. The local chemistry was enhanced by the presence of Mn, Si and Sr as graphitizers and Cr and S as cementite stabilizers. Kobota [24] presents a model that seems to adequately describe nucleation of secondary graphitization but the empirical model presented accounts for interstitial carbon diffusion but does not account for the substitutional diffusion of iron although it is acknowledged.

It is well known that rimmed and capped steels will not readily graphitize, so effort has been unsuccessfully expended trying to explain the nucleation properties associated with deoxidants such as aluminium and manganese. Early investigators directed efforts towards proving the influence of aluminium deoxidants on the graphitization of steel but many aluminium-deoxidized steels investigated would not nucleate graphite while many silicon-deoxidized steels would graphitize [25]. Hoyt et al. [6] gave conclusive proof that the aluminium deoxidation practice was key to the problem when graphitization occurred in post tensile test heat treatments in 1946. Seth [26] found that aluminium in Cr-Mo rotor steels in excess of 0.01% radically reduces creep ductility and increases diffusion rates.

While Seth did not tie the aluminium content to graphitization, the presence of aluminium clearly affects the microstructure stability of steels operating in the creep range.

3.2.2. Thermodynamic Driving Force

Samuels [15] shows that the graphitization process is often associated with heat treatments in the intercritical range above the A1 temperature and below the A3 temperature. Port's [27] analysis covering the "Innocuous Graphitization" as incidental with temperature that allow activation of the iron according to the Equation $Fe_3C \rightarrow 3Fe + C$ as a normal degradation of material process as the reaction is possible at temperatures over 735°F (390°C) but with enhanced kinetics at temperatures over 850°F (454°C). At temperatures below 735°F (390°C), iron carbide is more thermodynamically stable than carbide and should produce the same type of graphitization previously referred to as random graphitization. Another possible reaction is the dissolution of unstable ε carbides according to the Equation $\varepsilon \rightarrow Fe_3C + C$, but ε carbides are not commonly associated with low carbon steels [28]. The preferential thermodynamic stability of formation of pure carbon rather than iron carbide can be demonstrated by the two phase boundaries on the iron carbon phase diagram in Figure 3.2-1[29]. The thermodynamic improvement offered in carbon solubility is up to 0.003% greater for C in α iron than Fe_3C in α iron [29] but kinetically formation of Fe_3C is favoured.

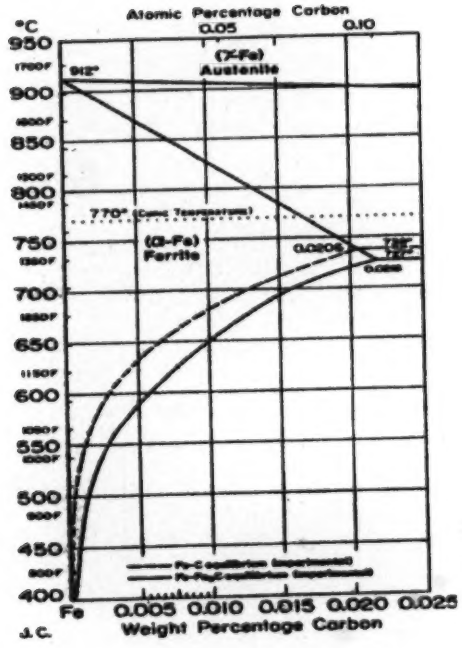

Figure 3.2-1 Iron-Carbon phase diagram showing preferential stability of carbon over cementite [29]

The solubility of carbon in ferrite is only 0.022% and this gradient can offer a significant driving force for diffusion at higher temperatures if a graphite sink is available. The diffusion rate is a log-log relationship between temperature and the diffusion coefficient as Table 3.2-1 shows.

Temp °C	Temp °F	D (cm^2/sec) x 10^8
400	750	1
435	815	2
490	910	5
540	1000	10
590	1095	20
675	1250	50

Table 3.2-1 Diffusion data for steels showing dramatic increase in carbon diffusion rates over narrow range [30]

Preferential grain boundary transport has long been known to be a low energy method of transporting of carbon in steels. The interatomic mismatch of grain boundaries allows the capture of tramp elements and inclusions. Port et al. [27] points out the propensity for graphite nodules to be found along grain boundaries. The mismatch of grain boundaries allows graphite nucleation and growth to a critical radius. Reed-Hill [31] notes the potential of cold work to store energy due to increased dislocation density. Thus, if a graphite nodule reaches a critical radius it becomes a sink and will spontaneously collect carbon atoms from the grain boundaries especially as a material is heated.

Achieving the activation energy for the base metal graphitization process according to Porter [32] is most likely achieved if the temperature is held near the lower critical temperature for phase transformation, where the Fe_3C is dissolved upon heating, dispersing extra carbon into the ferrite phase which would then be rejected as precipitated carbon upon cooling rather than reforming the Fe_3C. Foulds and Viswanathan [33] propose that nucleation of the graphite seeds occur by different methods for HAZ and base metal graphitization. Foulds and Viswanathan [33] suggest the HAZ nucleation is primarily an effect of the super saturation of carbon described by Porter [32], coupled with the chemical effects of aluminium and silicon, which are both considered to be graphite promoters in cast irons. A failure investigation by Furtado and Le May [34] blamed unbalanced carbon concentrations as the nucleation source for planar graphite, but none of the previous authors offer objective proof that the presence of a carbon gradient was responsible for graphitization.

3.2.3. Evidence of the Thermodynamic Driving Force

Bidash [35] investigated random graphitization in carbon steel plates, noted that under plastic deformation to stains of 50%, there was a change in X-ray diffraction patterns associated with the broadening of the $(220)_{\alpha}$. TEM studies show the change in diffraction pattern is been associated with the development of microcracks, voids and pores. Bidash [35] then shows that soaking at an intercritical temperature (between A1 and A3 temperatures) allows both graphite and spherodizing phases to be thermodynamically favoured. There exists at the same time a chemical inhomogeneity across the ends of the pearlite plates, which allows diffusion to areas of small radii of curvature, which increases local chemical potential. Bidash [35] suggests that only microstructures consisting of coarsely differentiated eutectoids which had been subjected to an intercritical temperature were subject to the phenomenon. Bel'Chenko [36] investigating the same phenomenon found that the dislocation structure for the graphitized steels had the same X-ray diffraction characteristics as the non-graphitized steels but the microstructure would be different and the microstress in areas of graphite was lowered 30%.

3.2.4. Unstable Precursory Microstructures

Both Kanter [37] and Smith et al. [25], in work on C-Mo steels found that the prior austenite grains size as revealed by the McQuaid-Ehn test were indicative but not absolute in determining secondary graphitization susceptibility. Both investigations found evidence of abnormal prior austenite grain boundaries before testing led to nucleation and growth of graphite nodules. If the observation is completely, valid grain boundary sweeping of

impurities such as sulfur, tin, lead and phosphorus would occur during phase transformation. Smith's work [24] does note that while flaked graphite nodules may be found in the presence of MnS inclusions, secondary graphitization could not be found to correlate with segregation during the $\alpha \rightarrow \gamma$ phase transformation. Smith et al. [25] did not find a microstructure association with the presence, type or quantity of graphite, but suggested that post weld stress relief was more likely to be the root cause of graphitization near welds.

Smith et al. [38] had previously suggested that in spite of evidence of Widmanstatten structures, the nucleation could be from the presence of martensite as a residual feature from high weld quench rates, which a properly applied post weld heat treat could alleviate. Work at US steel in the early 1950's showed that martensitic steels are very predisposed to precipitation of graphite. Extensive testing by Smith et al. [39] showed that martensite eutectoid steels could consistently preferentially graphitize under low temperature heat treat cycles. The test was conducted by pretreating the martensitic steel between 300 and 1300°F and following with a 1200°F bake. It was found that a larger volume of graphite was generated by treatment between 600-800°F. It was hypothesised that the low temperature pre-treatment enabled precipitation of ε-carbides and graphite nucleation followed.

Post weld heat treatment has long been a subject of controversy and has met with limited success in reducing weld related graphitization. In situ post weld heat treatments to re-adsorb the graphite into the matrix were found to mitigate graphitization but

graphitization could reoccur rapidly after return to service. Only grades containing molybdenum offered consistent test results after post weld heat treatment of different grades and chemistries [38].

It has long been known that graphitization has been possible with steels that contain higher than a eutectoid composition of carbon [35] [22], but steels under 0.4% carbon should ideally be immune to graphitization. Kanter [37] shows that spheroidization is often associated with graphitization, which follows Smith et al. [38] observations that precipitation of ε-carbides in pearlitic steels can influence graphitization. Only Samuels [15] gives any evidence of mechanisms of graphitization of the metastable low carbon pearlitic steels. The presence of iron carbides in low carbon steels is predominately in films of cementite associated with grain boundaries [15].

3.2.5. Effects of Plastic Deformation on Metastable Microstructure

Plastic deformation can be viewed as accumulated strain in contrast to stress which is pressure. Samuels [15], gives detailed effects of plastic deformation at intercritical and subcritical temperatures on carbons steels by grouping the microstructure in two distinct groups: compression effects and tensile effects. The breakdown of pearlite due to compression changes as a function of percent reduction. At strains of 20% the effect of reduction on pearlite is limited to formation of equiaxed subgrains and subsequent work past this point causes rotation and finally kinking of pearlite colonies. The kinking is a function of bending of the cementite plates while under local constraint due to mechanical instability, and results in voids being formed at the ends of the intact plates.

Tensile effects are often manifest as cracking of cementite plates which often open voids at the ends of cementite plates or at the edges of pearlite colonies [15]. Graphitization after this fashion can be described as the diffusion-controlled process whereby carbon atoms migrate between a supersaturated ferrite atom source and a graphite nodule sink [15].

While Hoyt et al. [6] did not define the difference between stress and strain, a correlation was developed between secondary graphite and stress/strain but no relationship was found between *Luder's lines* and the location of the graphite nodules. This work showed that material under compressive stress at creep temperatures readily nucleated and grew graphite, but no stress range or test duration was provided. Neri [40] performed extensive graphitization research on steels that were graphitizing during annealing between successive cold workings. The problem occurred when the steels were annealed at 560-680°C. It was found that depending on the steel type and whether or not the steel had been subcritically annealed, heavy cold working would tend to graphitize in as little as two hours. The investigation noted that graphitization was more common in steel that was in the normalized condition prior to rolling, than materials in the spheroidized condition. Neri concludes that when heavy cold work is to be used on high carbon steels that the annealing temperatures must be higher than 680°C to avoid graphitization.

It is well known that during the deoxidation process, ceramics form and are swept to grain boundaries during solidification. Porter [32] postulates that the aluminium deoxidant ceramics tear and form voids in the matrix during cold forming operations allowing formation of graphite nucleation sites. Plastic deformation can therefore be associated

with slip bands, which have resulted from slip of atoms along slip planes at deformations as small as 1.5%. The presence of numerous microscopic voids from slip and interaction with inclusions give rise to nucleation sites for graphite. The effect of strain in base metal graphitization can be attributed to Cottrell type atmospheres around lattice defects [39]. High dislocation density associated with plastic deformation on slip boundaries is the source of defects for carbon to congregate when thermodynamically preferred. The carbon would be preferentially supplied as a result of strain induced carbon super saturation especially on grain boundaries.

Port [27] demonstrated plastic deformation as a cause of graphite nucleation induced by prior cold working. Port showed planar non-weld related planar graphite reminiscent of the reoccurrence of graphitization of the Springdale piping and gives eight occurrences inside boilers of which three resulted in failure. The macrographs presented by Porter looked much like those presented by Emerson and Morrow [17], which they termed "slip plane" graphitization. In all cases of planar graphitization, the chain like planes of graphite are oriented at angles to the surface and appear to be oriented with slip planes from plastic deformation. Foulds and Viswanathan [33] felt that residual plastic strain would have little to contribute to graphite nucleation in HAZ but rather confined to base metal graphitization phenomenon.

3.2.6. Nucleation of Graphite in Weldments

The weld metal itself is not susceptible to graphitization as the pearlite constituent found in the base metal is absent due to the high rates of cooling. The relatively low heat input

for SMAW processes results in a weld metal that solidifies in columns with a proeutectic phase consisting of grain boundary allotriomorphs and Widmanstatten plates. The remaining cementite composition forms a degenerate form of pearlite and thin films of cementite along grain boundaries [15].

The heat-affected zone is in fact susceptible to graphitization as evidenced by previous case studies. A recent graphitization summary by Foulds and Viswanathan [33] show that the bulk of the graphitization failure cases have been associated with the A1 transformation temperatures. The partially melted zone is characterized by the existence of Widmanstatten plates resulting from the time spent at the austenite forming temperatures near the A1 temperature resulting in grain refining. The subtle changes near the A1 phase transformation temperatures have an effect of promoting graphitization that has never been fully understood, although Smith et al [38]. Foulds and Viswanathan [33] have studied the microstructure conditions.

The effects of welding process on graphitization were demonstrated by Pavlichko and Solomon [41] whereby a graphitization survey showed that out of 70 boat sections removed from power piping, that not one of the friction welded joints examined exhibited graphitization, although many multipass SMAW joints exhibited graphitization.

3.3. GROWTH OF SECONDARY GRAPHITE

Porter [32] shows that if graphite can nucleate and pass the critical size, then the secondary growth of the graphite is then a function of available growth volume of vacancies and

defects near inclusions, grain boundary and lattice defects. Foulds and Viswanathan [33] felt the growth of graphite nodules themselves is a completion between the rate-controlled processes of production of carbon and the diffusion. Foulds and Viswanathan [33] postulated that the curve itself is to be of sigmoidal shape for nucleation and a power law relationship for the balance of the process. As a result a linear time relationship for the growth between 20-80% of the carbon content of the base metal is established suggesting that the strength of the material will continuously drop to the strength of ferrite upon prolonged exposure [33]. Port et al. [42] detail the proposed *slip-plane* graphitization as a function of carbon gradient if graphite nodules have been nucleated.

Yang [43] shows that the graphite nodules must expand the physical size of the steel while growing. This was demonstrated by attempting to re-absorb graphite nodules in dilatometer experiment where graphitized 0.67% C steels with less than 1% carbide forming elements were held at a constant austenizing temperature. A physical decrease in sample size over time was demonstrated, indicating that re-adsorption of graphite into the matrix occurred. Whether this translates into a physical reduction in volume at below the A1 transformation temperature was not included in the investigation.

3.4. EFFECT OF GRAPHITIZATION ON SERVICEABILITY

Wilson [18] dealt with the stress-rupture properties of the graphitized refinery piping at stresses from 9000-14000psi (55.2-96.5MPa). The experiment was based on a limited number of samples of A201 steel, of which 30% showed chain graphite or planar graphitization in the HAZ. When only HAZ graphite was present, the tendency was to

fracture through the weld metal, but samples that had both the base metal and HAZ graphitization tended to rupture in the area of chain graphitization. Wilson [18] found that in spite of presence of graphite nodules, the Larson-Miller stress rupture values were within the safe values for the material as compared to the published ASTM values. It was found that the presence of planar graphite in the HAZ would reduce rupture life but weld quality was still of primary importance for most samples. Similarly random graphitization in the base metal was found to have minimal effect on the stress-rupture properties [17].

A201 Grades A and B steels were evaluated by Creamer [44] as part of long term material property research and found that although the lower carbon content Grade A steel had graphitized but in the higher carbon content Grade B steel only spheroidization had taken place. The Grade A steel was at the minimum design UTS and YS but showed enhanced ductility. Similarly evaluation of a fluid catalytic cracking unit by Ibarra [45] of A 201 Grade B steel showed that while planar graphitization was found near welded inlet pipes, overall presence of random graphite could be found in the A 201base metal. The base metal no longer met the UTS requirement but met YS and elongation properties and contrary expected temperature effects, the base metal showed enhanced levels of graphitization and microstructure degradation at the cooler pressure vessel head. In the cases of both Ibarra and Creamer, despite the random graphite induced microstructure and strength degradation, the vessels were successfully put back into service at a lower temperature with regular scheduled replications to extend service lives.

Port [27] was the only investigator to suggest that substrate graphitization was a significant factor in degradation in fitness for service but only suggested that areas that were plastically deformed during manufacture should be inspected but offered no quantitative evidence of when the piping should be replaced.

Furtado and Le May [35] found evidence that the occurrence of planar base metal graphitization showed little to no evidence of creep damage in a steam piping failure. The lack of general creep deformation near the localized fracture surface gave evidence that creep properties will not dominate mechanical properties; nor was there any evidence of purely mechanical overload. The only evidence was decohesion of graphite along a plane of defects. The unetched microstructure in Figure 3.4-1 shows the advanced planar graphitization concentration was far in excess of the presence of random graphite.

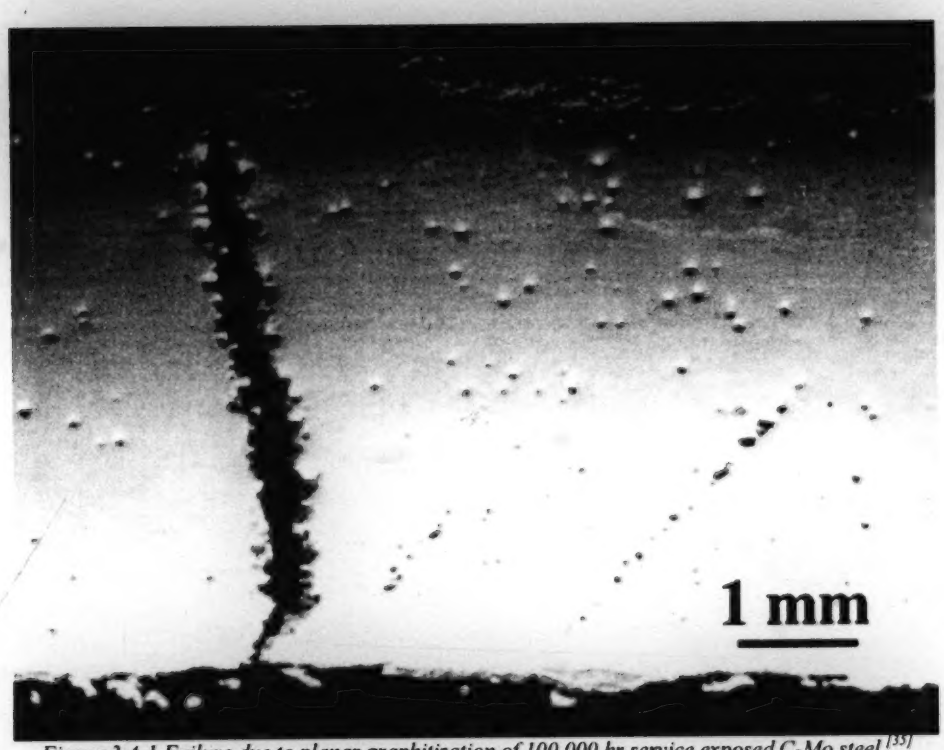

Figure 3.4-1 Failure due to planar graphitization of 100 000 hr service exposed C-Mo steel [35]

The traditional method of estimating the effect of graphitization on mechanical properties was developed by Thielsch [5] in the early 1950's for weld related graphitization by conducting room temperature bend tests of weld coupons retrieved from in service C-Mo and Cr-Mo piping. The model quantifies the graphitization into five levels of graphitization based on ASME IX bend test pass/fail criteria. The weld bend tests are loosely correlated to micrographs of weld related chain graphitization. Theilsch's model has been the foundation for the last 50 years of fitness for service of graphitized steels, but random material removal surveys conducted using this criterion have proven to have limited effectiveness at predicting failure.

4. FITNESS FOR SERVICE (FFS) REQUIREMENTS FOR HIGH TEMPERATURE DAMAGED COMPONENTS

High temperature materials have long been in service in many high capital cost industries. Due to increased economic, safety and environmental pressures it is now necessary to predict how long a component is cost effective to service with relation to probabilistic service lives. The relationship between testing methods and actual service lives is often dubious, but the key to successful prediction appears to lie in implementation of a strategy for life prediction by understanding the entire problem. Therefore, FFS is not a test or range of tests but rather, a philosophy.

4.1. RATIONALIZATION OF METHODS OF ANALYSIS

The dominant question is now "When and how much graphite is damaging under the prescribed service conditions?" Characterization of a material by physical metallurgical means can divide the problem into four interrelated parts. Chemistry, microstructure, mechanical properties and creep properties can determine all relevant bulk properties of a metal in elevated service conditions. Microstructure defines nearly all properties of a material and is a result of both chemistry and thermo-mechanical history of a material but may be difficult to analyse. Mechanical testing has been used for design purposes for over a hundred years but cannot be used to predict properties at temperature near to or over 0.4 times the absolute melting temperature due to diffusion effects of time at temperature. As a result mechanical testing can be used to give a datum for material

properties but cannot reflect actual service conditions. Creep testing shows how a materials microstructure and mechanical properties are affected by temperature and time. Accelerated creep testing is used to suggest a future time when a materials properties might be compromised. Furtado and Lemay's [34] experience with planar graphite (Figure 4.1-1), shows that choosing any one of the individual testing methods may not reflect the true criteria of a problem requiring that a comprehensive fitness for service assessment evaluate all related phenomena.

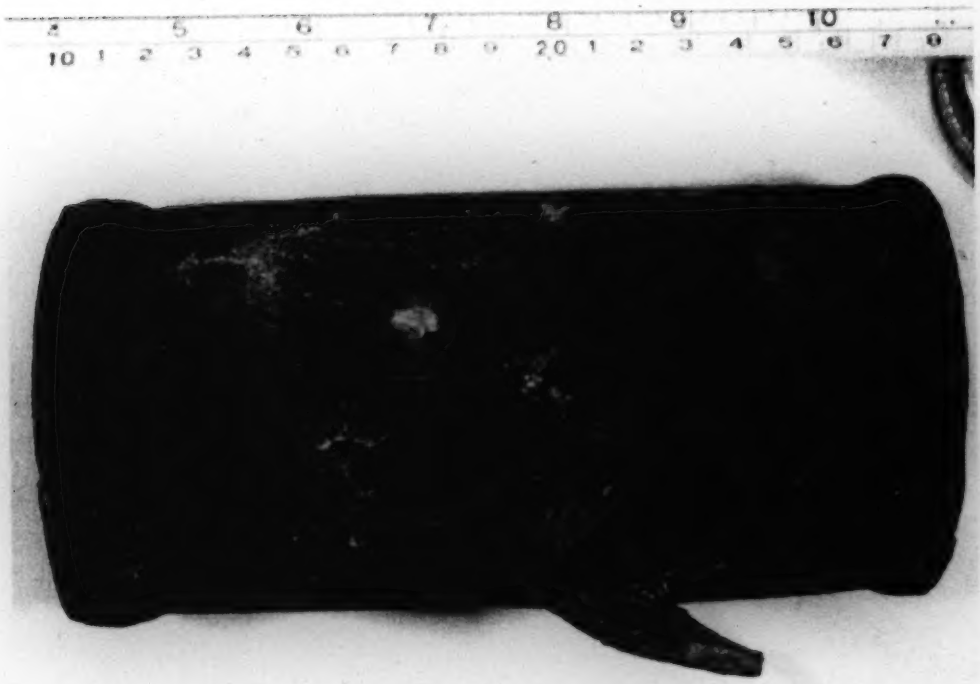

Figure 4.1-1 Steam piping ruptured due to planar graphitization [34]

4.1.1. Effects of Carbide Forming Elements and Microstructure

Townsend [46] illustrates the case in point for carbide forming ferritic steels is the break down of carbides in different microstructures.

Ferrite $M_2C \rightarrow M_6C$

$M_7C_6 \rightarrow M_6C$

$\uparrow$

Bainite Carbide $+M_3C \rightarrow M_3C + M_2C \rightarrow M_{23}C_6$

The chemical process may transfer carbon from primary carbide formers such as vanadium and iron to form chrome and molybdenum carbides due to thermodynamic high temperature stability of chrome carbides and molybdenum carbides [47]. This chemical change is accompanied by carbide particle coarsening which occurs as a function of a cube rate. When a ferritic material has no carbide forming elements, the choices for breakdown of cementite are to either spheroidize or graphitize.

The effect of breakdown of cementite due to diffusion is to open up the spacing between dislocation blockers while the temperature allows the simultaneous annihilation of dislocations. The net result is the ability to move dislocations freely resulting in change of yield stress.

4.1.2. Strain Capacity and Ductility of Materials

The first detail that must be ascertained in any fitness for service are the creep characteristics of that particular material. Creep characteristics that are relevant for 1.25 Cr-1Mo are not the same as 1.25 Cr-1Mo-V as the chemistry results in completely different mechanical properties. By the same token, thermo-mechanical history is just as important, as forgings and casting can have completely different properties than piping for the same alloy composition [47]. Care should be taken when comparing materials as creep ductile carbon steels are very strain tolerant, but creep brittle HK40 types have very

low strain tolerance. This often manifests itself in total strain achieved under creep testing but this property is not evident in mechanical testing. The strain capacity of the material will often allow determination of testing techniques that can be used.

Goodall [48] proposes that the single most important condition for creep life is ductility. Limited ductility is a detriment and ductility will determine the final creep load carrying capacity under creep conditions. Goodall determined that creep ductile materials will fail when the ratio of ultimate failure strain from formation of micro cracks (ε_u) a value that is ten times the point of tertiary strain (ε_r) suggesting that ductile materials will demonstrate significant tertiary strain before failure. Most materials will show some intermediate degree of ductility, therefore showing some intermediate amount of tertiary strain before failure, except in the case of true brittle failure which occurs when $\varepsilon_u / \varepsilon_r = 1$. This relationship will have a definite effect on welded joints due to the fact that welds tend to be less ductile than base metals, but Goodall expressly points out that there exists a limit load where safer operation is possible. Understanding how ductility affects testing and operating conditions is of paramount importance.

4.1.3. Effects of Aging Materials

Most materials begin high temperature service in microstructurally metastable conditions leading to significant changes in properties until the microstructure stabilizes. Ennis [52] found that creep testing new material relative to stabilized ex-service material gave false estimation of the level of stress a new material could sustain and also showed that the strain capacity of the material was much less than new material. Larson-Miller curves

showed that service exposed materials have short lives at high stresses and long lives at low stresses [52].

4.2. CREEP BASED LIFE PREDICTION

A material that is exposed to temperature above 0.4 absolute melting temperature (Tm) with an applied stress may continuously deform over time. This relationship can be summed up as

$$t = f(T, \sigma)$$

Equation 4-1

Where t is time for failure, T is temperature and σ is stress. Creep can manifest itself in many ways, all of which will plastically deform the microstructure. To predict lifetimes at service conditions, it is necessary to accelerate the conditions that influence creep by increasing either temperature or stress or both.

4.2.1. Creep Testing and Creep Deformation

Creep testing does not measure any one intrinsic property but rather they are a combination of properties, the most significant of which are the activation energy of dislocation diffusion and bulk diffusion [105]. Creep testing also offers a reasonable reflection of mechanical properties, such as strain rate, which can be related to bulk performance of the material. To achieve these conditions, creep testing may also be performed under either conditions of constant load, which should mimic service conditions, or constant stress, which can be used to understand fundamental material

properties. The testing conditions should emulate the service conditions for accurate results but this is often not possible and accuracy can vary widely with material and method. Grant [50] shows two major schools of thought for accelerated life prediction; stress rupture based and strain based creep testing. All methods are based on control of temperature and loading, but the main point of differentiation of the test methods is the level of strain achieved and sensitivity of control used. The stress rupture test is designed to yield one major parameter, rupture time, while controlling temperature and stress. Similarly, strain based tests control temperature and stress, but yield both strain rate and rupture times allowing a comprehensive understanding of the results of the test.

Early methods of life prediction were limited to plotting log rupture time against log stress to obtain a conservative estimate of elevated temperature life. Creep became a scientific method rather than a mechanical testing method with work by Orr and Sherby in 1954 [51]. The correlation was found when a plot of activation energy of self-diffusion was found to correlate with the energy of creep activation in a linear fashion for 25 metals [51]. This insinuated that for the first time creep could be examined qualitatively and quantitatively. The relationship is tied to Fick's law of diffusion (Equation 4-2).

$$D = D_0 \exp\left(\frac{-Q}{RT}\right)$$

Equation 4-2

Where Q is the activation energy for self-diffusion, R is the universal gas constant and T is the absolute temperature. If temperatures are adequate to promote diffusion, creep will be manifest by movement of dislocations or substitutional diffusion [105].

The accelerated high temperature test is a measure of a metals resistance to continuous deformation under thermal mechanical conditions and is governed by diffusion or conversely the resistance to diffusion along the grain boundaries or within the grains themselves. Unlike the tensile test, diffusion is manifest as a creep property of the material therefore this testing is indicative of fundamental properties of a material [50]. A fundamental point is the change in diffusion mechanisms. High temperature testing may encompass different mechanisms of diffusion when service conditions are normally dislocation-dominated regions of activation energy.

Understanding aging characteristics of a material and therefore the mechanism of creep damage allows understanding estimating damage to the materials in the creep range. This point is reinforced by the existence of creep deformation maps compiled by Ashby [53], shown in Figure 4.2-1a, b as originally proposed by Weertman. The Ashby maps show the relationship, between creep deformation mode by comparing strain rate response of a material by comparing normalized stress and homologous temperature. The strain rate divides the deformation maps into graphical representation of different creep domains. The creep deformation maps allow understanding of mechanism of creep deformation that dominate a materials performance under service conditions.

Every material has its own respective creep characteristics and correspondingly would have a unique Ashby map. The Ashby maps in Figure 4.2-1a, b show how a change of alloying element can change the mechanism of creep damage by an order of magnitude

for the stress required to cause diffusion and reduce the overall diffusion operational parameters. Cr and Mo are typically added to steel to modify the creep characteristics of the material by changing the carbide stability characteristics. It should be noted that while these maps are incomplete, it is worth noting that as the alloy level goes up the area of power law creep shrinks and diffusion flow area increases before the phase change temperature. The areas of power law creep and diffusion flow before the A1 transformation temperature are of significant interest in engineering applications.

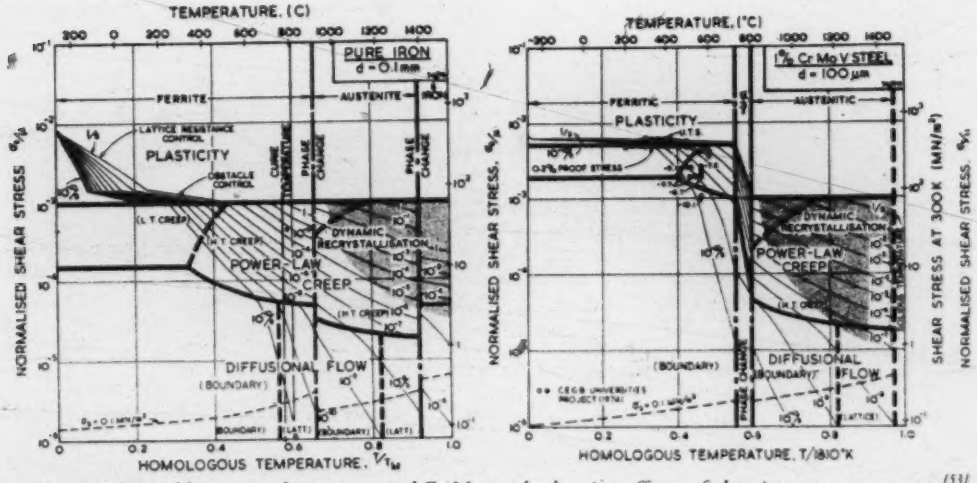

Figure 4.2-1 Ashby maps of pure iron and Cr Mo steels showing effects of chemistry on creep rates [53]

4.2.2. Creep Life Prediction Fundamentals

4.2.2.1. Robert's rule

An underlying condition that allows creep life prediction is Roberts rule which suggests that any lifetime will be the sum of consecutive life consumed cycles which must add up to unity[54]. The equation may be derived in terms of rupture time but may also be useful under conditions of hardness and percent damage to microstructure. Equation 4-3 is

Robertson's rule expressed in terms of rupture time, where t_i is the time spent at temperature and t_{ri} is the rupture time under the same conditions and the ratio of these parameters is known as the damage fraction. The equation may also be derived in terms of strain rate for life prediction dominated by strain accumulation. Robertson's rule is a guide to what all creep testing is based on but is marginally useful in actual life prediction.

$$\sum_i \frac{t_i}{t_{ri}} = 1$$

Equation 4-3

4.2.2.2. Parametric creep life prediction methods

Although there are over 30 parametric based methods filling volumes of information, stress rupture testing has three accepted major methods of defining rupture life. Larson-Miller [54], Orr-Sherby-Dorn [51], and Mason-Haferd [56] methods dominate all methods of life prediction due to their simplicity and relative accuracy. All parametric methods are used for correlation, interpolation and extrapolation but can not be expected to show the actual mechanism of failure [55]. All three methods are a product of two or more relations but have an underlying dependency on time to rupture and temperature. They also inherently rely on a master plot of the new material that has an average material property and a statistical minimum to represent material that is no longer fit for service. These methods have varying degrees of accuracy depending on type of material and operating conditions but suffer from a requirement that you must know the entire service history to make a qualified life prediction based on Roberson's rules.

4.2.2.2.1. Larson-Miller method

The Larson-Miller method [54] has enjoyed the most popularity due to its simplicity and the distinction of being the first successful attempt at high temperature life prediction. The premise of the parameter was based on work by Holman-Jaffe, which showed the temperature dependency of the rate of hardness drop during the tempering of steel. Larson and Miller expanded this based on the known fact that strain rate was related to activation energy for diffusion and temperature as shown in Equation 4-4.

$$\dot{\varepsilon} = A e^{\frac{-Q}{RT}}$$

Equation 4-4

The parameter was similar to the Holman-Jaffe relationship except that Larson-Miller showed by deriving Equation 4-5 that activation energy was related to strain.

$$T(20 + \log t_r) = C$$

Equation 4-5

Where T is the absolute temperate, t_r is rupture time and C became known as the Larson Miller constant. Historically, a Larson-Miller constant value 20 was felt to be a universal value of C and was derived by plotting inverse temperature against the log of rupture time and finding that the values linearly converge at different stresses to a single point. This method, know as temperature compensated time, does not adequately describe the entire phenomenon of life at elevated temperatures. The first deficiency is the fact that the value of C does in fact vary from 15- 27 for different materials depending on the resistance to

creep. The creep data from this type of testing is normally carried out in air and varies from overstressed, leading to plastic collapse conditions; to overheat which results in severe oxidation and loss of base material to corrosion. The second deficiency is the fact that activation energy for diffusion varies as temperature increases, making it difficult to compare tests as diffusion mechanisms may change across a test regime.

The Larson-Miller parameter should be valid if all the isostress lines on a log t_r vs. 1/T diagram intersect at a common *C* values at 1/T=0. A failing of the Larson-Miller method is the need to extrapolate a small range of information to an intersection six to ten times the length of the data range away. If a Larson-Miller constant is determined a master diagram can be generated using least squares regression to find the average non-linear relationship as shown by Equation 4-6 [56].

$$T(C + \log(t_r)) = a_0 + a_1 \log(\sigma) + a_2 \log(\sigma)^2 + a_3 \log(\sigma)^3$$

Equation 4-6

Master plots for high temperature steels are tabulated in ASTM DS 11S1 [57] and designated regression values for design purposes are included in codes such as API RP 530 [58]. A minimum trend line is then calculated at 1.6 standard deviations from the mean stress axis as the general guideline of acceptance for service. The Larson-Miller master plots assume that the product of any given time and temperature combination at a given stress level will result in a common Larson-Miller parameter. In fact short rupture times at higher temperatures may displace the Larson-Miller parameter towards the minimum

rupture time. This skewing of the data means that the Larson-Miller regression method is not always representative of the data.

Zhou [59] shows how a manufacturer's use of the accepted least square methods may misrepresent actual service conditions. A condition of lognormal distributions is that a histogram of residuals is plotted to determine if the data shows a normal curve. A skewed curve would show an inaccuracy in the regression equation. This error should manifest itself when the service conditions are: near the end of service life or extrapolated from data that does not cover service conditions

4.2.2.2.2. The Orr-Sherby-Dorn Method

The Orr-Sherby-Dorn method is more commonly known as the Sherby-Dorn method [51], and is considered an improvement in some cases over the Larson-Miller method but requires more information to complete an analysis. The results of this method offer more concise predictions, especially in the case of relatively pure metals, although some commercial alloys can be accurately modeled. Graphically deriving the activation energy for diffusion from rupture time and stress allows development of the parametric relationship. Orr et al [51] made the supposition that similar to diffusion and creep; the activation energy for rupture must be related to the annihilation of dislocations, which means that activation energy may be calculated directly from rupture time.

The parameter is most useful if the plot of log t_r vs. 1/T isostress lines yields parallel lines. The slope of the parallel lines is equivalent to the value of -Q/2.3R so this can then

be plotted to yield the Sherby-Dorn Parameter. The Sherby-Dorn Parameter is equal to log t_r - Q/2.3RT. Similar to Larson-Miller, a master plot can be derived by least squares regression to find the mean of the non-linear relationship in the form of Equation 4-7 [55].

$$\log(t_r) - \frac{Q}{2.3RT} = a_0 + a_1 \log(\sigma) + a_2 \log(\sigma)^2 + a_3 \log(\sigma)^3$$

Equation 4-7

Resembling the Larson-Miller relationship, the fundamental short fall of the Sherby-Dorn method is an inability to account for change of mechanism of diffusion. This means that the lines are unlikely to be parallel until the diffusion mechanism has changed to strictly bulk diffusion mechanisms from dislocation type mechanisms.

4.2.2.2.3. The Mason-Haferd method

Mason-Haferd method is considered to be the most accurate of the general stress rupture parameters but is the most difficult to use [56]. Based on the Larson-Miller premise, the parameter is different by the fact that the intersection point of the lines is a common point in space with an improved linear accuracy in the form of Equation 4-8. Extrapolation of isostress lines yield a common intersection point (T_a, log t_a) as determined from the plot of log t_r vs. T [56].

$$\frac{\log(t_r) - \log(t_a)}{T - T_a} = a_0 + a_1 \log(\sigma) + a_2 \log(\sigma)^2 + a_3 \log(\sigma)^3$$

Equation 4-8

4.2.2.2.4. Limitations of the parametric methods

One of the failing of all stress rupture based parameters is power law stress dependency and the associated strain rate changes. Creep is a complex mechanism that is more clearly modeled with a variable power law dependency as follows in Equation 4-9.

$$\dot{\varepsilon} = \sigma^{n} A e^{\frac{-Q}{RT}}$$

Equation 4-9

Where σ^n is Norton's law, which signifies that if stress exponent *n* increases, the effect of stress is magnified as a function of strain rate; therefore accelerating testing by increasing stress will compromise extrapolation to actual service conditions. The Ashby deformation mechanism maps [53] in Figure 4.2-1 show that most operating conditions and testing for iron based alloys in the creep range should be in the range of power law creep. A statistical overview of the accuracy of three different parametric and one rate method allows some comparison of the accuracies [60].

Parameter or Method	Ratio of expected to realized life		
	Min	Ave	Max
Larson Miller	0.34	1.57	5.64
Orr Sherby Dorn	0.11	1.09	4.01
Mason Haferd	0.44	1.51	6.30
Monkman Grant	0.33	0.93	1.83

Table 4.2-1 Survey of published creep life prediction accuracies [60]

Accelerated life testing does require that the stress or temperatures are raised to exacerbate the desired diffusion process but this may not mimic operating conditions. Viswanathan and Foulds [61] explain that in the parametric testing of ferritic steels the life

fraction rule is only valid for temperature accelerated testing and but is not valid for stress accelerated testing as demonstrated in Figure 4.2-2.

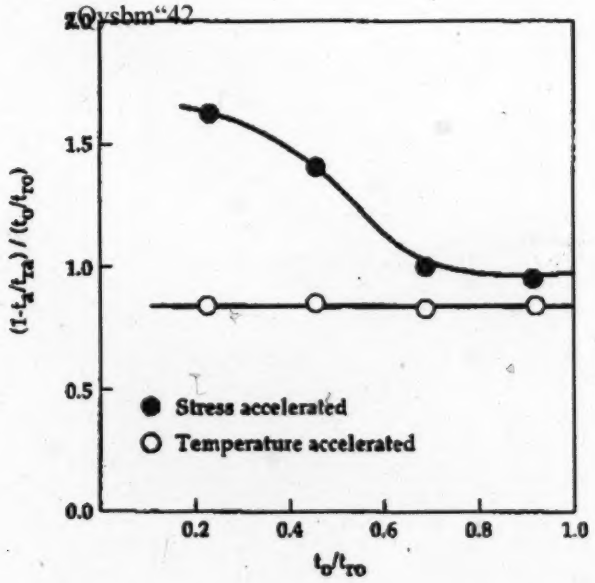

Figure 4.2-2 Effect of stress accelerated testing for ferritic materials [61]

By including the strain rate dependent Monkman-Grant method [60], with the parametric methods, the inaccuracies of the parametric methods become apparent. Consequently several methods are being developed that directly utilize the minimum creep rate as a factor in the calculations. The industry standard Larson-Miller method is overly conservative and may condemn piping long before its useful service life is achieved. Viswanathan [61] suggests that for ferritic steels, the Mason-Haferd will give the most accurate results of all parametric methods.

4.2.2.2.5. Stress dependency of parametric methods

An alternate method from API 530 [58] is using a linear rate between log stress and log rupture time using the form:

$$L_t = mS^{-n}$$

Equation 4-10

Where L_t is rupture time, m is a material constant, S is stress and n is the stress exponent. The stress exponent n may be determined by comparing time to rupture at a stress as follows:

$$n = \frac{\log\left(L_1 / L_2\right)}{\log\left(S_1 / S_2\right)}$$

Equation 4-11

Viswanathan [62] points out that the method expressed with Equations 4-10 and 4-11 are extremely conservative and are only applicable over a limited range of operating conditions

4.2.2.3. Creep rate based methods

4.2.2.3.1. The Monkman-Grant method

The first successful strain rate based method was expressed by Monkman-Grant [63] shortly after the discovery of the parametric based methods. The method assumes that the

steady state strain rate ε_{ss} for a material (alternately known in some literature as the minimum creep rate) is a constant value for all temperatures and stresses (Equation 4-12).

$$\log(t_r) + m\log(\varepsilon_{ss}) = c \quad \text{or} \quad t_r \times (\varepsilon_{ss})^m = c$$

Equation 4-12

Where m is a creep constant that may be related to diffusion mechanism and c is constant for a material. The assumption of Equation 4-12 is that the stage II steady state strain rate of accelerated creep testing can be plotted against rupture time and extrapolated to a desired creep rate to achieve a desired life expectancy. The use of the Monkman-Grant method for life assessment is best for materials that will suffer a continuous change of strain due to creep during the service life. A fundamental tenet is that the relationship of strain rate times the rupture time which should give a constant value for any high temperature material. Essentially it is a measure of a materials strain capacity over time if the relationship holds under isostress conditions.

The rupture exponent is of interest as it can indicate a change of stress rupture mechanisms. The Larson-Miller method is a special case of Monkman-Grant where m = -1. One of the best inherent features is that the testing is often across three or for decades of time and extrapolated for only three more decades of time which can improve accuracy when compared to extended extrapolations that are required for determining C in Larson-Miller analysis. While Monkman and Grant never offered a physical significance for ε_{ss} the method is qualitative at best but can have accurate results.

4.2.2.3.2. The theta project (Θ) method

Evans and Wilshire [64] developed the theta project (θ) from empirical evidence based on strain ε as a function of temperature T, where $\varepsilon = (\theta_1, \theta_2, \vartheta_3, \theta_4)^T$ are terms obtained from regression of creep curves expressed by Equation 4-13

$$\varepsilon = f(\theta, T) = \theta_1\left(1 - e^{-\theta_2 T}\right) + \theta_3(e^{\theta_4 T} - 1)$$

Equation 4-13

The strain rate then becomes an equation of the form:

$$\dot{\varepsilon} = \theta_1\theta_2 e^{-\theta_2 T} + \theta_3\theta_4 e^{\theta_4 T}$$

Equation 4-14

Evans proposes that when a material is strained, the onset of tertiary creep is shortly after creep conditions are met, but the material has a resistance or back stress to offset the creep. The significance of the first two terms is a materials resistance to deformation and the third and fourth terms are strain acceleration due to damage. A materials θ values are determined empirically by least squares regression techniques of data obtained under constant stress conditions. The test is therefore limited by the accuracy of regression techniques and the ability to perform true constant stress tests.

4.2.2.3.3. The Kachanov continuous damage method

Alternately Kachanov [65] independently developed a strain rate method of the form expressed in Equation 4-15

$$\dot{\varepsilon} = \dot{\varepsilon}_0 \left[\frac{\sigma}{\sigma_0}\right]^m \left[\frac{1}{1-\omega}\right]^\nu$$

Equation 4-15

Where $\dot{\varepsilon}$ is instantaneous strain rate, $\dot{\varepsilon}_0$ is the initial or reference strain rate, σ is the instantaneous stress, σ_0 is the reference stress, ν defines the rate of acceleration of creep at the onset of tertiary creep and ω is the creep damage function. The method itself is of little use, as it may not be practically integrated for purposes of determining strain but it does give a mathematical relationship to the existence of a continuous damage function. Kachanov [65] does not give a quantitative method to evaluate the value of the damage function ω but has laid the basis of a mathematical method of strain based testing. Kachanov did not elaborate on the significance of the exponent ν, but it is apparent from the equation that when ω =1 rupture will take place.

4.2.2.3.4. The Continuum creep damage mechanics

Continuum creep damage mechanics was developed out of Kachanov's work to represent cases of multiaxial creep with uniaxial creep testing. Leckie develops Kachanov's equation by giving a graphical interpretation with a uniaxial stress diagram figure 4.2-3 [66]. It is called continuum creep damage mechanics due to the tendency of the creep damage to collect in a smooth area as compared to the classic brittle fracture propagation along a well defined line [67]. Leckie shows how the slope of the inflection point after steady state creep is an indicator of the resistance to creep damage (figure 3.2-2). The

observation is built on two equations, the first of which is strain rate based and the second rupture time based.

$$\frac{\dot{\varepsilon}_{ss}}{\dot{\varepsilon}_0} = \left(\frac{\sigma}{\sigma_0}\right)^n \text{ and } \frac{t_r}{t_0} = \left(\frac{\sigma_0}{\sigma}\right)^v$$

Equation 4-16 a, b

Where $\dot{\varepsilon}_0$ is reference strain rate, σ_0 is reference stress and t_o is reference rupture time. The first equation is related to Ashby maps in such a fashion that plotting the log of the equation will yield a line of value n. The value of n is that of the stress exponent in Norton's equation and n should equal m in Kachanov's equation. A deviation in linearity of this line will show as a change of diffusion mechanism.

Plotting an isothermal stress rupture curve in terms of log stress vs. log time shows a change of mechanism in the tertiary performance of the materials yields a slope of v (figure 4.2-3). The upper flat portion of the curve indicates structural instability from high stresses forming a neck before the creep process occurs. The slope of v reflects the formation of microstructure defects until rupture occurs [68]. To determine lifetimes a reference stress and time is obtained and back calculated according to Equation 4-15b. The figure indicates how the t_0 and σ_0 values are subsequently taken at the appropriate regime to determine the appropriate numeric value of v.

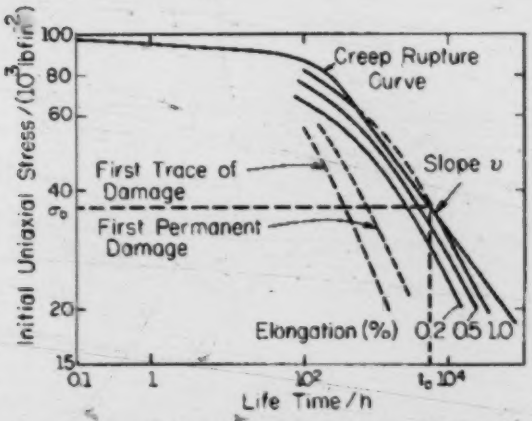

Figure 4.2-3 Leckie's interpretations of microstructure conditions that determine creep damage for a low alloy steel exhibiting brittle behaviour at 500°C [68]

Leckie [68] uses Kachanov formulations to develop a meaning for ν where the rate of void growth in a material has a direct relationship to the cumulative damage until failure. To make Kachanov's equation work, Leckie also devises a crude empirical method of counting creep cracks to determine the value of ω [69]. The exponential nature of Equations 4-17 a, b show the importance of stress exponent n and υ, but Equation 4-17a also infers the ambiguity of ω, a term with no concise definition.

$$\frac{d\omega}{dt} = -A\left(\frac{\sigma}{1-\omega}\right)^{\upsilon} \text{ and } \frac{d\varepsilon}{dt} = k\left(\frac{\sigma}{1-\omega}\right)^{n}$$

Equation 4-17 a, b

Leckie's interpretation shows that microstructure damage has often occurred long before damage is apparent, but there is no method of absolutely determining ω , so we can only estimate the rupture time with Equation 4-15b. Prager [70] points out that even under resolutions achieved by scanning electron microscopes, most common engineering materials will not show microstructure damage until it is advanced.

A failing of Leckie's method is the temperature at which the damage exponent is determined. The major premise of the method is that you would have to be near your operating temperature. Extrapolation would require that n would remain constant in the extrapolation area, ensuring the validity of constant values of v for the desired temperature.

4.2.2.3.5. The Omega (Ωp) method

A project was instituted by the Materials Performance Council in association with American Petroleum institute, Electric Power Research Institute and many industrial sponsors to find a method that is able to accurately correlate short term testing with long-term service [71]. The method referred to as Omega testing, uses elements of the results of Robinson, Monkman-Grant, Kachanov and Evans to make a refined estimate of life remaining based on tertiary creep. The basic premise of omega testing is that an engineering material has an ability to resist stress and under creep conditions the accumulated strain damage lowers a materials ability to resist stress. We can measure this increase in creep damage by the relative increase of strain rate over time. Using a derivation of Norton's law under true strain ε, we can show

$$\frac{\sigma^m}{\sigma_0} = e^{m\varepsilon}$$

Equation 4-18

Where m is the Norton's law stress exponent. Since true strain $\varepsilon = \ln(1+\varepsilon_e)$ where ε_e is engineering strain, we can apply this to the Kachanov type expression for strain rate $\dot{\varepsilon}$ and find an expression that can not be integrated easily (Equation 4-19)

$$\dot{\varepsilon} = \dot{\varepsilon}_0 e^{m\varepsilon}\left(\frac{1}{1-\omega}\right)^{v}$$

Equation 4-19

The expression now includes strain rate dependency as well as the microstructure damage term ω. The solution to the integration problem is to break the damage parameter into three empirically determined parts. The first part is m, which accounts for acceleration due to stress, p which accounts for microstructure damage and c which is a correction factor for deficiencies in the first two terms. The sum of $(m+p+c)$ now equals a term referred to as omega (Ω_P), which is a material property. The omega value can be shown to be a constant similar to the Monkman-Grant constants in Equation 4-20.

$$t_r = \frac{1}{\dot{\varepsilon}_0(m+p+c)} = \frac{1}{\dot{\varepsilon}_0 \Omega_p}$$

Equation 4-20

Prager [71] now shows that the definition of Omega is related to strain rate and true strain ε in Equation 4-21

$$\frac{d \ln \dot{\varepsilon}}{d \varepsilon} = \Omega_p$$

Equation 4-21

The relationship hold true for any material that exhibits linearity when plotted as true strain ε against log of time to rupture minus time *log* $(t_r - t)$ as demonstrated in Figure 4.2-4. The slope of this line has a value of ln Ω_p. Initial strain rate $\dot{\varepsilon}_0$ can be determined by extrapolating the line to zero time. A further significant finding is the mathematical relationship between strain rate and temperature to associate the Omega value and Larson-Miller parameters as the activation energy for creep has the same value [70].

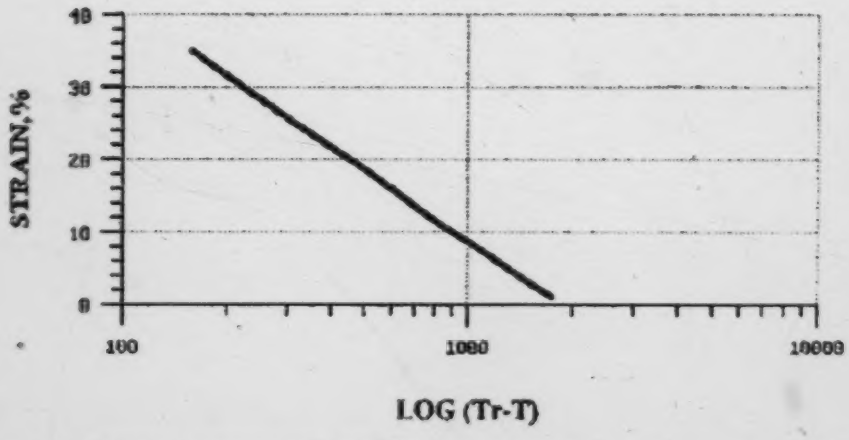

Figure 4.2-4 Criteria for Omega test validity [71] which is obtain from creep curve. Slope is $1/\Omega p$

Omega testing is the only type of testing that is performed near service conditions. The underlying assumption is that the process is a constant volume process and must be analysed as a function of true strain. The testing conditions are generally carried out at

service stress and only slightly elevated temperatures as compared to stress rupture testing. The testing method is optimized using Larson-Miller parameters to set baseline properties and test conditions are then modified to achieve instantaneous strain rates between 10^{-5}-10^{-6}/hr at temperatures of 80-90°C (120-150°F) above operating temperatures. The values needed for the calculations can be taken off graphs or determined through regression techniques. The points of interest in figure 4.2-5 are $\dot{\varepsilon}_0$, $\dot{\varepsilon}_s$, and $\dot{\varepsilon}$.

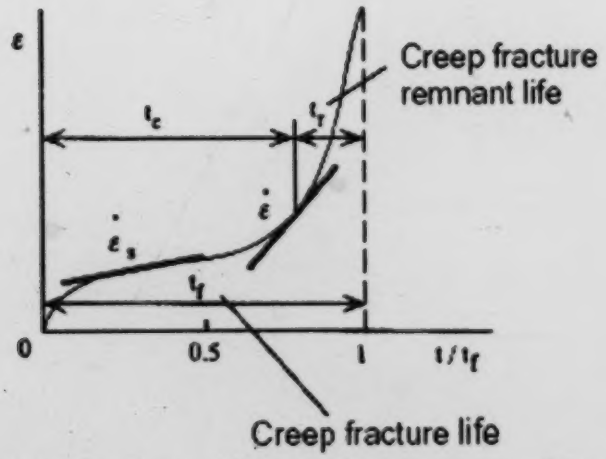

Figure 4.2-5 Important features of constant load creep curves according to Prager [70]

The Omega method must be calculated in terms of instantaneous strain rate as compared to the steady state creep rate used by Monkman-Grant, which allows continuous analysis of creep rate, allowing understanding of the change of creep resistance as the material deforms. Omega mathematically defines the tertiary creep rate manifested as $\dot{\varepsilon}$, as being a constant process, which is resisted by a materials capacity to resist strain damage

(Equation 4-20). One of the most attractive features is that if we know a material characteristically achieves the linear reverse curve condition, we can run a short term test of 400 hrs duration and plot the data as a function of ln $\dot{\varepsilon}$ against ε to directly determine a value of Omega from the slope of the line. This allows a very quick accurate way to check material performance.

The important steps for a test are as follows

Establish strain rate for life assessment under desired conditions

Increase Temperature or Stress slightly (6-10°C or 10% of stress)

Obtain Strain rate from this condition

Strain 0.5-2 percent (depending on material)

Obtain strain rate from this condition

Compute Omega from its definition

Correct Omega for test or service conditions using data published in API RP 579, Table F9

The Omega method simplifies life prediction calculations, as only the service time is required rather than a complete service history for traditional methods. The Omega life fraction in Equation 4-22 shows how simple the form is.

$$Life\_Fraction\_Used = \frac{\dot{\varepsilon}\Omega t}{1+\dot{\varepsilon}\Omega t}$$

Equation 4-22

The Omega test has proven its validity in case studies in the petroleum industry. Klehn [72] has published data on: the re-rating of pressure vessels that had exhausted most of their useful life according to the Larson-Miller, life assessment of reformer tubes that would have been retired, hydrocracking units and a catalytic cracking unit that were retired prematurely. These studies were initiated after microstructure methods and strain methods had been inconclusive. Ibarra [73] used the Omega method to verify safe operating conditions when extrapolation of Larson-Miller parameters would have resulted in a marginal life prediction, as the variation was more than a factor of five from minimum to maximum life. Initial estimates gave a predicted life of less than a year but the realistic service life will be closer to 20 years.

4.3. MICROSTRUCTURE CONCERNS

Microstructure is complicated by the fact that microstructure changes on the atomic level can affect the materials performance. Many times microstructure evolution can be inferred to understand the mechanisms of damage. The best modern breakdown of the complex microstructure problem is shown by McLean [74] to be the product of several competing factors. Maclean's basis for answering this question was by measuring damage from creep testing which may be related to material properties

4.3.1. What Constitutes Microstructure Damage

McLean points out that normalized creep curves may have the same shape but operate by completely different mechanisms for different materials. Some materials such as plain carbon steel are creep ductile while some of the Cr-Mo-V steels are creep brittle.

Similarly some materials such as many wrought materials tend to be ductile, while castings are tend to exhibit less ductility. Every engineering material has its own damage mechanism ranging from dislocation accumulation, particle coarsening, phase changes, cavitation, softening, strain accumulation and cracking as summarized in Table 4.3-1.

CREEP DAMAGE CATEGORY	DAMAGE MECHANISM		DAMAGE PARAMETER	DAMAGE RATE	CREEP RATE
Strain-Induced	Cavity Nucleation Control; Growth Constrained		$D_n = \frac{\pi d^2 N}{4} = \omega$	$\dot{\omega} = \frac{k_n}{\varepsilon_r}\dot{\varepsilon}$	$\dot{\varepsilon} = \dot{\varepsilon}_0 \sinh\left[\frac{\sigma(1-H)}{\sigma_0(1-\omega)}\right]$
	Cavity Growth Controlled by Creep-Constraint		$D_n = \frac{\pi d^2 N}{4} = \omega$ $D_0 = \left(\frac{r}{r_0}\right)^2$	$\dot{\omega} = 0$ $\dot{D}_0 = \frac{d}{2D_0}\dot{\varepsilon}$	$\dot{\varepsilon} = \dot{\varepsilon}_0 \sinh\left[\frac{\sigma(1-H)}{\sigma_0(1-\omega)}\right]$
	Dynamic Subgrain Coarsening		$D_g = 1 - \left(\frac{r_{sg}}{r_g}\right)$	$\dot{D}_g = (1-D_g)\frac{\dot{r}_{sg}}{r_g}$	?
	Multiplication of Mobile Dislocations		$D_d = \frac{\rho}{\rho_0} - 1$	$\dot{D}_d = C\dot{\varepsilon}$	$\dot{\varepsilon} = \dot{\varepsilon}_0(1+D_d)\sinh\left[\frac{\sigma(1-H)}{\sigma_0}\right]$
Thermally-Induced	Particle-Coarsening		$D_p = 1 - \frac{\bar{r}}{r}$	$\dot{D}_p = \frac{K_p}{3}(1-D_p)^{\gamma}$	$\dot{\varepsilon} = \dot{\varepsilon}_0 \sinh\left[\frac{\sigma(1-H)}{\sigma_0(1-D_p)}\right]$
	Depletion of Solid-Solution Elements		$D_s = 1 - \frac{\bar{c}}{c_0}$	$\dot{D}_s = K_s D_s^{m}(1-D_s)$	$\dot{\varepsilon} = \frac{\dot{\varepsilon}_0}{(1-D_s)}\sinh\left[\frac{\sigma(1-H)}{\sigma_0}\right]$
Environmentally-Induced	Fracture of Surface Corrosion Product		$D_{ox} = \frac{2x}{R}$	$\dot{D}_{ox} = \frac{1}{R}\left(\frac{K_p}{t}\right)^{\frac{1}{2}}$	$\dot{\varepsilon} = \dot{\varepsilon}_0 \sinh\left[\frac{\sigma(1-H)}{\sigma_0(1-D_{ox})}\right]$
	Internal Oxidation	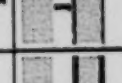	$D_{ox} = \frac{2x}{R}$	$\dot{D}_{ox} = \frac{K_{ox}}{R^2 D_{ox}}$	$\dot{\varepsilon} = \dot{\varepsilon}_0 \sinh\left[\frac{\sigma(1-H)}{\sigma_0(1-D_{ox})}\right]$

Table 4.3-1 McLean's methods of separating microstructural damage [74]

While McLean acknowledges under his proposed "Continuum damage mechanics model", that the traditional steady state strain rate is related to material life by stress and temperature, two additional terms are generated, one of which is for damage accumulation and the other for a materials inherent stress resistance. This method is not

novel in the respect that the basis for this was laid down by Kachanov [65] and Leckie [64]. McLean depicts the inherent stress resistance H as a result of dislocation jog, diffusivity, lattice constants and particle volume fraction and spacing. The damage parameter D is not defined in explicit terms but rather is determined empirically and applied to the appropriate equations in the Table 4.3-1. Damage to the microstructure at $\omega = 1$ is the point where the microstructure lacks integrity and fractures. McLean relates the method to $\dot{\varepsilon}_{ss}$ for a variety of materials but offers no proof of method.

4.3.2. Damage Measurement by Microstructure Methods

The recognized father of determining residual life based on microstructure was Neubauer [75], who devised a system of classification of creep life based on number of cavities and orientation along grain boundaries observed during replication which is summarized in Table 4.3-2. This method was refined with Wedel [76] based on cavitation of grain boundaries and is known as the A parameter. This association resulted in a simple conservative service recommendation.

Table 4.3-2 shows how the replication is used to determine the extent of material degradation such as presence of creep voids or linked cracks. Neubauer believes that the replications will give an estimation of the extent of the microstructure damage A, which may be used to correlate damage to the bulk material. The recommendation is that the inspection level be based on a logarithmic correlation between inspection interval and expended component life.

Class	Class of Degradation	Action Required	Next replication Required
A	Isolated Cavities	No Remediation Effort Required	3 years
B	Oriented Cavities	Replication Tests at Specified Intervals	1-1.5 years
C	Microcracks	Limited Service until repair	0.5 year max
D	Macrocracks	Immediate Repair	Do not operate

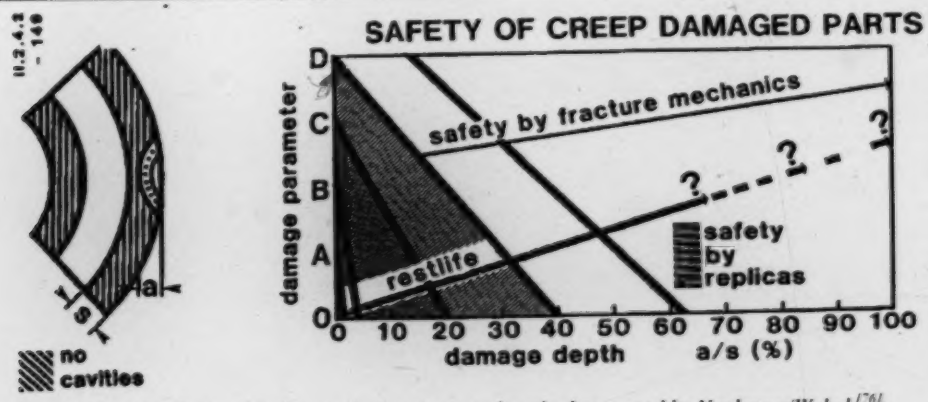

Table 4.3-2 Summary of creep designations and method proposed by Neubauer/Webel [76]

Similar to Leckie and Kachanov, the method McLean proposes uses microstructure damage as the indicator of damage as well. Leckie's damage parameter based creep method directly relates microstructure damage to the damage fraction ω [68], but McLean applies this to Neubauer's method. The value of $\omega = 1$ is the point where the microstructure is no longer continuous enough to exhibit microstructural integrity and the value of υ is used to indicate the rate of degradation of microstructure. The shortcoming of this method is that it only works for some materials. Indeed carbon steels may show no microstructure damage near the end of their service lives and HK 40 type materials will show creep voids near the end of the service life. Further complications to the method arise when we consider that field replication of the surface of a heterogeneously damaged material may not show damage because the surface constraint of the material may prevent

exposure of defects. Additionally, replication correlation to microstructure as proposed by Neubauer, must also be assessed prior to service [76].

Depending on the alloy composition being tested, a good indicator may be the shape of the grain. Westwood [77] shows that under creep conditions grain elongation can show strain damage in individual grains. Grains in some metals at low strain rates may remain equiaxed, but in some materials the creep strain will result in grain elongation in the principle axis of stress. The grain strain formula in Equation 4-23 is based on aspect ratio (AR) of the grains as follows:

$$AR^{\frac{2}{3}} - 1 = \%grainstrain$$

Equation 4-23

Westwood [77] applies this model to girth welds at susceptible locations, to ascertain predisposition to cracking through the heat affected zones. The observations were valid for a failed Cr-Mo-V power pipe subjected to bending stress from system loading.

Bolton [78] points out that the microstructure methods are often specific and only apply to heat-numbers and forms that were originally tested. This is compounded with the lack of accurate service condition replication for accelerated testing. Prager [70] backs this point, where he demonstrates that softening is not microstructure damage and microstructure replication will not show damage that is occurring in service. Prager further expounds the point; " In fact, for many or even most base metals commonly used in North America, optical metallography provides no hint of the existence of creep damage throughout most

of life, ie. There is no cavitation" [70]. Le May [79] points to the sensitivity of replication as a representation of microstructure with several case studies demonstrating that replication in an inappropriate area of piping will not provide useful results. Analysis of a failed extrados of an elbow revealed that a sufficient number of replications must be performed to represent average microstructure [34].

4.3.3. Effect of Creep on Joined Piping Materials

The effects of creep loading on piping material welds are generally not the same as those experienced by the base metal. One of the significant differences is the fact that while most base metals are wrought, welds are in effect small castings and have fundamentally different properties.

4.3.3.1. Weld related effects

Power piping is generally seamless with the exception of large diameters that are difficult to extrude. The joining of piping to other piping and fittings is a girth weld that is prevalently the site of failures. The primary causes of girth weld failure are often axial or bending stresses. The failure often manifest themselves under leak before break conditions and tend to concentrate at elbows, T connections and Y connections [62].

Figure 4.3-1[62][80] shows how the severe thermal cycles affect the microstructure significantly depending on level of phase transformation achieved which is dependent on temperature the microstructure has been exposed to. Figure 4.3-1[62][80] also shows the thermal relationship to different types of damage associated with girth welds. They are:

Type I -Damage, which is longitudinal or transverse in weld metal and remains entirely within weld metal
Type II -Damage that is longitudinal or transverse to weld metal but extends into heat affected zone (HAZ)
Type III -Damage in coarse grain heat affected zone (CGHAZ)
Type IV -Damage initiated or growing in the intercritical zone of the HAZ (the transition region between the fully transformed, fine grained HAZ, and the partially transformed base metal.)
Type V -Damage along the fusion line
Type VI -Damage in middle of weld, but at CGHAZ created between two rows of weld weaves

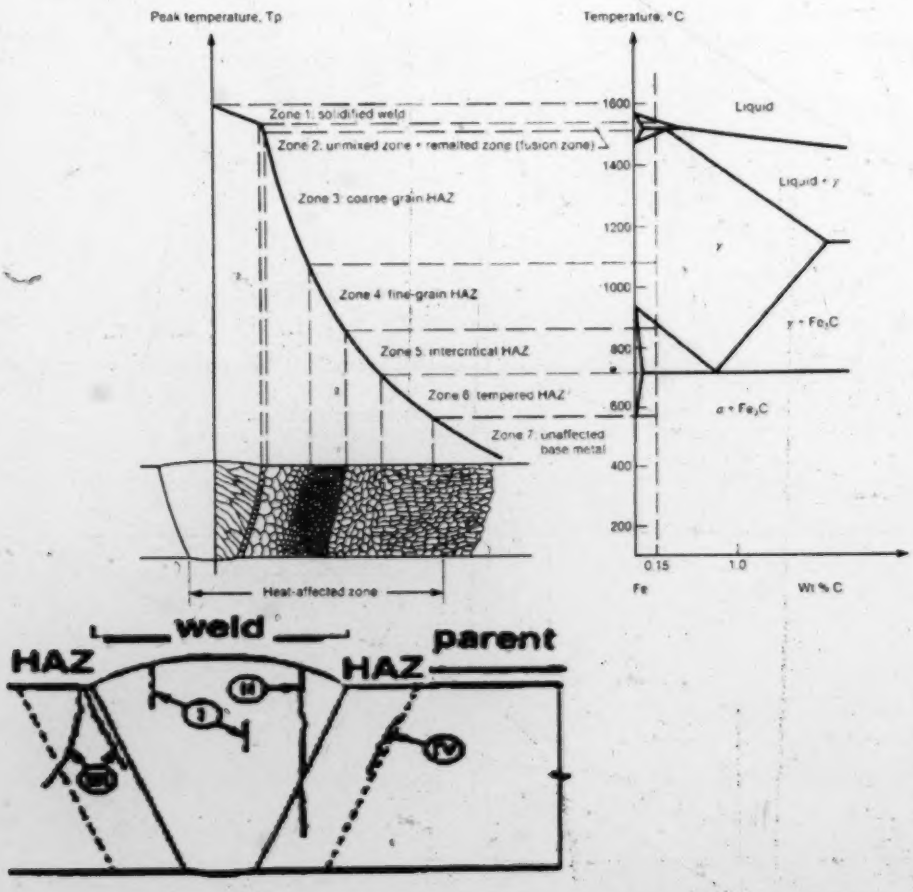

Figure 4.3-1 Relationship of weld damage to both microstructure and phase diagram. Types of damage in welds are shown and associated with expected microstructure (above) and critical temperatures for weld microstructure development (right) [62][80]

The most common mode of cracking in power piping is type IV and is generally attributed to localized creep deformation in the soft zone in the intercritical region under action of bending stresses and is frequently found in long seam welds. This can be exacerbated by the overmatched weld metal used manufacture of piping systems. Creep testing across the weld metal will result in significantly different stress conditions as compared to full size specimens.

Recent work by Storesund [81] has shown by using sub-size creep specimens that welds give stress magnifications of 24:1, which result in significantly shorter life. Post weld stress relief can also exacerbate this condition and change the stress magnifications to 57:1. The only significant improvement was to reduce the size of the heat affected zone by lowering heat input, which showed as an independent factor from the width of the weld. Viswanathan and Foulds [61] have performed testing based on ex-service material in various weld conditions and damage states finding that tripling specimen diameters based on maximum material conditions would result in increasing creep lives by multiple times calling the entire issue of overmatched weld metal into question.

4.3.3.2. Weld Repair

A technique that has merit is the repair of welds or replacement of affected piping and fittings. A statistical survey of 20 United States utility companies showed that many times weld repairs were effective for girth weld damage [82]. Although the survey only included Cr-Mo piping in service over 1000°F (538°C); the key factor was a metallographic examination to determine extent of creep damage and set an arbitrary

level of acceptable microstructure damage. Alternately economics dictated the repair feasibility as determined by a contractor. The result for repair of the piping systems was acceptable for service-induced flaws but fabrication and design related flaws required additional modifications.

A Viswanathan case study review [80] shows that the established method of post weld heat-treating (PWHT) aged materials is slightly more involved than virgin materials. The shortcoming of the review is that only Cr-Mo steels were included in the study. The study highlighted the predominant existence of creep failure in bends and welds. The as welded condition seems to give a better life expectancy especially at higher stresses but temper bead techniques appear to give better lives. Viswanathan found the case studies supported deviating weld repair from the standard industry shielded metal arc weld (SMAW) to gas tungsten arc welds (GTAW) making a significant increase in repair life. The single most important factor that is pointed out in the case studies is the importance of reducing or eliminating external loads, which apply undesired stress.

4.4. FRACTURE MECHANICS BASED METHODS

Fracture mechanics must be summed by the phenomena that need to be evaluated. While fracture toughness K_c demonstrates linear fracture mechanics, J integrals demonstrate materials that exhibit elastic/plastic fracture characteristics, at higher temperature most materials follow a viscous behaviour that is described by C^* [83]. The point of transition from elastic/plastic to viscous if generally defined as 0.3Tm.

Several of the major creep life methods have attempted to link fracture to creep. Larson-Miller, Monkman-Grant and Theta project have all attempted to make the correlation with varying degrees of success [84]. The progression of a crack due to creep is summed up in a term C* which is a mathematical measure of crack propagation through a viscous field [83]. Application of the Omega method to this problem results in a creep test that can either be smooth or contain flaws. Previous work by Yokobori had resulted in a term Q* that could derive activation energy, be equated to Larson-Miller parameters, model creep crack life and can be integrated. Since Q* and Ω_P are both related to Larson-Miller parameters they can be represented by $Q^* = 1/\Omega_p$ for creep ductile materials[84].

4.4.1. Potential for Fracture

When evaluating high temperature materials an important detail is related to the time frame between when a flaw develops and when the flaw will develop into a crack and subsequently propagate. The British R5 (Assessment procedure for high Temperature Response of Structures) is a Fitness for Service Standard (FFS) focused on this approach, which is derived out of creep/fatigue cracking. The familiar measure of fracture toughness "K" is used to derive the C^* integral in Equation 4-24.

$$C^* = \sigma_{ref} \dot{\varepsilon}_{ref} \left[\frac{K}{\sigma_{ref}} \right]^2$$

Equation 4-24

The C^* integral differs from the J integral by using strain rate instead of strain to ascertain condition at the crack tip in a viscous field rather than the J integrals elastic/plastic field [83] Nikbin's [85] investigations using R5 FFS shows those materials that are creep ductile demonstrate a narrower margin of transition from plane stress to plane strain fracture conditions. The R5 methodology assumes that cracks will develop under creep conditions and therefore is tied implicitly to the R6 (Integrity of structures containing defects). Laboratory controlled tests of Cr-Mo steels under temperature accelerated testing showed that the method was conservative for base metals and very close for weld cracking. Patel [86] determined that although the weld failure mode was different than predicted, the method has validity for predicting life. The shortcoming of the R5 method is that it uses empirically determined coefficients, which may not represent the material conditions; which required extrapolation of the life prediction results in Patel's paper. Furthermore, predicting a creep life of 20 000 hrs is much different than a creep life of 300 000 hrs due to evolution of microstructure when such long time scales are used.

A particularly good project by Grujic et. al. [87] looked at upper-shelf and lower-shelf behaviour using instrumented Charpy for upper shelf and J integrals for lower shelf to cover four operating temperatures and ambient start-up temperatures for virgin and 175000 hr aged GOST 10500-63 low carbon, low alloy steel. The instrumented Charpy was able to document 10-30 % decreases in the energy require to propagate cracks at service temperatures in service-exposed materials.

4.4.2. Low Temperature Fracture

Plant start-ups are an inherently dangerous time for ferritic steam piping as it is close or below the lower transition temperature and may be subject to condensates moving at high velocity. The *J* integral is important in a complete analysis as it indicates the static susceptibility of material to damage [58]. Grujic's [87] findings for J integrals was that the service-exposed material had was more resistant to growing static cracks and gave much better lower shelf Charpy impact energy absorption. Nikbin and Smith [88] found that the crack growth rate a, was related to the C parameter and the stress exponent n in Equation 4-25. This insinuates that the crack growth for a plane stress will be lessened for materials with greater ductility especially under conditions of triaxiality.

$$\dot{a} \propto \left(C^{*}\right)^{\frac{n}{n+1}}$$

Equation 4-25

Yang [43] modeled the crack growth behaviour of graphitized steel using ANSYS finite element software. Only Gleeble testing, which offered no evaluation of ductility, was performed, so the J integral was modeled for a material that had 1% ductility and the graphite nodules were hard like aluminium oxide particles. This resulted in a model that would break the matrix allowing rapid propagation of the cracks. The only variable from that changed between the aluminium oxide model and the graphite model was elastic modulus. When the elastic modulus for graphite was used was the observation that the graphite would be difficult to break or debond from the void wall with out further plastic deformation [43].

4.5. IN-SITU METHODS FOR LIFE PREDICTION

4.5.1. Non-Destructive Examination

Non-Destructive Examination (NDE) is the first line of defence in plant maintenance. It has a long proven history of effectiveness in assisting engineering decisions. All NDE methods are a snapshot in time although the value to fitness for service is realised through comparison of known current conditions to new material conditions or failed components. NDE generally samples small sections, which hopefully represents the approximate bulk material condition but a limitation is that most of the useful NDE techniques may only be used at ambient temperatures. Common techniques that are useful are: Replication to show microstructure, Ultrasonic testing, which reflects sound waves off of defects and flaws by measuring wave travel time and Magnetic Particle inspection, which is restricted to large defects.

Viswanathan [80] correlates microstructure damage measurement for girth welds by comparing replications with NDE techniques and suggests reasonable responses to the results. Table 4.5-1 shows some of the major NDE techniques used and their response to various materials conditions. The following corrective action suggestion correlates the response to all combinations of the NDE results with the various scenarios of remediation available. *RI* indicates a response for the method whereas *NRI* does not indicate that a defect/flaw is not present, but rather that the method merely did not detect the presence of a defect/flaw.

Inspection/Examination Technique & results				
Category	Magnetic Particle inspection (MPI)	Replication	Ultrasonic Inspection (UT)	Actions/Comments
A	No Recordable Indications	No Damage	No Recordable Indications	Return to service
B	Recordable Indications	Type I,II or III Damage	No Recordable Indications	Remove Unacceptable indicators by grinding. Confirm removal with MPI Repair if $t<t_{min}$ as per ASME B31.1
C	Recordable Indications	Type I,II or III Damage	No Recordable Indications	Remove unacceptable damage by grinding. Confirm removal by MPI and Replication. Replace if necessary. Repair if $t<t_{min}$ as per ASME B31.1
D	Recordable Indications	Type I,II or III Damage	Recordable Indications	Examine UT results in Detail If no action is required, treat as case C
E	No Recordable Indications	Type I,II or III Damage	Recordable Indications	Examine Replica and UT results in detail
F	No Recordable Indications	Type I,II or III Damage	No Recordable Indications	Examine Replica results in Detail
G	Recordable Indications	Type IV Damage	Do not UT if replication shows problem	Remove entire weld by gouging/machining including complete HAZ's or replace piping
H	No Recordable Indications	Type IV Damage		
I	No Recordable Indications	No Damage	Recordable Indications	Examine UT results in detail

Table 4.5-1 NDT correlations flow sheet that may be adapted to fit particular materials [80]

4.5.2. Small Punch Testing

Small punch testing is achieved by cutting a small disc from the material of interest and mechanically testing it to determine mechanical properties. The small punch test relies on a smaller sample removal than boat samples that have been used for many years in testing thick sections of power piping. The method has matured since its inception in 1982 by Huang [89] and demonstrates potential for determining mechanical properties. The full development of the method may be obtained from ASTM Special Technical Publication 888 [90].

An extensive review of the small punch technique may be found with Fleury and Ha [91]. The small samples are in the order of 10mm dia and 0.5mm thick. The samples are clamped in a jig and pushed with a tungsten carbide ball, until the load decreases by 20 % ensuring that the ultimate tensile stress has been exceeded. The resulting curve can then be portioned into sections of elastic bending, plastic bending, membrane stretching and plastic instability, which may be mathematically related to mechanical properties and toughness. The testing method lends itself to elevated temperature tests, allowing replication of service conditions [92]. The method may also be considered non-destructive as investigation by Parker and Wilshire [93] found that specialized equipment was available to remove sections in such a fashion that the power piping did not have to have weld remediation.

One of the fortuitous characteristics is the existence of brittle to ductile transition zones, which was related to Charpy testing [90]. The existence of the relationship to Charpy testing allowed Fluery and Ha [91] to show that fracture properties may be evaluated for fracture toughness and therefore be adapted to J integrals. Since small punch testing may be conducted at high temperatures an indicator of toughness properties at high temperatures can be obtained and related to Fracture Appearance Transition Temperature (FATT) properties.

Bullock [92] suggests that as many materials age, the FATT shifts in a non-linear fashion related to phosphorus content and grain size. Bullock found that different classes of steels

show FATT results related to grain size and chemistry. The implementation of small punch testing for aged materials can now be shown to have a margin of safety without having to subject large samples of material to destructive testing, but the test does not indicate the long term creep resistance of a material or when the appearance of defects will occur.

4.5.3. Damage Measurement by Hardness Based Methods

Damage may also be indicated using hardness. Hardness based life prediction of creep damage is common in Japan, where the method has been used with some success for rotor steels. The underlying assumption that the strength of steel follows the hardness has some validity with new materials, as there is a linear relationship between Brinell hardness and strength. The assumption assumes that the relationship will follow the relationship of hardness being proportional to the previously discussed Larson-Miller constant. In Equation 4-26 a relationship is drawn between hardness and a parameter P, which is composed of a temperature term and time to fracture term, at some temperature but Endo[94] did not point out how the term P was derived.

$$H = f(P)$$

Equation 4-26

The problem is that softening is not always indicative of a deficiency of strength. Viswanathan [80] shows that when service exposed piping may not conform to Larson-Miller type correlations, life prediction has been made successfully by this method in some cases by exploiting the relationship $dH/dP = constant$. This may be implemented

where pre-service hardness is known and Equation 4-26 is evaluated to find the desired temperature.

$$T = \frac{H_2 - H_1}{m \log t_2 / t_1}$$

Equation 4-27

An alternate Japanese method shown by Endo [94] correlates microstructure from replications to hardness and chemistry (figure 4.5-1). The assumption is that there will be no reduction in hardness until voids appear in the microstructure. The method has proven accurate in typically brittle 1Cr ½ Mo rotor forgings. Endo[94] refers to the method as "a non-destructive predictor of the fracture appearance transition temperature" (FATT).

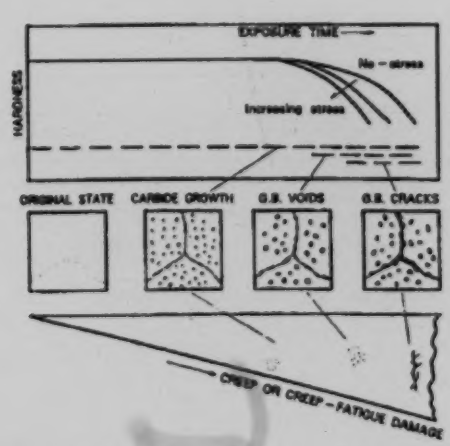

Figure 4.5-1 Relationship between hardness and creep damage for 1Cr ½ Mo rotor forgings according to Endo [94]

The method assumes that a number of competing factors can give rise to a critical temperature at which critical crack growth will occur. The method relies on a correlation

between hardness (Hv), etched grain boundary width (W) and chemical composition to determine FATT using empirically derived values for b_1-b_8 as shown in Equation 4-28.

$$FATT°C=aW+b_1Hv+b_2Si+b_3Mn+b_4P+b_5Cr+b_6Sn+b_7(SI+Mn)(P+Sn) \times 10^4+b_8$$

Equation 4-28

Equation 4-28 is similar to empirically derived formulas used for the welding metallurgy condition known as temper embrittlement, but no time frame is suggested for the appearance of the defects, nor does the formula explicitly include microstructure or forming method effects.

4.5.4. Neutron Diffraction

Neutron Diffraction has become an industry-accepted method of determining real time stress analysis for real components. Details of the mechanics of the process are beyond the scope of this review, but since neutrons can penetrate and be reflected through more than 25 mm of ferrous materials, stress analysis by diffraction techniques are possible. The unique feature of neutron diffraction is that it can be used to develop real time stress analysis. Figure 4.5-2 shows stages of strain accumulation during neutron diffraction mapping [95].

Alternately the same equipment may be used for a technique known as neutron scattering [96]. Neutron scattering may be used to detect sensitive elements in lattice locations that are sensitive to disruption in crystal lattices (figure 4.5-3). Where the X-ray diffraction techniques may find it difficult to distinguish between light elements, neutron diffraction can distinguish small changes, such as isotope variation, in most elements. Neutron

diffraction analysis suffers when materials are strong neutron absorbers such as cadmium, boron and to a lesser extent carbon [96].

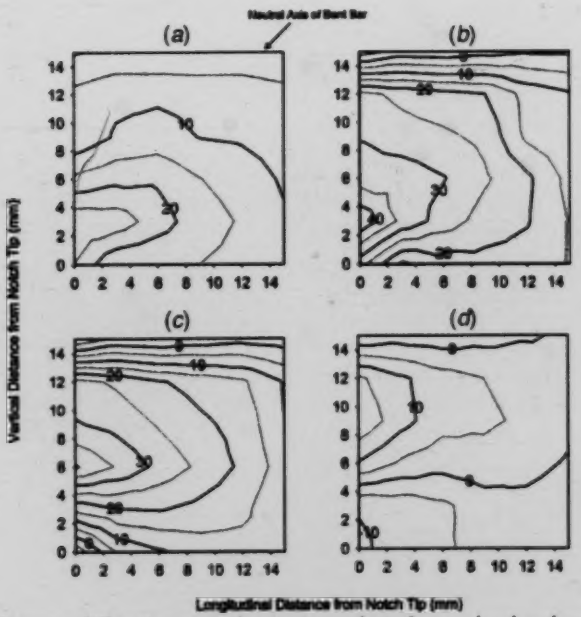

Figure 4.5-2 Neutron diffraction maps for strain analysis for one load and unload cycle [95]

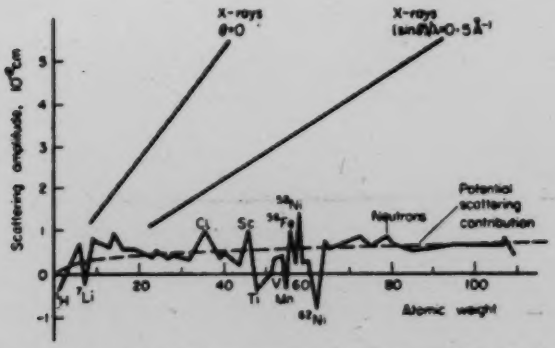

Figure 4.5-3 Elemental sensitivity of neutron scattering contrasted with X-ray scattering [96]

Since secondary graphite may be thought of as a defect in a material, it could be possible to superimpose neutron diffraction obtained stress maps over top of neutron scattering

maps. This would allow a core to be extracted from a piece of material under question and a damage evaluation could then be performed and the site of the material extraction could be weld repaired. This would be allowing growth of graphite growth to be monitored and a non-conservative replacement scheduled.

4.6. METHODOLOGY OF FITNESS FOR SERVICE

4.6.1. Historic Accepted FFS methods

Historically API 530 [58] life prediction methodology have been used to assess life predictions of ASME B31.1 (Power piping) and B31.3 (Process piping), as these standards do not deal with degradation of the material. The method focuses on knowing the operating conditions up to the point of testing and using Robinson's rules the forecast is made. Since operation records are difficult to accurately represent in consumed life due to temperature excursions, start-ups and shutdowns, a uniaxial rupture test does not truly represent operation conditions. Rarely does virgin original material exist to allow a complete comparison so even the best estimates will have to be conservative.

The use of Larson-Miller parameters in API 530 means that material is often discarded when it reaches the minimum or 63% life consumed line. The acceleration of the testing means that the material will be overstressed or overheated which insinuates the material will suffer stress induced failure or excessive surface oxidation rather than a true representation of service conditions. A promising method, that must have a known life history, is based on comparing microstructure related to isotherms to the Sherby-Dorn parameters [61].

4.6.2. API RP 579

With the fact that so many utilities and plants are reaching the end of their design service lives and replacement costs are prohibitive, stakeholders in the National Board, Petrochemical and Pulp industries looked to the Pressure Vessel Research Council to expand the scope of the successful API 510 (pressure vessel inspection, repair), API 570 (pipeline inspection, repair) and API 653 (tank inspection, repair) programs to fitness for service. This document API RP 579 [97] will become the defacto standard for fitness for service and covers 61 codes and standards representing European and North American philosophies including ASME, NACE, BSI and API [97]. The document is designed in sections to address different concerns for different problems with a multidisciplinary approach. The fitness for service is a framework designed to accommodate from simple routine investigations to in-depth analysis of structures depending on observed conditions in three levels of analysis. We will only concern ourselves with API RP 579 Level 3 assessments [97] due to the unfamiliar nature of the graphitized aged material.

The two sections that concern this investigation are: Section 9 (Assessment of crack Like Flaws) and Section 10 (Assessment of Components Operating in the Creep Range). One factor that is unknown is the potential of graphite nodules to link up and ultimately serve as a crack nucleation point and subsequently assist propagation of said crack. The second factor is the fact that the investigated piping operating temperature is at the bottom of the creep range.

4.6.2.1. Proposed creep based FFS methods

API RP 579 Section 10 [98] divides creep range life prediction into traditionalists who work traditional methods backwards to get a conservative life expectancy or those who use of Omega methods to mimic real service conditions. One of the most important advantages of using the Omega method for Fitness For Service is the adaptability to Finite Element Analysis (FEA). FEA is an important area of API RP 579 as it allows the detection of areas of stress. API RP 579 is not the same as the British R5 FFS standard, as the British standard is a creep fracture based model and does not accommodate materials that exhibit ductile creep.

4.6.2.2. Proposed fracture based FFS methods

Similar in content to the British R6 method, Section 9 of API RP 579 [98] gives a clear-cut method of determining dangers due to crack growth. As part of a level III assessment, the presence of crack like defects must be evaluated as to ascertain whether or not the presence of graphite is an anomalistic defect or a flaw with potential to degrade a structure. The data is collected by measuring crack opening displacement (COD) with a J integral test, and comparing to a failure assessment diagram (FAD). The method may be summed as follows in the following Figure 4.6-1. A FAD specific to the material may be constructed using the tensile testing data for level III assessments or a generic FED may be used for Level II assessments. Determining the stable crack growth regime for a material that has a growing crack-like defect can help determine potential life shortening defects. While API RP 579 does not recommend Crack Tip Opening Displacement

(CTOD) methods, the same data that is used to develop J integrals can be used to determine a critical flaw size δ.

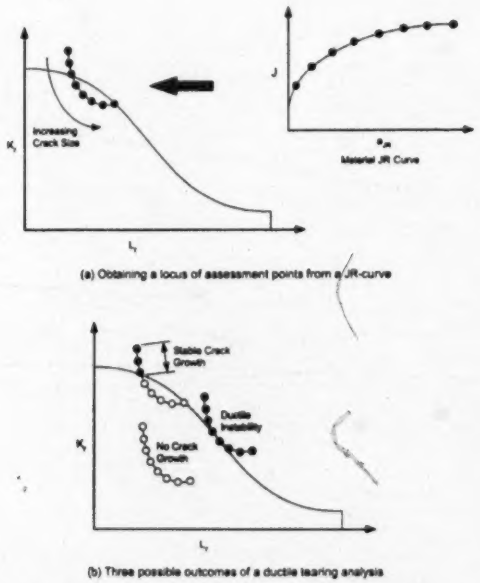

Figure 4.6-1 Crack growth assessment from API 579 based on a FAD [98]

4.7. NECESSITY OF UNDERSTANDING ALL CONDITIONS AFFECTING THE FITNESS FOR SERVICE PROBLEM

The need for a multi disciplinary approach to understanding fitness for service is that it is just as important to know what type of testing should be done on a particular material, as where that testing should be done. Stress analysis is of paramount importance to FFS as we need to determine any possible external stress concentrators that would invalidate results. Figure 4.7-1 shows estimated creep lives for some power piping components and estimated creep lives by Neubauer and Wedel [76]. Certainly the prospect of wasting NDE

and inspection time on the wrong component and then testing the better parts of the system will not give the margin of safety that a steam system should have for operation.

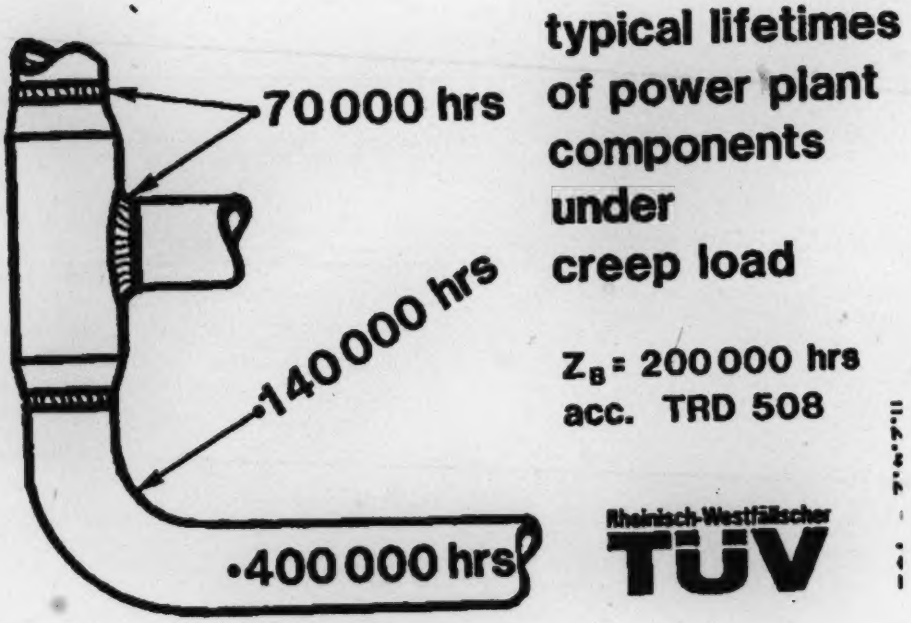

Figure 4.7-1 Estimated lifetime for different components under creep load [76]

5. PIPING SELECTION AND PRELIMINARY RESULTS

5.1. DIRECTION OF INVESTIGATION

The focus of the investigation is centered on material that had been in service for 20^{+} years at a nominal service pressure of 4.4 MPa and a maximum temperature of 435 °C. Initial material selection was based on accepted literature on the subject [5] [6] [7] and engineering reports [1] [2] [3]. All base metal materials were assumed to be of a homogeneous nature with degradation at the welds as per Canspec report [3]. The initial thrust was to understand the degradation mechanism of a material that only has iron carbide and therefore should have significantly different microstructure evolution as compared to readily available Cr-Mo steel data.

5.2. PIPING SCHEMATIC AND PRELIMINARY MATERIAL SELECTION

Figure 5.2-1 shows a section of the E1 WHB piping from the superheater to just beyond the first block valve. Elbows 1, 3, 4 and Reducer 3 have been labelled in this partial piping schematic. Numbering is based on the section cuts as detailed in the full piping schematic included in Appendix A. The focus of material selection was based on suspect weld joints identified by Canspec replication and Microdur hardnesses [2]. Additionally, eight neutrados sections of elbows near the graphitized replications, two reducers and several piping sections were retained, and the balance of material was disposed of. A further one half of Elbow 1, which is the mirror half of the elbow used by Canspec to perform microstructure analysis, was salvaged.

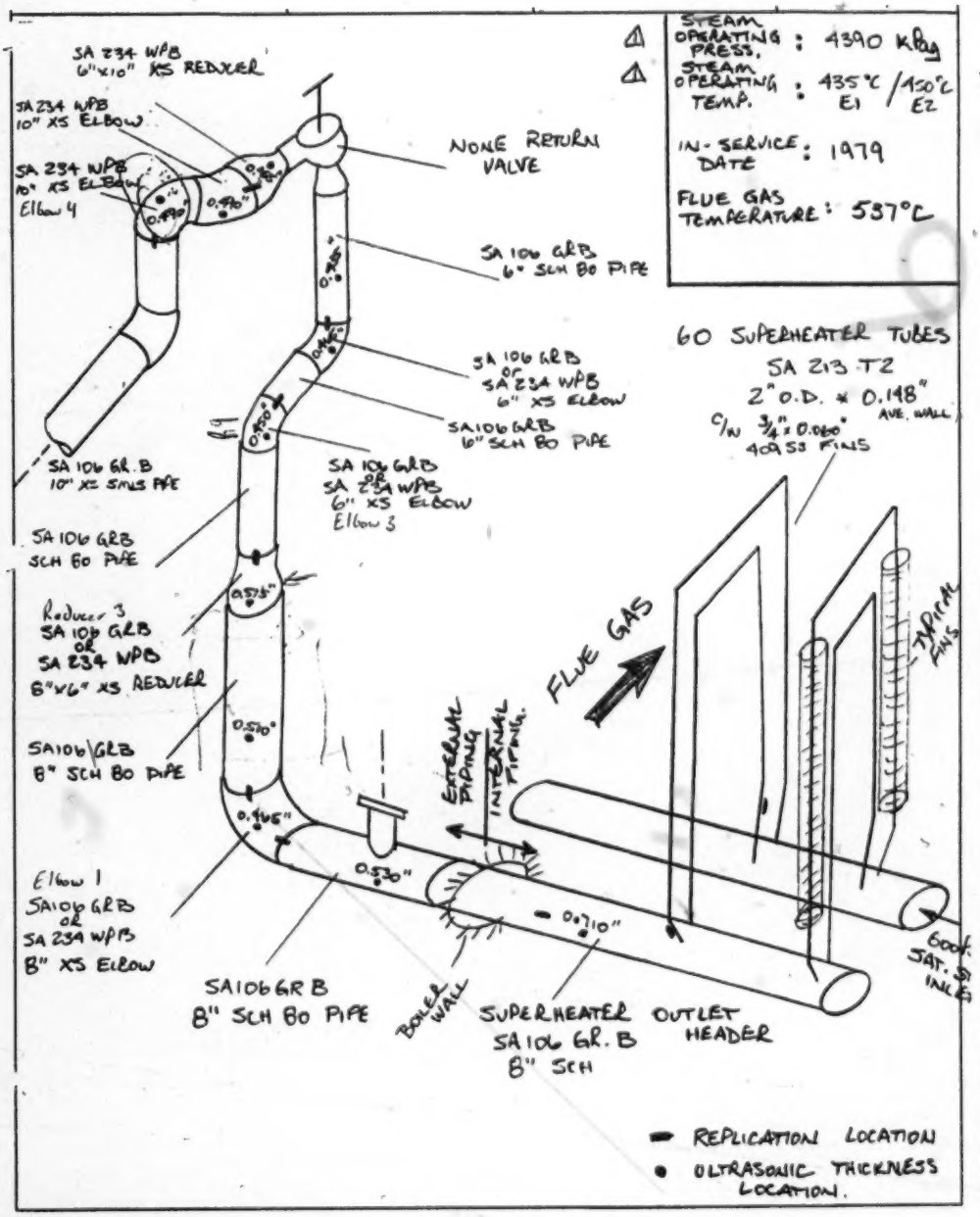
STEAM OPERATING PRESS. : 4390 kPag
STEAM OPERATING TEMP. : 435°C / 450°C
E1 E2
IN-SERVICE DATE : 1979
FLUE GAS TEMPERATURE : 537°C
SA 234 WPB 6"x10" XS REDUCER
SA 234 WPB 10" XS ELBOW
SA 234 WPB 10" XS ELBOW Elbow 4
NONE RETURN VALVE
SA 106 GRB 6" SCH 80 PIPE
SA 106 GRB OR SA 234 WPB 6" XS ELBOW
SA106 GRB 6" SCH 80 PIPE
SA 106 GR.B 10" XS SMLS PIPE
SA 106 GRB OR SA 234 WPB 6" XS ELBOW Elbow 3
SA 106 GRB SCH 80 PIPE
Reducer 3 SA 106 GRB OR SA 234 WPB 8"x6" XS REDUCER
SA106 GRB 8" SCH 80 PIPE
Elbow 1 SA106 GRB OR SA 234 WPB 8" XS ELBOW
SA106 GR B 8" SCH 80 PIPE
BOILER WALL
SUPERHEATER OUTLET HEADER SA 106 GR. B 8" SCH
60 SUPERHEATER TUBES SA 213 T2 2" O.D. x 0.198" AVE. WALL C/W 3/4" x 0.080" 409 SS FINS
FLUE GAS
EXTERNAL PIPING
INTERNAL PIPING
TYPICAL FINS
SAT. SS INLET
REPLICATION LOCATION
ULTRASONIC THICKNESS LOCATION.

Figure 5.2-1 Piping schematic from E1 WHB showing Non-Destructive Examination sites adjacent to boiler. Most of the research material comes from this section of piping and appropriate materials are labelled with their respective research designations.

5.3. PRELIMINARY MICROSTRUCTURE AND HARDNESS FOR CURRENT INVESTIGATION

Preliminary analysis started with cutting, and mounting samples of materials selected for microscopy. The A106 piping consisted mainly of proeutectic ferritic microstructure suffered some spheroidization and was free of graphite nodules (Figure 5.3-1). Basemetal of the elbows consisted of proeutectic ferrite and showed significant graphite quantities away from the suspect weld zones. The graphitization near the heat affected zone was further found to concentrate on the elbow side of the weld rather than the piping side.

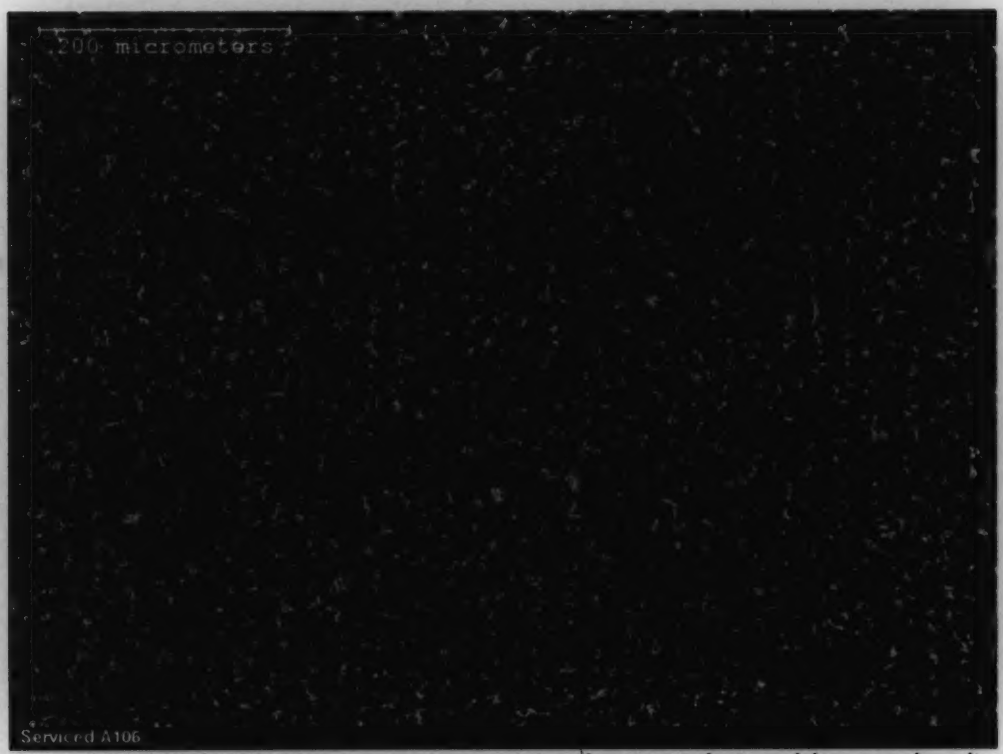

Figure 5.3-1 Typical A106 piping microstructure consisting of proeutectic ferrite and degenerated pearlite

The discovery of planar graphite in Reducer 3 with denser linear morphology than the HAZ graphitization directed the research towards looking at fittings and forgings rather

than the piping itself. Subsequent replacement of piping from the E2 WHB allowed a more controlled material selection. Table 5.3-1 is a partial summary of preliminary work of material from both the E1 and E2 ASME B31.1 WHB piping that was used to select materials for testing. The piping materials from E1 and E2 are assigned designations based on Nova Chemical supplied isometric sketches.

Although the replication performed on E2 piping three years prior to removal showed no graphitization, extensive graphitization was found in some of the fittings and was advanced in piping reducers. Based on these results it was felt that the E1 WHB had more advanced graphitization and in spite of a shortage of material, it was subsequently determined that concentrating the effort on E1 material would be more revealing.

Original designation	Hardness HRB			Graphite	Location in piping system	Selected for research
	weld	long	hoop			
E1 3a R7				Medium	Elbow 3	yes
E1 3a R9				Worst	Reducer 3	yes
E1 4				Medium	Elbow 4	yes
E1 5				Clean	Elbow 5	no
E1 6				Some	Flange 6	yes
E1 7				Medium	Elbow 7	yes
E1 10				Bad	Elbow 10	yes
E1 11				Minor	Elbow 11	no
E1 12				Minor	Elbow 12	no
unknown				Bad	Elbow	yes
E1 1 6R5 1		75	70	Good	Pipe 1	no
E1 1 6R5 2		60	59	Bad	Elbow 1	yes
E1 1 6R5 3		58	59	Bad	Elbow 1	yes
E1 1 6R5 4		59	62	Bad	Elbow 1	yes
E1 1 6R5 5		58	60	Bad	Elbow 1	yes
E1 1 R17		63	63	Bad	Elbow 1	yes
E1 2R16		75	76	Good	Pipe 1	no
E1 2R16		74	76	Good	Pipe 1	no
E1 2R16		73	74	Good	Pipe 1	no
E1 2R16		78	75	Clean	Pipe 1	no
E2 1a	73	82		Minor	Pipe 1	no
E2 1b	81	75		Minor	Elbow 1	no
E2 1c		75		Minor	Elbow 1	no
E2 2	77	74		bad line	Elbow 2	no
E2 2	75		73	Bad	Elbow 2	no
E2 3		59	64	Bad	Reducer 3 8x10	no
E2 4		73		Minor	Elbow 4	no
E2 5		68		Bad	Reducer 6x7	no
E2 6		73		Minor	Reducer 6x8	no
E2 10a	81	78		Clean	Pipe 10	no
E2 10b	79	78		Minor	Pipe 10	no

Table 5.3-1 Compilation of Tables used to select piping materials. Based on graphitization, E1 materials elbows and fittings were researched.

6. EXPERIMENTAL METHODS

6.1. CHEMISTRY

Preliminary chemistry was preformed in conjunction with phase analysis by using the energy dispersive x-ray (EDX) of the Hitachi SEM. EDX is not an accurate method but it may give results for metals presence in sufficient quantities. The most significant shortfall of EDX for this investigation is that although it can detect carbon, it cannot accurately quantify amount of carbon; therefore graphite can be identified as a separate phase but it cannot be quantified.

Absolute chemical composition was carried out by Altasteel on their spark analysis equipment to NIST traceable chemical standards. The chemical analysis was taken on the external surface of materials previously evaluated for hardness testing. Seven samples were tested based on their degree of graphitization as determined by metallography. The spark analysis method itself is an average of three spark burns and is considered to be accurate to +/-1 of the last digit for each element.

6.2. MICROSTRUCTURE AND PHASE DETERMINATION

6.2.1. Sample Preparation

The first microstructure requirement was to develop representative samples. Secondary graphitization is significantly different in polishing than standard steel samples. The secondary graphite nodules will not remain adhered to the matrix during traditional final polishing. Graphite nodules would fall out during final polishing phase, scratching the

face of the sample. The use of water-soluble polishing compounds exacerbated the condition as did the use of napped polishing cloth. The desire for a finely finished surface were traded for requirements of scratch free surface by using a two step final polish where the finish was final ground with 600 grit SiC paper and then finished polished using a two step diamond finish.

The final polish procedure required the minimum number of steps that could be used to achieve an effective finish. The first polishing step was six-micron diamond paste in an oil carrier applied to an eight-inch nylon pad. An initial two and a half kilograms load per sample while changing direction of polishing 90° every thirty seconds was used and after two minutes pressure was reduced to one kilogram of load per samples and polishing would continue till no 600 grit scratches could be observed. Failure to change polishing direction frequently or heavy pressure on the sample would pull carbon out of the matrix resulting in scratching or alternately, leaving streak marks across the surface. Final polishing time duration was determined by the time that one-micron diamond paste in an oil carrier under ½ kilogram of load would not pull the graphite nodules from the matrix. The final polishing was not necessarily scratch free but showed clear microstructure.

6.2.2. Microstructure and Image Analysis

Optical Microscopy was performed with an Olympus PME3 inverted Microscope with image acquisition using Image-Pro Materials-Pro software for general metallography and phase analysis. A Hitachi scanning electron microscope (SEM) with energy dispersive X-ray (EDX) capabilities was used for high resolution metallography and chemistry.

6.2.3. Macrostructure

Macrostructures are use to develop our understanding of bulk material properties since the scale of the micrograph does not allow complete analysis. Stitching unetched micrographs together developed macro representations of the material. A Nikon CoolPics 4500 camera with a microscope adapter was employed using the Olympus X-Y Table to obtain incremental square pictures, each representing a 2 mm x 3 mm size as shown in Appendix C. The samples were left unetched to enhance the presence of black graphite against yellow ferrite to improve the Image Pro graphite density analysis. Corel Draw 11 Photodraw was used to stitch the micrographs so the could show graphite density from inside diameter to outside diameter. These pictures will subsequently be referred to as macros or macrographs.

6.2.4. Graphitization Analysis

Quantifying graphite with the Image-Pro software phase analysis function was unsuccessful for micrographs due to a number of factors. Some include phase interruption from etching and blurring at the edges of the micrographs. The attempt at quantifying graphitization was passed onto macrostructure methods. The stitched composite macrographs were cropped to remove image distortion. The most successful analysis was performed by taking sections near the outside diameter (od), midwall (mid), and near the inside diameter (id).

6.2.5. Sulfur Printing

Sulfur prints were carried out under ASTM E 1180-94 [99]. The purpose of a sulfur print in this case is to establish the orientation of sulfur compound such as MnS, which will follow physical deformation trends in forging operations and segregation trends in casting operations. Sulfur prints are a macrostructure method that uses bromide photographic paper and sulfuric acid to create a reaction with the sample that stains the paper. It was hoped that the segregation of MnS indicated by EDX would follow the same pattern as the planes of planar graphitization. Although X-ray mapping with EDX will positively identify more elements of interest, it does not cover the large area required, as 50 times magnification is the lowest resolution that the SEM may successfully resolve.

The bromide paper was soaked in H_2SO_4 for three minutes and laid flat on top of a ground steel plate. Mounted samples that had been polished and etched were laid on top of the paper for durations of 50 seconds to two minutes. The samples were washed in water for 15 minutes and then were fixed for 15 minutes in a 1+8 solution of ammonium chloride and distilled water. Fixing the paper was followed by a second wash in water with a small amount of Photoflo.

6.3. HARDNESS TESTING

Hardness measurements were carried out on several different scales. The predominately ferrite matrix was amenable to methods using relatively low loads and large contact areas. A Wolpert Dia Testor 2N hardness tester was used for both Vickers (HV) and Brinell (BH) testing. Vickers hardness with a 30-kilogram load (HV30) is the laboratory

standard test method and load for steel. Due to similar operating principles it was hoped to have a relation to the industrial Microdur portable hardness testing devices. Brinell testing was conducted with a 250 kg load with a 10 mm ball (BH 250), was chosen as Brinell tests are know to be extremely useful for large grain structures and may generally be converted directly to ultimate tensile strength in steels. There is a theoretical linear relationship between Brinell hardness and ultimate tensile strength. This direct property relationship and ease of surface preparation has allowed its predominance in the inspection industry.

A Wilson 4TT Rockwell hardness tester was used to determine hardness on the HRB and HRF scales. The HRB scale with a 100-kg load on a $1/16^{th}$ diameter steel ball was picked simply for its accepted presence in the inspection industry. The HR30T scale is a superficial scale with 30-kg load on a $1/16^{th}$ diameter steel ball and is particularly useful for soft materials and coatings.

Hardness testing was conducted based on the results of preliminary metallography, which had determined relative amounts of graphite. Preliminary HRB testing was performed midwall on some specimens during preliminary evaluation all for selection purposes. Subsequent hardness testing was performed on the external surfaces to approximate field hardness testing. Specimens were sectioned out and ground flat. The testing was performed on what was the outside of the pipe after a final polish on 600 grit paper was performed to accommodate finish requirements of four different hardness testing

methods. All methods were conducted as per ASTM A370 [100] using three indentations for each method in two or three areas to collect average hardness values.

6.4. TENSILE TESTING

Tensile testing was carried out on materials selected after initial metallography. The tensile testing was carried out under ASTM A370 [100] using an Instron servo-hydraulic frame and Instron Series 9 software. The selected materials for tensile testing were tab-welded samples as the compound surface geometry could only yield two-inch long samples which required welding tabs on.

The tabs were ½ x 1 inch (13 x 25 mm) mild steel that were six inches (150 mm long, GTAW welded onto 2 inch (50 mm) sections of sample material. The GTAW heat input and interpass temperatures were controlled to ensure that the HAZ did not extend into the area being tested. A 0.375 x 0.500 inch (9.525 x 12.7 mm) cross-section was obtained while ensuring that the tabs were machined to 0.375 inch (9.525 mm) thick to ensure testing was axial to the sample material but the gauge length did not conform to the recommended ASTM [100] four time the thickness, as it was only possible to machine to 75% of the desired reduced section while maintaining a maximum material condition.

6.5. HOT TENSILE TESTING

Hot tensile testing was carried out under ASTM A370 [100] and ASTM E21 [101]. Hot tensile testing was conducted using an MTS servo-hydraulic frame as shown in Figure 6.5-1. Temperature measurement was performed with shielded ungrounded K type

thermocouples, which were verified in sets with their respective controllers using a Hart Scientific 9122 Drywell calibrator at 400, 500, and 600 °C. The temperature was maintained at 427 °C +/- 1 °C by a self designed three zone furnace, of three inch inside diameter and 13 inches long, using Eurotherm controllers. Figure 6.5-1a shows detail of the furnace showing ceramic insulation board on the top of the furnace and friction fitted ceramic rope between the extensometer and the furnace tube at the bottom to reduced environmental heat loss.

Figure 6.5-1b shows detail of the sheathed K type thermocouples attached to the ends and the middle of the gauge length as they snake through an Applied Test Systems extensometer. The extensometer was employed to keep the strain gauge away from the hot zone of the furnace. The pull rods were Cr-Mo steel with internally threaded Inconel 718 sample adapters to thread on to the specimens. Spherical rod ends were employed to ensure that the sample maintained axiality over the 4 feet (1.2m) between the jaws when the sample was loaded, minimizing extensometer binding.

The specimens shown in Figure 6.5-1b were designed to a nominal 6.34 mm diameter using ASTM A370 [100]. The machined gauge lengths of the samples were centered on the middle of the wall thickness and the ends were threaded ½" UNC class 2, axial to the reduced section. The specimens linear length of 4 1/8" (104 mm) extracted from compound curved elbows did not allow full thread depth but the use of deep engagement into the sample adapters allowed for trouble free testing. The repeatable 25 mm gauge length was maintained by use of a set point on the extensometer, which was moved when

the clip gauge was attached to ensure no binding during extensometer balancing and testing.

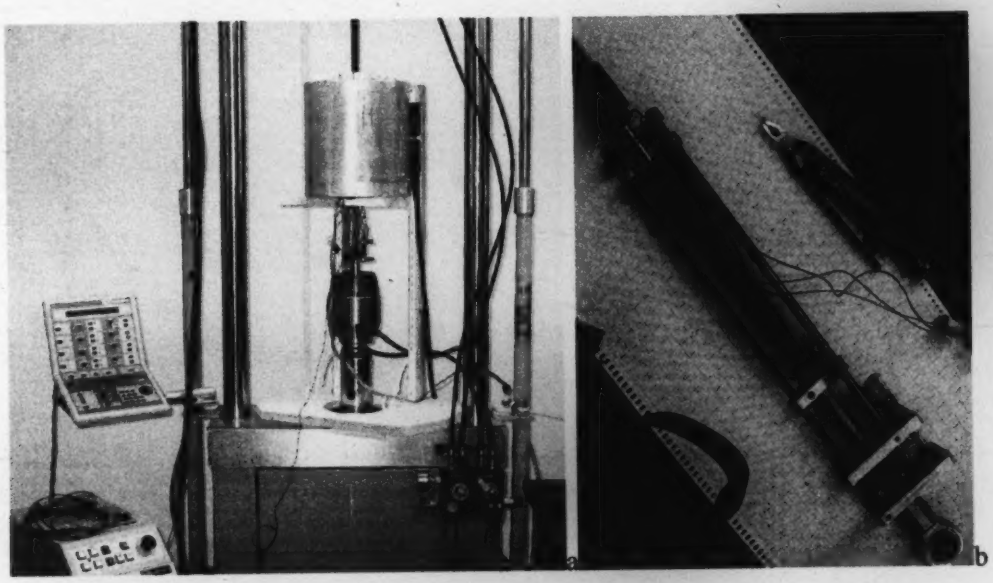

Figure 6.5-1 MTS/Instron servo-hydraulic tensile tester with hot tensile furnace and ATS extensometer is shown in the picture a. Detail of the specimen, thermocouples and extensometer are revealed in picture b.

Samples were mounted in the extensometer, checked for extensometer binding before inserting into the furnace, preloaded to 2 kN and checked again for extensometer binding before the testing began. A load of 0.2 kN was maintained during heating to ensure extensometer alignment did not change during the heating cycle. Under ASTM E 21 [101], a load of less than 10% of hot yield stress to maintain pretest alignment during heating is acceptable.

6.6. CREEP TESTING

Creep testing was carried out under guidelines of ASTM E139 [102]. Three creep frames using lever load multiplication were used. To achieve constant load conditions the levers were adjusted to balanced conditions by proximity switches to either an electric or hydraulic device to pull the lever back into acceptable arc range. The loading range was calibrated by using a NIST traceable load cell. Temperature for two of the frames was computer controlled and a third controlled by Eurotherm controllers. Temperature measurement was performed by the same shielded K thermocouple arrangement as hot tensile testing. The furnaces were of the same design used for creep testing with the exception of a smaller 2.5 inch (51 mm) inside diameter tube giving better heat transfer characteristics. Similar insulation techniques were used as the hot tensile testing.

The creep extensometer shown in Figure 6.6-1 is a tubular design, manufactured from heat treated Inconel 718 was designed to grip the shoulders of the specimen using a split sleeve design. The design is free of binding elements and did not require additional friction creating alignment bushings. PhD graduate student Hong Zhang used ANSYS FEA software to verify the design of the extensometer and specimen.

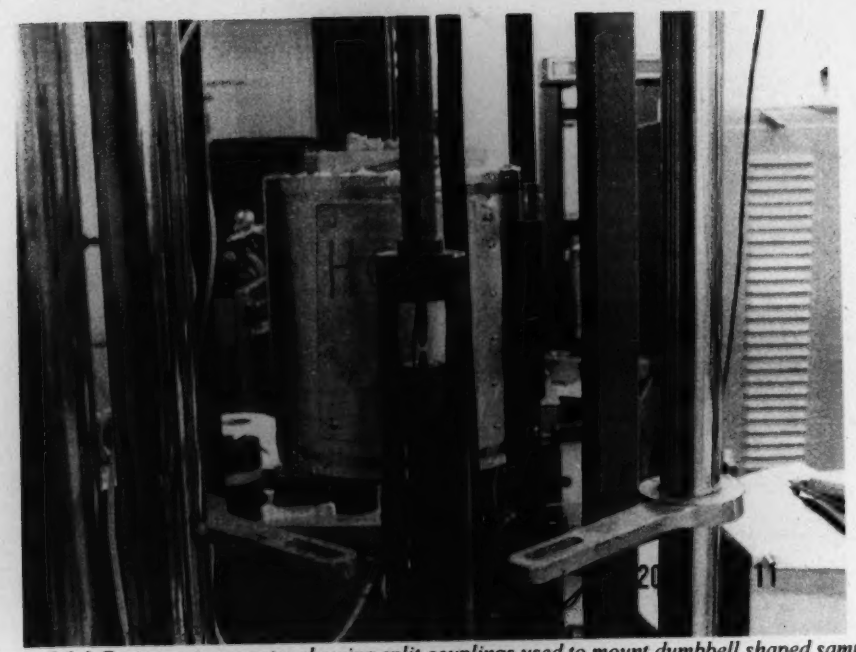

Figure 6.6-1 Custom extensometer showing split couplings used to mount dumbbell shaped samples.

6.6.1. Collection of Data

Data acquisition for each creep frame was performed by utilizing two Fowler Mark V, optically isolated digital indicators with a one μm resolution, which passed information to a custom-made Visual Basic logging system. The digital indicators were attached to a water-cooled extensometer and the tip of the indicator was a ceramic insulator, to reduce heat transfer and was a low coefficient of friction guide for accurate displacement reading. All frames had two methods of capturing rupture time; one of which was related to a microswitch tripped by physical breaking of the specimen and the other by deviation of the data acquired using the digital indicators. The sample was loaded using the creep extension compensating mechanism of each of the frames. The compensating mechanism generally applied the load slowly over 10-15 seconds allowing data collection points to be taken during initial strain ε_o and at terminal strain.

The data acquisition test files generated more than 2^{15} lines of data requiring that data analysis was performed by a programming solution rather than a spreadsheet. Data analysis was performed with a Matlab routine written to analyse the creep curve, minimum creep rate, and Omega parameters based on true strain. Steady state creep rate was obtained by extrapolating the steady state creep using a straight line traced off a printed creep graph and subsequently used to calculate the slope.

6.6.2. Creep Material Selection and Evolution

Initially 10 threaded samples were manufactured of which five were piping materials and five were from neutrados sections of random elbows. Subsequently 40 dumbell samples were machined by Nova Chemical from starting with Reducer 3 and Elbow 7 and the balance from Elbow10 and Elbow 3 early in the research based on the preliminary work summarized in Table 5.3-1.

The materials were assumed to have uniform properties so it was not specified to identify which elbows they were from. Early testing included Elbow 7 and Reducer 3 but scatter in the material variance of tensile testing results necessitated a more rigorous material identification program. Five additional materials were identified and tested as the testing program progressed. Materials that were left from the initial batch of samples identified as "assorted elbows" and were tested to ensure completeness and random selection of graphitized materials.

Due to the nominal ½ inch thickness and complex surfaces of the testing material, a specimen design that could use a maximum material condition resulted in a sample with a 6.34 mm diameter +0.00/– 0.01 mm and 25.4 +/- 0.1 mm gauge length. The head of the sample was shaped like a flattened dumbbell of 17 mm nominal diameter. The radius' were cut to exactly 9.525 mm radius with a form tool to transfer the loading of the shoulder to the split sleeve. This ensured that the specimen maintains contact on the corresponding radius of the split sleeve to avoid any stress magnification as previously determined by FEA.

Duplicate testing for each material would have added an untenable economic toll to testing, but deciding to repeat the Elbow 7 testing allowed a repeatability comparison. The New Elbow 7 specimens machined by Nova Chemicals were expected to give similar results to those machined by Canspec. Other repeat tests occurred if there was reason to suspect that there was a problem with the testing.

6.7. FRACTURE MECHANICS

Due to the unknown potential for propagation of cracks between nodules it was decided to perform a compliance test and compare the results to a Failure Assessment Diagram (FAD) [97]. The material selection for developing the FAD diagram was based on the poor mechanical properties of Elbow 1. Single Edge Notch Bending (SENB) specimens were chosen due to geometric concerns in a transverse-long direction, which orientates of the crack parallel with the axial direction. The SENB specimens were machined to a

maximum possible material condition of 8 mm thick and 16 mm wide in accordance to ASTM 1820 [103].

Since transverse long specimens have curvature in the hoop direction, specimens were bent using a 60 ton hydraulic press using 19 mm diameter mandrels with the radius centered two material thicknesses away, and the supports one material thickness away, from the center of the radius. This flattening procedure is covered in detail in British Standard BS PD 7448 Part 2 [103]. The microstructure was checked before and after to ensure no plastic deformation had occurred near the area of interest. After squaring to the correct dimensions, the root of the notch was machined by wire electro-discharge-machining (wire EDM), which assured no plastic deformation existed at the root of the notch before fatigue cracking.

Testing was carried out under ambient temperatures using an MTS servo-hydraulic frame with Instron controller and Instron J_{IC} software. A custom jig for bending was used with 16 mm diameter rollers set at 64 mm apart and a 16 mm diameter roller in the center to bend the 74 mm long specimen (Figure 6.7-1).

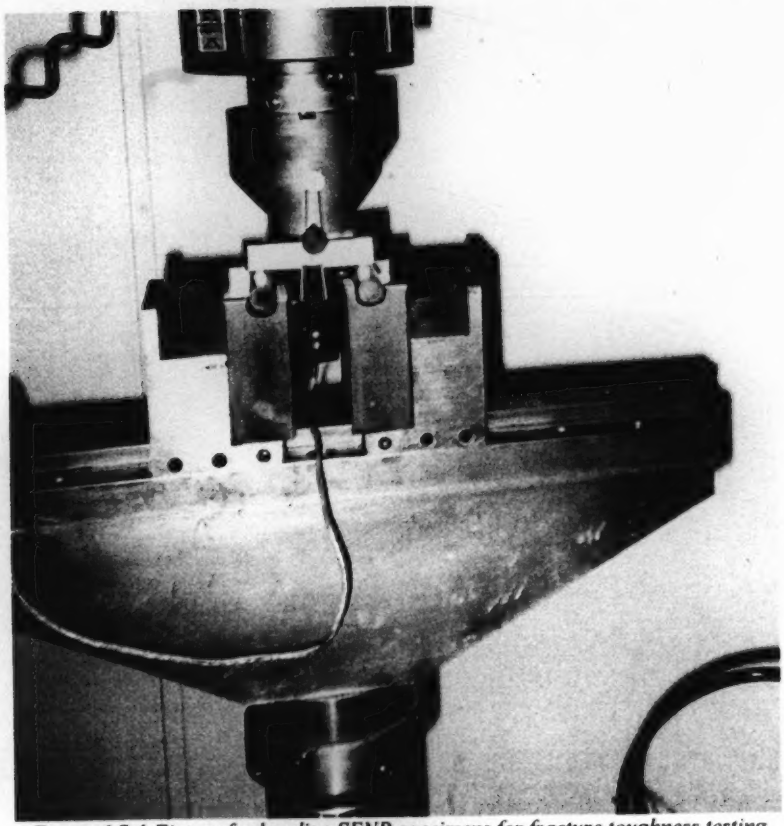

Figure 6.7-1 Fixture for bending SENB specimens for fracture toughness testing

7. RESULTS

7.1. QUANTITATIVE CHEMISTRY RESULTS

The Altasteel spark analysis results for selected materials in Table 5.3-1 were tabulated in Table 7.1-1 and were well within the tolerances of ASME SA181-77 chemistry requirements [9]. The spark analysis method itself is an average of three spark burns and is accurate to +/-1 of the last digit for each element tested.

The analysis shows the material tabulated in Table 7.1-1 is a semi killed steel. The A105 type forging Flange 6 showed the upper limit of manganese and is the only part analysed that has a carbon composition that conforms to expected carbon levels. The overruling design criteria ASME SA186 only specifies maximum carbon chemistry, so the low carbon content still meets chemical requirements as long as the manufacturer can achieve strength and creep rupture requirements. The tramp elements phosphorus and sulfur are well under the specified maximum limit of 0.05%

Sample	C	Mn	Si	P	S	Al sol	Al tot	Ca	N
Elbow 1	0.14	0.48	0.29	0.007	0.017	0.035	0.035	0.0002	0.0016
Reducer 3	0.12	0.51	0.24	0.014	0.019	0.008	0.017	0.0002	0.0033
Elbow 4	0.15	0.51	0.20	0.022	0.011	0.001	0.001	0.0002	0.0036
Flange 6	0.26	0.88	0.23	0.026	0.027	0.020	0.028	0.0010	0.0080
Elbow 7	0.15	0.48	0.20	0.023	0.013	0.001	0.004	0.0002	0.0048
Elbow 11	0.15	0.51	0.26	0.008	0.022	0.000	0.006	0.0040	0.0085
Elbow 12	0.14	0.48	0.20	0.026	0.014	0.001	0.001	0.0002	0.0071

Table 7.1-1 Nova El power piping section chemistries given in weight percent as per Alta Steel spark analysis.

Graphical representation of the chemical analysis does not show any obvious deficiency trends (Figure 7.1-1a), but the expanded residual element graph demonstrates higher average deviation for some of the selected materials (Figure 7.1-1b). The aluminium deviation for Elbow 1, Reducer 3 and Flange 6 show a significant deviation from the other samples. Although the aluminium chemistry is within ASME specifications, it exceeds the 0.010% limit suggested by Seth for the onset of degradation of creep properties [26].

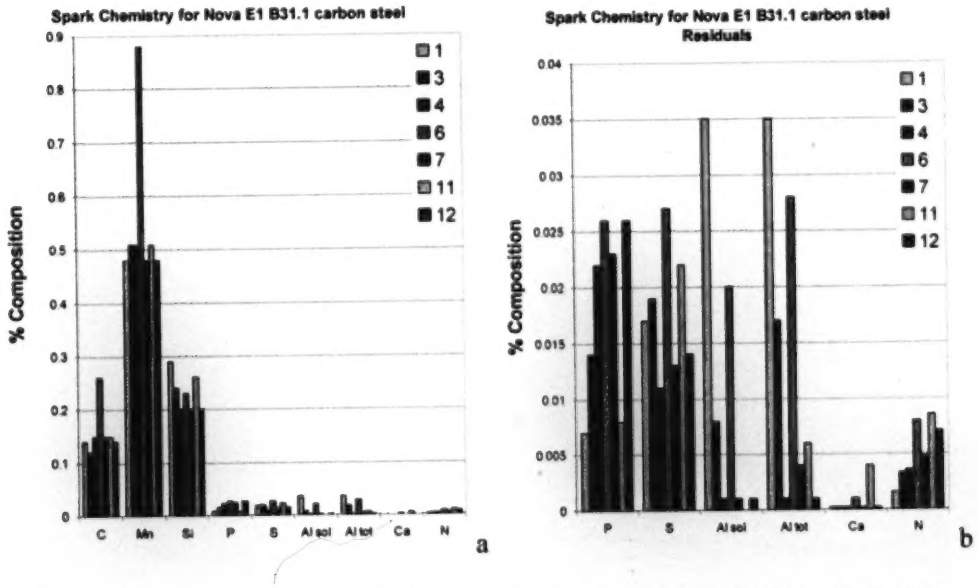

Figure 7.1-1 Graphical representation of results of spark analysis chemistry for Nova power piping sections showing conformance to design standard. Graph b shows expanded chemistry for residual elements.

7.2. CHARACTERIZATION OF MICROSTRUCTUE AND PHASE DEGRADATION

7.2.1. Characterization of Microstructure

The E1 piping materials selected for research in Table 5.1.3 were prepared for microstructural analysis in both hoop and circumferential directions. The findings of the

E1 piping microstructure sections studied are summarized in Table 7.2-1 and representative microstructures for materials included in this investigation are included in Appendix B. All microstructures consist of ferrite and degraded pearlite, some spheroidite and varying sizes of graphite nodules with a typical microstructure shown in Figure 7.2-1. Grain sizes in Table 7.2-1 show small grain sizes that are associated with tough steels that are designed to be operated below the creep regime. Although the A106 piping exhibited no graphitization, the piping from the WHB header adjacent to Elbow 1, designated as Pipe 1 was included for microstructure completeness. Lacking microstructures from the original materials, a new A234 WPB elbow was also evaluated.

E1 sample ID	Graphite type	Averaged Diameter		ASTM grain size	Microstructure
		Min (μm)	Max (μm)		
Elbow 1	Random	4.9	34.3	9	Proeutectoid ferrite , spheroidite and graphite
Reducer 3	Planar	2.6	17.8	9.5	
Elbow 3	Random Planar	5.5	20.7	9	
Elbow 4	Random	9.8	47.0	9	
Flange 6	Random	11.2	32.2	9.5	
Elbow 7	Random	19.7	43.8	9	
Elbow 11	Random	5.5	26.0	8	
Elbow 12	Random	4.4	29.8	8	
Pipe 1	None			9	Proeutectoid ferrite, spheroidite
New A234				9	Proeutectoid ferrite, pearlite

Table 7.2-1 Summary of microstructure observations for E1 piping analysed in this investigation

7.2.1.1. Microstructure results of selected materials

Although the micrographs show similar phase composition, the variation of grain size changes the overall grain shape slightly resulting in a microstructure that has similar

phase composition but different grain morphology. Figure 7.2-1 is very typical of the microstructures observed. The grain size of A234 elbows is not consistent despite being formed from A106 piping. The grain size of the service exposed piping material has similar ASTM average grain size to most of the other piping components examined. Grain growth is unlikely to have played a role as the most severely graphitized fittings have small grains, despite the fact that all piping and fittings were exposed to the same thermal operating conditions.

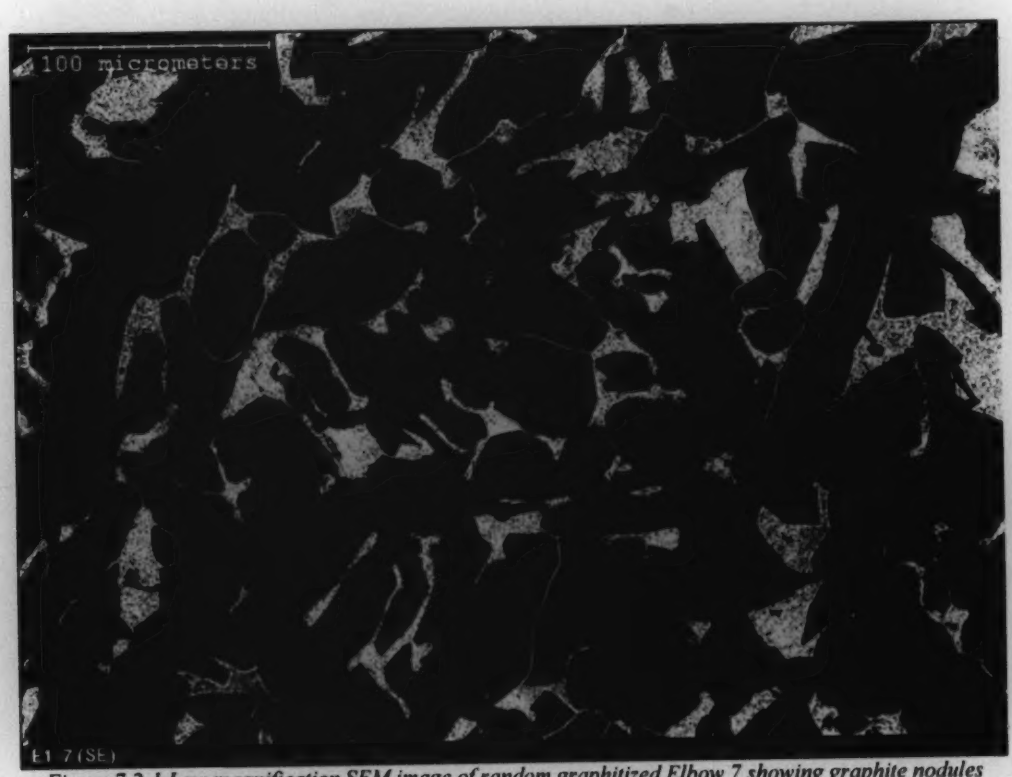

Figure 7.2-1 Low magnification SEM image of random graphitized Elbow 7 showing graphite nodules among proeutectic ferrite and degraded pearlite colonies

While some of the representative microstructures included in Appendix B look different but after accounting for etching variations, the only significant variation under high

magnification, outside of grain size and shape, are high concentrations of degraded pearlite in Flange 6 microstructures. The higher carbon content observed during spark analysis of Flange 6 shows in the observable amount of degraded cementite at high magnifications.

Figure 7.2-2 shows the cementite phase degeneration representative of the elbows and fittings which leaves a material that is dominated by the presence of the ferrite phases. The material shows presence of graphite interspersed among spheroidite and proeutectic ferrite phases. This would be an indicator that the temperature that caused the degradation of microstructure in elbows and fittings is much lower than high temperatures necessary for grain growth by substitutional diffusion.

While the microstructure consists primarily of ferrite with degraded pearlite, a large part of the carbon component has migrated to graphite nodules between 2.5 and 50 micrometers (μm) in diameter but the most nodules are about 20 μm in diameter. Inspecting Figure 7.2-2 shows the diameter of a typical nodule in the graphitized Reducer 3 microstructure. The nodule diameter values presented in Table 7.2-1 are averages of 6 scans as the implied diameters varied significantly depending on location due to the heterogeneous nature of graphitization. The graphite nodules are dispersed in an unsystematic (random) fashion for most material types with no general connection between spacing and size.

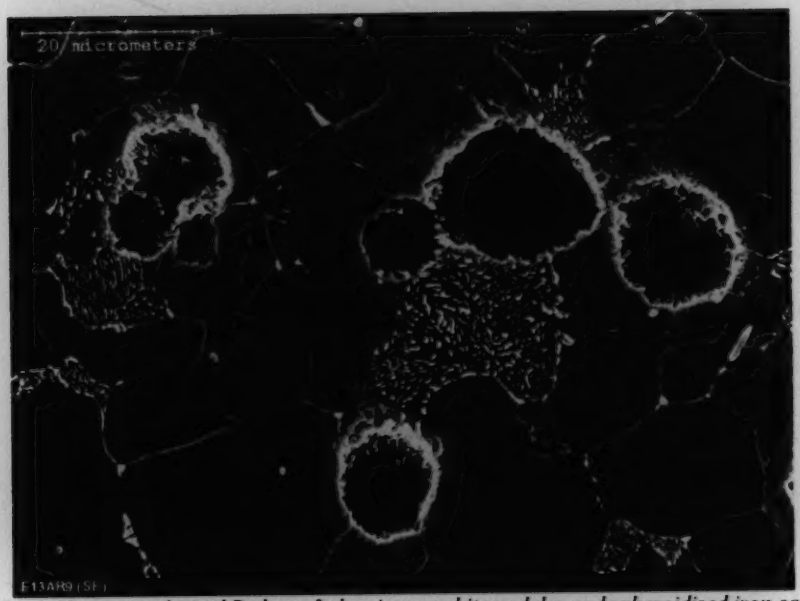

Figure 7.2-2 Planar graphitized Reducer 3 showing graphite nodules and spheroidized iron carbides in degraded pearlite colonies.

The presence of the large holes and remains of graphite lends credence to the theory that secondary graphite nodules are composed of very small graphite flakes [20] although the flake nature of complete graphite nodules was not absolutely confirmed due to the breakdown of the nodules during polishing. Reducer 3 in Figure 7.2-2 shows a high magnification SEM image showing the features of the damaged nodules that are not apparent at lower magnifications. The EDX confirmation of graphite adhering to the walls of the cavities lends credence but does not prove that the graphite nodules are composed of flakes. The bright areas around nodules in Figure 7.2-2 are charged surfaces resulting from the use of secondary electrons as opposed to backscattered electrons for SEM images and do not contribute to understanding the morphology of graphite nodules.

While Reducer 3 shows the radically degenerated form of iron carbide left over from degeneration of pearlite colonies in Figure 7.2-2, it does not directly offer a mechanism

for the process, but the presence of small carbides decorating grain boundaries shows that grain boundaries may be involved in the diffusion process [27]. The carbides are often found at triple points on the grain boundary similar to some of the smaller graphite nodules. The observation can not be extended to the larger nodules as we can only observe a 2-D cut through a 3-D object.

Planar graphite was initially found in two different types of samples. One suspected case of HAZ graphitization was assumed to be developing in E2-2 material (Table 5.3-1), but distribution of nodules away from the edge of the coarse grain HAZ, meant that this form of graphitization could not be classified as HAZ graphitization. The classic HAZ planar graphite would be found at the fine grained HAZ and should be detectable as a line at the surface of the material similar to type IV cracking in Figure 4.3-1. HAZ graphite cannot be found in the weld metal itself, as there is no pearlite to break down, since weld deposits are composed only of ferrite of different allotropes and iron carbide.

Planar graphite was found to exist in Reducer 3 and Elbow 3 (Figure 7.2-3). The samples were A234 type materials from a 6 x 8-inch reducer and a 6-inch 45° elbow respectively, and were located between the first block valve and the WHB. The planar graphitization was found to exist in similar directions at oblique angles to the inside or outside diameter although they could not be considered parallel planes. Micrographs could offer no correlation in the direction of the planar graphite with relation to either the hoop or longitudinal directions but a lack of random graphite is apparent.

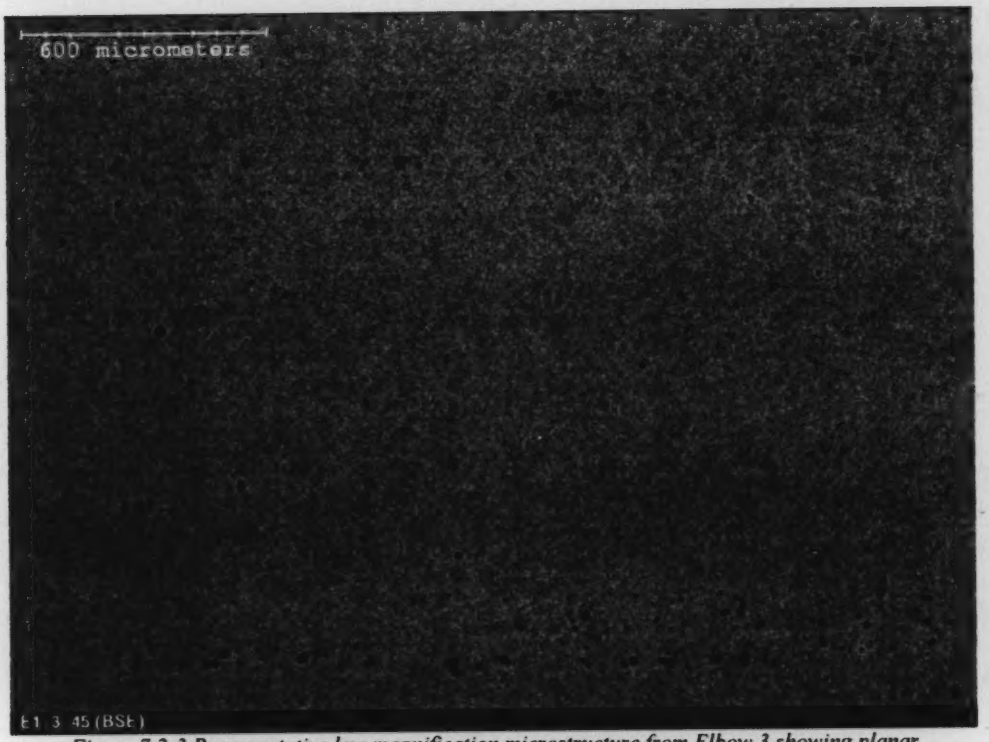

Figure 7.2-3 Representative low magnification microstructure from Elbow 3 showing planar graphitization.

7.2.1.2. Macrostructure results of selected materials

Low magnification micrographs that were stitched together, much like building a jigsaw puzzle, allowed a more comprehensive understanding of the extent of graphitization to be developed. Representative pictures of the low magnification images of the samples used for this analysis are included in Appendix C. Figure 7.2-4 shows an image representing the 3 mm x 2 mm pictures that were stitched together to make composites pictures representing a nominal 13 mm wall thickness.

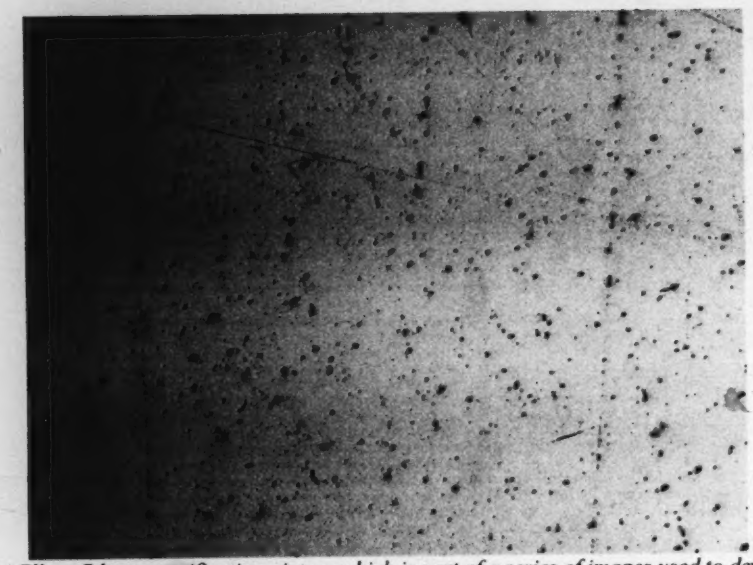

Figure 7.2-4 Elbow 7 low magnification picture which is part of a series of images used to develop macrographs

Visually, the macro images show interesting trends in graphitization that were not apparent with single micrographs, as many features that could be observed with the naked eye were obscured by high magnification. Figures 7.2-5 through Figure 7.2- 8 show macrographs from Elbow 7 and Reducer 3 respectively. These images have been cropped for image analysis due to aberrations at the edges, which removed a region near the surface that had little graphite or sometimes showed surface graphite clusters.

The macrographs show the consistent heterogeneous nature of the pipe wall as the exterior surface and the interior surface of the piping demonstrate lower apparent graphite concentration than the midwalls. This trend is with all samples. The macrographs show the significance heterogeneous extent of the graphite morphology that neither replications nor micrographs can show. This can be confirmed by viewing graphite morphology of low magnification pictures in Appendix C.

This large scale representation of graphitized microstructure clearly shows the two major morphologies, planar and random graphitization. The first morphology is that of the random graphitization, which consists of nodules that show relatively even spacing to their immediate neighbours, but bulk nodule distribution varies due to the heterogeneous nature of the distribution. This means that even for the low magnification images in Appendix C, nodule distribution varies from their neighbouring images. Elbow 4 shown in Figure 7.2-5 and Figure 7.2-6 is the worst case of random graphitization, showing a tendency for the graphite to align in distribution patterns similar to banding from intercritical rolling when viewed as the longitudinal direction.

The second morphology is the planar graphite which shows the tendency to collect in pseudo planes which are not oriented with the overall forming direction as demonstrated by Reducer 3 in Figure 7.2-7 and Figure 7.2-8. This morphology shows the tendency of graphite band formation through the midwall section especially in the longitudinal section reminiscent of the Furtado and Le May [35] failure picture in Figure 3.4-1. The presence of random graphite may be discerned distributed as a heterogeneous phase between the graphite planes.

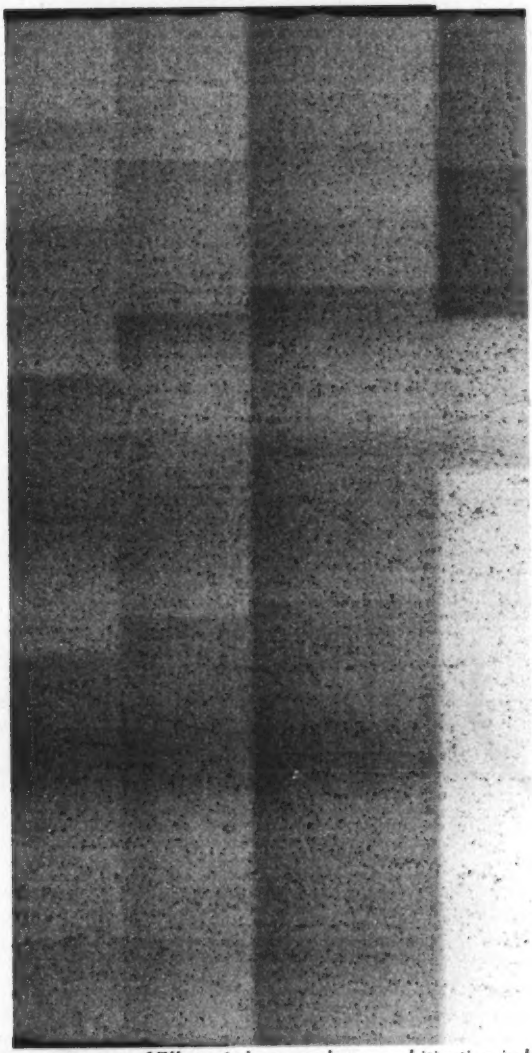

Figure 7.2-5 Macrostructure pictures of Elbow 4 show random graphitization in hoop direction. A slight tendency for banding may be observed. The individual overlapped micrographs are 2mm high and 3mm wide resulting in a full section nominal thickness of 12 mm

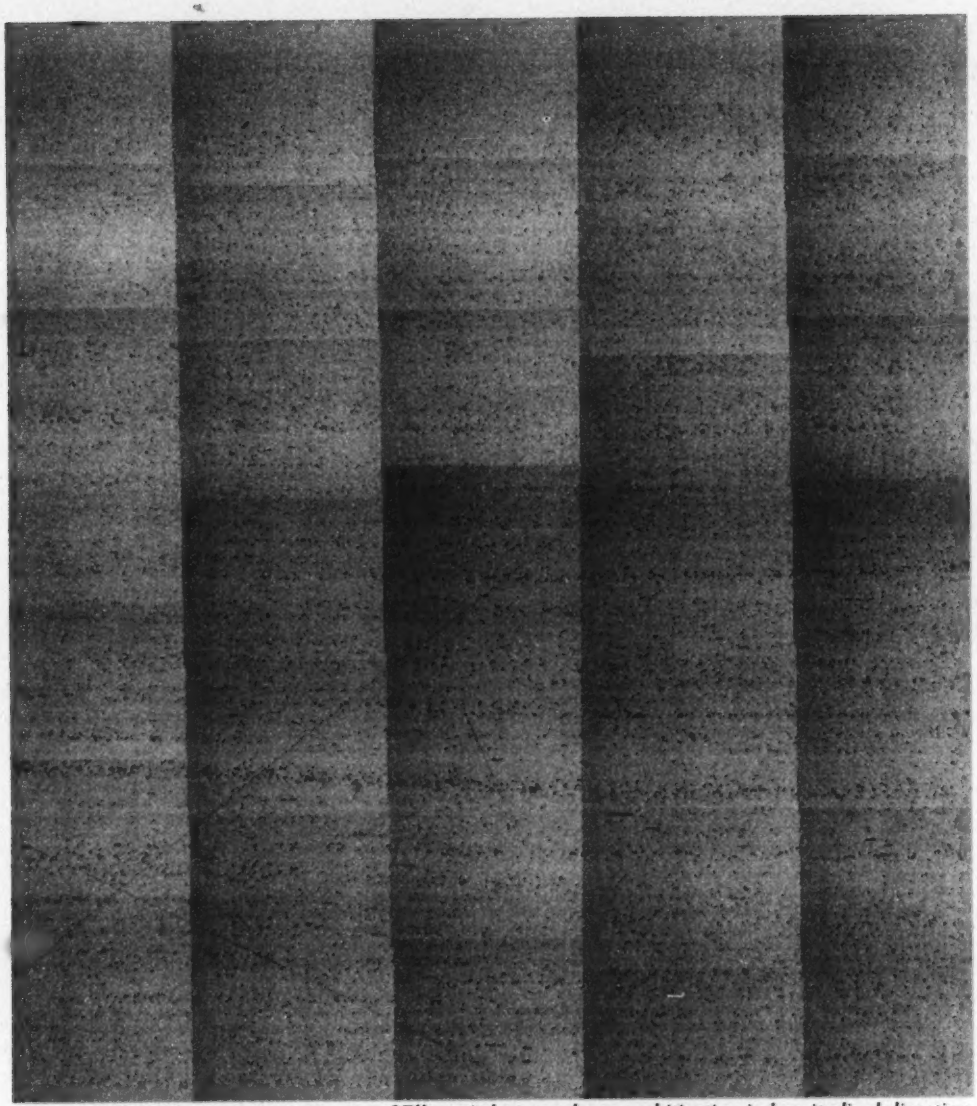

Figure 7.2-6 Macrostructure pictures of Elbow 4 show random graphitization in longitudinal direction. Banding of graphite nodules is apparent in this orientation. The individual overlapped micrographs are 2mm high and 3mm wide resulting in a full section nominal thickness of 12 mm

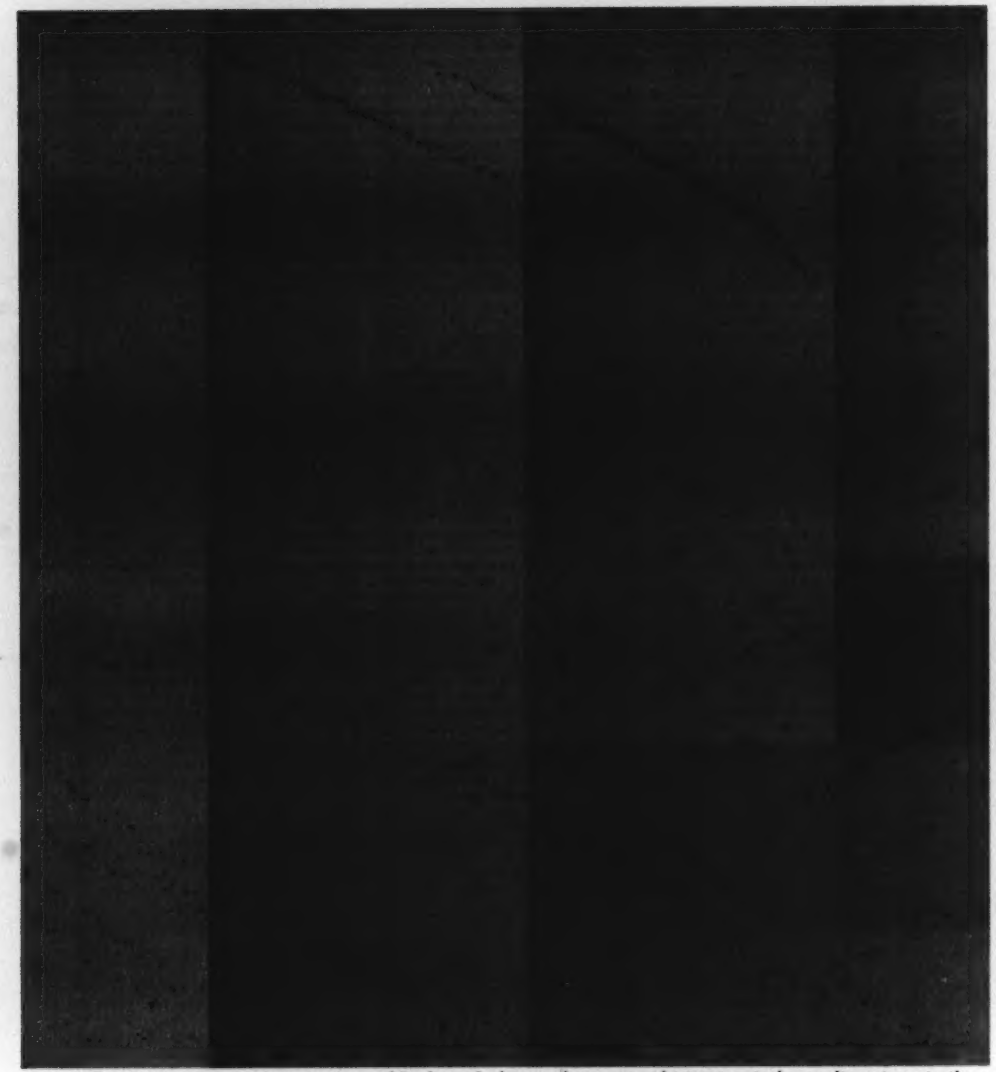

Figure 7.2-7 Macrostructure pictures of Reducer3 shows planar graphitization in hoop direction similar to Figure 4.3-.1

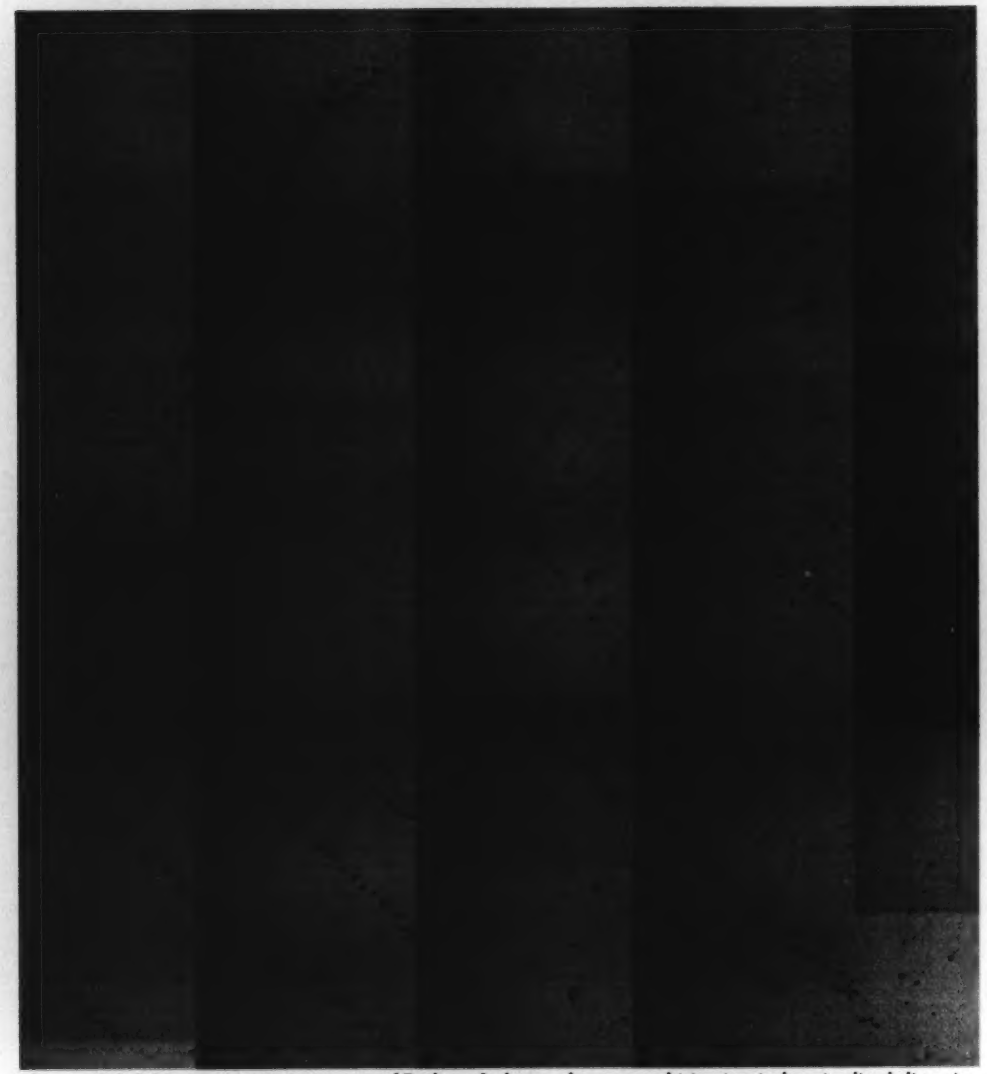

Figure 7.2-8 Macrostructure pictures of Reducer3 shows planar graphitization in longitudinal directions.. The individual overlapped micrographs are 2mm high and 3mm wide resulting in a full section nominal thickness of 12 mm

Planar graphitization was positively identified in two sections both of which had been taken from an area where the piping was constrained, most likely imposing a significant external stress. Reducer 3 (Figure 7.2-7, Figure 7.2-8) consistently demonstrated planar graphitization but Elbow 3 had localized planar graphitization. The planar graphite showed reduced levels of interparticle spacing as seen in Figure 7.2-7 and Figure 7.2-8,

where a significant volume fraction of the graphite is concentrated along randomly oriented planes. The longitudinal macrograph (Figure 7.2-8) shows how areas of planar graphitization have a reduced tendency to exhibit random graphite as observed in Figure 7.2-5 and Figure 7.2-6. The presence of planar graphite does not preclude the existence of the random graphite, but the observation of the coexistence of random graphite with planar graphite in Reducer 3 demonstrates that we can not ascertain that random graphite is benign.

7.2.2. Graphitization Results

Phase analysis of the microstructures was performed using Image Pro software. The images were analysed for nodule size ranges (Table 7.1-1) and graphite volume (Table 7.2-2). Analysing micrographs had yielded inconsistent results and picture quality gave problems. As previously mentioned even low magnification micrographs could not represent the size and heterogeneous distribution of the graphite. In an attempt to classify the heterogeneous nature of the distribution, the use of sectioned macrographs allowed phase analysis of the images.

Phase analysis was performed by sectioning macrographs into outside diameter (od), middle (mid) and inside diameter (id) slices shows the weak tendency to develop midwall graphite. The tabulated data (Table 7.2-1) shows a wide range of values of volume fraction of graphite. The tabulated graphitization results by themselves can not show whether the graphite morphology would be planar or random.

Material	Hoop composite	Hoop od	Hoop mid	Hoop id	Longitudinal composite	Longitudinal od	Longitudinal mid	Longitudinal id	Graphite Morphology
Elbow 4	4.000	3.390	5.100	3.570	4.000	4.840	5.130	4.000	random
Reducer 3	1.100	0.817	1.470	1.550	1.180	0.781	0.895	0.971	planar
Elbow 3	0.730	0.492	0.917	0.947	0.428	0.213	0.571	0.200	random/planar
Elbow 7	0.844	0.924	1.030	0.534	1.370	0.829	1.570	1.107	random
Elbow 1	0.420	0.359	0.487	0.456	0.807	0.587	0.894	0.763	random
Flange 6	0.560	0.480	0.560	0.711	0.590	0.401	0.573	0.637	random
Elbow 11	0.311	0.296	0.364	0.227	0.131	0.091	0.147	0.050	random
Elbow 12	0.802	0.551	0.977	0.551	0.307	0.398	0.338	0.205	random

Table 7.2-2 Variation of graphite volume percentage and morphology for selected E1 piping materials

Although there is no distinct trend to follow between relative amounts of graphite for each wall location, the following graphs in Figures 7.2-9 and 7.2-10 show that often it is indeed the middle of the pipe that has the greatest amount of graphite. It may be surmised that there is a slight tendency for the graphite to follow a midwall trend when analysed in terms of wall location.

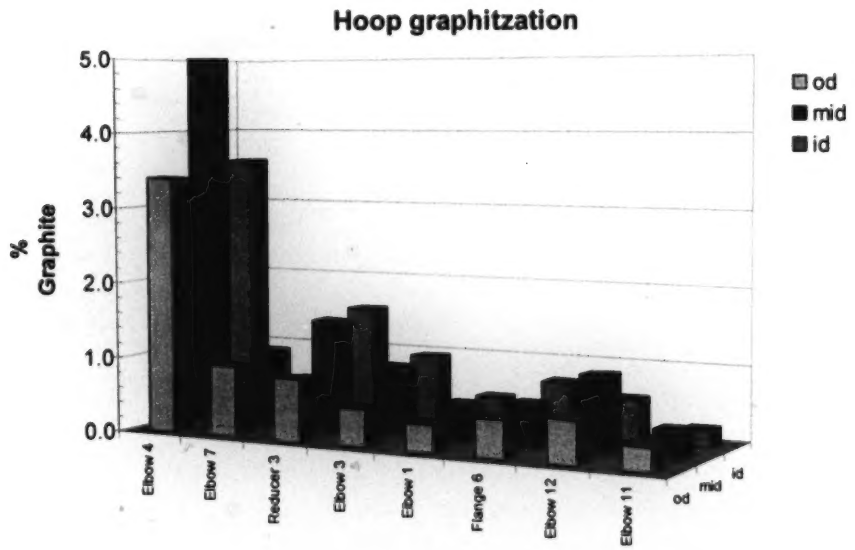

Figure 7.2-9 Relationship of graphite location to average graphite composite for selected material types, location as well as average composite density for hoop direction.

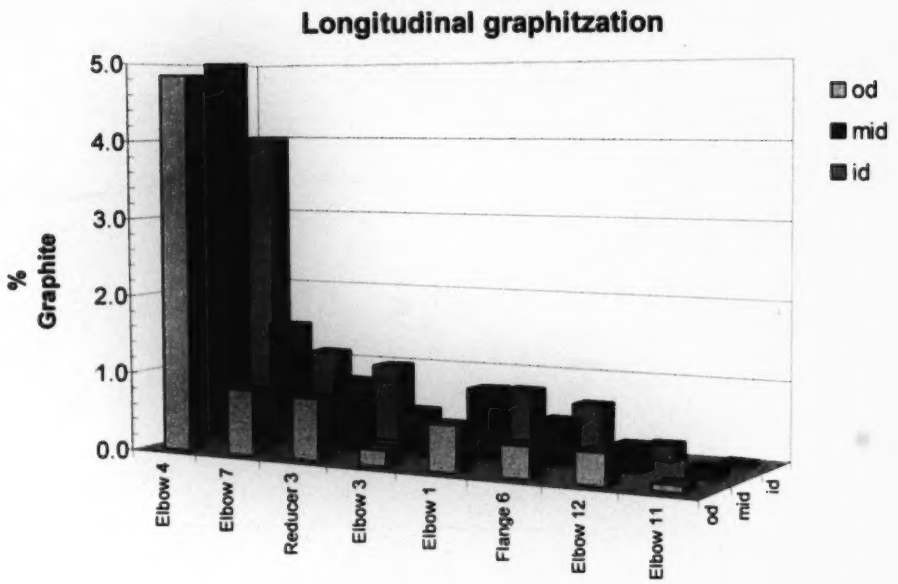

Figure 7.2-10 Relationship of graphite density relative to wall location as well as average composite density for longitudinal direction

Another observation is the composite graphite volume shown in Table 7.2-2 does not reflect the sum of average total amounts of graphite. Lack of agreement with the sum of the sections may be due to the crude partitioning methods used in cropping the pictures. The cropping was a subjective manual operation, which was more sensitive to the heterogeneous nature of the outside diameter, middle and inside diameter sections, than to the summation of the composite. The type of graphitization did not make an impact on separating the materials as the random graphitized materials cover the extremes of graphite volumes overlapping the volume fraction range associated with planar graphitized Reducer 3.

The volume fractions in the hoop and longitudinal directions are significantly different in several cases and this is often reflected in the appearance of the microstructure. The mid wall banded appearance of random graphitization in longitudinal direction for Elbow 4 macrograph (Figure 7.2-7, 8), are reflected in the phase analysis with a higher mid wall graphite concentration whereas the hoop graphite concentration is constant. The macrograph for Reducer 3 (Figure 7.2-9, 10), which demonstrated planar graphite, shows the relatively nodule free matrix coexisting with the planes of graphite which may explain the relatively small deviation for this sample type.

Figure 7.2-11 shows that there is slight bias in graphite volume for the hoop directions for any of the section types regardless of material analysed. It would be assumed that the materials would concentrate along the 50/50 balance line shown in Figure 7.2-11, but no clear trend emerges. Elbow 4 was excluded from data to expand the sensitivity along an interval in which most materials are concentrated. Elbow 4 showed the same distinct randomness demonstrated by the rest of the data. Not surprisingly, the planar graphite found at oblique angles in Figure 7.2-9, 10 shows different bulk volume fractions of graphite regardless of orientation.

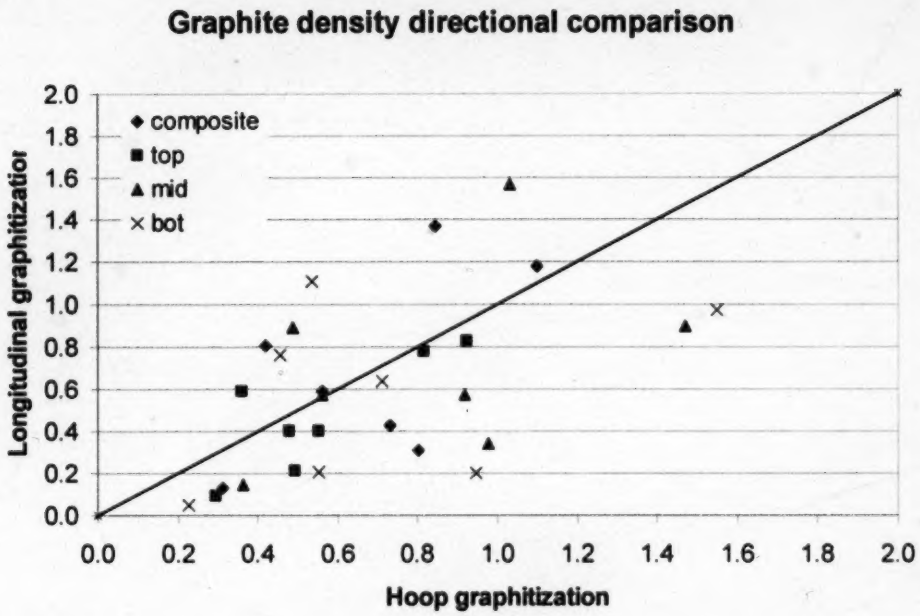

Figure 7.2-11 Lack of relationship between graphite volume fraction depending on wall location for selected piping materials

There is no rational reason why the volume fractions of graphite are so high in Elbow 4, as its location in the piping does not give obvious clues as to why it would develop such an advanced concentration of graphite. Reducer 3's graphite volume distribution trend is similar that of Elbow 7, but the development of planar graphite morphology shows no relationship to graphite volume fraction.

The volume fraction of graphite did not show a relationship with particle size range except in the case of Elbow 4 which showed an increase in average particles size. Average nodule size is often similar for all morphologies at 20 micrometers as can be observed in Figures 7.2-2 and 7.2-3. The observed graphite nodule size range does not explain how the nodule size affects nucleation and growth, even though there seems to be

a critical nodule size. This can be confirmed by the conspicuous absence of graphite nodules smaller than 2 microns. The nodule size range raises questions about nodule formation. The most obvious question is how much time is required to grow the nodule by interstitial diffusion? i.e. making it a carbon sink. The related questions are: why do some graphite nodules grow from the size of a flaw to the size of a defect?, and why would nucleated nodules stop growing and are they cannibalized by more thermodynamically stable nodules? i.e. making them a carbon source [33]. Another relevant unanswered question is how incoherent nodules form, when they have to displace iron atoms either by substitution or dislocation movements, both of which require high energy input.

There is no evidence to support Le May's postulation of graphitization of formed parts being related to segregation of carbon during forming operations [79], especially in light of the lack of relationship of planar graphite nodules in Figure 7.2-9 and Figure 7.2- 10 to distinct Furthermore there is a significant variation in graphite volume between all the elbows in spite of the fact that service pressure and temperature are all the same, which ideally would leave all the elements of the piping system with the similar flaws. Since the manufacturing and service conditions are the same, then only piping stress would remain as an unknown variable. Without analysis of piping stress, which is beyond the scope of this work, there is no quantitative data to confirm this.

7.2.3. Qualitative Chemistry and Phase Analysis

Initial chemistries were performed by EDX in conjunction with phase analysis. Of special interest was the plausible presence of potent graphite forming elements, titanium and aluminium. The two main phases identified as extraneous to steel were manganese sulfide and graphite (Figure 7.2-12a). The MnS phases are simple to identify by EDX, but the graphite is a pure carbon phase which difficult to quantify with EDX. EDX investigations show a tendency for incomplete dissolution of the deoxidation elements aluminium and silicon and also found evidence of the graphitization promoting elements titanium and aluminium (Figure 7.2-12b). EDX point analysis at point 3 in Figure 7.2-12a, shows the presence of titanium, aluminium, silicon and manganese. Additionally Point 1 was silicon and points 2, 3 have similar composition which shows incomplete dissolution of ferrosilicon and aluminium deoxidizers. Although these inclusions could frequently be found near graphite nodules, neither the graphitization promoting elements nor the deoxidation elements were conclusively found it association with the graphite nodules.

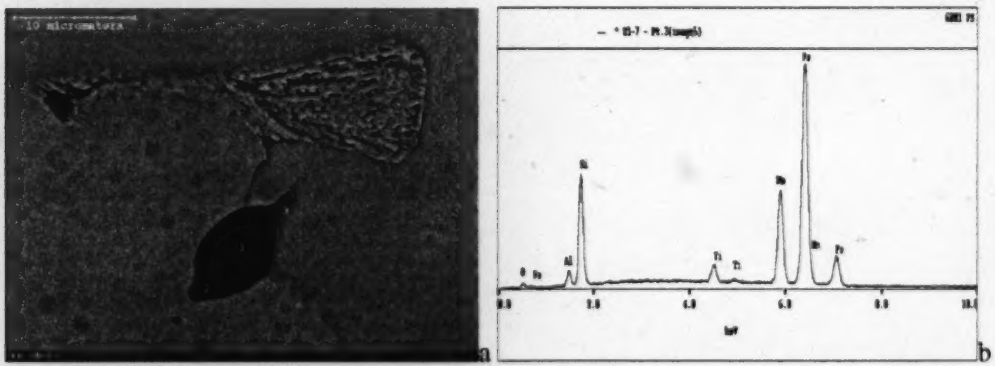

Figure 7.2-12 SEM image of Elbow 7 inclusion showing EDX points (a) and EDX analysis (b)

7.2.4. Sulfur Print Results

The sulfur prints were not able to discern any direct relationship between the presence of planar graphite and microstructure effects due to the steel forming operations. A sulfur print was prepared from sample Elbow 3 in which the presence of planar graphite could be observed with the naked eye. The sulfur printing of Elbow 3 in Figure 7.2-13a shows grain flow associated segregation of manganese sulfides during forming operations. The associated SEM microstructure in Figure 7.2-13b shows the graphite nodules interdispersed along a graphite plane running at oblique angles to the surface containing manganese sulfides, although this was not reflected in the sulfur printing.

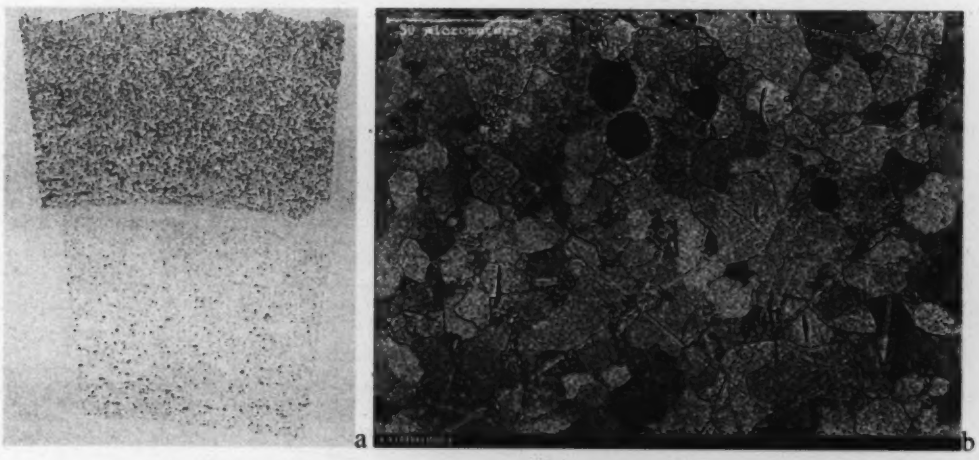

Figure 7.2-13. Sulfur print of Elbow 3 45°, which contained graphite planes that were observable to the naked eye. The hoop direction appears on top and longitudinal direction on the bottom (a). SEM image of planar graphite in Reducer 3 showing presence of MnS (b)

While a pattern of MnS density was associated with graphite planes was observed in Elbow 3 in the hoop direction the sulfur print did not confirm the presence of the sulfur in a similar orientation to the graphitization planes. Therefore MnS could not be absolutely associated with the planar graphite. The longitudinal sulfur print clearly shows the

significant MnS density towards the insides of the pipe but cannot relate the forming operation to the presence of graphite.

Figure 7.2-14 shows a sulfur print of the weld zone investigated by Canspec [3], showing Pipe 1 on the left side of the weld and Elbow 1 on the right side of the weld. If a correlation was present between forming method and distribution of graphite, the sulfur print of randomly graphitized Elbow 1 should show distinct trends. The top of the sulfur print shows the arced section of Elbow 1 corresponding to piping exterior. Examining the sulfur print shows an increase in the present of sulfur towards the inside of the elbow and this sulfur segregation trend is similar to the Elbow 1 longitudinal graphitization trend in Table 7.2-2, but the observation in itself does not constitute proof or relationship although Figure 7.2-15 shows the change of graphite distribution and size for Elbow 1. The Elbow 1 sulfur printing trend could be considered conclusive if there was a correlation with Figure 7.2-14.

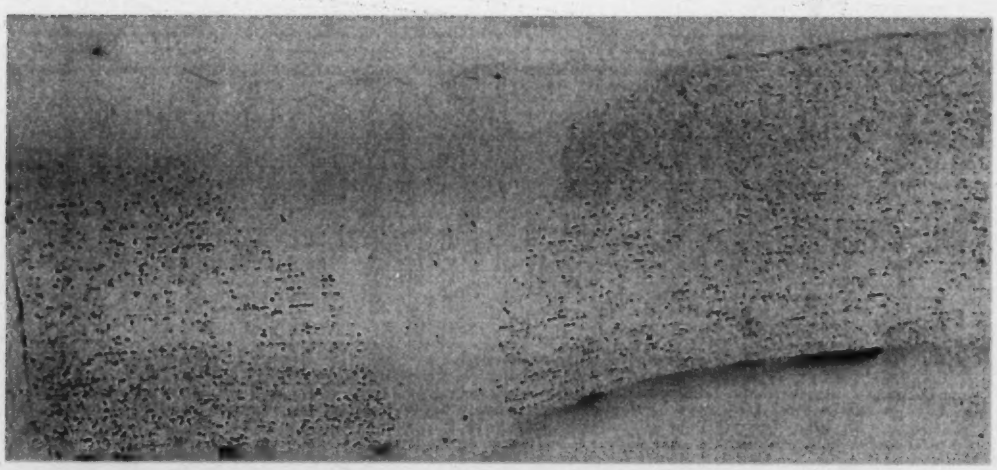

Figure 7.2-14 Sulfur print of Elbow 1 longitudinal direction showing Pipe 1 to the left of the multipass weld and graphitized Elbow 1 to the left. Segregation of Sulfur to the center of the weld was also observed.

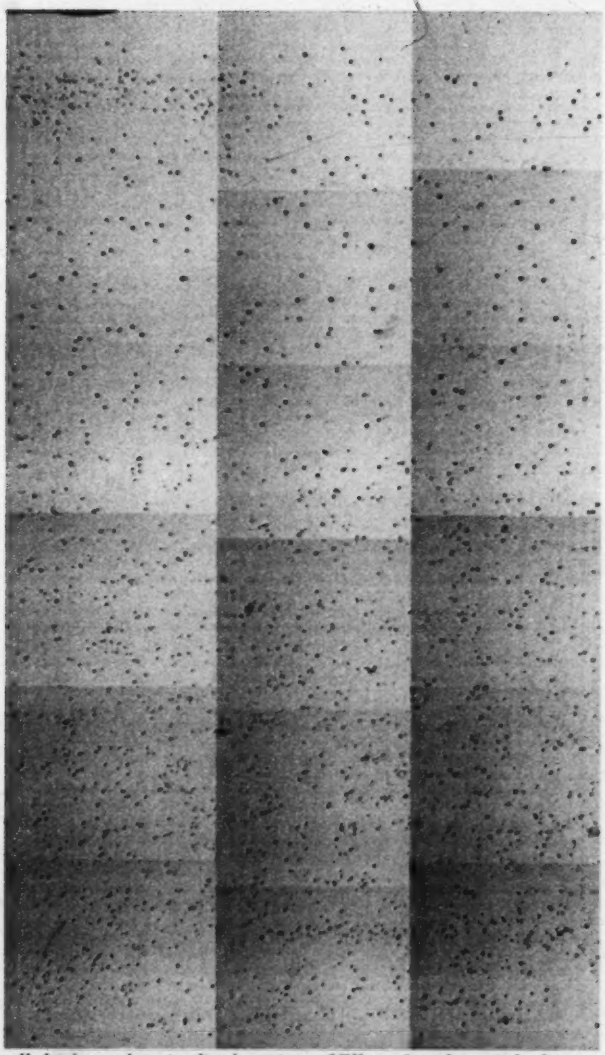

Figure 7.2-15 Full wall thickness longitudinal section of Elbow 1 with outside diameter at top. The change of graphite size and density is noticeable but graphite distribution cannot be absolutely associated with sulfur distribution in the Figure 7.2-11 Elbow 1 sulfur print

Pipe 1 shows stronger reaction to sulfur printing in Figure 7.2-14, while showing no graphitization, but this may be an orientation effect similar to Figure 7.2-13a. The Pipe 1 side of the weld does show effects of sulfur segregation in the HAZ while the Elbow 1

side does not show any effects of sulfur segregation in HAZ. Unfortunately chemistry for Pipe 1 was not included in the spark analysis shown in Table 7.1-1.

The weld in Figure 7.2-14 did not sulfur print well except where the sulfur segregated to the middle during solidification. The weld is very faintly visible due to the low sulfur associated with SMAW process, and although not apparent in this reproduction there is a discernable area of sulfur segregation in the top and middle of the weld, that is associated with hot cracking. This weld related sulfur segregation is a typical phenomenon for older steels and can affect creep performance.

7.2.5. Neutron Scattering Results

Kelly Conlon at National Research Council of Canada, Chalk River, attempted to determine whether the graphite nodules were detectable using neutron scattering techniques. Due to the relatively small graphite nodule size and the relatively high absorption of neutrons by carbon, the graphite nodules were not detectable by scattering techniques. No further attempt was made to develop a stress map that would match with the neutron scattering map. The failure of the technique highlights the difficulty of detecting small graphite particles using non destructive examination techniques.

7.3. CHARACTERIZATION BY HARDNESS TESTING

Hardness trends for some standard industrial and superficial testing methods did not give a clear correlation with any one method. Table 7.3-1 illustrates the hardness methods were not consistent for any particular type of sample material and that some average

values had a significant deviation. All methods show there was a significant drop in hardness from the new material that they were base lined against.

Sample	HRB range	HRB ave	30T range	30T ave	HV30 range	HV 30 ave	BH 250 range	BH 250 ave
Elbow 1	69.0-71.0	69.7	60.0-62.0	61.5	124.8-130.6	126.8	105.0-109.7	107.4
Reducer 3	71.0-74.0	72.3	63.0-65.0	64.0	130.6-136.9	134.2	114.7-125.6	118.3
Elbow3	74.0-79.0	76.5	61.0-64.0	62.3	110.3-116.0	113.1	114.7-120	115.5
Elbow 4	69.0-74.0	72.2	57.0-60.0	58.6	114.3-120.3	118.1	100.7-105.0	102.1
Elbow 7	63.0-65.0	64.2	53.0-55.0	53.8	134.7-142.8	136.6	89.0-92.6	91.4
Elbow 11	71.0-78.0	74.8	61.0-62.0	61.7	123.9-131.6	129.4	96.5-120.0	113.4
Elbow 12	67.0-72.0	68.1	54.0-57.0	55.4	107.3-118.5	112.8	92.6-96.5	95.9
Flange 6	78.0-80.0	79.0	63.0-64.0	63.5	117.2-165.3	141.1	114.7-125.6	121.9

Table 7.3-1 Hardness results showing range and average of the four methods used.

The trend is demonstrated in Figure 7.3-1, illustrating the variation of hardness for each method. Observing the trends for each type of testing shows that the trends are more consistent for hardness testing methods that rely on measuring depths of indentation (HRB, HR30T) rather than impression length (HV30, BH250). Hardnesses obtained with Brinell hardness, try to mimic the trends for the depth of indentation techniques (HRB, HR30T) but shows enhanced sensitivity to hardness. Conversely, Figure 7.3-1 also shows significantly different hardness behaviour for Vickers methods, showing the greatest sensitivity to hardness, but it does not show appreciable correlation to the other methods.

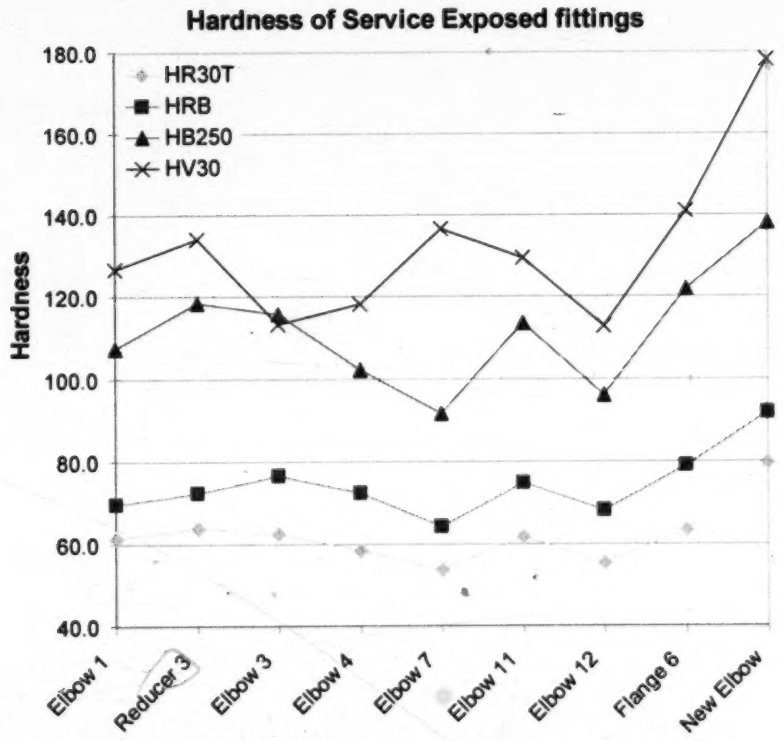

Figure 7.3-1 Plot of relative hardnesses to show variation of hardness across selected materials and new baseline material. There is no hardness distinction between planar graphitized Reducer 3 and the random graphitized fittings and elbows although softening is evident.

The variation of the average hardness trend was exacerbated by scatter in the hardness values for most methods. Figure 7.3-2, shows that indentation depth methods showed significantly less scatter than the impression length methods in terms of absolute variation. Sensitivity can be expressed as both variation for a particular method and as scatter in the data of the method. Figure 7.3-2 shows that the scatter of the impression length methods is not as variable between materials as the scatter of the indentation method. It is very interesting to note here that only the new flange shows zero deviation for the Brinell hardness values. It may also be observed that Flange 6 offers the most variation from the average HV value but exhibits almost no deviation for the HR30T

values. It would be expected that planar graphitized Reducer 3 would show distinct differences in sensitivity due to the highly heterogeneous nature of the microstructure but only a slight increase in sensitivity for the impression length methods can be observed.

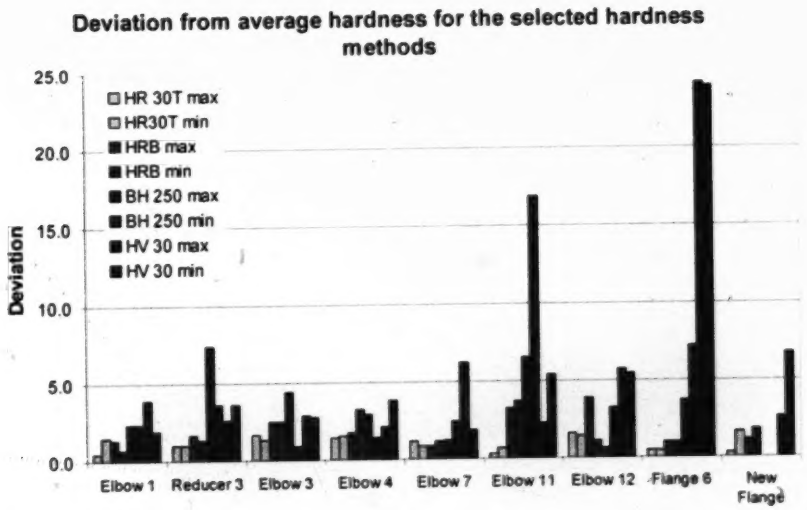

Figure 7.3-2 Deviation of hardness methods from average hardness for selected materials and methods. Brinell hardness and Vickers hardness give the largest variation for most selected materials. Graphite morphology has no distinct effect on hardness value variation

Sensitivity to the method may also be demonstrated by normalizing the deviation from average results as shown in Figure 7.3-3. Normalization will help show if a method has a particularly large variation from the average. Normalized values in Figure 7.3-3 show very similar trends as Figure 7.3-2, but the indentation methods show that they have a larger error relative to the average hardness. While this is a valid observation, it will have little effect on the use of hardness as a validation tool as the absolute error of the indentation depth methods are still multiples of the normalized deviation of the impression length methods.

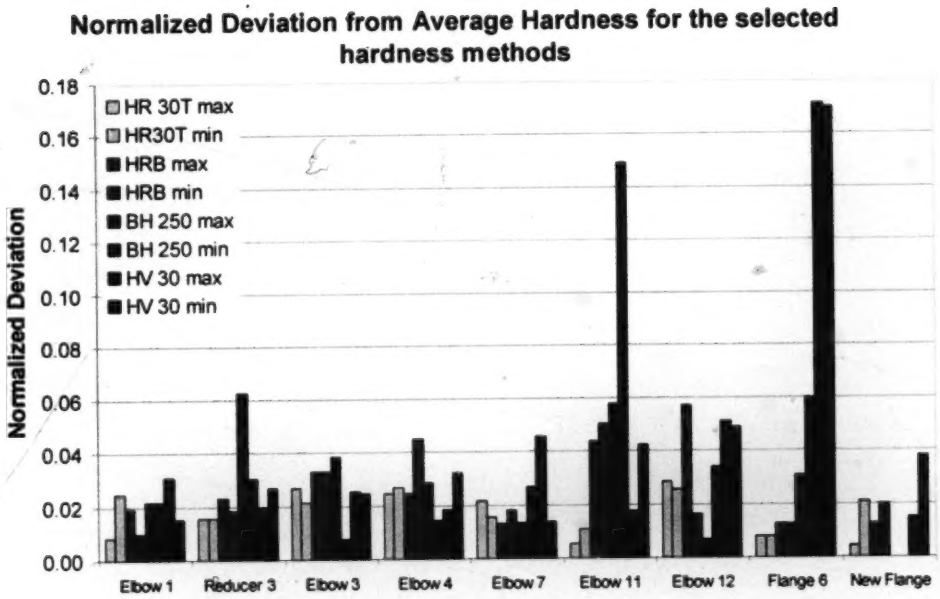

Figure 7.3-3 Normalized deviation from average hardness values for selected materials and methods showing how relative error in the method increases for indentation depth methods

7.4. CHARACTERIZATION BY TENSILE TESTING

Tensile relationship for A105 and A 234 materials gave a range of room temperature mechanical properties. Recommended strength expectations from ASTM in Table 7.4-1 were above the observed strenghts. Due to the maximum cross-section requirement, all samples had non-standard gauge lengths except Reducer 3, which achieved the standard gauge length. The non-standard short gauge length used for tensile testing increases the values of ductility higher than would be observed for a standard gauge length, and are non convertible. Ductilities are only specified as a minimum elongation in code and all materials tested would still exceed these requirements.

Sample		UTS (MPa)	YS (MPa)	% el
A234 WPB	Reference	415-585	240	min 22
A105	Reference	482	248	min 16
Elbow 1 (A234)	1.1	368.8	239.8	58.61
	1.2	374.8	253.8	56.74
	1.3	370.1	232.8	58.18
	1.4	369.5	237.6	59.45
Elbow 4 (A234)	4.1	410.1	255.8	50.2
	4.2	407.5	226.8	49.32
	4.3	410.2	241.4	52.49
	4.4	410.5	243.2	50.7
Flange 6 (A105)	6.1	496.4	277.1	27.87
	6.2	495.5	269.6	24.87
Elbow 7 (A234)	7.1	391.2	197.3	51.23
	7.2	391.5	206.4	51.83
	7.3	394.9	215.5	51.04
	7.4	390.8	205.7	51.38
Elbow 11(A234)	11.1	390.0	191.5	51.64
	11.2	393.9	192.9	51.59
	11.3	390.0	190.9	51.59
	11.4	394.0	208.5	51.43
Elbow 12 (A234)	12.1	395.9	213.5	51.01
	12.2	394.1	199.9	49.87
	12.3	394.6	206.7	52.34
	12.4	395.1	204.8	50.53
Reducer 3 (A234)	3.1	458.1	223.1	34.28

Table 7.4-1 Summary of room temperature tensile testing results for selected materials

Results were analysed for each material to develop organizational trends for future research. Figure 7.4-1 shows that the material can be separated into three distinct groups, based on yield strength and ultimate tensile strength. The first grouping is Flange 6 and Reducer 3, which have similar tensile properties. At the other extreme is Elbow 1 with distinctly the worst mechanical properties. The remaining A234 elbows, are all after the first block valve (Figure 5.2-1) with the worst properties belonging to the lightly graphitized Elbow 11 and the best of the group belonging to heavily graphitized Elbow 4.

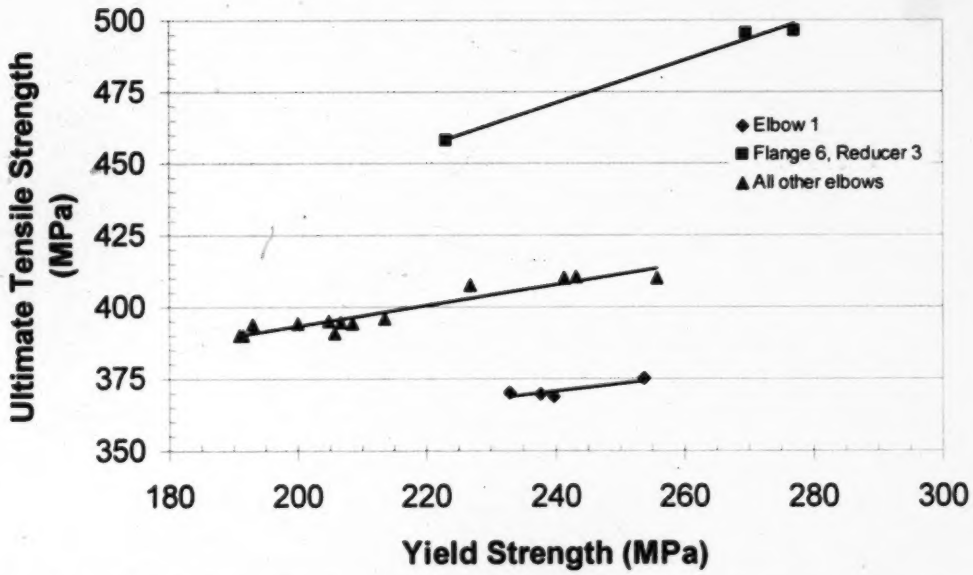

Figure 7.4-1 Exploitable mechanical properties relationships based on averaged tensile testing results. Groupings separate into 3 distinct categories

Analysing the data in terms of yield strength in Table 7.4-2 divided by ultimate tensile strength showed that the data separates into two distinct groups. The first group with a high strength ratio is the heavily graphitized Elbow1 and Elbow 4. The second group has low levels of graphitization and includes the balance of materials tested. The presence of Reducer 3 with the lowest YS/UTS ratio can not be construed as a definitive feature as is only represented by one data point and has a similar ratio to many other materials.

Sample	YS/UTS Ratio
Elbow 1	65 %
Elbow 4	59 %
Flange 6	55 %
Elbow 7	53 %
Elbow 12	52 %
Elbow 11	50 %
Reducer 3	49 %

Table 7.4-2 Ratio of mechanical strengths for materials tested

Figure 7.4-2 shows the trend is consistent in both the tensile graph vs. yield and tensile vs. elongation graphs. Reducer 3 was not included in the regression due to its different gauge length, but its presence denoted by a triangle, does correlate to the regression line. The overall grouping shows that Reducer 3 and Flange 6 have similar properties. Elbow 1 has distinctly different properties and the rest of the elbows are grouped in the middle in a similar fashion with the heavily graphitized Elbow 4 showing the least ductility.

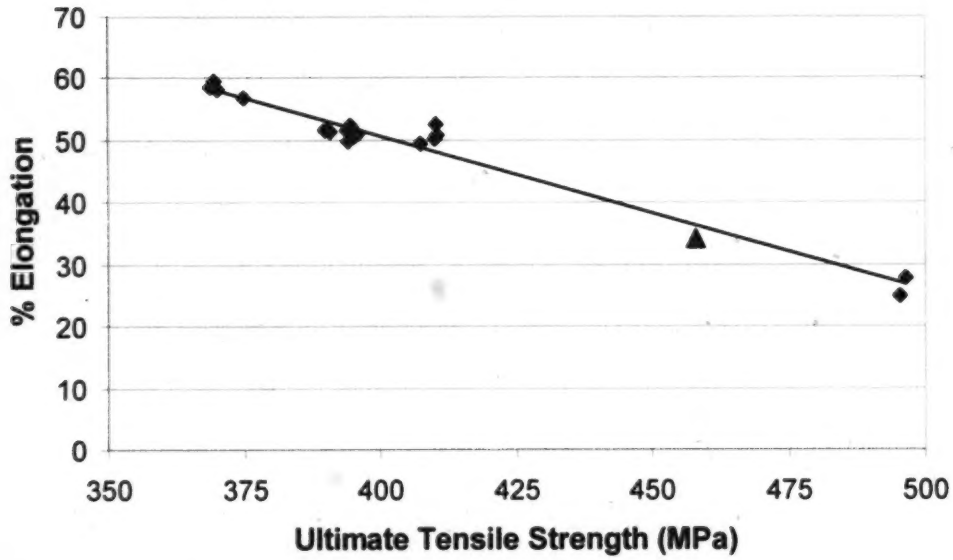

Figure 7.4-2 Exploitable mechanical properties relationships based on averaged tensile testing results. shows relationship between ultimate strength and elongation

Analysing the material in terms of yield strength and elongation does not offer any exploitable trend. While we can separate out the hot forged Flange 6, most of the A234 materials are indistinguishable in terms of elongation. Due to the non standard gauge length used on the other samples, Reducer 3 was again left out of this analysis but would be associated with Flange 6. Almost consistently, the remaining A234 elbows, are all

after the first block valve with the worst properties belonging to the lightly graphitized Elbow 11 and the best of the group belonging to heavily graphitized Elbow 4. If Reducer 3 had the same gauge length as the rest of the materials tested, it might reduce the groupings to 3 distinct groups.

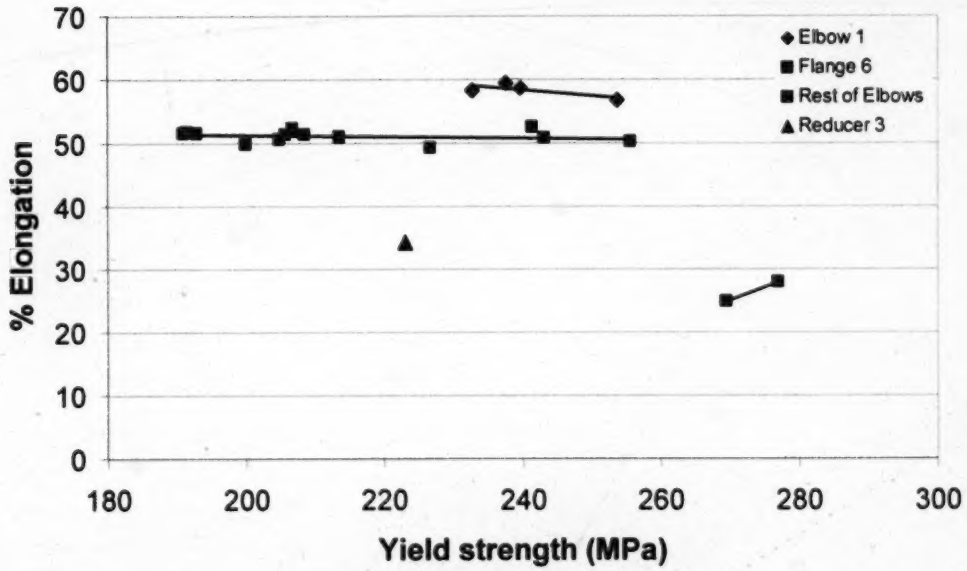

Figure 7.4-3 Analysis in terms of yield strength and elongation offers similar property groupings but no exploitable trend.

The difference in the tensile results can be illustrated in Figure 7.4-4 which shows how the ductility and the tensile strength changes at the extremes of the materials results range. Although both Flange 6 and Elbow 1 are manufactured by different methods and have different mechanical properties, but they have similar volume fractions and morphologies of graphite and grain size. The only difference was the analysed carbon content was twice as high for Flange 6 as compared to all of the other fittings but carbon chemistry cannot account for the different strength between Elbow 1 and the other

elbows. The strength properties of planar graphitized Reducer 3 lie close to Flange 6 in Figure 7.4-3, but we can not compare ductilities gauge length differences. A significant observation is that the ductility of Elbow 1 was so high that the tensile testing machine did not break the samples before the limits of the test were reached.

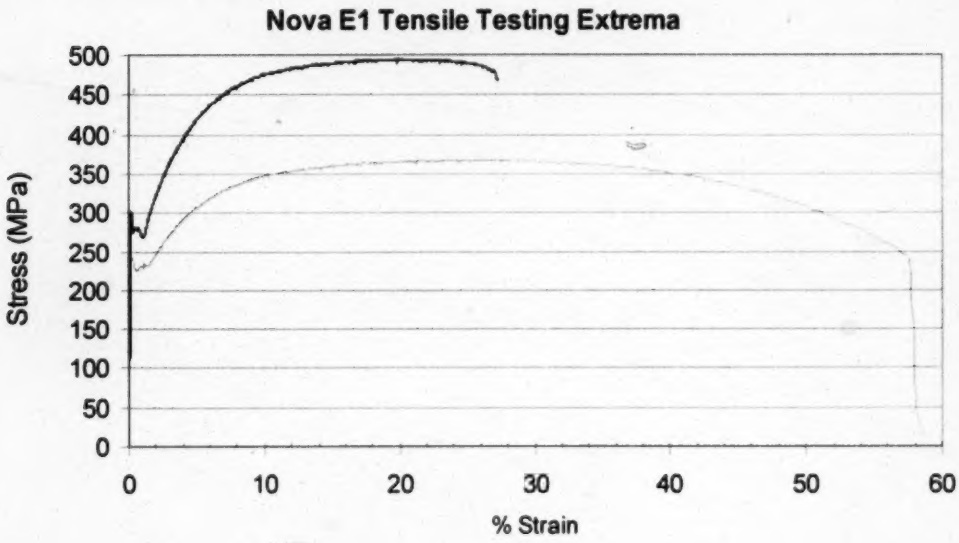

Figure 7.4-4 Extrema of tensile testing showing high strength, limited ductility of Flange 6, and lower strength high ductility of Elbow 1 Serrated yielding is typical for all testing

The high ductility of Elbow 1 was characterized with the observation of Luder's bands on sample after testing indicating a competing balance between strain hardening and reduced cross sectional area. The presence of the graphite has a distinct effect on mechanical properties of the low strength Elbow 1.

7.5. CHARACTERIZATION OF ELEVATED TEMPERATURE PROPERTIES BY HOT TENSILE TESTING

Hot tensile was carried out using an extensometer to move the clip gauge outside the furnace hot zone. This mechanical rigging gave erratic strain readings which required that the raw files be reanalyzed to determine the correct yield stress (Table 7.5-1). The Series 9 software calculated yield stress had significant scatter, which may be partially attributed to binding of the extensometer used.

A limited number of material types were hot tensile tested for the sake of economy and were chosen based on the incomplete creep testing results and prior tensile results (Table 7.5-1). The planar graphitized Reducer 3 could not be tested with the group as no material was left. ASTM 11S1 and API 530 design data in Table 7.5-1, treats the piping as a system and do not differentiate between A234, A105 and A106 individually but rather focuses on the A106 piping unit as a whole.

The hot tensile results are compared in Figure 7.5-1 and may be grouped into two major areas: hot forged (A105) and warm formed (A234). The hot forging processes of the piping and the flange have significantly different thermal-mechanical history than the warm forming processes characteristic of A234 materials, which will help account for differences in strength after long term service.

	UTS (MPa)	YS (MPa)	% el
ASTM DS11S1	400	200	na
API 530	317	155	na
A106 pipe	367	200	
	369	207	43.3
	360	310	
	343	319	28.5
Elbow 1 A234	276	143	50.2
	274	155	49.1
Elbow 7 A234	283	147	57.9
	290	155	52.9
	294	139	50.6
Elbow 4 A234	307	155	53.0
	307	142	57.4
	306	131	58.6
Flange 6 A105	375	171	37.1
	374	170	35.5
	374	182	42.6

Table 7.5-1 Summary of Mechanical properties as determined by hot tensile testing at 427 °C

The tensile strength values indicated in Table 7.5-1 show that all the elbow mechanical properties have changed significantly. Mechanical properties have dropped 31% for UTS and 34.5% for YS when compared to ASTM DS 11S1 but have only dropped 12% for UTS and 15% for YS when compared to API 530 minimum design criteria. At an operating hoop stress of 35 MPa, the stress is approximately 25% of the minimum yield strength.

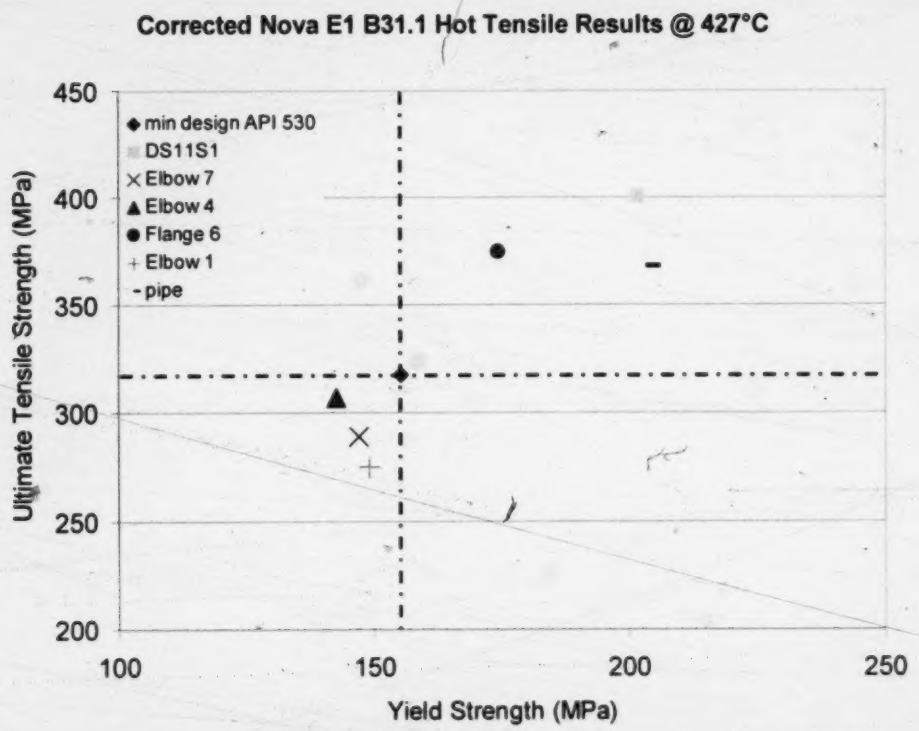

Figure 7.5-1 Strength relationship for hot tensile testing plotted with literature values for A 106 type carbon steels. Intersection of lines is minimum design strength specified by API 530 so desired properties are in the upper right quadrant.

Ductility and strength expectations were not realized for all varieties of elbows but the piping and flange still met the minimum API 530 design strength requirements. Similar to room temperature tensile test results in Figure 7.4-3, Elbow 1 and Flange 6 were at the extremes of the materials tested (Figure 7.5-2) and showed a significant loss of strength from the API 530 values.

Although we can not directly compare the materials because of the gauge length ratios, a surprising trend is the change of ductile behaviour for the materials. It would be expected that the value of ductility would decrease for a longer gauge length. It is also well known

that materials tend to become more ductile as they get warmer. If there was no effect of temperature on ductility and the effect was purely geometric, we should see a decrease in ductility when comparing the non standard gauge length to the standard gauge length. Dividing the elongation for the elevated temperature test by the elongation of the ambient temperature test shows that the ductility for Flange 6 increased to 140% which contrasted with Elbow 1's decrease to 86% elongation. In contrast to room temperature testing, Elbow 1 did not experience the highly plastic behaviour that was observed which suggest that there may be a temperature effect here.

Figure 7.5-2 shows that Elbow 1 material experiences a long term balance between strain hardening and reduction of area followed by the onset of gradual necking that we would expect from high ductility materials. This is consistent with observation of elongation over the entire gauge length, suggesting that the material is not likely to fail suddenly. Flange 6 material suffers from the earlier onset of necking instability and would not experience as much reduction in cross sectional area before failure.

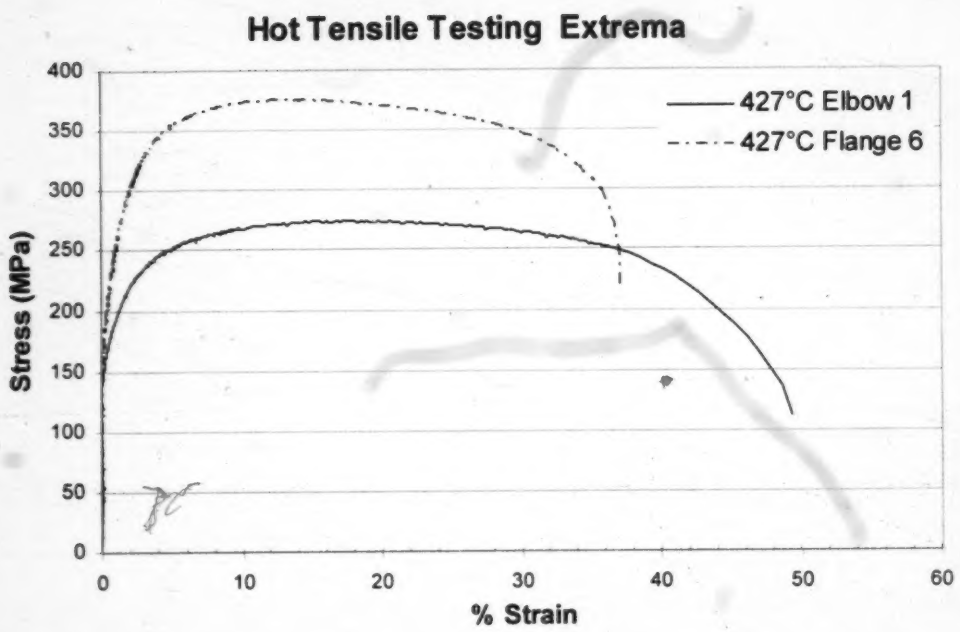

Figure 7.5-2 Hot tensile results are similar to room temperature results showing significant difference in material types.

7.6. CHARACTERIZATION OF FRACTURE POTENTIAL

Fracture testing was carried out unsuccessfully due to load cell instability on the MTS tensile testing machine and a finite number of available samples. While precracking using the fatigue criteria in ASTM E1820 [103], the selected Elbow 1 material was found to resist fatigue crack nucleation. Valid J integrals were not obtained as the testing did not meet conditions for validation under ASTM E1820.

Although the results of compliance testing were invalid the loading cycle did show that the material was tough and that the crack was resistant to propagation as the specimen bent like a plastic hinge. Crack advance was only 1mm for 17° of rotation of the

specimen. Figure 7.6-1 shows the crack surface resulting from crack propagation by ductile tearing.

Figure 7.6-1 Surface resulting from compliance testing of Elbow 1 showing fracture surface due to ductile tearing

Figure 7.6-2 shows an SEM image of the ductile tearing zone of Elbow 1 after heat tinting, showing the unique graphite morphologies that show that the nodules must have a flake composition. The low modulus nodules do not appear to have a role in the initiation of fracture. The measured crack front variation was within permissible ranges for two of the three samples tested which would generally indicate that crack growth is stable although we can not determine the point of crack instability.

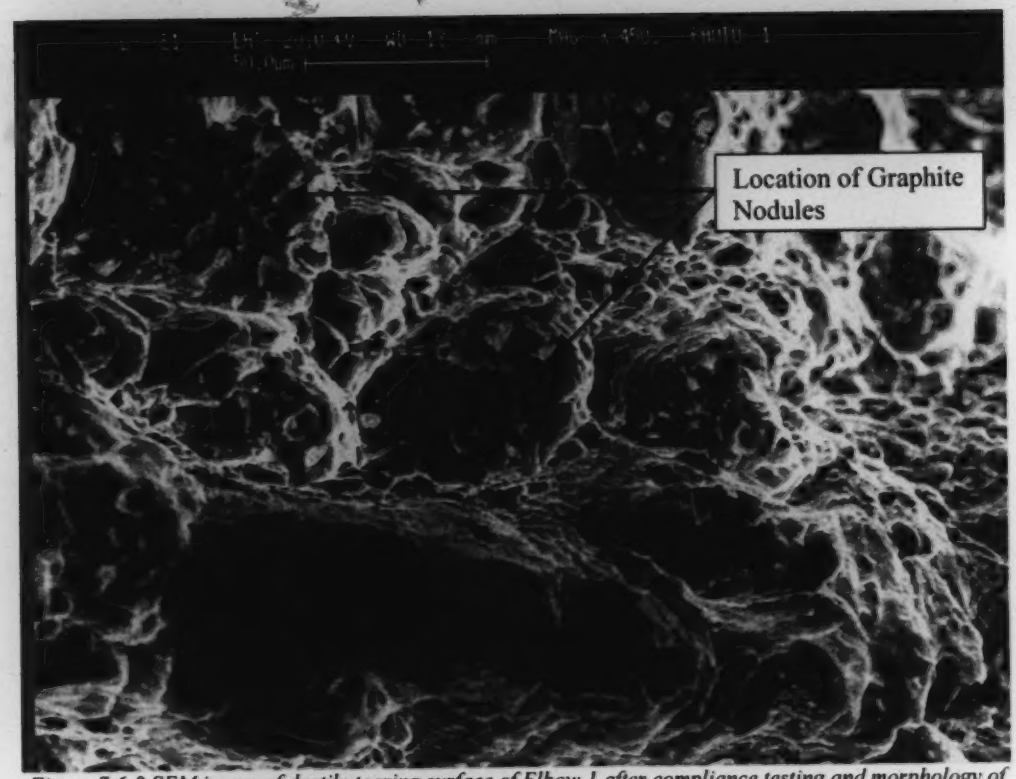

Figure 7.6-2 SEM image of ductile tearing surface of Elbow 1 after compliance testing and morphology of unusual shaped graphite nodules.

7.7. CHARACTERIZATION OF CREEP PROPERTIES

7.7.1. Creep Characteristics

Creep studies were carried out in a manner that multiple methods of parametric creep equations could be studied. The creep curve in Figure 7.7-1 is typical of the results for graphitized materials tested and shows ductile creep characteristics that are common to all materials tested. The weld metal creep curves look very much the same but generally show fracture in the range of 19-36 % elongation. Ductile creep is characterised by the high elongations and severe reduction in areas at fracture that are not typical of high temperature materials. The selected materials tended to fail at one end outside the necked

area but often showed characteristic reduction in cross section area at both ends of the sample especially at the higher temperature ranges.

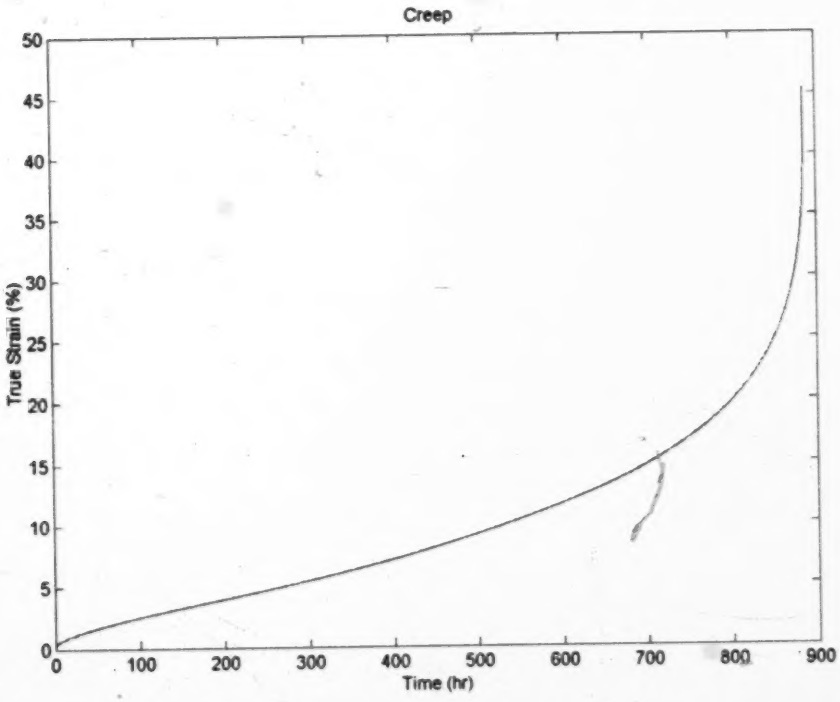

Figure 7.7-1 Matlab generated creep curve typical of graphitized A 234 type steel showing ductile creep characteristics. New Elbow 7 tested at 525 °C and 12000 psi (82.7 MPa)

Creep ductile materials will experience higher strain rates than creep brittle materials for the same time frames. Strain rate acceleration has a significant effect on a material as creep damage rate becomes greater than the materials ability to resist strain. Although these materials suffer from degradation of the major strengthening mechanism, the materials capacity to resist strain is still significant. Figure 7.7-2 shows that strain rates are very reasonable. We know that the pearlite has spheroidized and graphite is present as a non-coherent phase which leaves no obvious method of blocking dislocation

movement. In a metal with stable carbide forming elements, the presence of random fine stable metal carbides maintain stability of the matrix as the pearlite colonies are reduced to graphite and ferrite. Transmission electron microscopy analysis could be utilized to explore microstructure characteristics to determine the continued stability of the matrix.

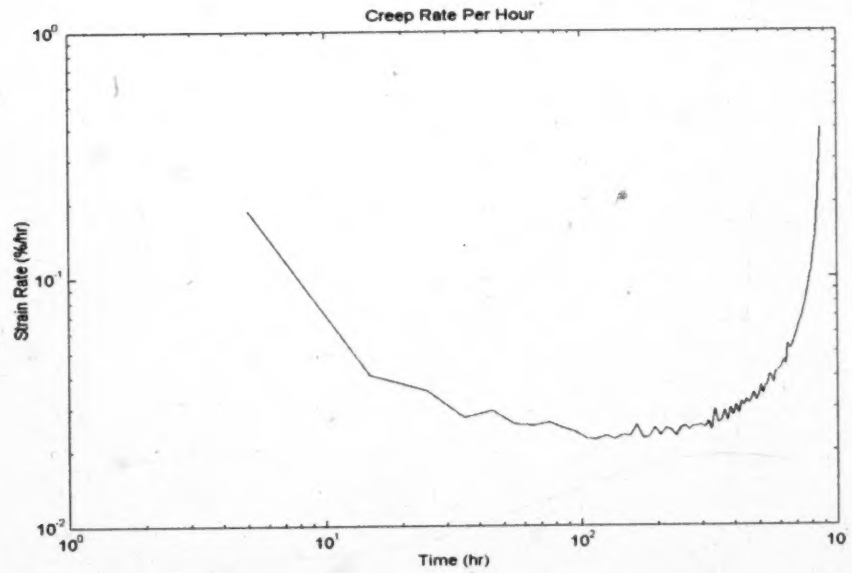

Figure 7.7-2 Matlab generated creep rate curve showing change in acceleration of true strain over time during testing. New Elbow 7 tested at 525 °C and 12000 psi (82.7 MPa)

Material was tested under conditions from high stress to approximately service stress and temperatures ranging from 670 °C to 475 °C to allow accelerated testing conditions. In all 92 successful tests were logged as indicated in Table 7.7-1 using imperial stress units to allow correlation to the original ASTM DS11S1 Larson-Miller design data as per ASME rules [9] . Most of the testing was performed in the region where necking due to excessive stress was unlikely and oxidation at high temperatures is not a significant factor. As a general observation, temperatures above 575 °C intensified oxidation in an exponential

fashion, and stresses above 82.7MPa (12000psi) showed a propensity to cause premature necking.

7.7.2. Creep Data Summary

Table 7.7-1 reveals that data acquisition was not ideal in some cases and 18 files were lost for a variety of reasons, which did not allow for complete analysis of all the testing. Most parametric methods rely on rupture time so the data acquisition had a redundant method of collecting elapsed time which ensured that all rupture times were preserved even when the data files were lost. Several cases of lost data are identifiable by the lack of ε_{ss} and ε_{min} values in Table 7.7-1.

Sample	Stress (psi)	Temperature (°C)	Rupture time (hrs)	Strain at failure	ε_{ss}	ε_{min}	time to min (hr)
New Elbow 7 (repeat of Elbow 7)	12000	575	37.1	0.506	0.00500	0.00467	8
		550	188.3	0.637	0.00064	0.00040	30
		525	887.5	0.575	0.00015	0.00013	200
	10000	600	27.6	0.693	0.00586	0.00604	8
		575	122	0.778	0.00080	0.00079	10
		550	584.5	0.525	0.00017	0.00015	70
	8000	625	29.4	0.724	0.00356	0.00350	5
		600	104.9	0.568	0.00032	0.00053	7
		575	392.1	0.564	0.00004	0.00003	40
Elbow 7	12000	575	9.1	0.599	0.02080	0.01929	2
		550	35.7	0.602	0.00482	0.00248	45
		525	276.89	0.309	0.00025	0.00019	100
	10000	600	33	0.568	0.00406	0.00386	10
		575	97.3				
		550	349.1	0.599	0.00040	0.00038	40
	8000	625	29.1	0.608	0.00445	0.00432	3
		600	149.45	0.544	0.00064	0.00025	15
		575	624.1	0.600	0.00018	0.00015	200
Reducer 3	20000	510	54.8	0.394	0.00141	0.00135	2

	12000	600	26.2	0.807	0.03118	0.00257	2
		575	87	0.437	0.00068	0.00075	10
		550	484.4	0.391	0.00010	0.00009	30
	10000	600	64.2	0.541	0.00184	0.00149	9
		575	312.7	0.384	0.00035	0.00025	20
		550	1301	0.241	0.00003	0.00003	100
	8000	625	57.9	0.459	0.00033	0.00030	3
		600	296.6	0.406	0.00034	0.00030	15
		575	355.87	0.429	0.00034	0.00031	10
	4800	670	10.46	0.505	0.01076	0.01084	2
		650	210	0.490	0.00055	0.00046	15
		635	122				
Elbow 4	12000	575	16.1				
		550	60.8	0.748	0.00374	0.00354	10
		550	65.97				
		525	209.5	0.835	0.00111	0.00098	15
	10000	600	10.2	0.890	0.02318	0.02102	2
		600	28.7	0.793	0.00650	0.00599	4
		575	62.4	0.762	0.00298	0.00284	10
		550	130.8	0.771	0.00159	0.00150	2
		550	477.68	0.206	0.00346	0.00149	18
	8000	600	50.1	0.827	0.00427	0.00386	10
		575	161.1	0.787	0.00134	0.00107	40
		550	579.7	0.644	0.00033	0.00029	100
Assorted Elbows	12000	575	18.6	0.769			
		550	56	0.659			
		525	581.9	0.626			
	10000	600	18.6	0.484			
		575	84.6	0.805			
		550	270.8	0.574			
	8000	625	47.1	0.693	0.00221	0.00210	7
		600	224.5	0.650	0.00018	0.00013	15
		600	219.3	0.381			
		575	343.5	0.640			
		475	1300				
Flange 6	20000	500	87.7	0.621	0.00242	0.00216	15
	18000	500	16.55	0.652	0.01481	0.01345	4
		475	876.8	0.719	0.00025	0.00022	110
	16000	525	83.4	0.528	0.00236	0.00213	10
	14000	525	188	0.741	0.00116	0.00100	40
	12000	575	32.18	0.692	0.00642	0.00595	4
		550	114.7	0.699	0.00154	0.00162	15
		525	472.6	0.754	0.00041	0.00039	70
	10000	600	27.62	0.924	0.00758	0.00698	4

		575	129.58	0.794	0.00142	0.00133	15
		550	427.7	0.721	0.00034	0.00033	60
	8000	600	81.47	0.750	0.00229	0.00197	10
		575	305	0.913	0.00060	0.00051	4
		550	343.5				
		525	under test 1.443mm 3400 hrs Jan31				
	5000	650	64.86	0.840	0.00215	0.00169	10
		625	297	0.577	0.00052	0.00048	40
Elbow 1	12000	550	34.3	0.667	0.00655	0.00619	4
		525	283.1	0.914	0.00075	0.00070	40
		500	255.2	0.850	0.00044	0.00039	80
	10000	575	20.2	0.963	0.01297	0.01169	2
		550	99.2	0.976	0.00165	0.00225	15
		525	527.9	0.774	0.00038	0.00037	100
	8000	575	53.9	0.950	0.00495	0.00435	9
		550	283.7	0.917	0.00083	0.00080	40
		525	1682.2	0.827	0.00015	0.00013	500
		500	under test 1.1137mm 2881hrs Jan31				
	7000	670	10.45	0.504	0.01121	0.01084	1
	4500	670	22.41	0.783	0.00756	0.00454	4
		650	47.6	0.407			
		650	13.6	0.305	0.01451	0.01370	2
		630	98	0.409			
		630	78.5	0.591	0.00142	0.00112	3
Elbow 1 weld	12000	550	46.2	0.197	0.00125	0.00112	8
		525	459.9	0.241	0.00009	0.00016	70
		510	339.3	0.272	0.00016	0.00016	45
	10000	550	114.5	0.364	0.00061	0.00056	10
		525	386.6	0.222	0.00016	0.00011	80
		500	2189.4	0.222	0.00003	0.00002	300
	8000	575	161.9	0.355	0.00052	0.00025	2
		550	375.4	0.286	0.00023	0.00022	80
		525	678.6				
		550	1070				

Table 7.7-1 Raw data from creep testing based on ASTM DS11S1 design data

The selected materials in Figure 7.7-2 showed significant variation in creep lives when compared in a matrix of temperature and stress with respect to rupture time. The planar graphitized Reducer 3 required 50 °C higher test temperatures to attain similar rupture times to random graphitized Elbow 1 at both 82.7MPa (12000 psi) and 55.2MPa (8000

psi). The expected variation in rupture times for the weld material Elbow 1 Weld did not emerge as a factor in separating materials in early groupings as testing conditions were similar to the poorly performing Elbow 1.

Reducer 3aR9				Elbow 1				Weld Elbow 1			
σ psi	12000	10000	8000	σ psi	12000	10000	8000	σ psi	12000	10000	8000
MPa	82.7	68.9	55.2	MPa	82.7	68.9	55.2	MPa	82.7	68.9	55.2
T 625			59.0	T 575		20.2	36.3	T 575			161.9
600	26.2	64.2	279.0	550	34.3	99.2	283.7	550	46.2	114.5	375.4
575	87.6	312.0	355.9	525	283.1	527.9	1350.0	525	459.9	386.6	678.5
550	484.4	1301.0		500	533.0			510	339.3	1000.0	

Table 7.7-2 Matrix of creep results showing variation of temperature (°C) at prescribed stresses (psi/MPa) to set up rupture time estimations

7.7.3. Stress Sensitivity of Norton's Law

One of the two fundamental terms in the mathematical definition of secondary creep rate was Norton's Law as shown in Equation 3-9. The stress sensitivity can be determined several ways all of which have their respective uses. API 530 Appendix E shows an exponential increase in the stress sensitivity exponent as the temperature decreases in the test range of interest. Design stress exponents were interpolated and tabulated in Table 7.7-3 from API 530 Appendix E [58] for purposes of comparison. To follow the trend, stress exponent values should increase as temperature decreases.

7.7.3.1. API 530 derived stress exponents

Using the method of determining stress exponent where $n = (t_r, \sigma)_T$ prescribed by API 530 [58], Table 7.7-3 summarizes the rupture based stress exponents that were determined. Where duplicate isothermal tests exist at two different stresses, the higher stress is denoted first in the table. The table shows that the dual values of the stress exponent often

show little correlation for isothermal conditions and further analysis of this data does not result in any useable trends. It would be expected that if the first of the two stresses was higher the susceptibility to material strain exhaustion could be verified, but this trend was never consistent. Compounding this problem is that the nature of accelerated testing means that the only test that was ever within range of the service stress was conducted 195 °C above service stress, making the sensitivity of the rupture based stress results dubious at best.

	Temperature °C					
Sample	670	600	575	550	525	500
Elbow 1 weld				5.0 / 5.3	1.0 / 2.5	
Elbow 1	1.7		4.4	5.8 / 4.7	3.4 / 5.2	
Assorted		11.2 / 11.1	8.3 / 6.3	6.6 / 7.0		
Reducer 3		4.9 / 6.9	7.0 / 0.58	5.4		15.7
Flange 6		4.8	7.6 / 3.8	7.2 / 1.0	6.0 / 6.0	
Elbow 4		4.3 / 7.1	5.2 / 4.3	7.1		
Elbow 7		6.8	13.0 / 8.3	12.5		
New Elbow 7		6.0	6.5 / 5.2	13.0 / 8.3		
API 530		4.6	4.8	5.3	5.8	6.5

Table 7.7-3 Rupture based parameters based on method from API 530 and design values.

Plotting the stress exponent determination for Elbow 7 with New Elbow 7 in Figure 7.7-3 shows the scatter that must be accounted for when developing a trend in the data. This combined with the low number of data points has the potential to lead to significant error in the subsequent analysis.

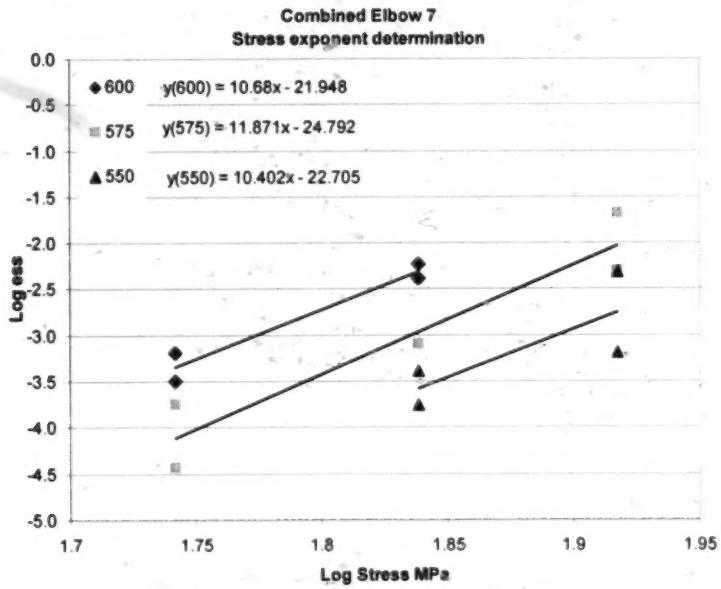

Figure 7.7-3 Typical isothermal relation graph tabulated in Table 7.6-3 to determine stress exponent 'n'

7.7.3.2. Strain rate based stress exponent determination

The sensitivity to stress may also be investigated through the relation $n = \left(\dot{\varepsilon}, \sigma \right)_T$ by plotting log $\dot{\varepsilon}_{ss}$ against log σ to determine the stress sensitivity exponent *n*. The values of *n* should be consistent for any isothermal condition if the materials are similar and homogeneous. Although a complete analysis was compromised by missing strain rate data, Table 7.7-4 shows the random nature of the stress sensitivity and lack of uniform properties for all samples except Reducer 3, Flange 6 and Elbow 7. Attempts to refine the method by plotting log $\dot{\varepsilon}_{min}$ against log σ did not improve the stress exponent analysis.

Sample	Temperature °C 600	575	550	525
Elbow 1 weld			4.2	
Elbow 1		4.3	5.0	4.0
Reducer 3	7.6	10.7	16.4	
Elbow 4	4.7	3.6	4.0	
Flange 6	5.4	5.8	8.2	6.7
Elbow 7	8.3	11.7	13.7	
New Elbow 7	13.0	12.4	7.2	
composite 7	10.6	11.9	10.4	

Table 7.7-4 Strain rate based summary of creep stress exponent n for graphitized materials

Plotting the stress exponents for $\dot{\varepsilon}_{ss}$ for the test temperature range in Figure 7.7-4 show that planar graphitized Reducer 3 is significantly more stress sensitive than any of the other materials. The significant exponential increase in the stress exponent at lower temperatures may be an indicator of strain exhaustion of graphitized Reducer 3 and Elbow 7. Elbow 1 and Elbow 4 show nearly constant values of stress exponent unlike the stress exponent trend published in API 530 [59]. These stress exponent values are typically less than 5 for pure metals and single phase alloys and greater than 5 for precipitation hardened alloys. The low values of stress exponent observed in Elbow 1 and Elbow 4 indicate an insignificant effect of carbides on creep resistance. This seems consistent with the fact that these two materials exhibit the worst mechanical properties of the materials tested.

The supposedly duplicate testing of material Elbow 7, New Elbow 7 in Figure 7.7-4 showed the opposite trend observed in the original Elbow 7 test. The behaviour is contrary to expected behaviour shown in Table 7.6-3 summarized from API 530 [58]. The strain data was rechecked many times and although rupture behaviour and elongation are similar, this questions the accuracy of the small sample sizes tested in this study.

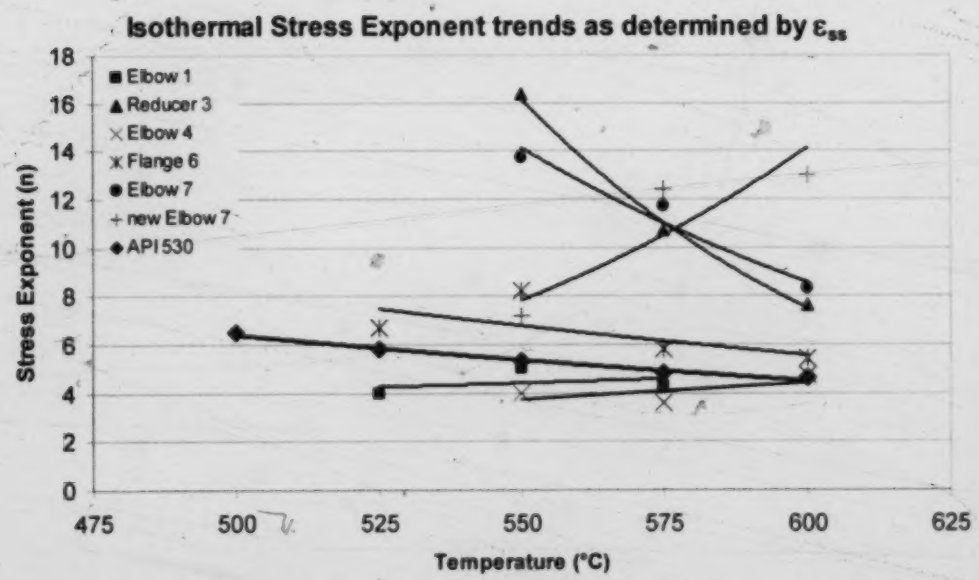

Figure 7.7-4 Response of stress exponent of service exposed materials against expected API 530 exponential trend. Elbow 7 and New Elbow 7 should be duplicates

7.7.3.3. Observations from stress exponent determination

Overall the determination of the stress exponent was unsatisfactory for service exposed materials. While this may be due to the fact that most of the stress exponent regressions were performed with three or less data points, it would be more likely that there is too much variance in the material. Neither the volume fraction of graphite nor the presence of planar graphite offered conclusive proof to allow separating materials based on the stress exponent.

7.7.4. Relationship of Creep Elongation to Creep Life

During mechanical testing, elongation was valuable for groupings the tested materials. Figure 7.7-5, compares two materials at the extremes of the analysis. The first material is

Elbow 1, which shows significantly more ductility than any other material, regardless of rupture time. (Elbows 7 and Flange 6 exhibited very similar performance to Elbow 1, but showed 10% less ductility across the range). Planar graphitized Reducer 3 shows a distinct reduction in ductility for longer tests. This reduction in ductility is what would be expected for a normal material as it indicates that a material is becoming creep brittle. To make this relation work, it was necessary to include only tests that were longer than 25 hours and tested at stresses higher than 34.5MPa (5000psi) as the material properties appear to scatter outside these stress and time ranges.

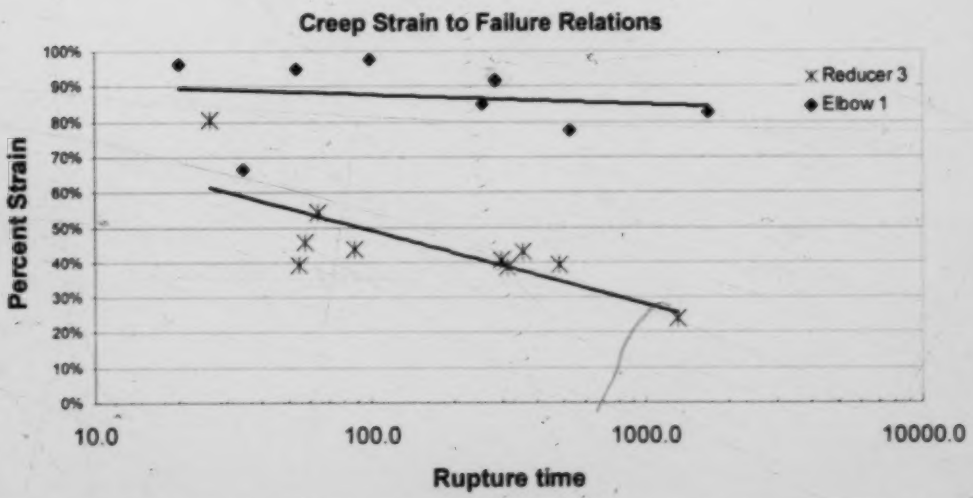

Figure 7.7-5 Strain to failure relationship for selected materials. The extreme performers are Elbow 1 and Reducer 3, where the data includes all temperatures and stresses within the selected range.

7.7.5. Microstructure Effects of Graphite on Creep

The effect of the graphite on the creep characteristics was not associated with catastrophic failure of the sample. All graphitized samples failed by gradual acceleration of the creep rate until failure, rather than a sudden catastrophic failure characteristic of

brittle fracture materials. The resultant microvoid coalescence morphology of the fracture is more consistent with FCC materials such as pure aluminium and nickel than with standard high temperature materials such as Cr-Mo steels. To contrast material performance, during initial machine verification, low grade carbon steels that were tested under similar test conditions would suffer brittle fracture. Figure7.7-6b shows the potential relationship between planes of secondary graphite material and the microvoid coalescence at the side of the fracture cone in Figure7.7-6a.

The presence of graphite could not be positively identified as the source fracture intiation of the microvoid coalescence in the cup/cone fracture surface as the graphite is likely to have oxidized during the two hour cool down period after the sample fractured. Circumstantial evidence of larger voids in Figure 7.6-6a shows the exposed pseudo planes at the root of the fracture surfaces which stand out in contrast to the transgranular fracture nature of most of the ductile fracture surface. The pseudo planes of the graphite in Figure 7.7-6a demonstrate a near perpendicular orientation to the exterior of the pipe. The presence of pseudo planes in the ductile fracture surface may indicate fracture nucleation on graphite nodules.

A cross section was performed by cutting a cross section in the axial direction, adjacent to the fracture surface, to relate the fracture mechanism of the microstructure to presence of planes of graphite. The effect of the extreme ductility is apparent even near the fracture surface, as the graphite maintains adherence to the matrix and lacks the expected creep crack voids. While this microstructure was the result of testing at the high end of the test

temperature range, it is representative of all creep microstructures obtained in the 8000-12000 psi (55.2-82.7 MPa) range.

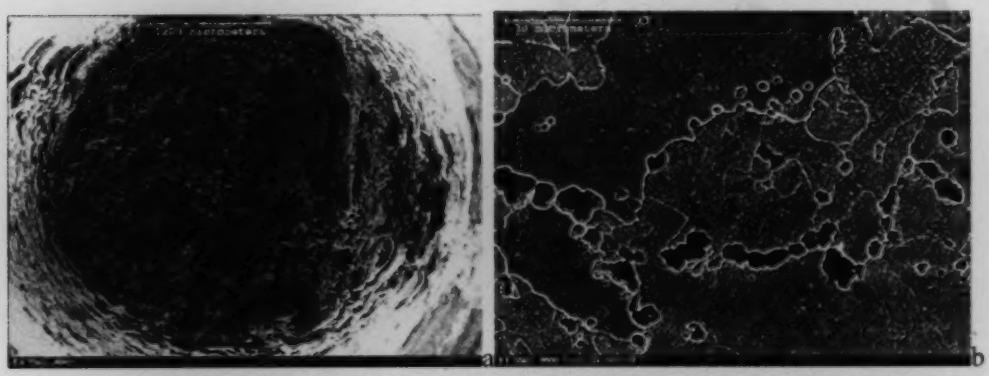

Figure 7.7-6 Elbow 1 tested at 550 °C and 8000psi (55.2 MPa) fracture cone (a) showing lines of graphitization that may be associated with final fracture. Cross section of the same sample (b) showing plane of graphite adjacent to fracture tip.

7.7.6. Creep Mechanisms of Graphitized Steel

Materials with planar graphite and the random graphite showed different post creep microstructure characteristics as shown in Figure 7.7-7a, b. Most post-creep samples are similar to Figure 7.7-7a and only Reducer 3 exhibits microstructure found in Figure 7.7-7b. The different grain shapes indicates that a separate creep mechanism may be responsible for the different creep microstructures of the material.

Although an exact Ashby map for the material is not available, we can compare between characteristics of pure iron and Cr-Mo maps in Figure4.2-1. The holomogenous testing temperature range was from 0.38-0.45 and the normalized tensile stress ranged from $1.3x10^{-3}$ to $3.3x10^{-4}$. Comparison to Ashby iron map suggested a power law creep mechanism would be dominant in a material that was mostly ferrite. This suggests that using the pure iron map is probably reasonable for random graphite. Creep of planar

graphite seems to operate with a different diffusion mechanism, which would require significantly different creep deformation map.

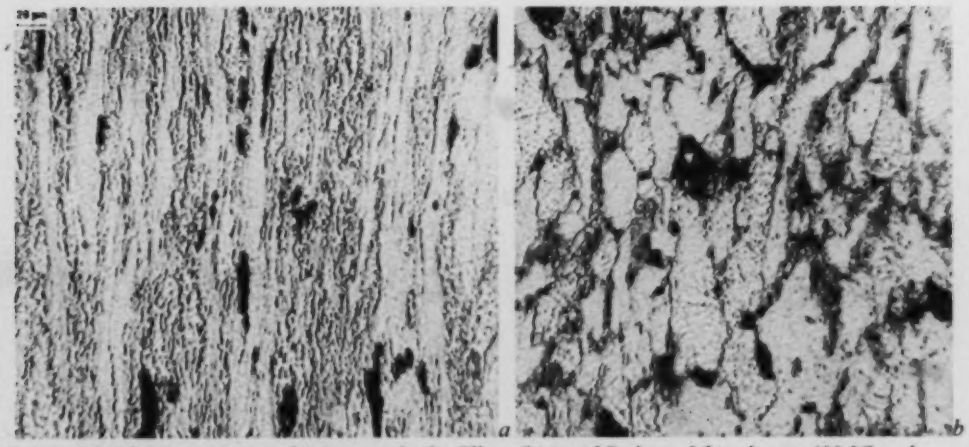

Figure 7.7-7 Post-creep optical micrographs for Elbow 7(a) and Reducer 3(b) taken at 600 °C and 68.9MPa (10000psi) near the fracture surface

7.7.7. Creep Effects of Graphite on Weld Microstructure

The post creep weld microstructure was considered initially but was found to be insignificant when it was determined that material was fracturing outside of the A3 temperature zone (Figure 4.3-1). The observation was limited by the machining, as not all welds were centered in the gauge length, so some materials fractured in the root of the gauge length. Although it has been proven that welds can significantly reduce creep life, in this case the limiting factor is the microstructure of the base metal microstructure and not the weld metal. Figure 7.7-8 shows a post creep micrograph containing a multipass weld that had parted along the A3 temperature. The graphite free A3 temperature zone Elbow 1 weld is the faint diagonal line in the microstructure and the onset of graphitization may be observed starting after A1 temperature. The fusion line is at the lower left corner.

Figure 7.7-8 Post creep micrograph of Elbow 1 Weld tested at 525°C and 12000 psi(82.7 MPa) with direction of stress shown. Lines have been added to show the A3 temperature zone, A1 temperature zone and fusion line. The presence of graphitization starts after the A1 temperature line indicating the graphite is not a weld related effect.

Figure 7.7-8 shows no observable microstructure damage to the weld side of the HAZ, but the base metal graphite planes have been pulled along the indicated axis, into a crude alignment pointing towards the rupture. It would appear that the material in the HAZ is more stable than the basemetal. The observation can be made that the behaviour of creep rupture of base metal graphitization next to weldments is dependent on the base metal properties such as in Figure 6.7-6 as the graphite density is significantly denser outside the fine grain heat affected zone than inside the coarse grain heat affected zone. The

location of the graphite in relation to the weld calls into question the relevance of using HAZ graphitization theories for base metal graphitization [33].

7.8. PRELIMINARY CREEP RANKINGS OF MATERIALS

Most materials have significantly different rupture times for similar test conditions as demonstrated in Table 7.7-2, so a ranking was prepared to separate materials. The ranking was determined using both isostress and isothermal conditions using Figures 7.8-1 thru 7.8-4.

The ranking of the materials in Table 7.8-1 is subjective but it helps organize the materials. Planar graphitized Reducer 3 is a distinctly separate material from the other materials. The second grouping contains materials that had similar properties during mechanical testing. The third grouping contains Elbow 1 with its poor mechanical properties and also the heavily graphitized Elbow 4. The fourth grouping is not based on a single type of mechanical properties but rather the deviation across the range as shown in Figures 7.8-3 and 7.8-4.

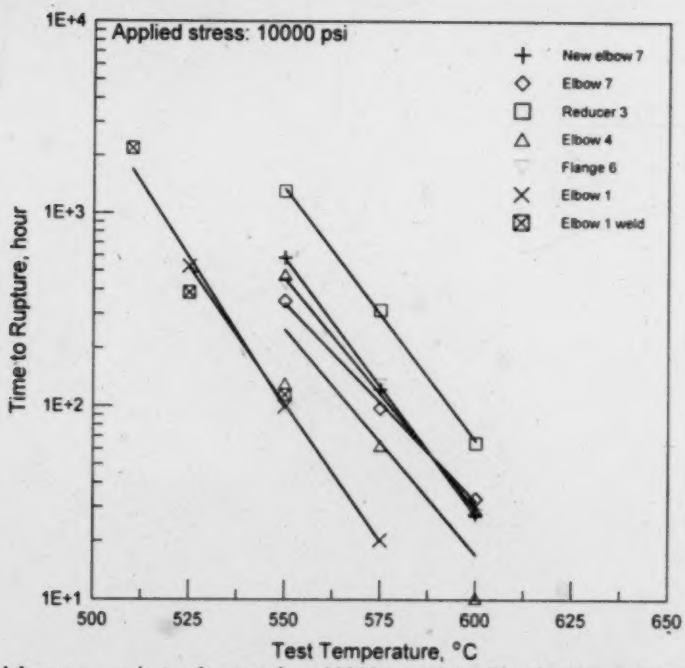

Figure 7.8-1 Isostress analysis of materials at 10000 psi (68.9 MPa) showing 3 distinct groupings

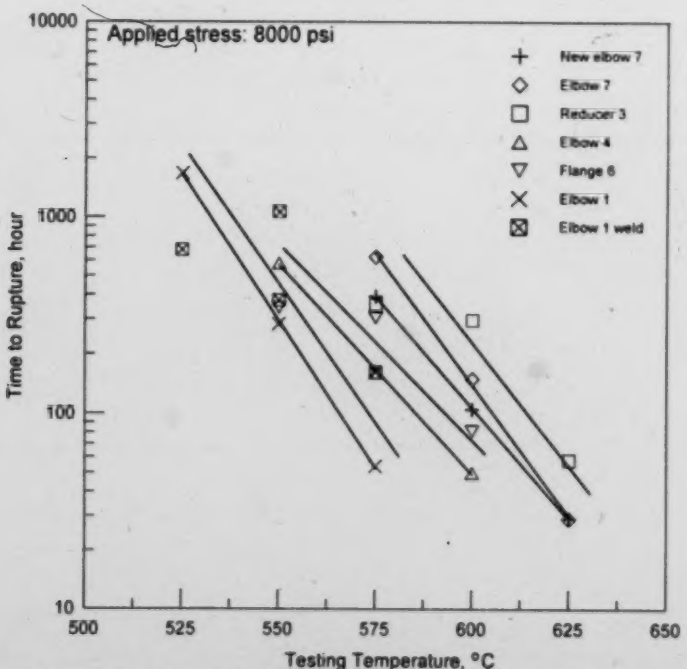

Figure 7.8-2 Isostress analysis of materials at 8000 psi (55.2 MPa) showing similar ranking trend but lacks the 3 distinct groupings

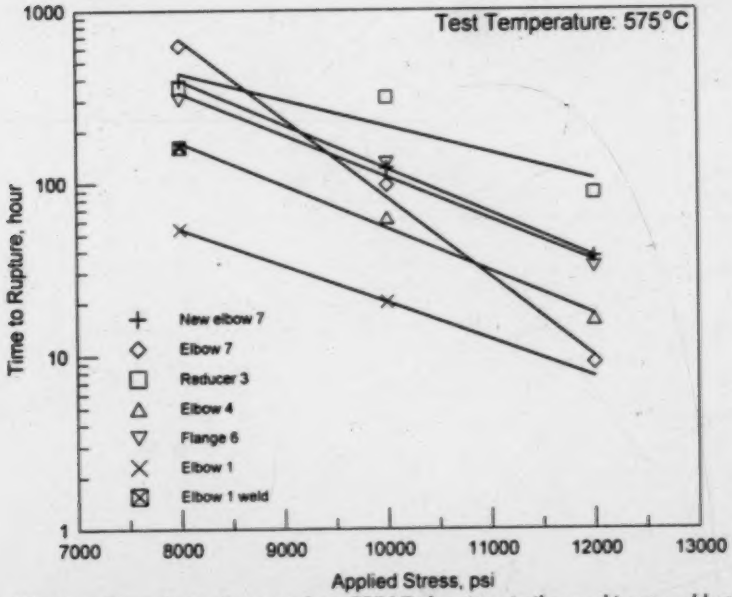

Figure 7.8-3 Isothermal analysis of materials at 575 °C showing similar ranking trend but lacks the 3 distinct groupings. Elbow 7 shows significant deviation behaviour

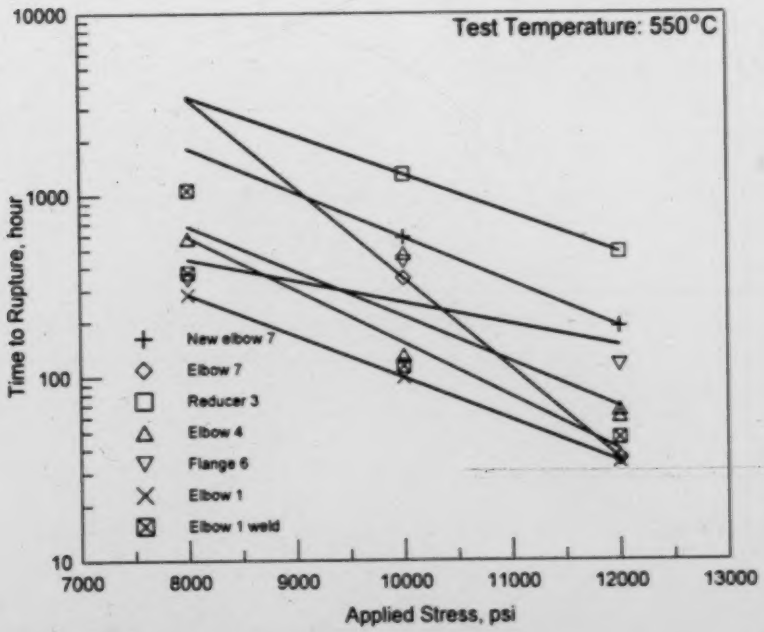

Figure 7.8-4 Isothermal analysis of materials at 550 °C showing similar ranking trend but lacks the 3 distinct groupings. Elbow 7 shows significant deviation behaviour

Relative Grouping	Separation Criteria			
	Figure 7.7-1 10000 psi (68.9 MPa) Reducer 3	Figure 7.7-2 8000 psi (55.2 MPa) Reducer 3	Figure 7.7-3 575 °C Reducer 3	Figure 7.7-4 500 °C Reducer 3
Group 1				
Group 2	Elbow 7	New Elbow 7	New Elbow 7	New Elbow 7
	New Elbow 7	Flange 6	Flange 6	Flange 6
	Flange 6	Elbow 7		
Group 3	Elbow 4	Elbow 4	Elbow 4	Elbow 4
	Elbow 1	Elbow 1	Elbow 1	Elbow 1
	Elbow I weld	Elbow I weld	Elbow I weld	Elbow I weld
Group 4			Elbow 7	Elbow 7

Table 7.8-1 Summary of creep ranking based on raw data.

8. CREEP RESULT ANALYSIS

Creep results for constant load testing are compiled as two types. The parametric based methods rely on the temperature and rupture time (Table 7.8-1) while the creep rate dependent methods require continuous data collection during creep testing.

8.1. PARAMETRIC METHODS RESULTS

8.1.1. Larson Miller Parameter

Larson Miller based testing is the de facto standard of understanding materials that spend time at temperature. Although the method has a large error associated with it there is a large amount of engineering data available to give a starting point for an investigation. Larson Miller parameters published in ASTM DS11S1 were used throughout to track progress and correlate testing by allowing a comparison to accepted performance limits. The Larson-Miller master graph for this research was developed by recreating the basic ASTM DS11S1 graph and plotting results against these points (Figure 8.1-1). The regression lines have been extended one half of a Larson Miller point past the original DS 11S1 data. The top line represents average new material condition and the bottom line represents minimum expected properties at 63% consumption of service life. Figure 8.1-1 shows the Larson Miller composite of all the materials that were tested. Scatter in the data reveals that we must analyse each material independently.

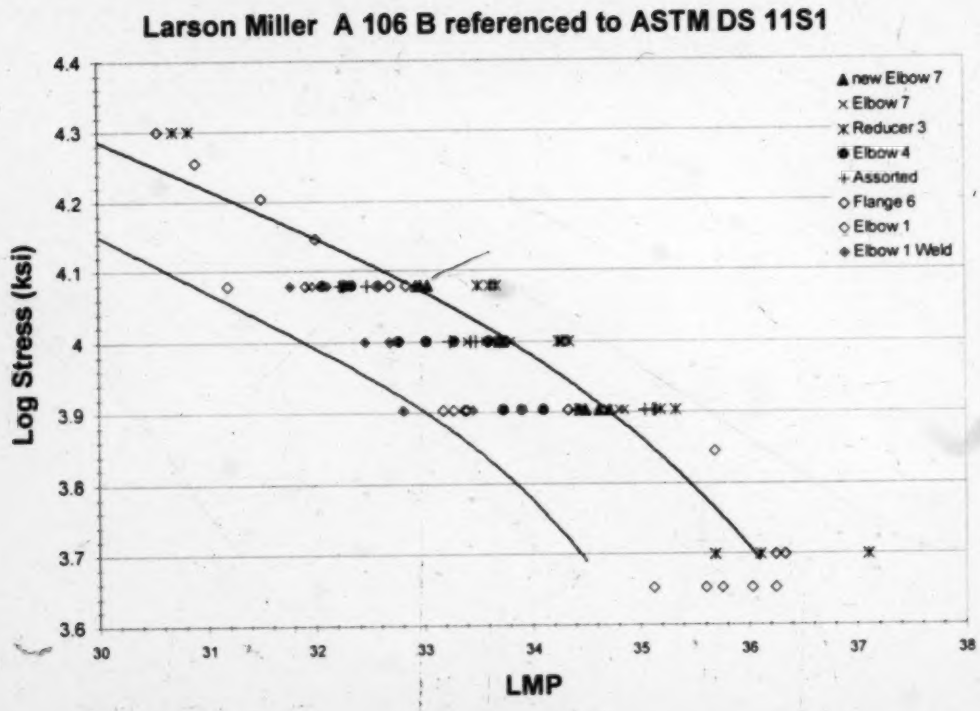

Figure 8.1-1 Compilation of Stress rupture data for the universally accepted Larson-Miller parameter (LMP). Stresses ranged from 34.5MPa (5000psi) to 137.9MPa (20000psi) while temperatures ranged from 475 °C to 670 °C.

The scatter of data for any given material at any given stress shows that the effect of temperature is very significant. A material which follows Larson-Miller behaviour will have a very similar Larson Miller Parameter (LMP) value for any given stress, regardless of temperatures used to obtain the value. The basic form of the LMP equation shows significant sensitivity to temperature as it is the only variable that is not logged. When a material is retested it should have consistent LMP values but rupture values showed significant variation for most materials retested. A significant difference in material properties must then be responsible for the scatter of Larson-Miller parameter for each isostress condition.

8.1.1.1. Larson-Miller constant

Regression to obtain the Larson-Miller constant C was not able to be replicated for any material. Figure 8.1-2 demonstrates that the materials gave a range of C from 8 to 27 and were not consistent for any material. The average value for C was 17.2 which is well below the literature value of $C = 20$. Figure 8.1-2 shows the scatter of the value of the Larson-Miller constant, which shows no trend regardless of material analysed. The only materials that offered a consistent range were Elbow 4 with an absolute variation of 2.3 on an average C of 16.5, and Flange 6 with an absolute variation of 3.0 on an average C of 17.3.

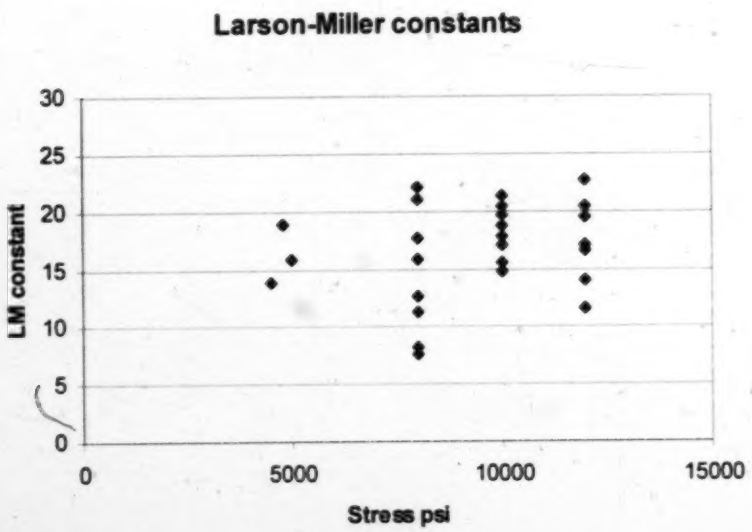

Figure 8.1-2 Aggregate Larson-Miller constants C for all materials. There is no trend between the materials or within groups of materials.

The deviation of C shown in Figure 8.1-2 is not critical as the value of C is considered to be constant for purposes of calculation for the life of the material and, thus, allows use of

the life fraction rule. The only reason to use a different value of *C* for calculations other than the original published value is when there is reason to suspect that the original published *C* value may not have been accurate. Prager [70] claims that exhaustive testing of carbon steel shows that the value of *C* for Larson-Miller methods applied to carbon steel should realistically be set to 16. Determining the value of *C* did show that service exposure has changed the material performance significantly as the microstructure changes.

8.1.1.2. Separating material based on Larson-Miller performance

Separating the materials out gives a more comprehensive picture of Larson-Miller behaviour. Figure 8.1-3 shows results for Flange 6 which was picked for a full stress range of testing based on the results after at 550 °C, 55.2MPa (8000psi) test. The early test results for this material indicated it would have poor performance when compared to the test matrix, but final analysis demonstrated good agreement with Larson-Miller theory, essentially following the ASTM DS 11S1 average line. The deviation from the average line at low stresses near the end of service life shows agreement with predictions of Zhou [59] that least squares regression, may not be the most appropriate method of generating an average value trend line.

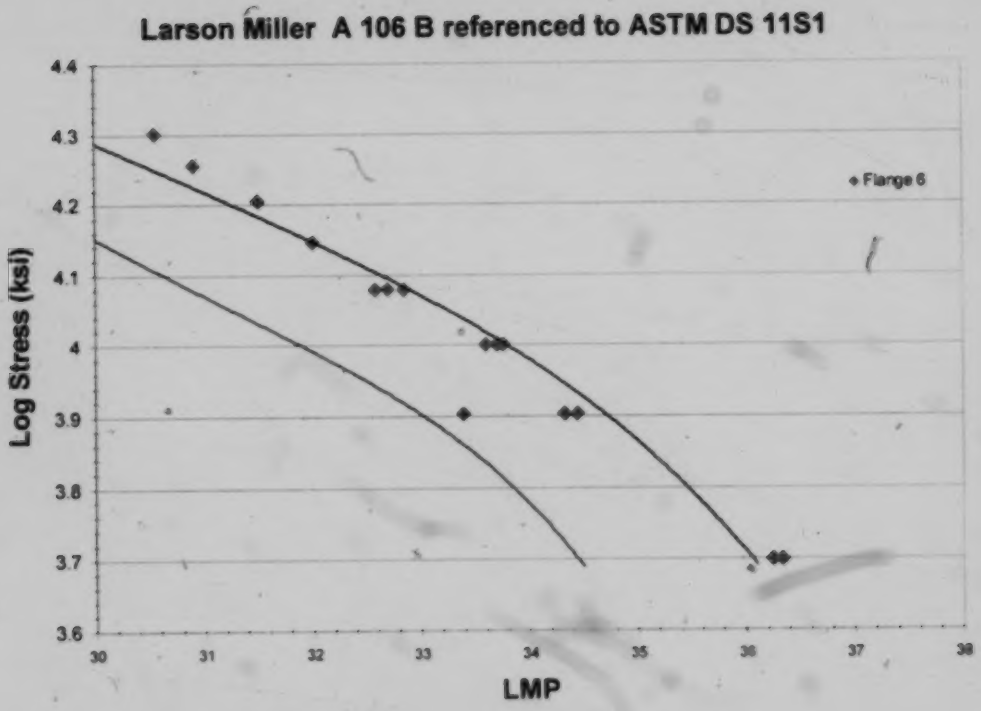

Figure 8.1-3 A full stress range of testing using Flange 6 material to develop a comprehensive Larson-Miller master for the service degraded materials.

Elbow 7 and New Elbow 7 gave reasonable agreement with Larson-Miller theory while following the DS11S1 average line (Figure 8.1-4). One notable deviation was the change in properties at 82.7MPa (12000psi) with the original group of materials showing a slight shift in Larson Miller values which may be interpreted as stress sensitivity.

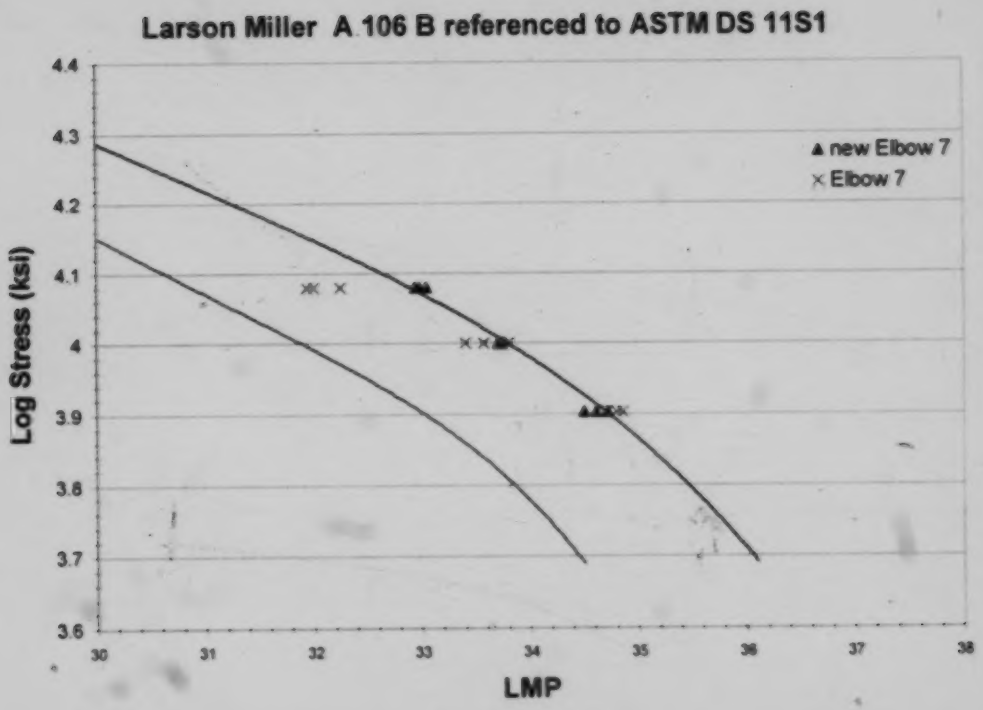

Figure 8.1-4 Comparison of the New Elbow 7 and Elbow 7creep rupture properties. The rupture times and temperatures are similar for both 8000 psi (55.2 MPa) and 10000 psi (69.0 MPa) but deviate for 12000 psi (82.7 MPa)

Larson-Miller evaluation of the planar graphitized Reducer 3 (Figure 8.1-5), gives an extremely optimistic life prediction. Earlier discussion showed that post-rupture microstructure of Reducer 3 specimens had not opened voids or creep cracks in the vicinity of graphite nodules, but accelerated creep testing can not show the fracture effect of connecting ligaments along planes of graphite over tens of thousands of hours. Reducer 3 shows divergent behaviour at low stresses which is unlike any other material tested but there is no evidence whether this is an anomaly in the data or if there is a true divergence in LMP values.

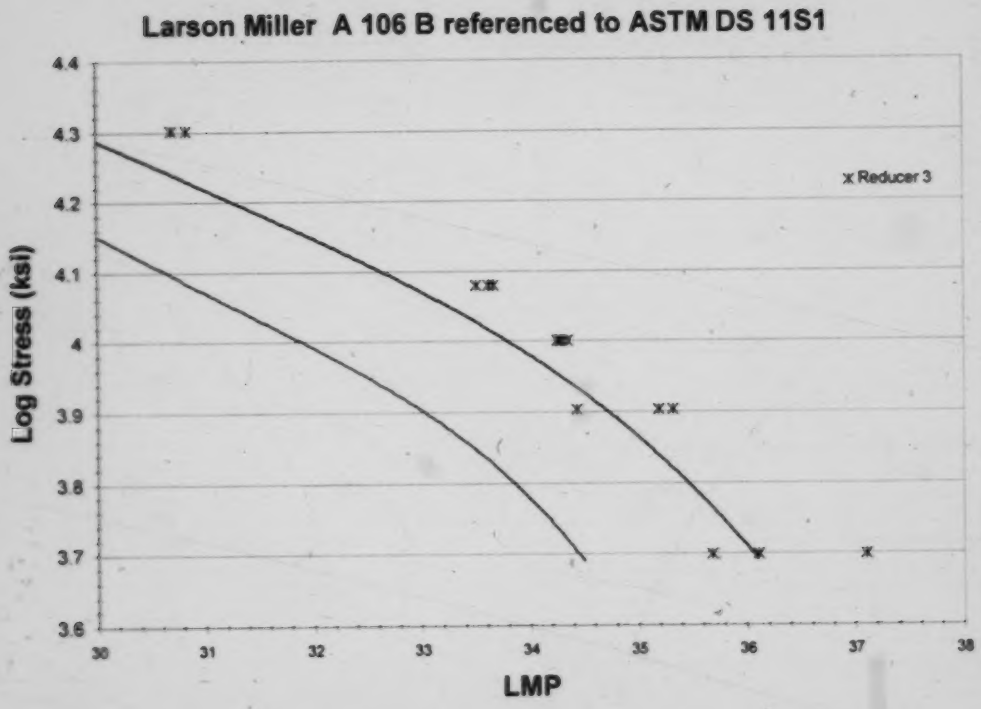

Figure 8.1-5 Larson-Miller estimation for Reducer 3 showing a service exposed material that has better than average life remaining. The lower stresses show a divergent trend showing a change of creep mechanism.

Elbow 1 (Figure 8.1-6) gave the most inconsistent Larson-Miller behaviour. As previously observed (Figure 8.1-3) the ideal LMP behaviour will form a tight grouping of LMP values but Elbow shows the deviation of LMP values at different stresses. If the isostress scatter is insignificant this allows ease of calculation of predicted lifetimes, but when we have a large variation of LMP values under isostress conditions, we also have significant problems extrapolating to determine lifetimes at stress values that lie outside the testing range.

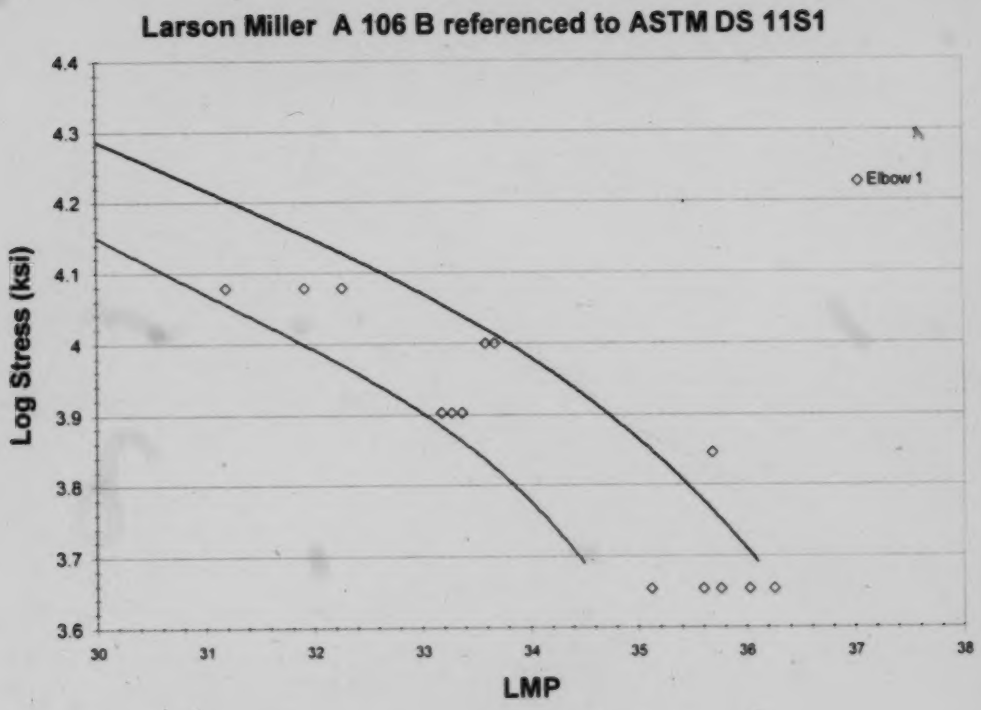

Figure 8.1-6 Larson –Miller parameter value scatter for Elbow 1 materials

Other materials that also followed the divergent trend of Elbow 1 included Elbow 4 and Elbow 1 weld. The creep performance of Elbow 1 weld was slightly better than that of Elbow 1. While the weld itself did not creep, the creep occurred outside of the HAZ (Figure 7.6-8) in the base metal reflecting the service degradation of Elbow 1. While the heavily random graphitized Elbow 4 had many creep characteristics that were common to Elbow 1 and Elbow 1 weld, the large volumes of graphite did not reduce life expectancy.

8.1.2. Sherby-Dorn Parameter Results

8.1.2.1. Traditional Sherby-Dorn analysis

The Sherby-Dorn regression method for activation energy was used to determine slopes which would allow construction of a Sherby-Dorn master graph for life prediction (Figure 8.1-7). The use of three stresses is not optimal for any regression and thus, for this study the method is subject to significant variation, which can influence the Sherby-Dorn parameter (PSD) values.

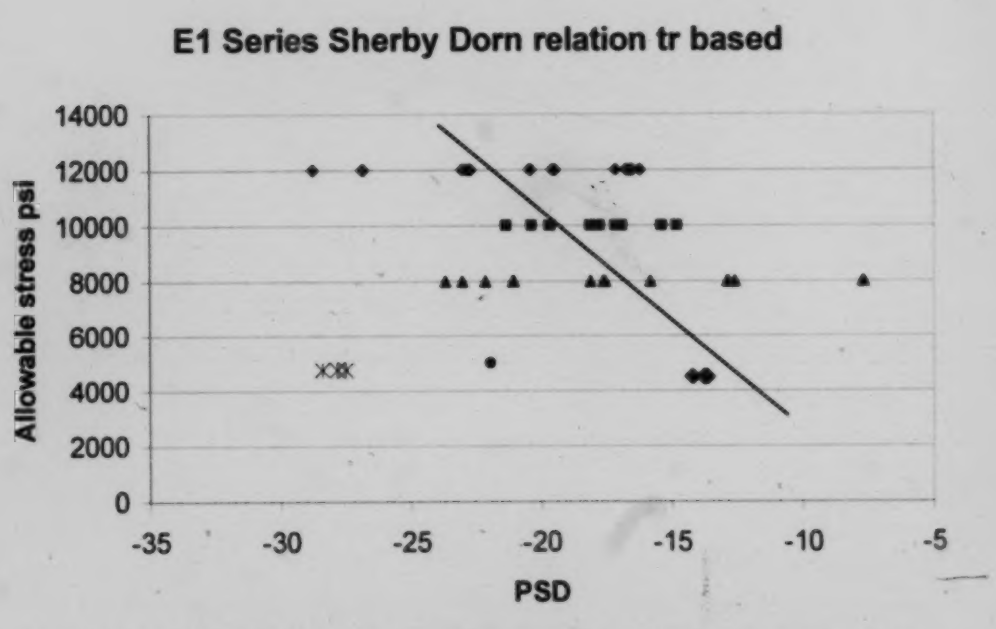

Figure 8.1-7 Plot of Sherby-Dorn activation energy as determined from activation energy slopes as described in Figure 8.1-8. Line shows expected regression trend.

The plot of activation energy showed that the isostress lines such as shown in Figure 8.1-8 had very good correlation but the values of activation energy for each isostress condition showed significant deviation. Figure 8.1-7 shows the variation of the activation

energy slopes was inconsistent and this error will have a dramatic effect on the determination of the Sherby-Dorn parameter, accounting for the scatter in figure 8.1-7. Some of the scatter was initially attributed to machining during sample preparation, but even better machined specimens showed similar variation in activation energy.

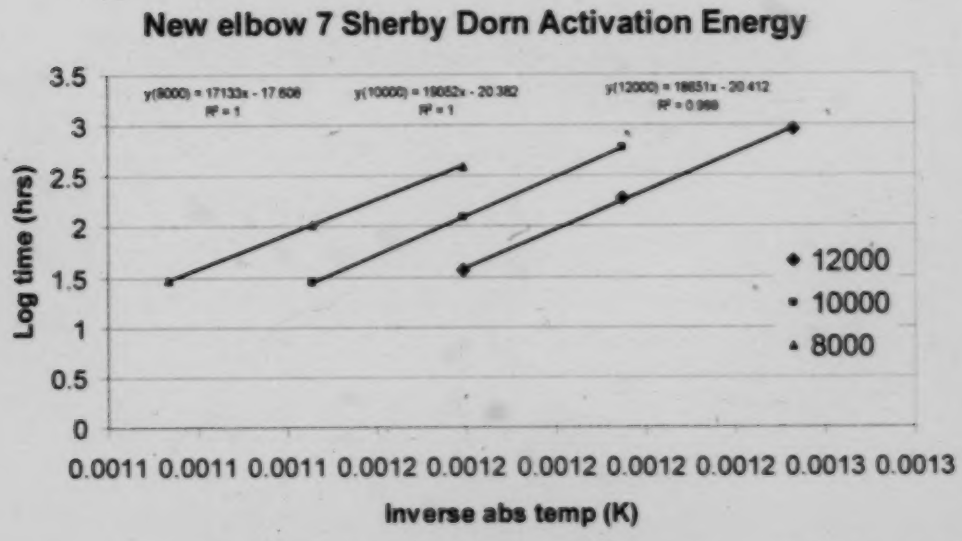

Figure 8.1-8 Plot of Sherby Dorn activation energy as determined from rupture time. Value of slope is Q/R where Q is in Joules where R is the universal gas constant. The statistical correlation is very good but the values of Q/R do not follow a logical trend.

8.1.2.2. Strain rate based Sherby-Dorn parameter determination

Although using secondary creep rate ε_{ss} to calculate the Sherby-Dorn Parameter is not an accepted method, an analysis calculation of activation energy Q should be the same regardless of whether the calculation method used is rupture based, or based on the strain rate and the strain rate based curves are plotted in Figure 8.1-9, to correlate activation energy. The -2.3Q/R slope differs little from activation energies given for Sherby-Dorn

calculated activation energies. Figure 8.1-10 shows the ε_{ss} method exhibits the same scatter as the rupture time based method in Figure 8.1-8. Most samples tested would show a statistical correlation (R^2) above 0.95 regardless of method, but almost all values in the 34.5MPa (5000psi) range had little R^2 correlation, but were in close enough numerical agreement to determine an activation energy range.

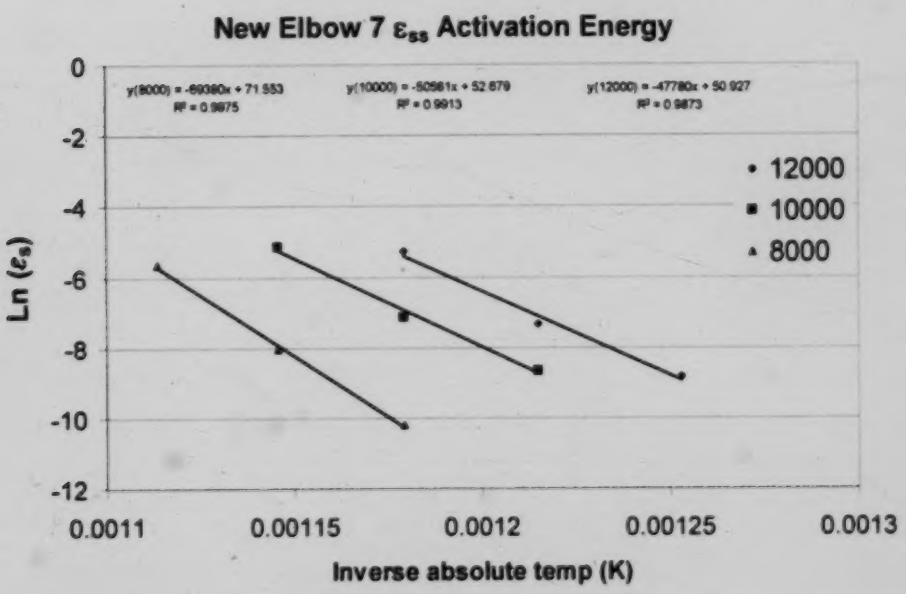

Figure 8.1-9 Activation energy as determined from secondary creep strain plotted as isostress creep curves.

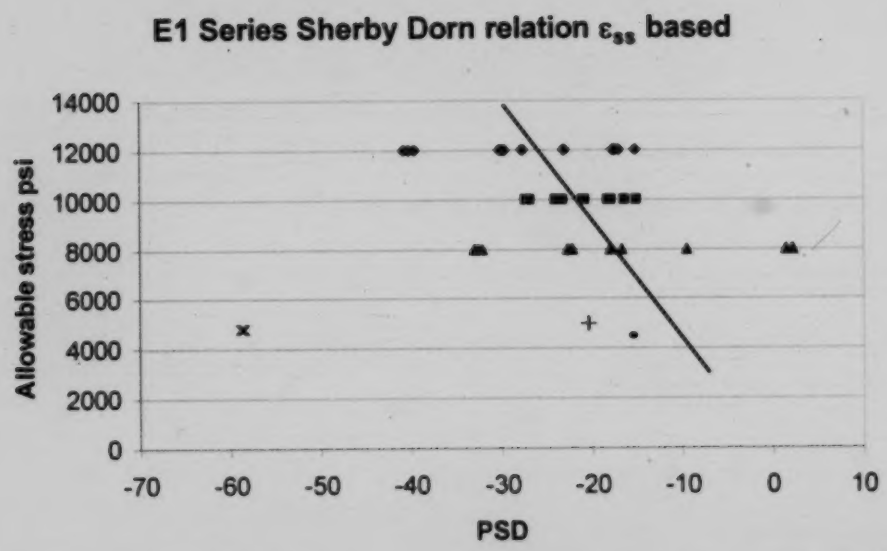

Figure 8.1-10 Sherby-Dorn parameters based on secondary creep strain rate showing similar patterns but significantly more scatter range over the values of PSD. Desired trend is marked on graph

However, regression using ε_{ss} did not improve the overall quality of the analysis of the data and increased scatter on the master Sherby-Dorn graph. The data shows very similar trends to the t_r based graphs with significant scatter for most materials but no noticeable trends that will allow classification of materials are apparent. For example the extreme variations are tabulated in the following Table 8.1-1 but no clear correlation can be observed. Furthermore little agreement with Larson-Miller based rankings or raw stress rupture time rankings.

Stress MPa (psi)	Lowest PSD tr based	Lowest PSD ε_{ss} based	Highest PSD tr based	Highest PSD ε_{ss} based
82.7 (12000)	Elbow 4 Elbow 1 Weld	Elbow 4	Elbow 1	Reducer 3
68.9 (10000)	Elbow 7	Elbow 7	Elbow 1	New Elbow 7
55.2 (8000)	Elbow 1 Weld	Elbow 1 Weld	Reducer 3	New Elbow 7

Table 8.1-1 Variation in Sherby-Dorn parameter by material type

The strain based Sherby-Dorn method was particularly ineffective analysing Reducer 3 at 55.2 MPa (8000psi) giving results that seemed unrealistic with almost non-existent activation energy for both the t_r and $\dot{\varepsilon}_{ss}$ methods. A logical explanation is lacking as this planar graphitized material performed normally under at this stress under Larson-Miller conditions. The activation energy of the material is very sensitive for this method and little useful service life data can be extracted from the method for the overall grouping of material. Although many times a statistically useful correlation for activation energy could be found, plotting would never result in a useful trend for individual materials.

Compiling all of the activation energies as a composite value and taking the average slope gave a poor statistical correlation but the master graph in Figure 8.1-11 improves to a useful range. A similar graph was produced using the t_r based values and it shows the same scatter. The lack of obvious trends dictates that better correlation is needed to make a PSD master graph.

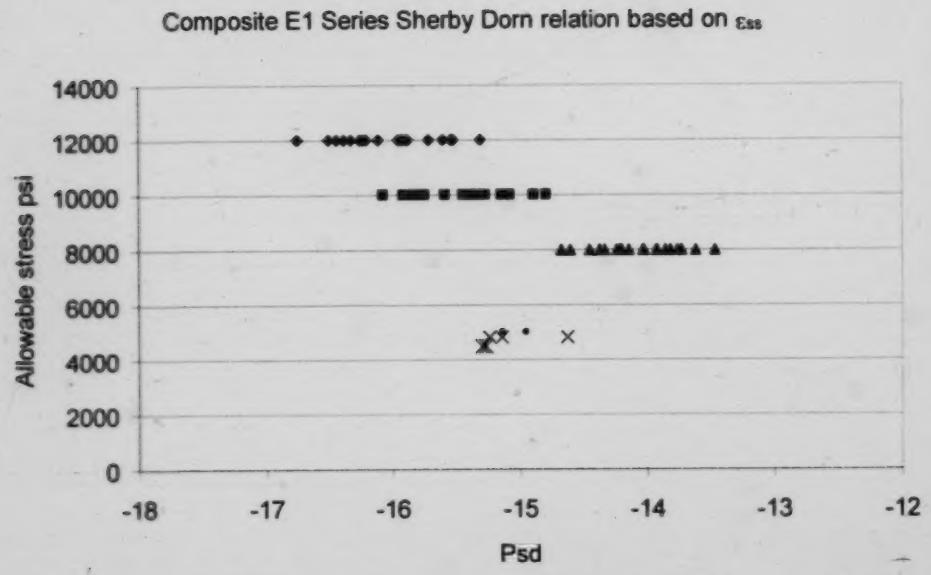

Figure 8.1-11 Best fit Sherby-Dorn correlation based on steady state strain rate, averaged for all materials developed using activation energy aggregate for entire data set. Valid trend line can not be developed for this material.

8.1.2.3. Separating materials based on traditional Sherby-Dorn methods

The method of separating each of the materials being researched was useful for Elbow 1. Both the rupture method and the secondary creep rate method showed correlation of data. Figure 8.1-12 shows the alignment of data that may be interpreted as a trend for Elbow 1. Since the Sherby-Dorn method is most applicable to pure metals, the development of a trend for Elbow 1 may be due to the severely degraded microstructure looking more like a pure ferrite material than steel. Unfortunately the Sherby-Dorn method did not model a trend for Elbow 4 and Elbow 1 weld as accurately although they share similar characteristics under Larson-Miller analysis.

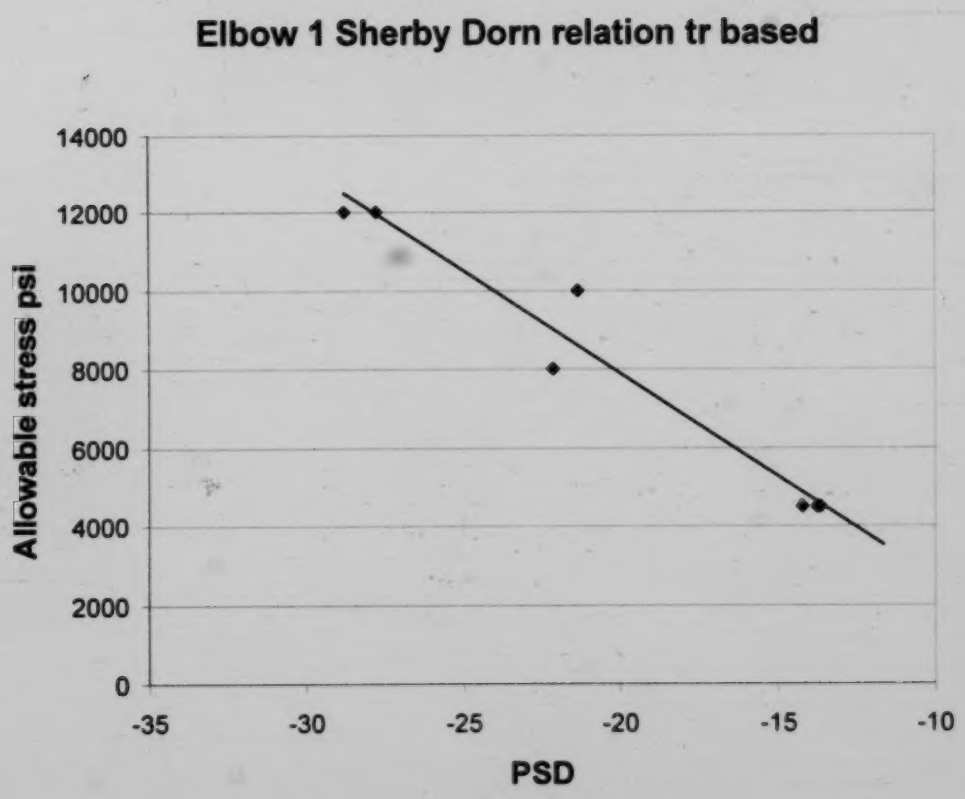

Figure 8.1-12 Rupture based Sherby-Dorn method showing usable trend for Elbow 1 material.

This leaves an open question as to how accurately Sherby-Dorn models the creep of graphitized service steels. Using the strain rate based method may be showing the known material effect of adjusting the balance beam. Since most creep frames that do not use dead weights have to adjust position to maintain the permissible load on the specimen, it would stand to reason that a material that is stress sensitive could have its rupture time decreased by the sudden adjustment of the beam. While this would be an inconsequential point in Larson-Miller analysis where all factors except temperature are logged, the change in stress could have an effect on life prediction.

8.1.2.4. Separating materials based on non-traditional Sherby-Dorn methods

The strain based method (Figure 8.1-13) shows some promise as a methodology to separate graphitized materials quickly. The most significant benefit would be the ability to conduct a short term test and retrieve a long term prediction

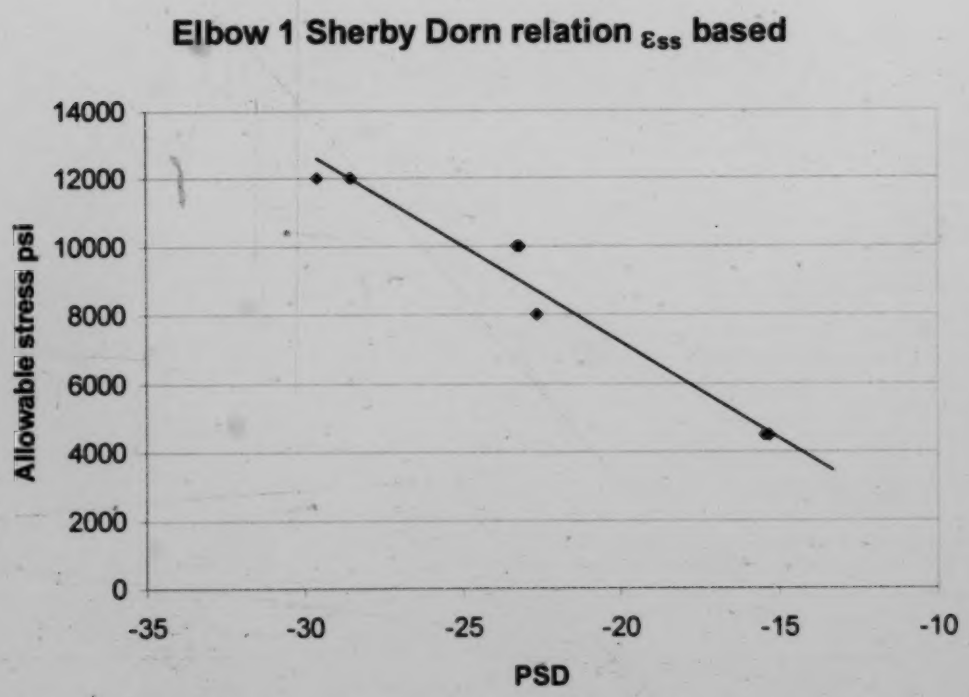

Figure 8.1-13 Strain rate based Sherby-Dorn showing improved correlation of parametric values.

8.1.2.5. Comparison of Sherby-Dorn methods

Not all the materials that scattered during the Larson-Miller analysis reacted well to Sherby-Dorn analysis. For example Elbow 4 reacted poorly to both the rupture based and the strain rate based Sherby-Dorn analysis at the 87.2 MPa (12000 psi) stress. Elbow 4 gave similar trends at the 55.2MPa (8000psi) and 68.9MPa (10000psi) stress levels, with

the rupture based method being slightly conservative. The 82.7 MPa (12000 psi) stress where Elbow 4 shows significant deviation from the expected trend is possibly a result of the significant volume of graphite rendering the material more stress sensitive. The tight grouping of the PSD values show the strain rate based method appears to be slightly more accurate as the expected error in Figure 8.1-14 is quite low with the exception of the 68.9MPa (10000psi) outlying point.

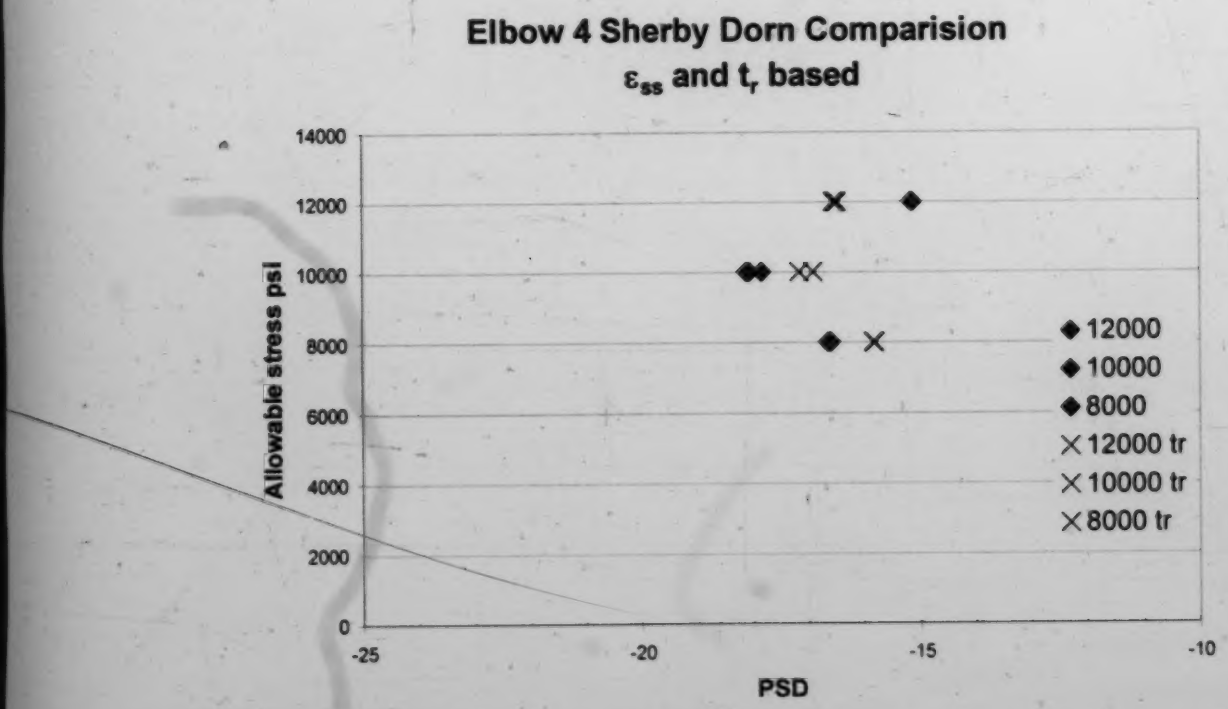

Figure 8.1-14 Elbow 4 comparing ε_{ss} to t_r based methods. The t_r based method is more conservative until the higher stress.

8.1.3. Manson-Haferd Parameter Results

The Mason-Haferd method should give improved results for ferritic materials since extrapolation should yield a specific point at the intersection of stress and inverse

temperature. Figure 8.1-15 shows a major variation in results as the extrapolation results in several intersections. The extreme variation in data offers R^2 values so low that we can not be sure the trend line is pointed in an appropriate direction.

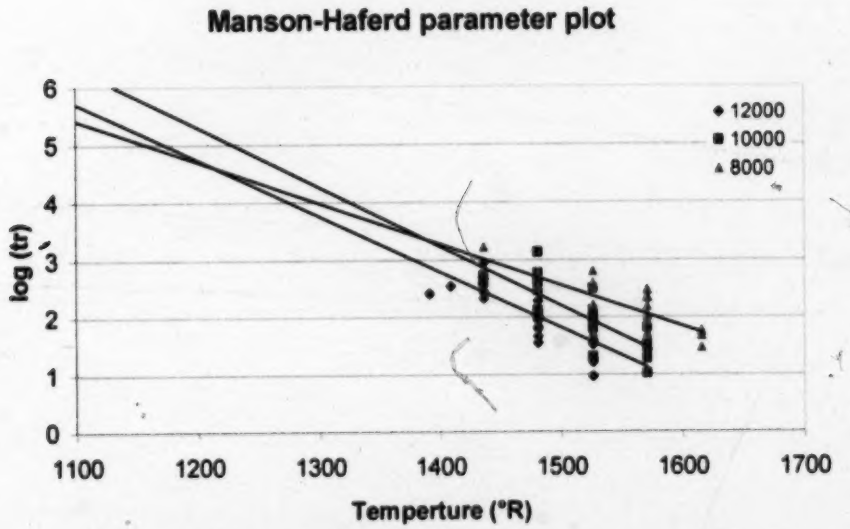

Figure 8.1-15 Plot of Manson-Haferd parameter to determine common isostress line intersection. Point of line intersection would determine master rupture life diagram.

Separating out the Flange 6 did improve the R^2 agreement with the data (Figure 8.1-16), but the prediction method still was unable to attain the desired (Ta, t_r) intersection. Flange 6 performed the best but lacks any portrayal of a trend. Figure 8.1-16 now shows that isostress lines in the area of the best data are now divergent, so this method can not be used to analyse the materials tested.

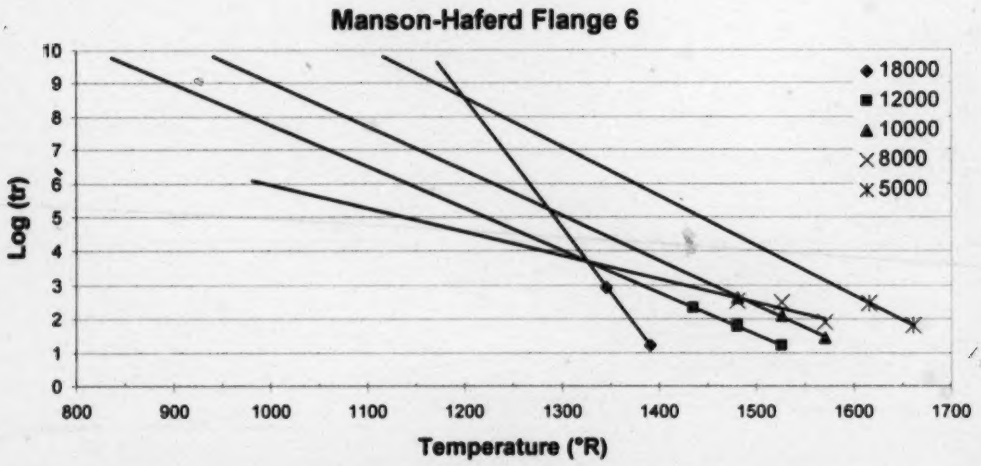

Figure 8.1-16 Mason-Haferd method for Flange 6 showing good statistical R^2 agreement with the data but lack of correlation of isostress lines

8.1.4. Aggregate Parametric Method Results

The parametric methods of creep analysis show that the materials can be grouped into distinct groups. The planar graphitized materials show good correlation with Larson-Miller methods and give extremely optimistic lifetime predictions of 80 million hours at 427 °C. The planar graphitized materials can be identified by the reduction in elongation during long term creep testing. A second grouping can be made based on New Elbow 7, Elbow 7 and Flange 6 which show similar creep behaviour and elongation characteristics and an expected life of 60 million hours. The last grouping contains Elbow1, Elbow 1Weld, and Elbow 4, which only gave a comprehensible creep life prediction of two million hours when analysed under Sherby-Dorn criteria. These numbers are not unrealistic as testing is performed well into the creep temperature domain but operation temperatures are at the cusp of the creep temperature range.

8.2. STRAIN RATE BASED METHODS

8.2.1. Monkman-Grant Method

The piping system in question is unlikely to experience any creep deformation at service temperatures which limits the usefulness of Monkman-Grant analysis. Determining the creep exponent *m* will help in the analysis as it should predict if any of our materials will follow Larson-Miller behaviour. The relationship was tested with both the steady state creep rate (ε_{ss}) and mathematical minimum creep rate (ε_{min}) to evaluate whether the isostress condition holds. The composite Figure8.2-1 is presented to show the considerable amount of scatter to the isostress relationship between materials.

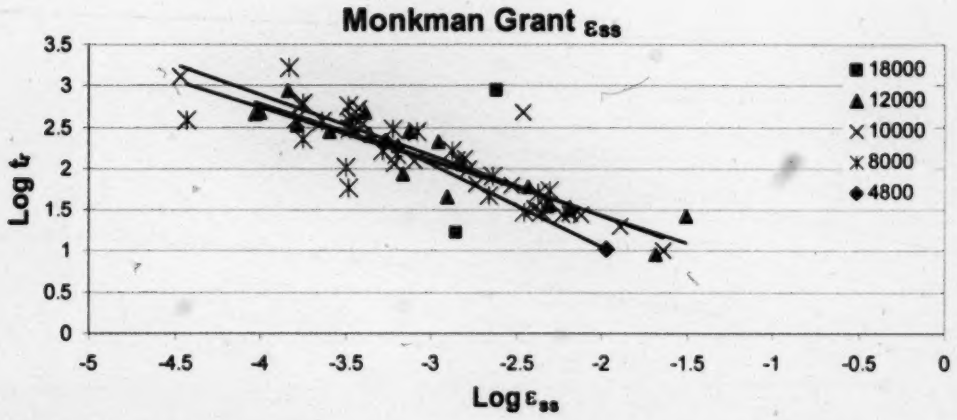

Figure 8.2-1 Composite strain rate based Monkman-Grant relationship showing loose isostress relationship to k=log tr x log εss

Graphing individual materials in tems of Monkman-Grant, similar to of Figure 8.2-1 shows very good R^2 for the isostress lines, although the composite relationship showed significant variation in the data. Ideally a material that displays correlation to the Larson-Miller parameter should show a slope of unity but none of the individual materials

analysed showed a consistent trend for the isostress material constants. Table 8.2-1 shows the variation of isostress constants for both steady state and minimum methods creep rate analysis but no trend arises out of the data.

It was not possible to separate materials out based on this method with the exception of Reducer 3. The reoccurrence of Reducer 3 at 55.2MPa (8000psi), shows a distinct deviation once again due to the unnaturally small values of strain rate over the temperature range. This low strain rate previously posed a problem for the Sherby-Dorn method.

Sample	Strain type	Stress Mpa/psi				
		124.1 18000	82.7 12000	68.9 10000	55.2 8000	~34.5 ~5000
Elbow 1 Weld	ss		0.910	0.948	1.036	
	min		1.091	0.851	8.660	
Elbow 1	ss		0.811	0.915	0.981	0.754
	min		0.795	0.942	0.982	0.709
Reducer 3	ss		0.480	0.745	50.440	1.006
	min		0.863	0.778	29.920	0.952
Elbow 4	ss		1.108	1.014	0.957	
	min		0.964	1.220	0.941	
Flange 6	ss	1.152	0.977	0.883	0.983	1.072
	min	0.968	0.990	0.895	0.973	1.203
New Elbow 7	ss		0.891	0.860	0.567	
	min		0.854	0.829	0.516	
Elbow 7	ss		0.764	1.017	0.944	
	min		0.740	1.014	0.799	

Table 8.2-1 Constant m values as derived from slope of Monkman-Grant Analysis

The wide variation of values derived from the Monkman Grant method has shown that the material has a stability problem. This stability means that most of materials would follow a power law creep pattern, with the exception of Reducer 3 and both Elbow 7

materials which a significant deviation from the rest of the materials consistent with stress analysis of Figure 7.4-4.

8.2.2. Continuum Damage Mechanics

Leckie's analysis of the isothermal creep process gave an accurate determination for materials that follow Larson-Miller and Sherby-Dorn trends. The major limitation of the method is that the minimum test temperature for this data was on average 100 °C over the nominal service temperature. Leckie's method is most suitably conducted near a creep temperature of interest. This combined with a relatively small number of data points for isothermal testing (Figure 8.2-2), can pose problems for some materials.

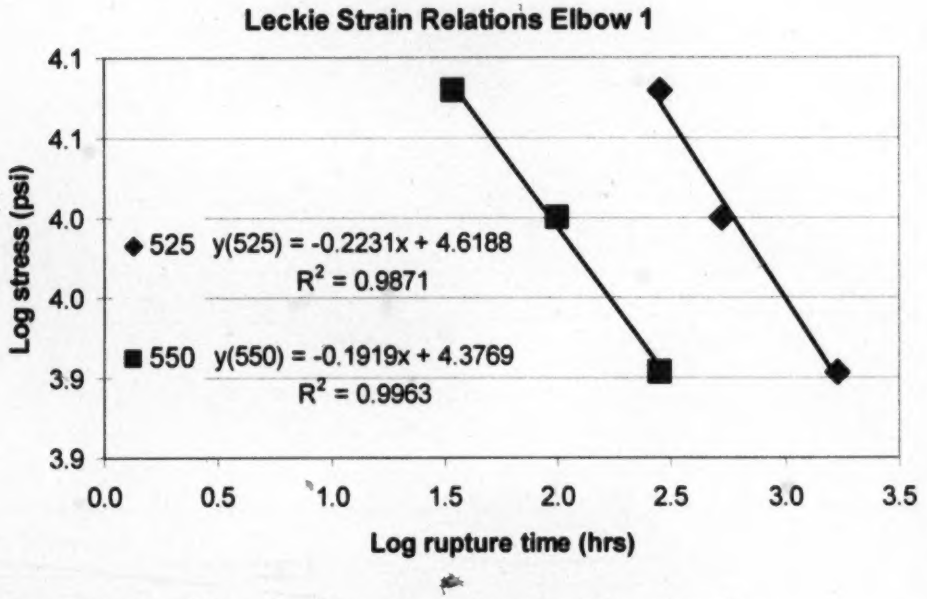

Figure 8.2-2 Isothermal plot to determine continuum damage mechanics values of v.

Table 8.2-2 shows that the trend of damage parameter increases for both 550 °C and 575 °C as one moves down the table. Sorting the data based on 550 °C allows analysis of the data set revealing that on average the damage parameter becomes less negative under the same isothermal conditions ie. -0.16 ranges as compared to -0.20 ranges. The value for Reducer 3, 575 °C does not reflect the trend as there is significant deviation in the plotted values with an extremely low R^2 correlation. The Elbow 7 data set shows distinctly different values of ν, similar to those seen in earlier stress exponent determination, which is expected as the stress exponent data was also determined using ε_{ss}. While the data set is too small to determine the values of stress exponent n by Leckie's method, the damage parameter trend shows that materials have a relationship to the damage parameter. A desired trend of similar slopes as testing temperatures are decreased towards operations temperature was not realized.

	Temperature °C			
Sample	525	550	575	600
Elbow 7		-0.080	-0.095	-0.148
Elbow 1 weld		-0.135		
New Elbow 7		-0.161	-0.172	-0.167
Reducer 3		-0.185	-0.229	-0.165
Elbow 1	-0.223	-0.192		
Elbow 4		-0.198	-0.173	-0.140
Flange 6	-0.196	-0.213	-0.176	

Table 8.2-2 Tabulated damage exponent ν as determined graphically using Leckie's method

The limitation of using this method is that while the value of damage exponent ν can be determined, we can not determine the value of damage parameter ω or the growth characteristics $d\omega/dt$. Determination of a damage function would require some type of information that damage progression could be determined, which cannot be quantified

from the current data set, micrographs or macrographs. An aging experiment to determine growth characteristic of graphite nodules was in progress at the time of writing, which possibly may offer some idea of the damage parameter.

8.2.3. Omega Method

The Omega method had shown promise based on early tests. The key to Omega testing is the reverse creep curve (Figure 8.2-3) must exhibit linear behaviour in the middle of the creep curve at a strain rate of 10^{-6} to 10^{-5} to be a valid test. Although initial testing on Flange 6 suggested that we were close to the strain rate of interest at 7.3x10^-4 per hour, analysis of Elbow 1 at 525 °C and 55.2MPa (8000psi) showed that the material was clearly not conforming to expected predictions. The reverse creep curve for Elbow 1 in Figure 8.2-3 does not even approximate the conditions that we expected to observe. Examining in Figure 8.2-4 shows that the minimum strain rate is achieved between four and five hundred hours into testing. This is significantly different than most creep minimums which occur between 10-20 % of rupture time (Table 7.8-1). In an attempt to generate a valid Omega plot for Elbow 1 material, a test is running at the time of writing that is hoped will conforms to required test prerequisites.

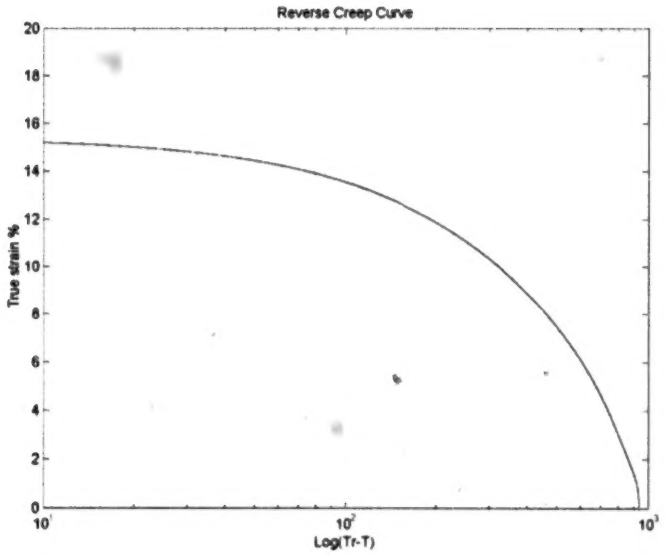

Figure 8.2-3 Reverse creep plot for Elbow 1 showing deviation from linear trend, negating useful Omega analysis

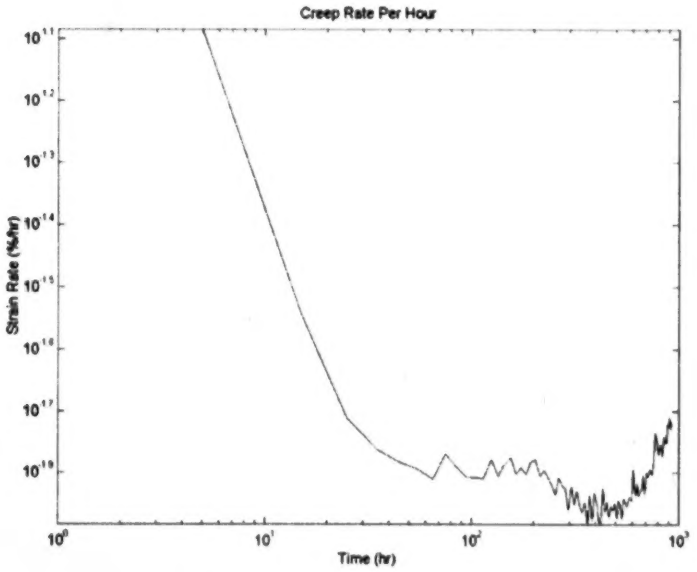

Figure 8.2-4 Strain acceleration for Elbow 1 525 °C 55.2MPa (8000psi) showing minimum creep rate achieved at half of rupture life

9. DISCUSSION

9.1. REPLICATION AND MICROSTRUCTURE

9.1.1. Evaluation of Replication

The cross-section microstructures were significantly different from the surface microstructure established by replication during NDE [1] [2]. For example, the Reducer 3 replication referred to in the schematic as R7, was determined by the inspection company to have little graphite but was affected by planar graphitization [3]. Replication showed that Flange 6 suffered from HAZ graphitization on the flange side but the cross section microstructure determined it to be suffering from base metal graphitization of the forged fitting. The Elbow 1 replication and the cross-section microstructure agreed completely with the inspection report but the claims of HAZ graphitization are disputable (section5.1) (section 7.6.7).

Although a previous replication inspection on E2 had shown a complete lack of graphitization [2], exercising due diligence, the E2 power piping was replaced as a safety measure as the results of this investigation were yet not available. Preliminary E2 microstructure results in Table 5.1-1 showed that the observation of graphitization and fittings was indeed present contrary to the results of the original replication. Inspecting Figure 9.1-1 showed E2 replication performed by accepted industry practice completely missed the presence of graphite, which would have existed at the time of inspection.

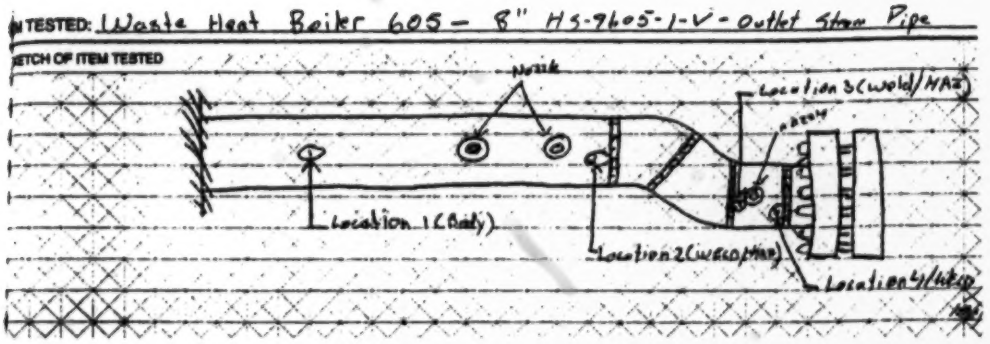
TESTED: Waste Heat Boiler 605 - 8" HS-7605-1-V - Outlet Steam Pipe
ETCH OF ITEM TESTED
Location 3 (weld/HAZ)
Location 1 (Base)
Location 2 (weld toe)
Location 4 (base)

Figure 9.1-1 Sketch of Replication sites of E2 WHB showing locations only taken on piping and adjacent to weld on piping side [2]

9.1.2. Evaluation of Microstructure

The base microstructure is unremarkable beyond the observations in the results. It becomes apparent that any features that would be of interest in the nucleation and growth stage are long since past. The only real question that may be asked when looking at microstructure is: What are future graphite growth characteristics like?

The presence of both random graphite and planar graphite in microstructure needs an explanatory comparison of growth characteristics and why planar graphitization only appears in some areas. The most interesting part is the lack of random graphite in the immediate proximity to the planar graphite but it would be erroneous to presume that if you have one form of graphitization, you will not have the other. Evidence for this is that while the graphite is grown under similar thermal conditions and the hoop stress would be the same, prior external stresses such as bending moments and torsion can not be evaluated after the fact, nor can residual stress from forming operations, but stress states on piping systems across different geometries are well known.

The most disconcerting observation is if the piping in Figure 5.2-1 was constrained, then the presence of planar graphite would have found in fittings that were exposed to a bending moment. This opens the relationship of Furtado and Le May's pictures [35] in Figures 3.4-1 and 4.1-1 which show a failure of a pup off of a steam chest. Could this piping have been exposed to a torsional load which would have precipitated the formation of the planar graphite? If carbon migrates interstitially to areas of high stress concentration to attempt to lower stress, then as the nodules grow the interparticle stress concentration would increase causing a further increase in carbon movement. Is it possible that this could this be the mechanism of formation of planar graphite? This observation may be associated with the piping schematic by Emerson and Morrow [17]. It is unlikely that any other contributing factors would have played as large of a role as external stress.

9.2. ROOM TEMPERATURE MECHANICAL PROPERTIES

Room temperature properties of the material are important for two different reasons. The previously mentioned lower shelf fracture temperature can become apparent during cold start up as the steam condenses to liquid water moving at high velocities in the piping leading to a condition known as slugging. This necessitates a material that has good mechanical properties and toughness. The second reason is that all fitness for service testing is performed at ambient temperatures; therefore the method must reflect the high temperature properties even though testing is performed at ambient temperatures.

9.2.1. Hardness as a Fitness For Service Method.

Hardness testing has been successfully correlated with mechanical properties for many material systems. The mechanical strength is often used as it is quick and easy to obtain reasonable properties in a minimum of time. However, the classic methods of estimating material properties based on hardness show severe limitations for hardness based property extraction for materials in this study. The Microdur hardnesses observed during NDE [1] [2] demonstrated no correlation to any observations in this investigation but investigators such as Endo [94] have found useful hardness relationships in the past for Cr-Mo materials.

9.2.1.1. Hardness relationship to tensile strength

Figure 9.2-1 attempts to demonstrate tensile strength measured against surface hardness methods, using surface preparation methods that would be used in the field. The classic relationship for Brinell hardness and tensile strength is plotted for reference, but the observed Brinell hardnesses show little to no correlation. Only two points at the low end of the ultimate tensile strengths for the experimentally obtained Brinell hardnesses even came close to the theoretical values, but with the scatter in hardness values obtained, this result could be erroneous. The Brinell hardness does show enough of a variation of slope over the tensile values that the method could be used to separate out materials that are hard and have a higher tensile strength from materials that are soft and weak. This would allow separation of Reducer 3 and Flange 6 form the rest of the materials.

Statistically both Brinell hardness and the Rockwell B hardness were able to demonstrate a similar poor linear relationship, but the Vickers hardness and the superficial Rockwell method show no relationship to either ultimate tensile strength or the slope required to make a correlation to the ultimate tensile strength.

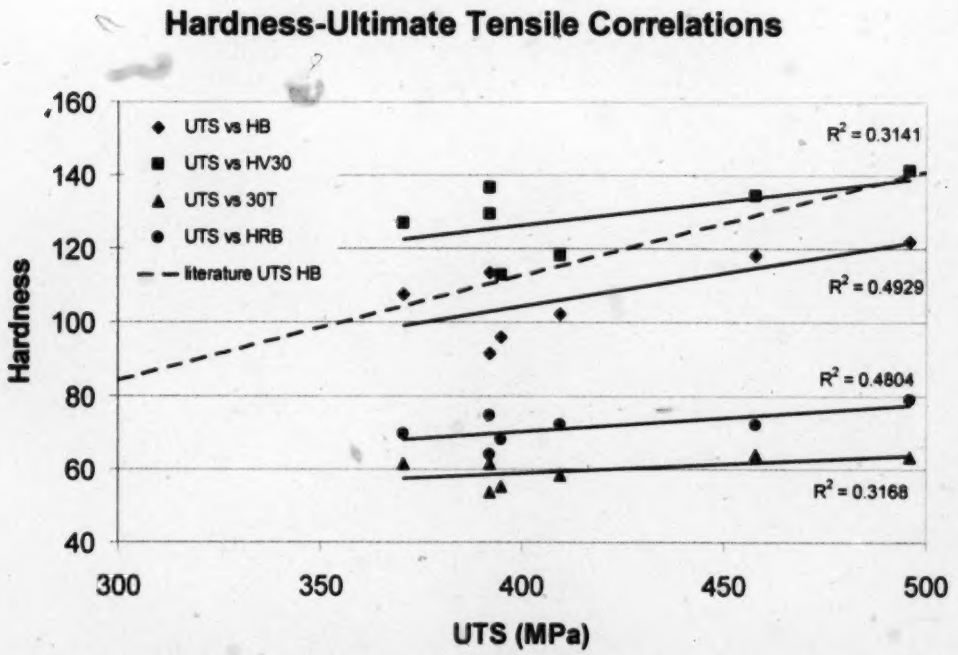

Figure 9.2-1 Relationship between selected hardness methods and ultimate tensile strength. Theoretical Brinell hardness is plotted to give a reference trend. Planar graphitized Reducer 3 is found at 460 MPa while Flange 6 is shown at 495 MPa.

9.2.1.2. Alternate hardness relationship to tensile strength

If average properties are thought to influence the results we can look at the raw hardness and tensile data. The plot in Figure 9.2-2 shows HRB hardnesses taken from the neck of the tensile samples prior to testing; that show the sensitivity of the method is significantly worse than the comprehensive hardness survey in Figure 9.2-1. The surface would be

closer to midwall microstructure due to the maximum material condition of the tensile specimens.

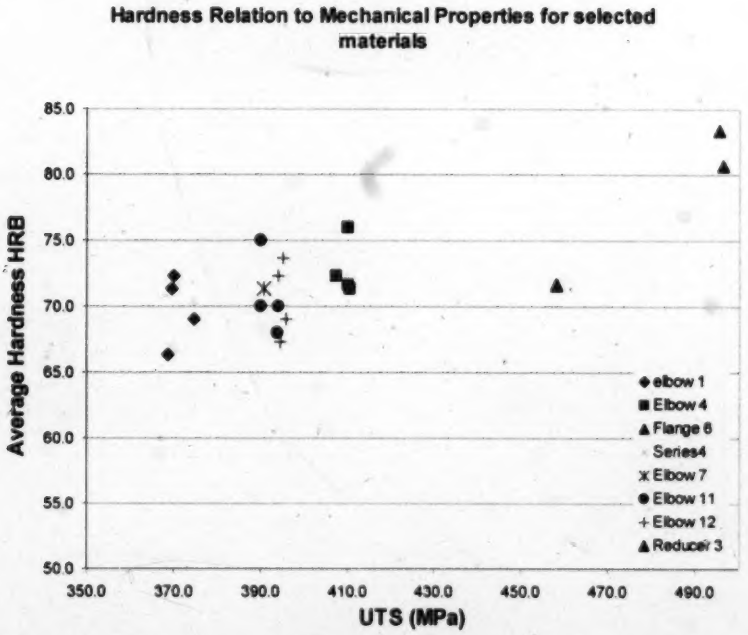

Figure 9.2-2 Raw data showing scatter for all three HRB hardness tests taken on each tensile test sample. Due to scatter in the results, only Flange 6 at 495 MPa would be distinguishable from other materials

Analysing the raw data from the actual tensile sample showed the excessive hardness scatter values obtained from each tensile test sample damages the results. Without the smoothing effect of averaging, the overall hardness error has increased from the hardness relationships explored in section 7.3. The net result is that the randomly graphitized elbows overlap the entire hardness range across the UTS range, which will not allow separation of materials.

9.2.1.3. Yield strengths relationship with hardness

Exploiting the elastic plastic behaviour of a material, the alternate rule of thumb relationship is the relationship of yield strength and Vickers hardness. The relationship

shown in Figure 9.2-3 is not related to either the empirical trend, nor is there a relationship between methods or even the same types of materials. Once again, a conclusive relationship cannot be draw as the hardnesses of the materials shows excessive scatter. Just as with Brinell hardness trend shown in Figure 9.2-1, the theoretical yield strength trend to Vickers hardness relationship in Figure 9.2-3 does not reflect the hardness trends of the service exposed materials. Based on the evidence, the service exposed carbon steel shows very poor correlations between hardness and yield strength properties.

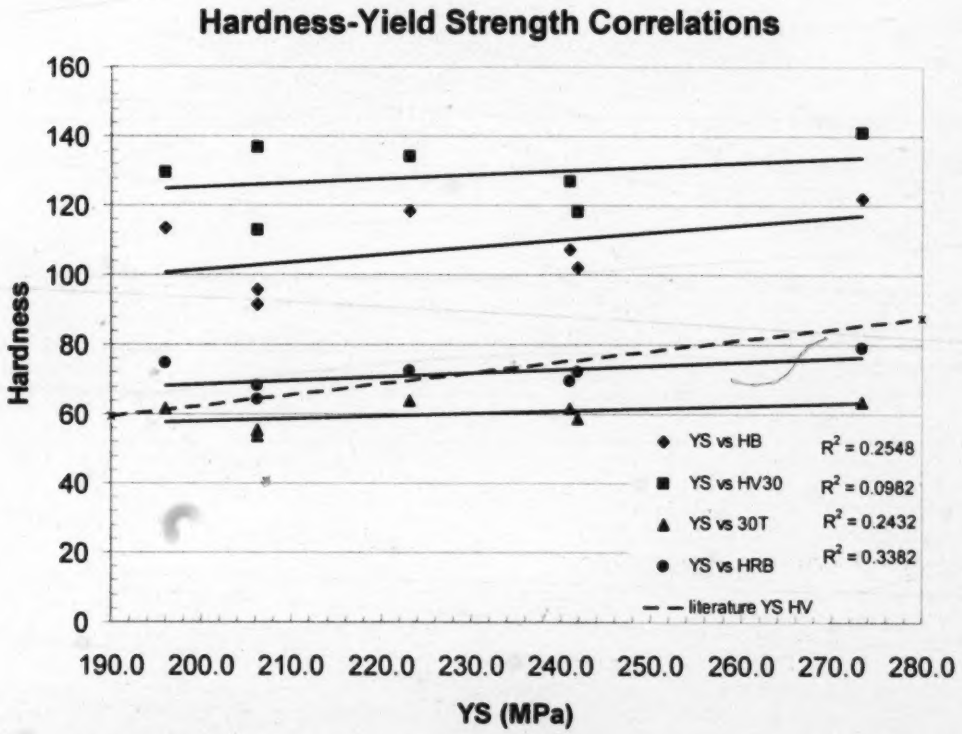

Figure 9.2-3 Relationship between selected hardness methods and yield strength. Theoretical Vickers hardness is plotted to give a reference trend. Planar graphitized Reducer 3 is found at 240 MPa while Flange 6 is shown at 275 MPa.

9.2.1.4. Hardness relationship to room temperature ductility

In Figure 7.4-1 elongation separated the materials based on their ranking according to the relationship of ultimate tensile strength. The elongation was based on ductility ranking in order of increasing ductility starting with the low ductility Flange 6 followed by Reducer 3, followed by the group of Elbows 4,7, 11 and 12 and finally Elbow 1 showing the most ductility. The observation is consistent as higher strength ferritic materials are associated with lower ductility.

While the relationship between elongation and ultimate strength in Figure 7.4-1 may not be directly exploited for NDE purposes; Figure 9.2-4 shows the ductility reducing the materials to four distinct groupings and a trend for the relationship with hardness using Brinell hardness evolving. The groupings of Flange 6, Reducer 3 followed by all the elbows, save Elbow 1, which comes last, give a distinct separation. Since the relationship is the same sequential relationship as Figure 9.2-4; the Brinell hardness starts to show enough sensitivity that by drawing the conclusion that if the material is hard and shows low ductility we should be able to separate the planar graphitized Reducer 3 from the random graphitized elbows. Unfortunately we can not validate the method with current elongation data due to the non-standard gauge length but the use of hardness to infer elongation would be valid for this method.

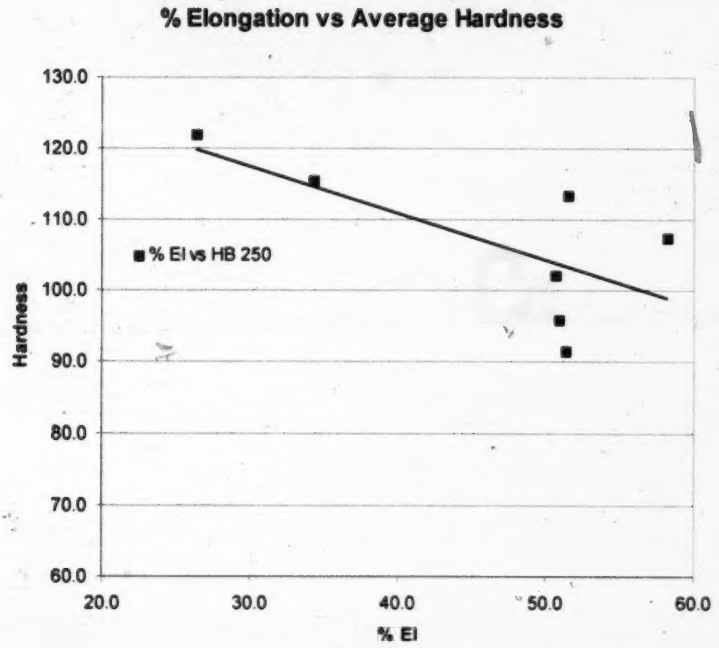

Figure 9.2-4 Brinell hardness relationships with respect to ductility showing poor correlations but reasonable groupings. The planar graphite shows relatively hard microstructure and is associated with the low ductility grouping

9.2.2. Comparison of Elevated and Room Temperature Mechanical Properties

It is important to know if the room temperature test conditions reflect service conditions so the limited hot tensile testing data set allowed some comparison of properties. Comparison of two material types at the extreme ends of test data at both room temperature and service temperature (Figure 9.2-5) show unexpected changes in properties.

The overall performance was marked by the expected loss of yield strength and tensile strength. The elbow materials suffering advanced microstructure decomposition maintained similar performance for both the elevated temperature and room temperature

testing. The only characteristic that changed for Flange 6 was that the elevated temperature ultimate tensile strength was achieved with very little elongation. Figure 9.2-5 also demonstrates the termination of load carrying capacity of the materials was quite abrupt for flange materials at both high temperatures and at room temperature which is quite different from the gradual and significant reduction in load carrying capacity that may be observed from Elbow 1 material. Since the overall ranking of the materials tested at service temperature has not changed from the room temperature results, all ambient temperature hardness trends can infer high temperature mechanical strength

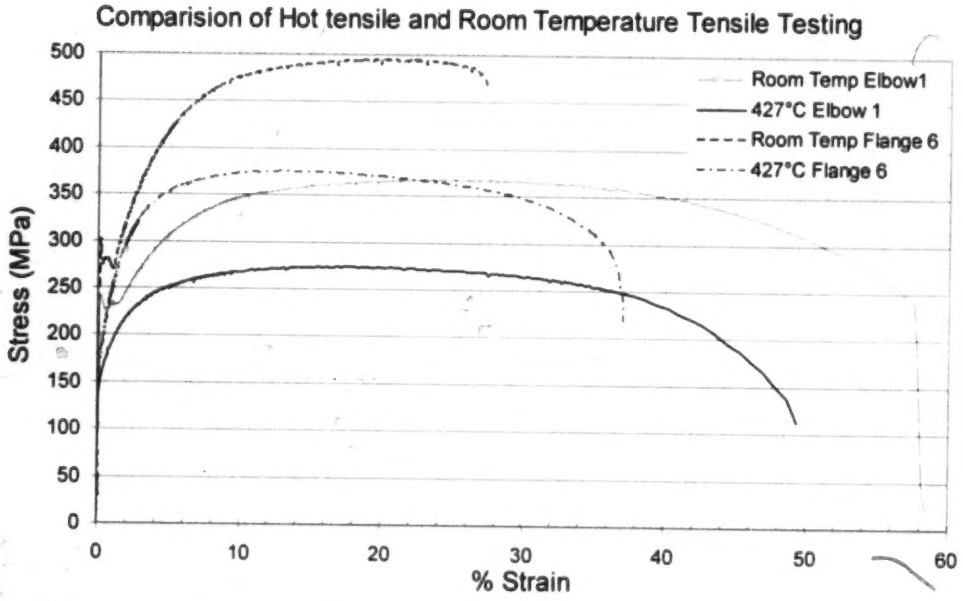

Figure 9.2-5 Change in tensile properties with temperature for Flange 6 and Elbow 1. This comparison shows the significant loss of strength with increased temperature. The apparent changes in ductility are not convertible due to different gauge lengths used at the different temperatures.

A decisive conclusion can not be drawn by comparing tensile properties, but the forming method would be expected to make a significant performance difference on graphitized

materials with similar volumes of graphite. From the similar mechanical performance of random graphitized elbow materials, at both ambient and elevated temperatures, it may be inferred that they will not lose strength catastrophically.

9.3. EFFECT OF GRAPHITE ON MECHANICAL PROPERTIES

9.3.1. Effect of Analysed Carbon Content on Tensile properties

Classic literature can show that the strength of carbon steel can always be linked to the carbon content. Figure 9.3-1 shows agreement with theory with the exception of the ultimate tensile strength of planar graphitized Reducer 3. There will be some variation in this type of analysis due to the effects of grain size but the strength of graphitized carbon steel is certainly associated with carbon content.

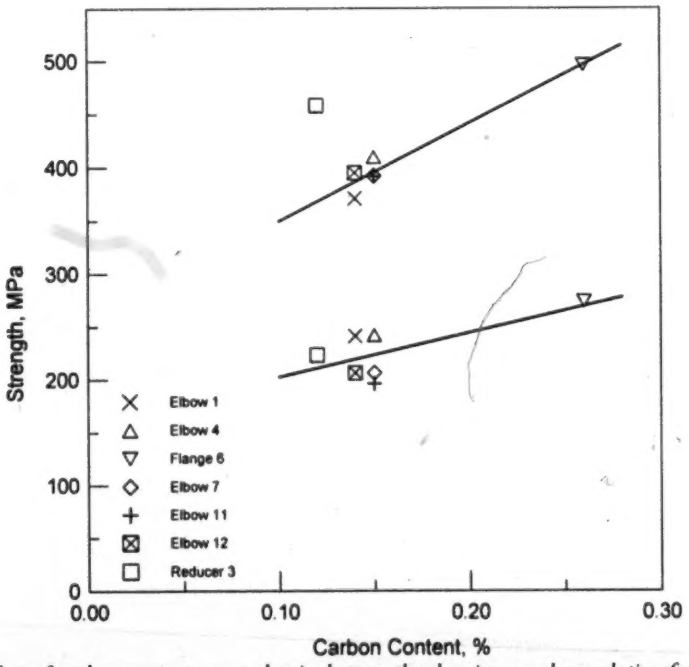

Figure 9.3-1 Effect of carbon content on mechanical strengths showing good correlation for ultimate tensile and yield strength with the exception of ultimate strength of planar graphitized Reducer 3

9.3.2. Effect of Graphite on Tensile Properties

Figure 9.3-2 shows the relationship of graphite with tensile strength. The graphite was analysed with respect to wall location, orientation and bulk volume of graphite. The groupings are based on trends observed during tensile testing with Elbow 1's low strength followed by Elbow 7, 11, 12's slightly better strength. Elbow 4 shows that its graphite volume is clearly not related to ultimate tensile strength. The high strength and low volumes of graphite associated with Reducer 3 and Flange 6 then confirm there is no correlation of graphite volume to tensile strength. This trend was consistent regardless whether the sample locations were separated into by wall location, orientation or a composite value was used. Figure 9.3-2 shows that the graphite volume does not have a distinct effect on ultimate tensile properties.

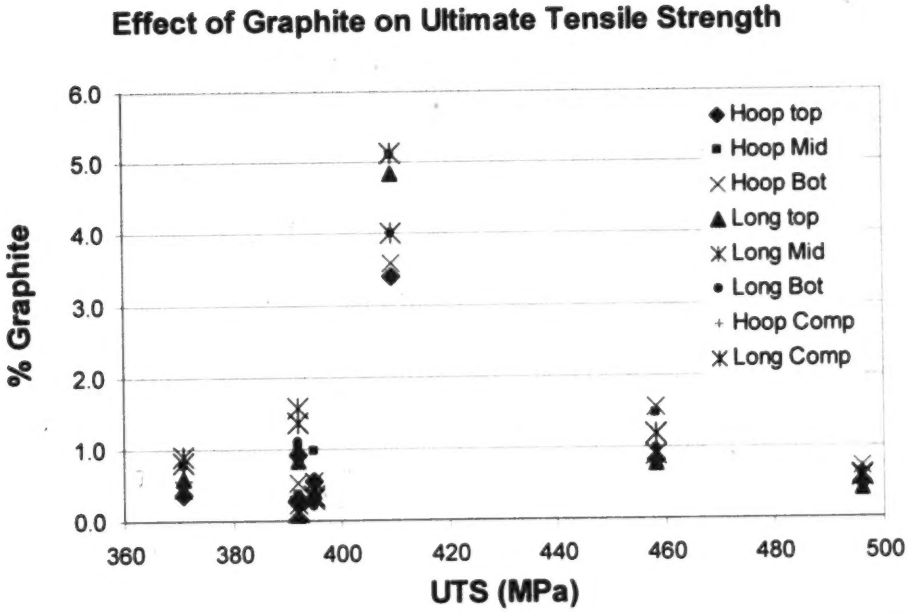

Figure 9.3-2 Relationship between volume percent graphite and average ultimate tensile strength. The planar graphite shown at 460 MPa cannot be separated from the other materials as the volume of graphite overlaps

Although a similar trend would be expected using percent elongation as the independent variable, Figure 9.3-3 shows a significantly different grouping of materials. The first group is forged Flange 6, the second group is Reducer 3, followed by the largest grouping containing Elbows 4, 7, 11 and 12 and the last group Elbow 1. The variation of elongation shows only four groupings of material, but the graphite volume fraction covers most of the elbows which precludes exploiting the phenomenon entirely. The grouping now includes all the random graphitized elbows, save Elbow 1, into a cohesive group giving the only method of reducing the number of types of materials. Although the material is now separated into usable groups, the materials cannot be separated based on amount of graphite due to the overlap of the graphite volumes.

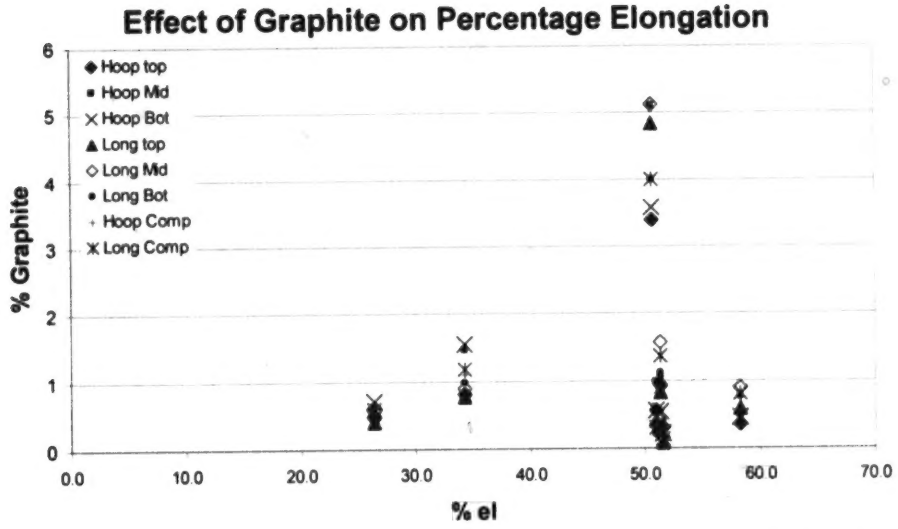

Figure 9.3-3 Relationship between room temperature elongation and graphite volume The Planar graphite at 35 % cannot be separated from the other materials as the volume of graphite overlaps.

9.3.3. Effect of Graphite on Hardness Properties

One of the original goals of this research is to develop a relationship between hardness and volume fraction of graphite based on the assumption that there should be a linear relationship to softening as the microstructure degrades (section 4.5.3). The relationship between graphitization volume and hardness is dubious at best and from this study the only industrially accepted method that showed promise for this material was Brinell testing. This study indicates that a weak relationship may be developed using the Brinell hardness to separate the material shown in Figure 9.3-4. The Brinell data separates the planar graphite from most of the random graphitized data. The series in Figure 9.3-4 starts from the left with randomly graphitized Elbows 7, 12, 4, 1 and 11 and then finishes with planar graphitized Reducer 3 and finishes with random graphitized Flange 6.

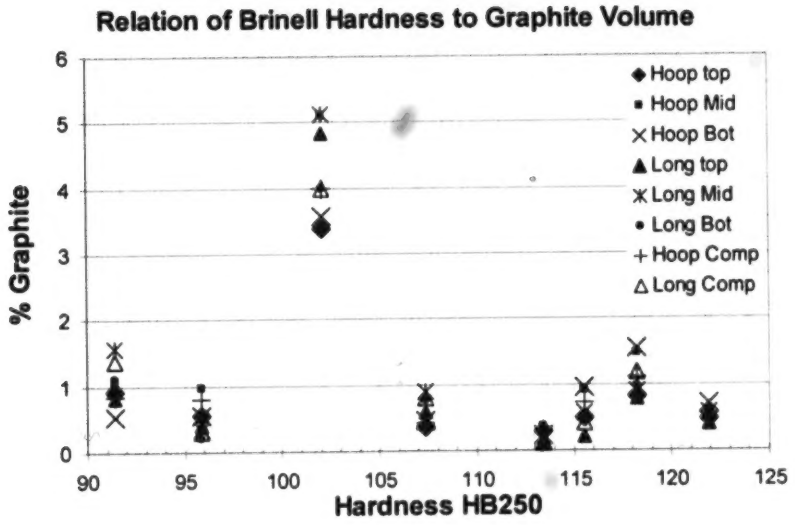

Figure 9.3-4 Relationship between hardness testing and degree of graphitization The series starts from the left with randomly graphitized Elbows 7, 12, 4, 1 and 11 and then finishes with planar graphitized Reducer 3 and finishes with random graphitized Flange 6

Based on results of Figure 9.3-4, all materials with a hardness exceeding BH 115 would be rejected. This would not separate the random graphite from planar graphite due to different hardnesses associated with different manufacturing methods, but the presence of graphite and the indication that the matrix is hard would indicate the possible existence of planar graphite rather than random graphite. Since the forming method has an influence on hardness, separating based on higher base metal hardness can not separate Flange 6 from Reducer 3. Furthermore the method could only be used if there is significant degradation of the microstructure which is associated with base metal graphitization. The method would not be able to help or assist in cases of suspected HAZ graphitization nor would it be useful at this stage for materials other than carbon steel. The rule would only be useful when replications indicate graphite and hardnesses indicate higher relative Brinell hardnesses, limiting the observation to service exposed materials. It must be

remembered that a new elbow showed a BH 250 baseline hardness of 138.2 with zero scatter but has no graphite.

From a material science point of view, it was hoped that the superficial test methods would offer a separation method. The superficial HR30T method did separate out the planar graphite from the rest of the materials when average values are plotted but the variation of the hardnesses would overlap the values from Flange 6 materials. This would mean that the HR30T method could only make an analysis similar to the proposed Brinell hardness method. The results of the hardness survey show when performing field hardness tests to check for material degradation in service exposed material, that hardness test method are inconvertible and the correct hardness method must be used to both, show evidence of service degradation and determine morphology of graphitization if present.

9.4. DETERMINING GRAPHITE MORPHOLOGY FROM MECHANICAL PROPERTIES

9.4.1. Separating out Planar Graphite

After all measurable properties are considered, the only phenomenon that are exploitable for determining separation of random and planar graphite are the ultimate tensile strength, elongation and potentially Brinell hardness. The difficulty of determining mechanical properties without taking a material out of service can only be overcome with the small punch test [90] [91] [92]. The small punch test can be adapted as methods are available to remove very small sections of metal for fabricating the disc [93]. The hollow left from sampling with these sampling methods would expose the graphite in the base metal that

does not come to the surface to replication techniques. The planar graphite associated with weld graphitization could also be exposed in detail to avoid false positives that were associated with surface replication.

9.4.2. Separating out Quantities of Random Graphite

Using the varying quantities of random graphite in the materials as an evaluation technique was not able to give any hard evidence on the material's mechanical performance, but the presence of varying quantities of graphite in the original replications, although erroneous, allowed identification of suspect materials. Analysis of the original replication reports [1] demonstrated that the presence of graphite may be detected but replication does not allow verification of the type of graphitization nor the breakdown between random or planar graphitization. Cross section micrographs can determine type and morphology of graphite but none of the mechanical tests explored in this research could determine graphite morphology.

9.4.3. Detecting Extent of Graphitization

The neutron scattering experiment, although it failed as an analytical technique for the materials in this study, allowed us to examine the problem of detecting graphite in more detail. Detecting graphite using NDE has proven to be a difficult task. The methods that are in common use seem to be of limited use but some of the mechanical properties such as elongation could be exploited using small punch testing to solve problems of determining the extent of graphitization. The obvious choice of field X-ray would pose particular problems as the source is bright and hard to control for the small defect size. It

was suggested to use Time Of Flight Diffraction (TOFD) as a potential ultra sonic detection method, but an extensive project in TOFD research was beyond the scope of the project. The only proven NDE recommendation from this investigation is to focus on doing replications in susceptible areas and backing the replications up with Brinell hardness testing.

9.5. EFFECT OF GRAPHITTE ON FRACTURE PROPERTIES

An investigation into the lower shelf performance was intended to show if the presence of graphite changed the fracture characteristics of a material that had been rendered very ductile by high temperature service conditions. Although including the planar graphite into the fracture investigation would have been revealing, material shortage dictated that only crack propagation potential of the worst performing random graphitized material could be investigated. The fracture properties for Elbow 1 showed that the material was very damage tolerant by its damage characteristics but was unable to generate valid J integrals. The fact that the graphite nodules did not affect the ductile tearing characteristics gives a measure of security, in spite of the lack of quantitative evidence to support the observations. Base metal random graphitization is inherently safer than HAZ and planar graphitization as the domination of ductility characteristics mean that growth of a defect into a growing crack is unlikely.

The presence of planar graphite and the propensity of continued plane growth until linkup should be investigated, but, from this study, the detection of the mere presence of planar

graphite is sufficient reason to remove it from service. Based on the planar graphite morphology shown in Figure 7.2-8, if the planar graphite linked to form a crack like defect, it would require twice the stress to propagate a crack as the HAZ graphite type morphologies which intersect the surface. Visual comparison of Figure 7.2-7 and Figure 7.2-8 to a prior failure in Figure 3.4-1[35] give evidence of domination of the fracture characteristics of planar graphitization over all methods of testing. Base metal planar graphitization is inherently safer than HAZ graphitization as the presence of the planes on the surface is unlikely which means that the basic opening of a defect into a growing crack is much more unlikely.

The high temperature fracture characteristics remain unknown and should be investigated as temperature does seem to have an effect on ductility and in this case should have a bearing on fracture characteristics.

9.6. EFFECT OF GRAPHITE ON CREEP

9.6.1. Creep Interaction

Does creep at the cusp of operational envelope determine mechanical behaviour? The question is of primary importance in determining fitness for service. As the only quantitative method of measuring time dependent high temperature material performance it has been insightful into material properties.

9.6.1.1. Stress Sensitivity

A basic assumption with this material is that it will not have structural stability with the presence of graphite nodules. It is reasonable to assume that a weak, ductile material with large flaws will tend towards plastic collapse at high stresses, so the determination of the stress sensitivity should have given an indication of the material's behaviour during high temperature operation. To generalize, a high stress sensitivity value can be equated with low ductility in a material and conversely low stress sensitivity with high ductility. Both the t_r and ε_{ss} based methods noted Elbow 1 as having the lowest stress exponent and this corresponds with very high ductility in both the hot tensile and room temperature tensile testing. Based on this observation the ε_{ss} results can be re-examined for other materials. These results would then show that the Reducer 3 material which exhibited an exponential stress relationship in this testing regime would have low ductility, as was observed.

If Prager's [70] philosophy that one of the fundamental characteristics of creep resistance is that of a materials ability to resist strain damage, then the stress exponent differences between materials such as Elbow 1 and Reducer 3 material would have shown a difference in behaviour which would allow culling the planar graphitized material but this could not be conclusively established.

9.6.2. Parametric Method Results

While the parametric methods are easy to collect and analyse without the advanced data collection and analysis techniques required for strain based methods, the wide variation in

results do not add credibility to their use for materials separation. Trying to analyse service aged materials that formerly had uniform properties, and now act as separate material types each responding to a different parametric method, complicates the analysis, therefore only allowing loose generalities to be drawn.

9.6.2.1. Larson Miller Parameter behaviour

While two creep material grouping gave credible life prediction results, there is a wide variation in correlation with mechanical testing properties. The most often quoted is the relation to tensile properties.

The first creep grouping containing Reducer 3 has an absolute correlation to high ultimate tensile strength and low elongation. The first group also responded well to hardness testing methods with a relatively hard matrix which was reflected in both tensile testing and creep testing. The perception of long service lives with HAZ graphitization was also observed by Wilson [18] but Wilson only produced figures in terms of rupture times and stress which offered no correlation to current test methods.

The second creep grouping would be Flange 6, Elbow 7 and New Elbow 7 which tend to follow Larson-Miller behaviour but show some divergence in the relation. While flange 6 has mechanical properties that can be related to Reducer 3, neither Elbow 7 and New Elbow 7 materials has tensile, yield or elongation properties that can be related.
The third creep grouping showed no relationship to Larson-Miller behaviour but showed a tendency to correlate with Sherby-Dorn behaviour. In short, based on this study there is

no effective method of correlating the mechanical properties to Larson-Miller parametric creep properties.

9.6.2.2. Sherby-Dorn Parameter Behaviour

The third parametric creep grouping contained materials that analyse best under Sherby-Dorn criteria. While the Elbow 1, Elbow 1 weld and Elbow 4 materials offer some correlation to creep properties, they are divergent with respect to mechanical properties.

The Flange 4 materials behaved poorly in both tensile testing and hot tensile testing with less than 40 MPa difference in both tests. This sounds reasonable, but the group also overlaps with materials from Elbow 7, 11 and 12 with Elbow 4 at the top extreme of the mechanical properties grouping, rather than Elbow 1 whose creep properties it shares.

The only significant correlation for materials that respond to Sherby-Dorn analysis is that Elbow 1 material was extremely ductile in both tensile and creep testing. While no material from Elbow 1 weld was available for tensile testing, the creep testing ductility was mainly associated with elongation of elbow material in the reduced area of the specimen as the matrix was very soft compared to the piping and weld material.

9.6.2.3. Strain based creep observations.

The poor results of Omega method at temperatures of interest left the Monkman-Grant method as the only available method of attaining a viable result for strain methods. The

Continuum Damage method and White-Le May strain based methods were also tried, but the failing of most strain based methods is that the assumption is that the life limiting factor will be strain deformation. The Continuum Damage method could be analysed in terms of finding the exponents but lack a defect growth relationship to allow a time factor to be derived. The Omega method is the only accepted method that can directly convert strain to time as the life limiting factor. Development of the strain based Sherby-Dorn analysis in this investigation, could offer similar results.

Although the Monkman-Grant method shows us the creep exponent *m* suffers instability, the material should be capable of being analysed under Larson-Miller criteria. The stress exponent *n* showed significant scatter but reasonable correlation to Larson-Miller for most of the service exposed materials. This indicates that the creep exponent *m* is valid. The highlight of Monkman-Grant observations is the deviation of the planar graphitized Reducer 3 from the rest of the data.

9.6.2.4. Chemistry/Creep relations

While hard to quantify, a creep relationship with chemistry in absolute terms, one may observe that the presence of aluminium in quantities over 0.01wt % does appear to have an effect on the stress rupture life. On the other hand, the presence of sulfur in the observed quantities did not appear to have any effect on the creep life even though it was observed segregated to the center of the weld in creep tested Elbow 1 weld. It is unlikely that chemistry played a significant role in causing graphitization and there is not enough evidence to support field spark analysis as a NDE tool.

9.6.2.5. Mechanical property creep rankings

The competing factors of mechanical properties and creep properties allow analysis in terms of relative rankings in their respective groupings. One may observe in Table 9.6-1 that the best tensile properties did not result in the best creep properties, as Flange 6 had similar creep properties to the Elbow 7 type materials. Alternately Elbow 1 consistently scored at the bottom of the rankings. The heavily graphitized Elbow 4 showed better mechanical strengths than most materials tested but it's poor creep performance under stress shows lack of high temperature structural integrity.

The most radical difference in creep testing was the observed strain to failure relationship for planar graphitized Reducer 3 which showed radical differences in strain capacity for the long term tests in Figure 7.7-5.

	Test method			
Ranking	Tensile	Isostress Creep	Isothermal Creep	LM Creep
Group 1	Flange 6	Reducer 3	Reducer 3	Reducer 3
Group 2	Reducer 3	Flange 6 New Elbow 7 Elbow 7	Flange 6 New Elbow 7 Elbow 7	Flange 6 New Elbow 7 Elbow 7
Group 3	Elbow 4 Elbow 7 Elbow 12 Elbow 11	Elbow 4 Elbow 1 Elbow 1 Weld	Elbow 4 Elbow 1 Elbow 1 Weld	Elbow 4 Elbow 1 Elbow 1 Weld
Group 4	Elbow 1			

Table 9.6-1 Subjective rankings of materials based on stress rupture performance

When materials are operated on the cusp of competing design factors, the decision may well have to be based on possible out comes if a material continues to degrade. Using the

results of Furtado and Le May [35], it would be useful to additionally rank the materials based on their fracture properties, especially since no samples of planar graphitized material was available to test.

9.6.2.6. Importance of the creep results

One difficulty with studying a material operating on the cusp of creep regime is to know how much weight to place on the results of the creep testing, especially with the potential for growth of the nodules into crack-like flaws despite evidence of acceptable elevated temperature mechanical properties. While many cases of planar type base metal graphitization have been documented, no failure cases of random type base metal graphitization have ever been observed. Furthermore there have been no published failures attributed to creep failure for either type of base metal graphitization. The generalizations available from analysis of the time dependent failure do show that the effect of time at temperature will contribute greatly to the overall failure mode of the random graphitized failure but there has been no evidence that creep testing can show the detrimental potential offered by planar graphitized materials.

10.FUTURE WORK

Of primary importance to this material problem is whether or not the graphite nodules will continue growing and, if so, at what rate? Since the investigation has taken place on materials long after the nucleation of the nodules; investigating the potential for nodule growth is recommended, such as the current effort outlined in section 9.5.

This testing in Section 9.5 is designed to measure temperature effects of graphite growth and has been running since July 2004. Since the effect of both applied stress and environmental stress cannot be positively accounted for. Several random graphitized material samples and a new material control sample have been put in furnaces at 550, 600, and 650 °C. If the graphite grows significantly in this test, it can be confirmed that temperature drives the growth and formation of the nodules. If the graphite nodules do not grow significantly, then it is more likely that the mechanism is stress activated and thus, further study could possibly give an understanding of the role of stress in planar graphitization.

The continuation of development of nodule growth data would allow evaluation of the material in terms of $d\omega/dt$ using Continuum Damage mechanics work that was performed in this investigation. It may be necessary to expand the experimentation to represent a more complete scope, such as stress and temperature, acting with or without synergistic effects.

If a section of planar graphitized carbon steel base material can be found, a full fracture testing regime and stress analysis should be tried to understand the necessary criteria that leads to failure

The ability to detect graphite using NDE techniques is of paramount importance to the early detection of graphitization. Thus, the development of alternate NDE methods such as TOFD or possibly an X-ray technique would be required to allow for more accurate in depth analysis of suspect areas.

If it is economical, replacement of graphitized elbows in service exposed piping is a possible remediation method. Ideally the joining process should not use overmatched weld metal. Sections of left over A106 piping from E2 could be welded to new fittings and weld procedure qualified to comply with Alberta Boiler standards.

The observation that ε_{ss} could be used interchangeably with t_r in Sherby-Dorn analysis should be developed to find out if it would make an alternative short term test to Omega method. A master diagram could be generated very quickly as a creep frame could generate more results for a given time.

11.CONCLUSIONS

11.1. CHARACTERISTICS OF MICROSTRUCTURES

a) Plain carbon steel materials for high energy service that have been graphitized in service have significantly different mechanical and creep properties than graphitized Cr-Mo steels, as they lack the more stable carbide formation of alloy steels.

b) The chemistry of all the sections being evaluated meets the minimum requirements stated in ASME SA186-77.

c) The degree of spherodization does not correspond to the degree of graphitization

d) Spheriodization and carbide coarsening occurred in the entire piping system, but graphitization was primarily found in piping sections with non-uniform geometries such as reducers, elbows, and flanges.

e) Graphitization is consistently more significant at mid wall section than at the surface. Within 0.5 mm range to the surface, graphitization was either very benign or completely absent even when severe graphitization exists in midwall.

11.1.1. Planar Graphite

a) Planar graphite was found in sections that were subjected to severe mechanical loading during service. Planar graphitization in this investigation was not observed in the heat affected zone, as normally believed.

b) The observed length of planar graphite on a sectioned surface can be several mm long and is oriented various directions. The current two dimensional

microstructure characterization could not yield absolute direction and orientation of graphite planes

c) The formation of planar graphite does not preclude the formation of random graphite.

11.1.2. Random Graphite

a) Strong segregation of graphite particles along pipe direction was observed in many sections with random graphitization.

b) The formation of random graphite does not preclude the formation of planar graphite.

c) Although no absolute direct links have been found yet, it appears that random graphite is associated with undesired external stress as it is generally found in areas of higher stress intensity.

d) Manufacturing method of carbon steel materials appears to have influence on the nucleation of random graphite

11.2. FITNESS FOR SERVICE RECOMMENDATIONS

11.2.1. Short Term Mechanical Properties Assessment

a) Depending on degree of material degradation, some sections being evaluated had mechanical properties below the design requirements of API 530.

b) The mechanical properties of pipes and elbow are related to analysed carbon content, and generally follow a trend consistent with that reported in classic literature.

c) Reducer 3, however, showed significantly stronger strain hardening and higher tensile strength as compared to elbows of similar chemical compositions.

d) For sections of similar analysed carbon content, graphitization less than about 4% does not cause noticeable reduction in mechanical properties.

e) Different hardness testing methods were adopted or assess various sections of pipe. Indentation methods showed significantly less scatter than indentation area based methods. However, values of hardness testing yield poor correlation for both hardness and yield strength. The only method that showed ability to make a distinction between graphitized samples was Brinell hardness.

11.2.2. Residual Life Assessment

a) All sections being assessed had a remaining creep life greater than 63% of service life consumption as defined in ASTM DS11S1. A number of sections that were evaluated showed little reduction in remaining creep life as compared to the average new material condition as defined by ASTM DS 11S1.

b) For material with similar analysed carbon content, there exists a correlation between remaining life and room temperature tensile strength but poor correlation with yield strength and remaining life. In general, the materials with markedly higher room temperature tensile strength exhibited better creep life

c) Materials possessing higher analysed carbon content and higher tensile strength did not yield better creep rupture lives indicating that creep service lives would be similar to other materials.

d) There was no conclusive creep rupture evidence that that the presence of graphite volumes less than 4 vol.% degraded expected creep lives regardless of morphology. However, the presence of aligned graphite nodules was observed near rupture failures. This suggests the inherent danger of planar graphite, which can not be judged based on volume concentration.

e) Although creep was determined not to be the expected failure mechanism, other graphitization sensitive failure mechanisms are possible, especially in the case of planar graphite, and should be investigated.

11.2.3. Operation and Inspection Recommendations

a) Temperature excursions over 427°C are unacceptable for graphitized carbon steel. If the process requires that carbon steel be operated over 427°C, a change to a Cr-Mo piping system or piping with at least 1% Cr should be made.

b) Investment in pipe stress analysis to determine areas of stress concentrations should be made and any areas of stress concentration mitigated.

c) Special attention during NDE inspections must be given to piping sections with non-uniform geometries such as elbows and reducers, where graphitization is likely to occur

d) Surface replications may not indicate the internal severity of microstructure graphitization and should be interpreted with caution. Only mechanical testing and microstructure were able to conclusively demonstrate extent of graphitization

e) For the piping materials investigated, hardness was of limited value for prediction of graphitization. If hardness testing is performed, a test which uses a large load

and large spherical indenter to reduce effects of heterogeneity of material must be used. No hardness conversions can be allowed.

f) While tensile testing and microstructure are recommended as a preliminary graphitization assessment technique, the viability of Small Punch testing as a viable NDE Fitness For Service technique for graphitization should be investigated.

12.REFERENCES

[1] Canspec. (1998). "Insitu Metallography of WH605 Steam Outlet Piping." *EDM-98-06-13127*, Canspec Material Engineering, Edmonton.

[2] Canspec. (2001). "Insitu Metallographic Inspection of WHB 601 Header." *206-01-08-17682*, Canspec Material Engineering, Edmonton.

[3] Canspec. (2001). "Examination of Elbow from WHB 601 Header." *206-01-05-17495*, Canspec Material Engineering, Edmonton.

[4] Wiesberg, H. "Report on High-Temperature Pipe Weld investigation." *Graphitization of Steel Piping*, New York.

[5] Thielsch, H., Phillips, E., Jerome, E. Jr. (1955). "Considerations in the Evaluation of Graphitization in Piping Systems. Graphitization in Piping." *Welding Journal*, 34.

[6] Hoyt, S., Williams, R., Hall, A. (1946). "Summary Report on the Joint E.E.I.-A.E.I.C. Investigation of Graphitization of Piping." *Transactions of the ASME*, 68.

[7] Wilson, J. (1957). "Graphitization of Steel in Petroleum Refining Equipment." Bulletin 32, Welding Research Council.

[8] ASME. (1998). "Section IX, Qualification Standard for Welding and Brazing Procedures." ASME Boiler and Pressure Vessel Code, ASME.

[9] ASME. (1977). " Section II, Part A: Ferrous Material Specifications." ASME Boiler and Pressure Vessel Code, ASME.

[10] ASTM (2002). "A106-99 Standard specification for seamless Carbon steel pipe for High-temperature service." Steel--Piping, Tubing, Fittings, ASTM International, West Conshohocken.

[11] ASTM (2002). "A234/A234M-04 Standard Specification for Piping Fittings of Wrought Carbon Steel and Alloy Steel for Moderate and High Temperature Service." Piping, Tubing, Fittings, ASTM, West Conshohocken.

[12] Peachy, J. (2003). "RE: A234 Elbows." E. Vokes, Personal Communication. Tube Forgings of America, Portland Oregon.

[13] ASTM (2002). "A105-99 Standard specification for Carbon Steel Forgings for Piping Applications." Steel--Piping, Tubing, Fittings, ASTM International, West Conshohocken.

[14] Parker, J. "Life Assessment of Power Plant Components Operating in the Creep Range." *Third International Conference on Creep and Fracture of Engineering Materials and Structures*, Swansea.

[15] Samuels, L. (1999). *Optical Microscopy of Carbon Steels*, American Society for Material, Materials Park.

[16] Eberle, F. (1946). "Influence of Heat-treatment Upon the Susceptibility to Graphitization of High-Aluminum-Deoxidized Carbon Molybdenum." *Transactions of the ASME*, 42.

[17] Emerson, R., Morrow, M. (1946). "Further Observation of Graphitization in Aluminum-Killed Carbon-Molybdenum-Steel Steam Piping." *Transactions of the ASME*, 42.

[18] Wilson, J. (1957). "The Effect of Graphitization of Steels on Stress-Rupture Properties." Bulletin 32, Welding Research Council.

[19] Emerson, R. "Carbide Instability in Carbon-Molybdenum-Steel Steam Piping." *Report on High-Temperature Pipe Weld investigation. Graphitization of Steel Piping*, New York.

[20] Smith, A., Urban, J., Bolton, J. (1946). "Graphitization in some Cast Steels." *Transactions of the ASME*, 42.

[21] Kerr, H., Eberle, F. "Graphitization Caused by Testing Conditions on Carbon - Molybdenum Tubular Creep Specimens." *Graphitization of Steel Piping*, New York.

[22] Zhukov, A. (1987). "New trends in the theory of graphitization. The electron structure of graphitization systems." *Met-Sci-Heat-Treat*, 29(1-2).

[23] l'inkii, V., Zhukov, A., Kostyleva, L., Adbullaev, E. (1990). "Recent Advances in the Graphitization Theory. Relationship between Primary and Secondary Crystallization of Graphitizing Iron-Carbon Alloys." *Met-Sci-Heat-Treat*, 30(9-10).

[24] Kobota, K. (1986) "Kinetics of Graphitization of Cementite". *Transactions of Japan Institute of Metals.* 27

[25] Smith, A., Urban, J., Bolton, J. (1946). "Graphitization in some Cast Steels." *Transactions of the ASME*, 42.

[26] Seth, B. "Effect of Aluminums on Creep Ductility of 1 Cr-1 Mo-0.25 V Steam Turbine Rotors." *International Conference on Engineering Aspects of Creep*, Sheffield; England.

[27] Port, R., Mack, W., Hainsworth, J. "The Mechanisms of Chain Graphitization of Carbon and Carbon/Molybdenum Steels. Heat Resistant Materials." *Heat Resistant Materials. Proceedings of the First International Conference*, Fontana.

[28] Smith, W. (1981). *Structure and Properties of Engineering Alloys*, McGraw Hill, New York.

[29] ASM. (1998). "Materials Characterization." ASM Handbook, R. e. a. Whan, ed., ASM International.

[30] Smithells, C. (1997). *Smithells Metals Reference Book*, ASM International.

[31] Reed-Hill, R., Abbachian, R. (1991). *Physical Metallurgy Principles*, PWS, Boston.

[32] Porter, D. (1992). *Phase Transformations in Metals and Alloys*, Chapman and Hall, New York.

[33] Foulds, J., Viswanathan, R. (2001). "Graphitization of Steels in Elevated-Temperature Service." *Journal of Materials Engineering and Performance*, 10(4).

[34] Furtado, H., Le May, I. (2003). "Evaluation of Unusual Superheated Steam Pipe Failure." *Materials Characterizaion*, 49.

[35] Bidash, V., Prikhod'ko, A. (1987). "Graphitization of Low-Carbon Steel During a Spheroidizing Anneal." *Met-Sci-Heat-Treat*, 29(1-2).

[36] Bel'chenko, G., Shevtsov, A., Prikhod'ko, A. (1990). "Structure and Mechanical Properties of Graphitized Low-Carbon Steel with working." *Met-Sci-Heat-Treat*, 32(3-4).

[37] Kanter, J. (1946). "Studies on the Susceptibility of Casting Steels to Graphitization." *Transactions of the ASME*, 42.

[38] Smith, G., Brambir, S., Benz, W. (1946). "Comparative Graphitization of Some Low-Carbon Steels With and without Molybdenum and Chromium." *Transactions of the ASME*, 42.

[39] Smith, G., Dulis, E., Royle, B. (1955). "Effect of Pretreatment of Martensite on Subsequent Graphitization at 1200°F. Graphitization in Piping." *Welding Journal*, 34.

[40] Neri, M., Colas, R. Valtierra, S. (1998). "Graphitization in High Carbon Commercial Steels." *Journal of Materials Engineering and Performance*, 7(4).

[41] Pavlichko, W., Solomon,A. "Graphitization Studies at Fossil Fuel Power Plants." *12th Annual Technical Meeting of the International Metallographic Society*, Taminment.

[42] Port, R., Mack, W., Hainsworth, J. "The Mechanisms of Chain Graphitization of Carbon and Carbon/Molybdenum Steels. Heat Resistant Materials." *Heat Resistant Materials. Proceedings of the First International Conference*, Fontana.

[43] Yang, J. (1999). "Influence of Graphitization on Phase Transformation," Oregon Graduate Institute of Science and Technology, Beaverton.

[44] Creamer, E. (1980). "Metallurgical Condition of Several Steels after Long-Term, Elevated Temperature Exposure." MPC 12, ASME, New York.

[45] Ibarra, S. (1980). "On-site Metallurgical Evaluation of an FCCU Reactor." MPC 12, ASME, New York.

[46] Townsend, R. "Mechanisms of High Temperature Structural Degradation and Techniques of Life Prediction." *First International Conference on Microstructures and Mechanical Properties of Aging Materials*, Chicago.

[47] Bolton, C., Dyson, B., Williams, K. (1980). "Metallographic Methods of Determining Residual Creep Life." *Materials Science and Engineering*, 46.

[48] Goodall, I., Ainsworth, R. "Failure of Structures by Creep." Third International Conference on Pressure Vessel Technology. Part II: Materials and Fabrication, Houston.

[49] Port, R. "Non-Weld related Graphitization Failures." *Corrosion 89*, St Louis.

[50] Grant, N. (1965). "Stress Rupture Testing." Deformation and Fracture at High Temperature, N. Grant, Nicholas, J., Mullendore, A., ed., MIT press, Cambridge.

[51] Orr, R., Sherby, O., Dorn, J. (1954). "Correlation of Rupture Data for Metals at Elevated Temperatures." *Transactions of the ASME*, 76.

[52] Ennis, P. (1995). "A Comparison of the Creep Rupture Behavior of New and Service Exposed Low Alloy Steels." *Materials at High Temperatures*, 13(2).

[53] Frost, H., Ashby, M.F. (1982). Deformation-Mechanism Maps: The Plasticity and Creep of Metals, Pegamon, Oxford.

[54] Larson, F., Miller, J. (1952). "A Time Temperature Relationship for Rupture and Creep Stresses." *Transactions of the ASME*, 74.

[55] Conway, J. (1965). *Stress Rupture Parameters: Origin, Calculation and Use*, Gordon and Breach Science Publishers, New York.

[56] Manson, S., Haferd, A. (1953). "A linear Time-Temperature Relation for the Extrapolation of Creep and Stress Rupture Data." *NACA Technical note*, 2890.

[57] ASTM (1971). DS11S1 An Evaluation of the Elevated Temperature Tensile and Creep Rupture Properties of Wrought Carbon Steel , ASTM Philidelphia.

[58] API 530. (1988). *Calculation of Heater Tube Thickness in Petroleum Refineries*, American Petroleum Institute, Washington.

[59] Zuo, M., Chiovelli, S., Nonanka,Y. (1994). "Fitting Creep Rupture Data using Accelerated Life Testing Data." *Journal of Pressure Vessels and Piping*, 122.

[60] Voorhees, H., Prager, M. (1990). "Assessment and Use of Creep Rupture Properties." ASM Handbook: Mechanical Testing and Evaluation, R. B. Shipley, W., ed., ASM International, Materials Park.

[61] Viswanathan, R., Foulds, J. (1998). " Accelerated Stress Rupture Testing for Creep Life Prediction-Its Value and Limitations." *Journal of Pressure Vessel Technology*, 120.

[62] Viswanathan, R. (1989). Damage Mechanisms and Life Assessment of High Temperature Components. ASM International, Materials Park.

[63] Monkman, F., Grant, N. (1956). "An Empirical Relationship between Rupture Life and Minimum creep Rate in Creep-Rupture Tests." Proceedings of ASTM, 56

[64] Evans, R., Wilshire, B. (1985). *Creep of Metals and Alloys*, Institute of Metals, London.

[65] Kachanov, L. M. (1986). "Introduction to Continuum Damage Mechanics." Mechanics of Elastic Stability, Dordrecht.

[66] Leckie, F. A., Hayhurst, D. (1974). "Creep Rupture of Structures." *Proceedings of the Royal Society London Series A*, 340.

[67] Leckie, F. A. (1978). "The Constitutive Equations of Continuum Creep Damage Mechanics." *Philosophical Transactions of the Royal Society Series A*, 288.

[68] Leckie, F. A., Hayhurst, D. (1974). "Creep Rupture of Structures." *Proceedings of the Royal Society London Series A*, 340.

[69] Leckie, F. A. "Creep Data and Design Decisions." *The Presentation of Creep Strain Data*, London.

[70] Prager, M. (2000). "The Omega Method-An Engineering Approach to Life Assessment." *Journal of Pressure Vessel Technology*, 122.

[71] Prager, M. (1995). "Development of MPC Omega Method for Life Assessment in the Creep Range." *Journal of Pressure Vessel Technology*, 117.

[72] Klehn, R., Laughlin, C. (1994). "Cheveron's Experience Using Omega Creep Test Methods for Life Assessment of Refinery Equipment." *Pressure Vessels and Piping*, 288.

[73] Ibarra, S., Konet, R. (1994). "Life Assessment of 1 ¼ Cr- ½ Mo Steel Catalytic Reformer Tubes Using the MPC Omega Method." *Pressure Vessels and Piping*, 288.

[74] McLean, M., Dyson B. (2000). "Modeling the Effects of Damage on Microstructure Evolution on the Creep Behaviour of Engineering Alloys." *Journal of Engineering Materials and Technology*, 122.

[75] Neubauer, B. "Criteria for Prolonging the Safe Operation of Structures Through the Assessment of the Onset of Creep Damage using Non destructive Metallographic Methods." *Proceedings of Creep and Fracture of Engineering Materials and Structures*, Swansea.

[76] Neubauer, B., Wedel, U. "Restlife Estimation of Creeping Components by Means of Replicas." *International Conference on Advances in Life Prediction Methods*, New York.

[77] Westwood, H., Clark, M. (1995). "Metallographic Methods for Creep Life Assessment of Plant Components." *Materials at High Temperatures*, 13(3).

[78] Bolton, C., Dyson, B., Williams, K. (1980). "Metallographic Methods of Determining Residual Creep Life." *Materials Science and Engineering*, 46.

[79] Le May, I., Da Silveira, T., Cheung-Mak, K. (1994). "Uncertainties in the Evaluation of High Temperature Damage in Power Stations and Petrochemical Plants." *International Journal of Pressure Vessels and Piping*, 59.

[80] Viswanathan, R. (2000). "Life Management of High-Temperature Piping and Tubing in Fossil Fuel Plants." *Journal of Pressure Vessel Technology*, 122.

[81] Storesund, J., Tu, S. (1995). "Geometric Effect of Creep on Cross Weld Specimens." *International Journal of Pressure Vessels and Piping*, 62.

[82] Gandy, D., Findlan, S., Viswanathan, R. (2000). "Weld Repair of Steam Turbine Casings and Piping-An Industry Survey." *Journal of Pressure Vessel Technology*, 122.

[83] Anderson, T. (1995). Fracture Mechanics. Fundamentals and Applications, CRC, New York.

[84] Yoshimitsu, A., Prager, M. (2002). "Proposal of a New Concept on Creep Fracture Remnant Life for a Precracked Specimen." *Materials at High Temperatures*, 16.

[85] Nikbin, K. "Role of R5 in European Assessment Practice." MPC/PVRC Workshop on Elevated Temperature Behaviours and Life Assessment of Components in the Creep Range, Houston.

[86] Patel, R. (2003). "Creep Life of Welded Trunnion and Branch Components using the R5 Procedure." *International Journal of Pressure Vessels and Piping*, 80.

[87] Grujic, B., Sedmak, S., Burzic, Z., Sedmak, A. (1999). "Crack growth resistance of Creep Damaged Material." *Facta Univesitatis. Mechanics, Automatic Control and Robotics*, 2(9).

[88] Nikbin, K., Smith, D., Webster, G. "Influence of Creep Ductility and Stress on Creep Crack Growth." *International Conference on Advances in Life Prediction Methods*, New York.

[89] Huang, F. (1982). "Bend Testing for Miniature Disks." *Nuclear Technology*, 57

[90] Baik, J., Kameda, J., Buck, O. (1986). "Development of the Small Punch Test for Ductile-Brittle Transition Temperature Measurement of Temper Embrittled Ni-Cr Steels." The Use of Small Scale Specimens for Testing Irradiated Samples ASTM STP 288, W. L. Corwin, G, ed., ASTM, Philadelphia.

[91] Fleury, E. Ha., J. (1998). "Small Punch Tests to Estimate the Mechanical Properties of Steels for Steam Power Plant: I. Mechanical Strength." *International Journal of Pressure Vessels and Piping*, 75.

[92] Bullock, J. (1998). "Toughness Losses in Low Alloy Steels at High Temperatures: An Appraisal of Certain Factors Concerning the Small Punch Test." *International Journal of Pressure Vessels and Piping*, 75.

[93] Parker, J., Wilshire, B. (1992). "Non-destructive Life Assesment of High Temperature Components." *International Journal of Pressure Vessels and Piping*, 50.

[94] Endo, T. (1994). "Progress in Life Assessment and Design Methodology for Fossil Fuel Plant Components." *International Journal of Pressure Vessels and Piping*, 57.

[95] Root, J., Katsaras, J., Porter, J., Leitch, B. (2002). "Neutron Diffraction Maps of Stress Concentration Near Notches Under Load at Temperature." *Journal of Pressure Vessel Technology*, 124.

[96] Smallman, R., Ashbee, K. (1966). *Modern Metallography*, Peragamon, Oxford.

[97] API 579. (2000). *Recommended Practice for Fitness-for-Service*, American Petroleum Institute, Washington.

[98] Anderson, T., Osage, D. (2000). "API 579 A Comprehensive Fitness-For-Service Guide." *International Journal of Pressure Vessels and Piping.*, 77.

[99] ASTM. (2002). E 1180-87 Standard Practice for Preparing Sulfur Prints for Macrostructure examination, ASTM International, West Conshohocken.

[100] ASTM. (2002). "A370-02e1 Standard Test Methods and Definitions for Mechanical Testing of Steel Products." Mechanical Testing; Elevated and Low-Temperature Tests; Metallography, ASTM International, West Conshohocken.

[101] ASTM. (2002). E21-03a Standard Test Methods for Elevated Temperature Tension Tests of Metallic Materials, ASTM International.

[102] ASTM. (2002). E 139 Standard Test Methods for Elevated Temperature Tension Tests of Metallic Materials, ASTM International.

[103] ASTM (2002). E1820-01 Standard Test Method for Measurement of Fracture Toughness, ASTM International, West Conshohocken.

[104] BSI (1991) PD 7448 Fracture Mechanics Toughness Tests

[105] Meyers, M., Chalwa, K. (1984) MECHANICAL METALLURGY Principles and Applications. Prentice Hall

13.APPENDICES

APPENDIX A Total Piping Schematic

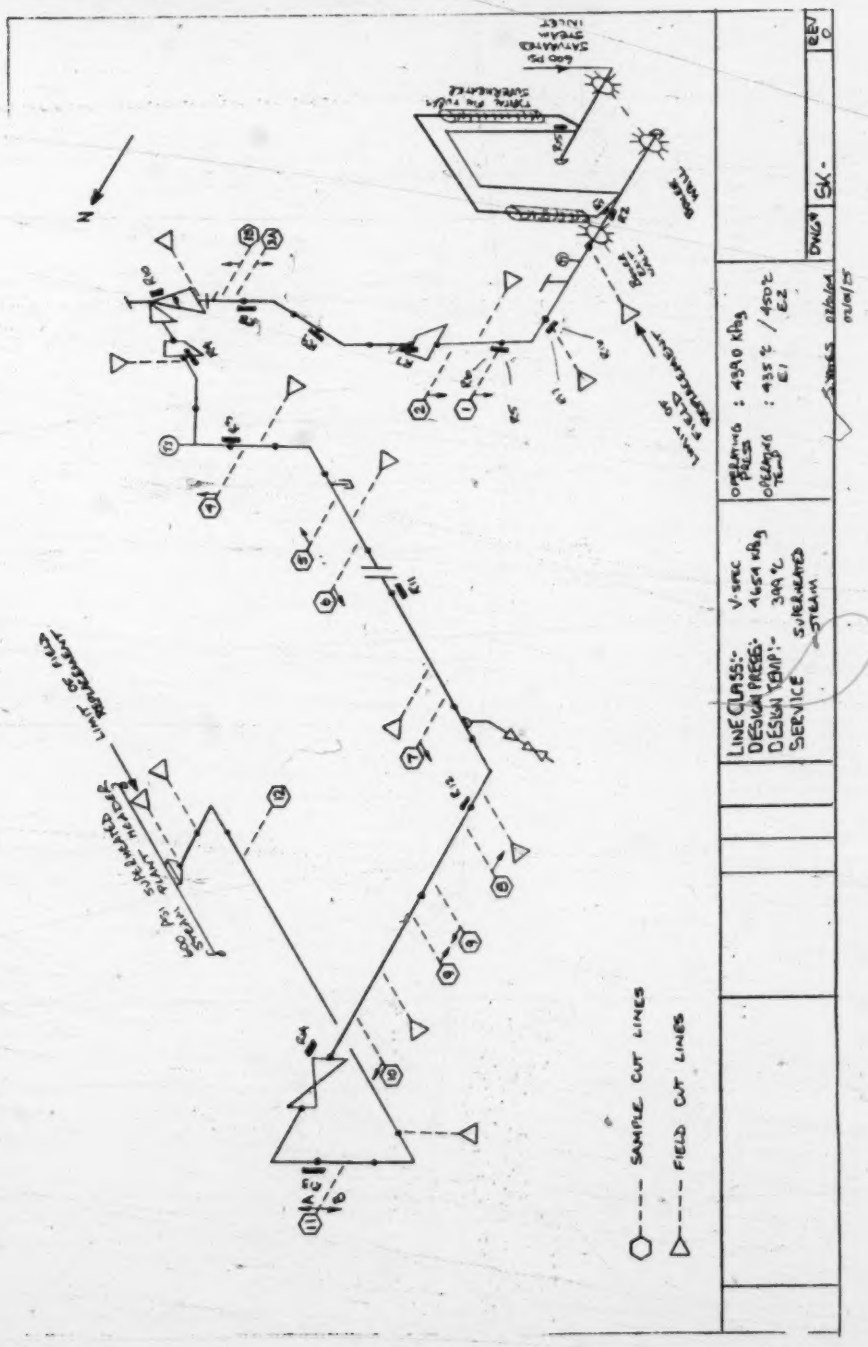

APPENDIX B Representative Microstructures

These micrographs are not representative of graphitization but rather are representative of the degraded pearlite and areas the show fewest scratches from decohesion of graphite from the matrix while polishing

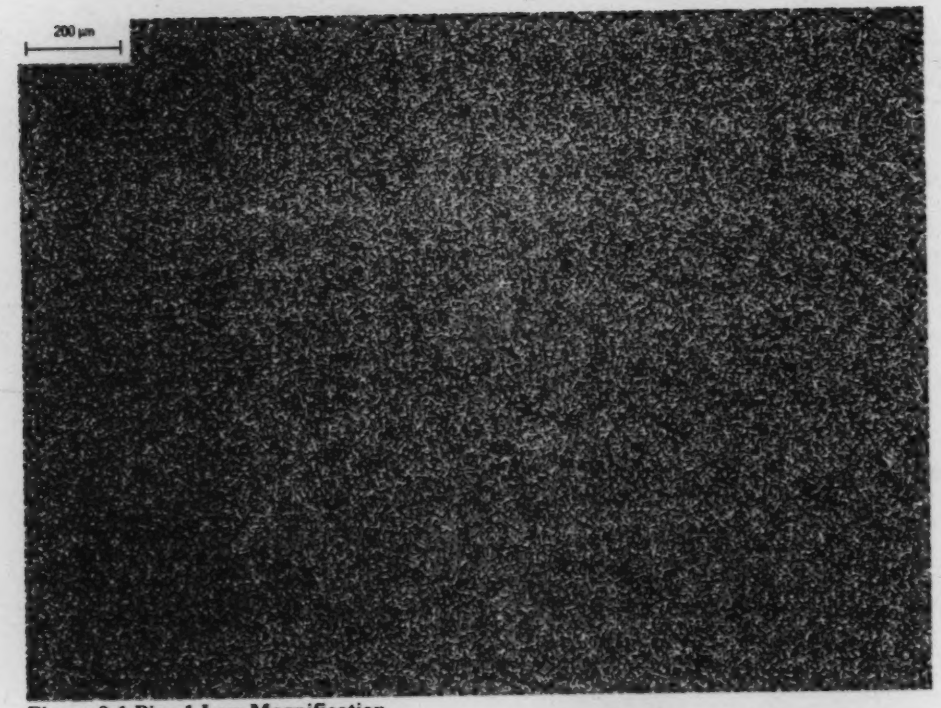

Figure 0-1 Pipe 1 Low Magnification

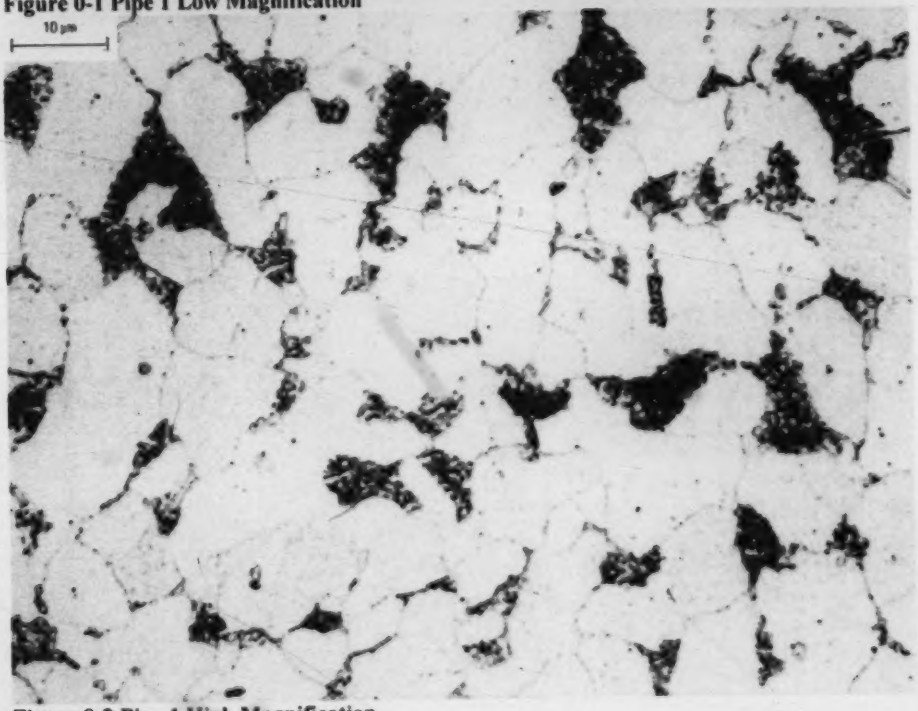

Figure 0-2 Pipe 1 High Magnification

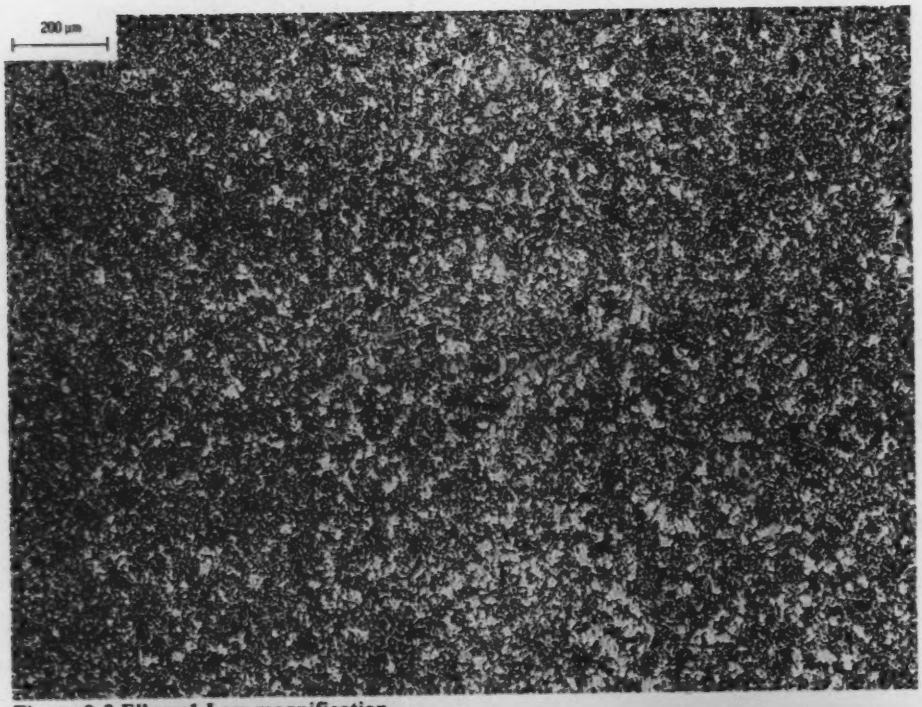

Figure 0-3 Elbow 1 Low magnification

Figure 0-4 Elbow 1 High magnification

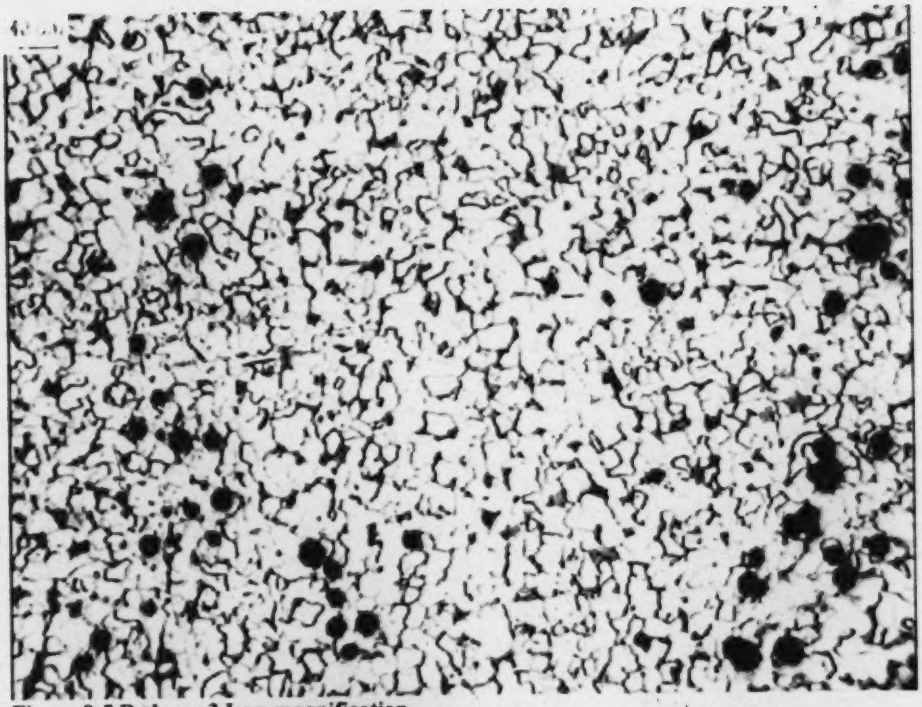

Figure 0-5 Reducer 3 Low magnification

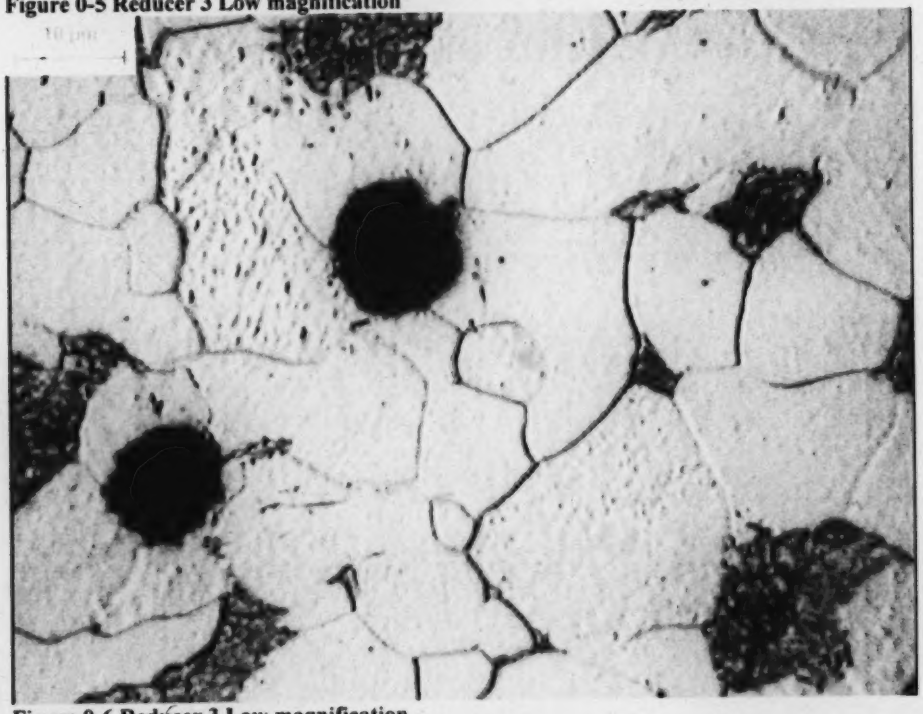

Figure 0-6 Reducer 3 Low magnification

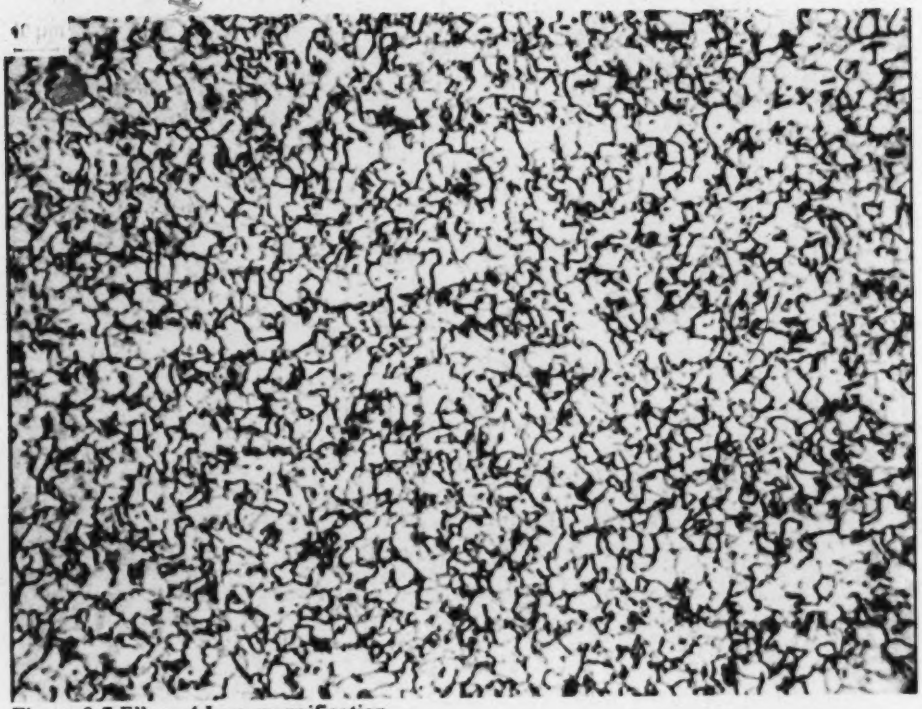

Figure 0-7 Elbow 4 Low magnification

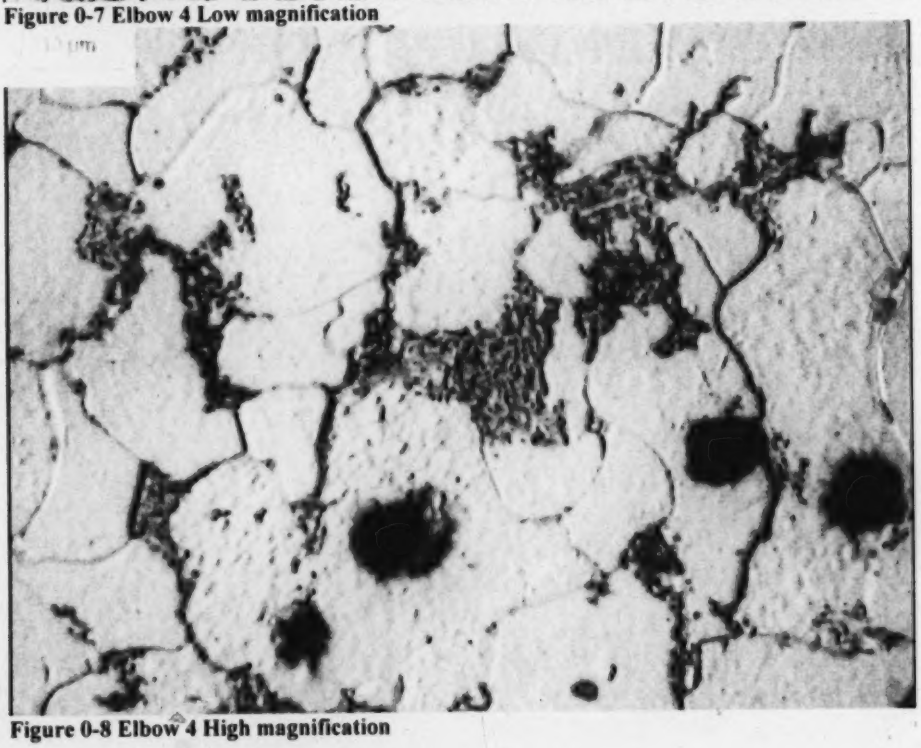

Figure 0-8 Elbow 4 High magnification

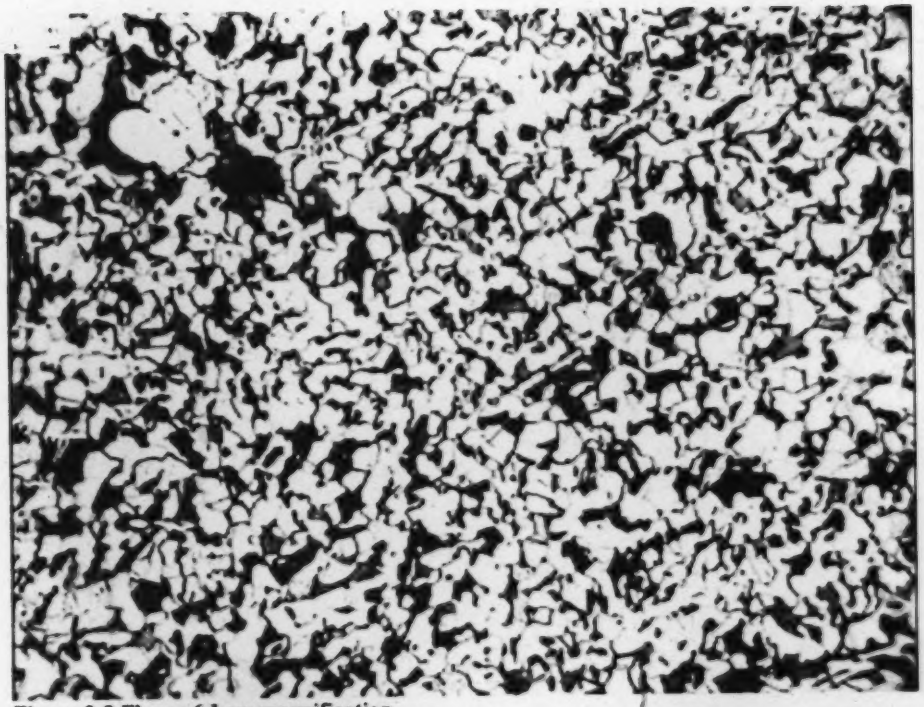

Figure 0-9 Flange 6 Low magnification

Figure 0-10 Flange 6 High magnification

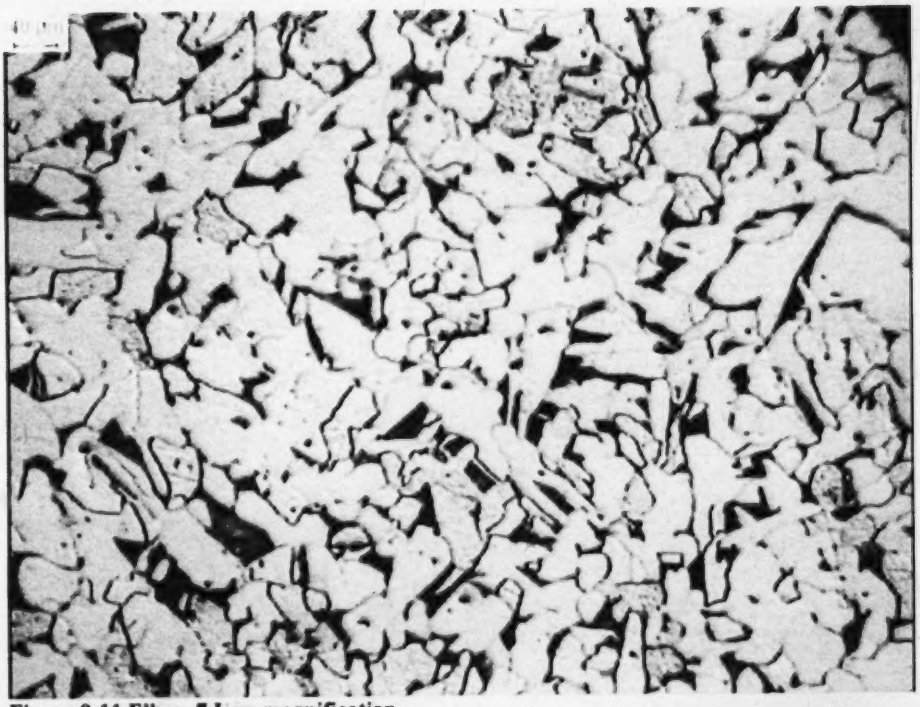

Figure 0-11 Elbow 7 Low magnification

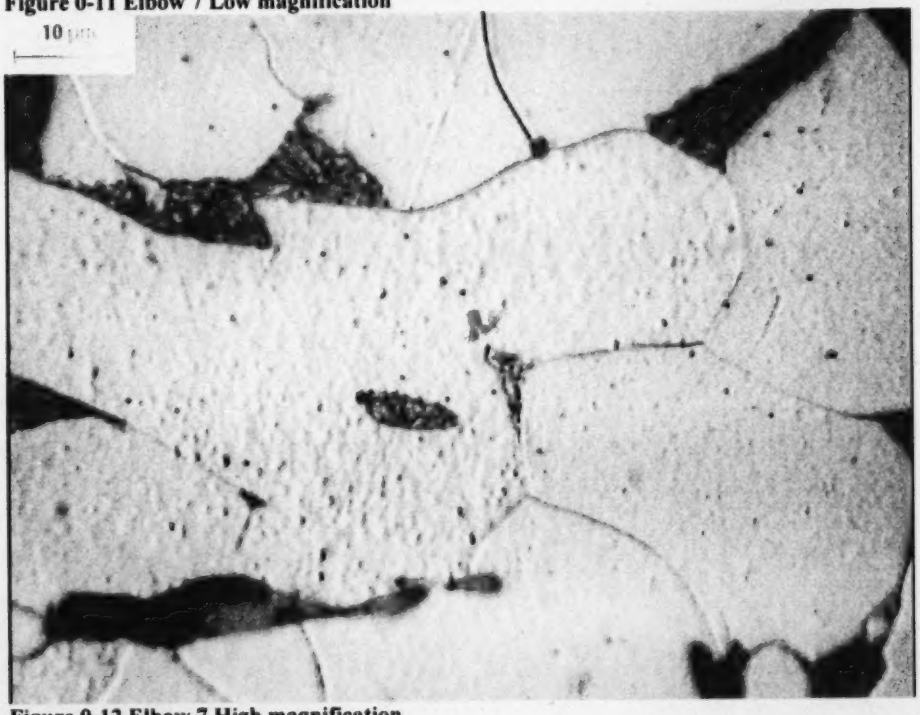

Figure 0-12 Elbow 7 High magnification

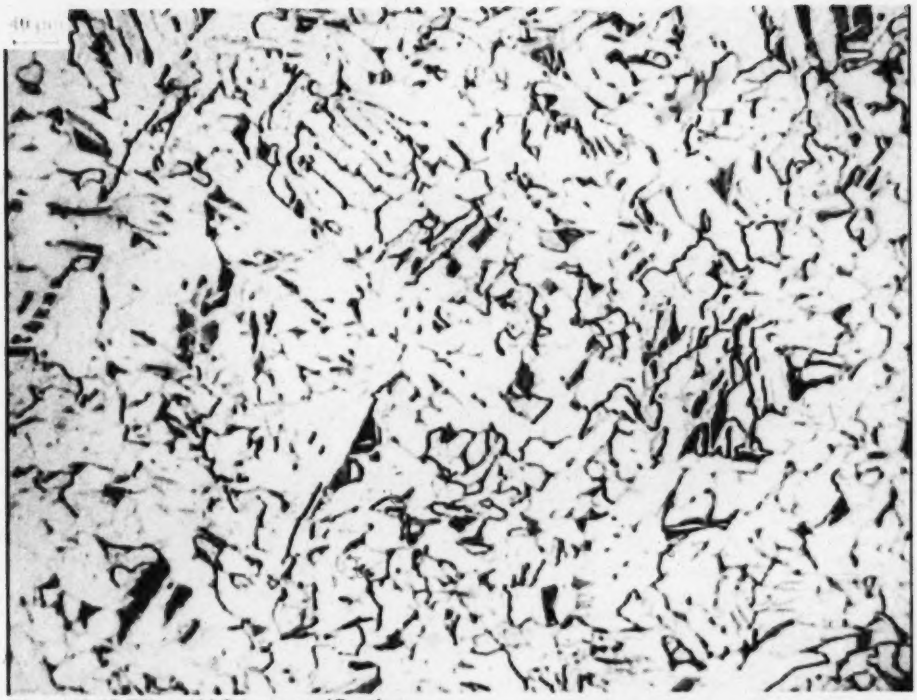

Figure 0-13 Elbow 11 Low magnification

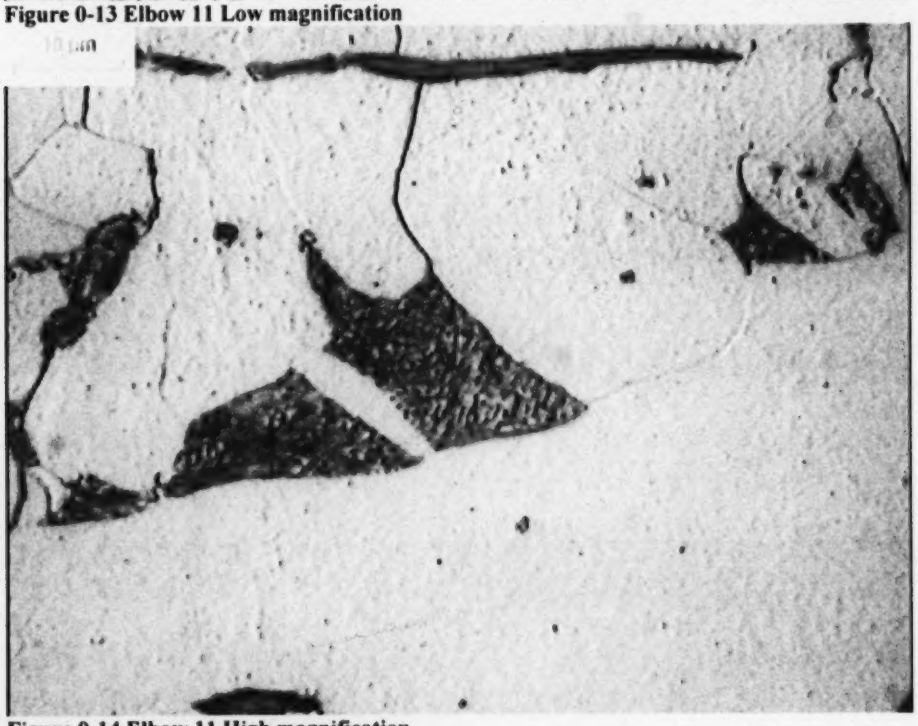

Figure 0-14 Elbow 11 High magnification

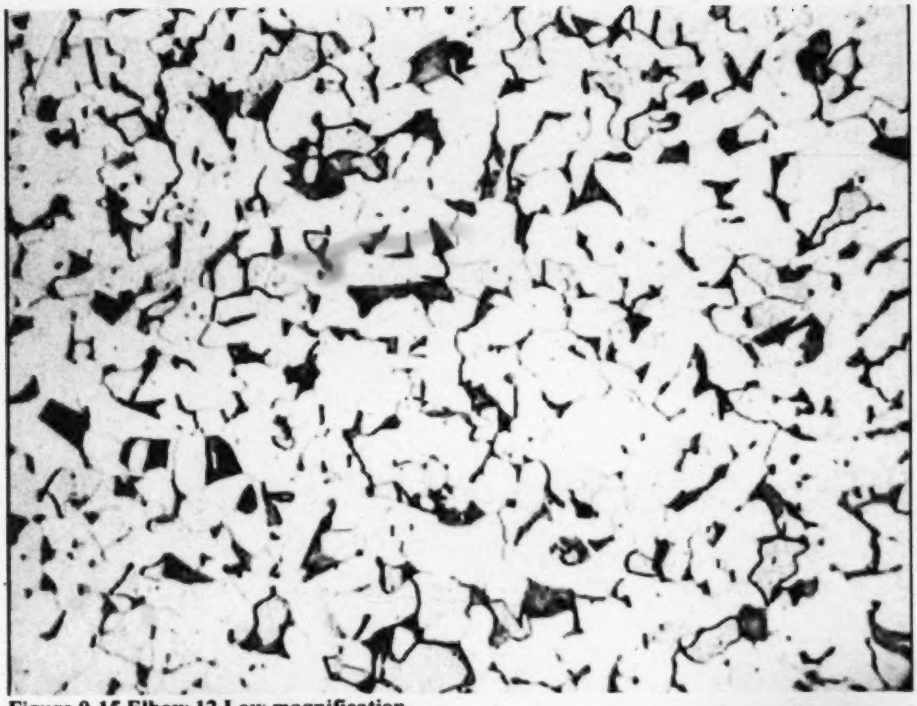

Figure 0-15 Elbow 12 Low magnification

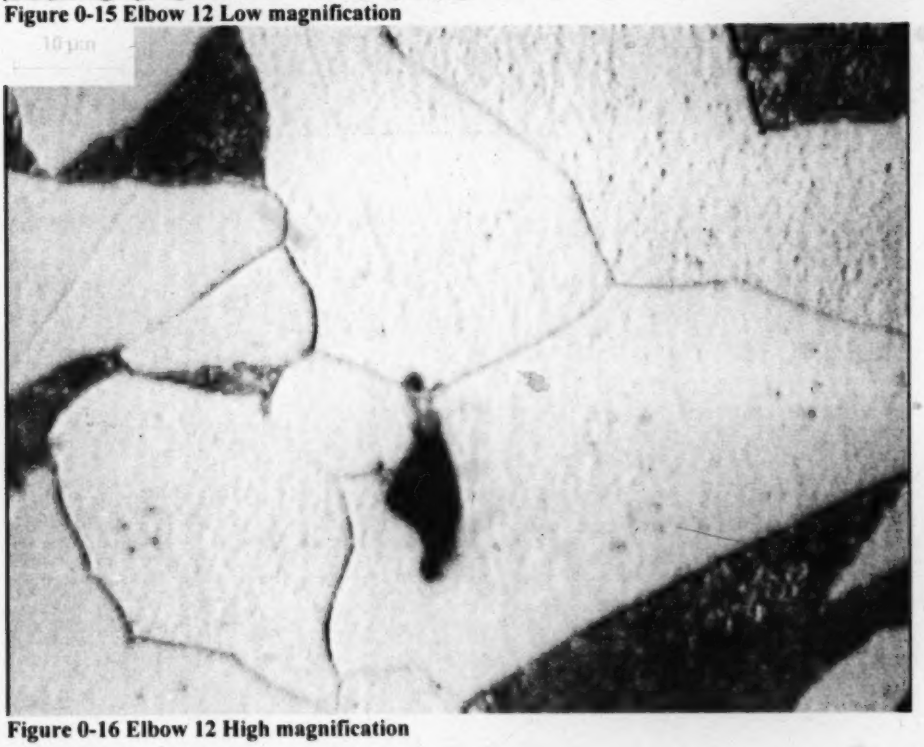

Figure 0-16 Elbow 12 High magnification

APPENDIX C

Pictures used to assemble macrographs

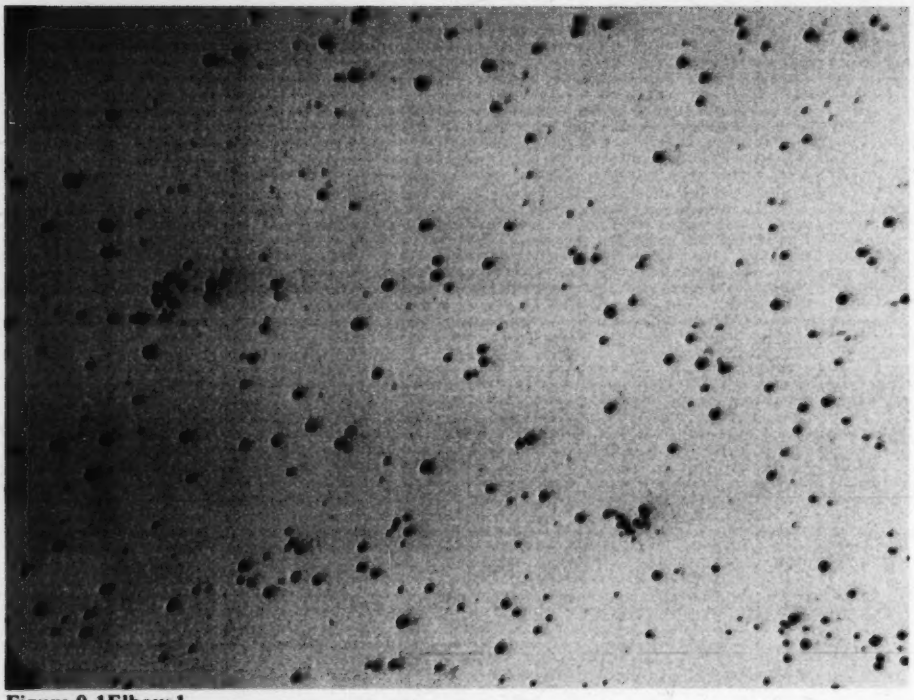

Figure 0-1Elbow 1

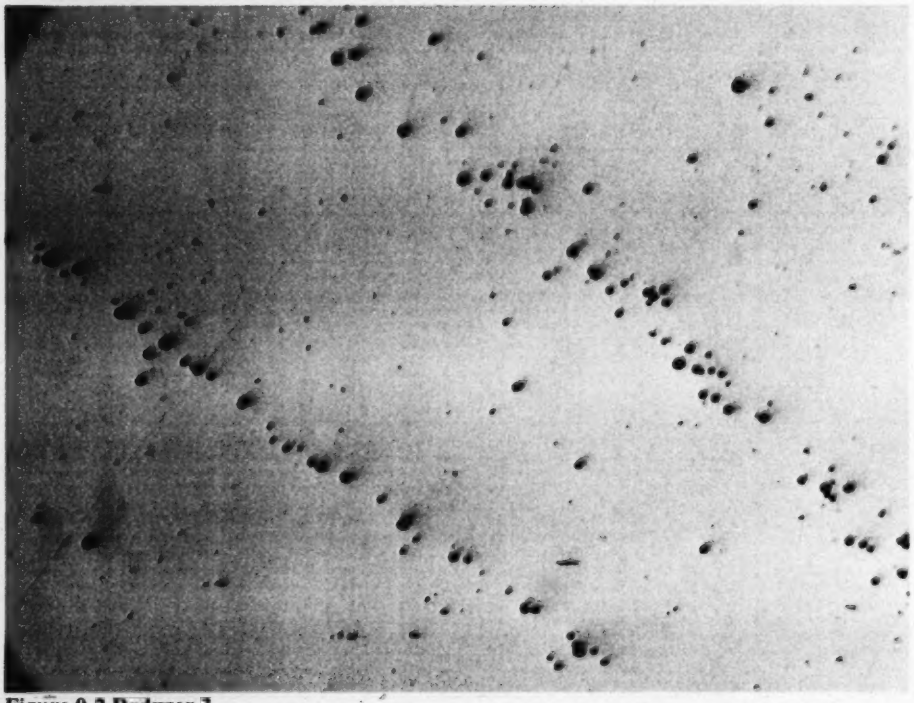

Figure 0-2 Reducer 3

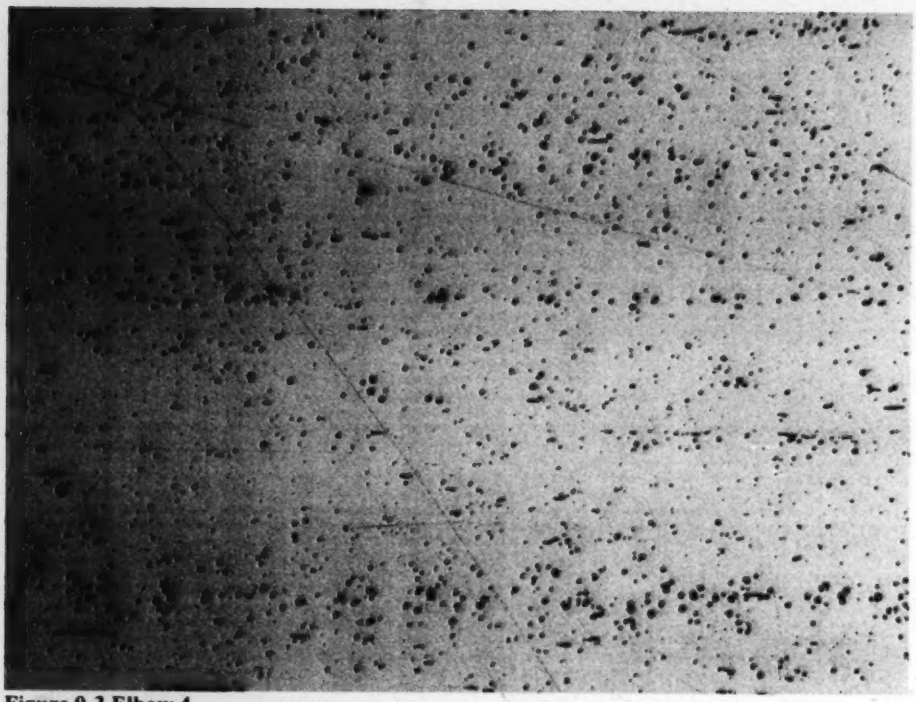

Figure 0-3 Elbow 4

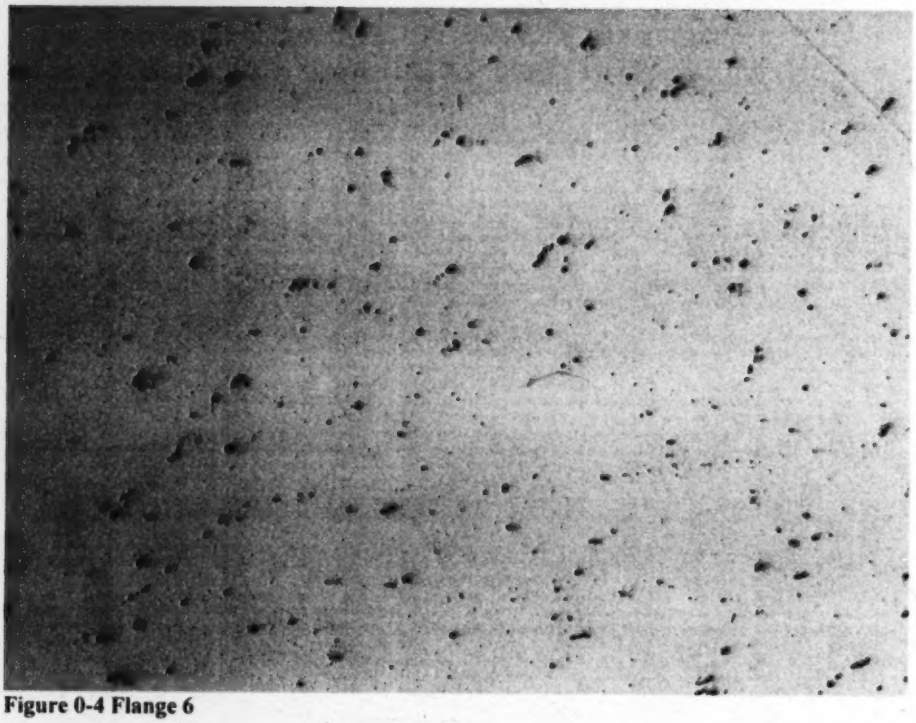

Figure 0-4 Flange 6

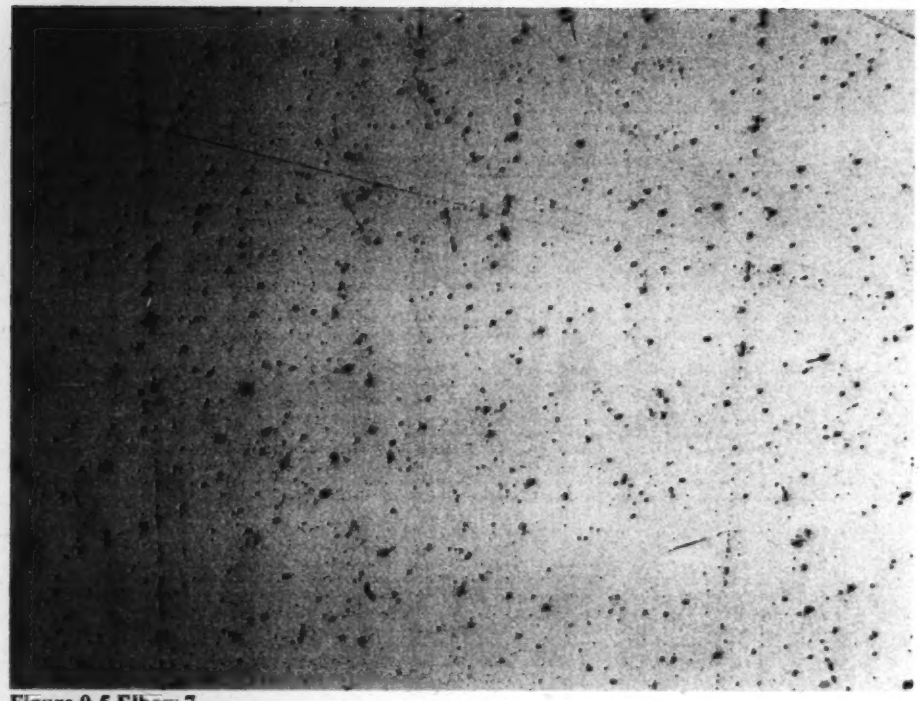

Figure 0-5 Elbow 7

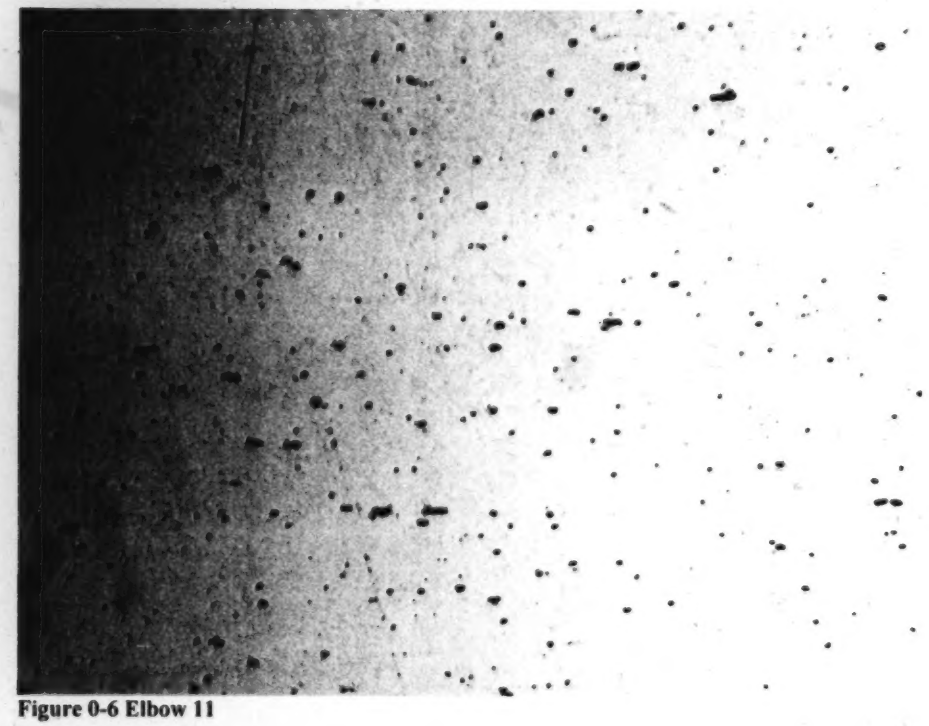

Figure 0-6 Elbow 11

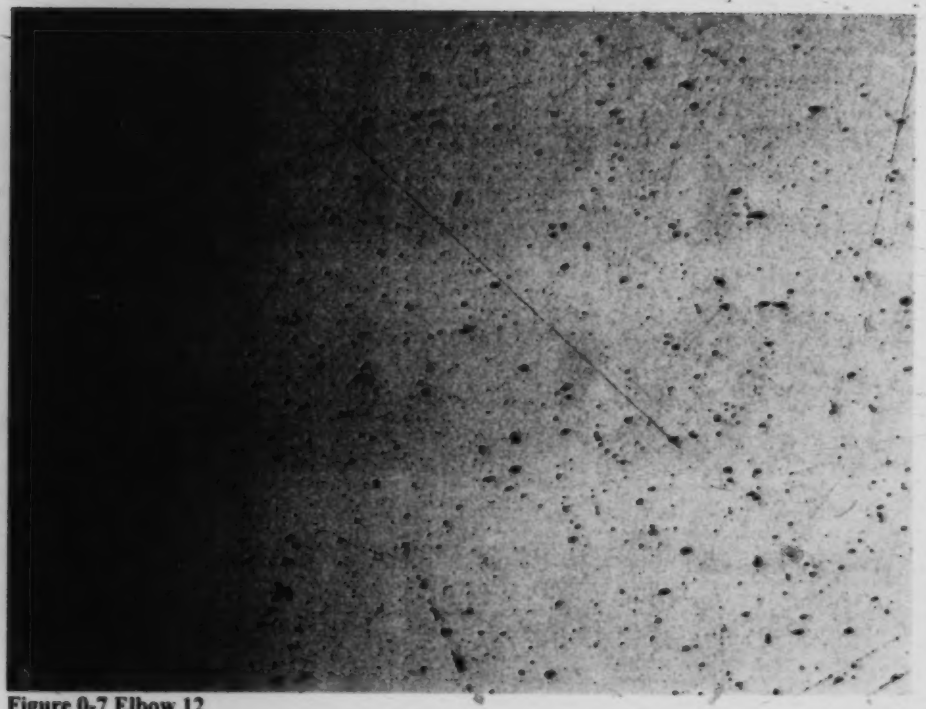

Figure 0-7 Elbow 12